MINERAL PROSPECTING VIA BIOGEOCHEMICAL SIGNALS AND SURFACE INDICATORS USING HYPERSPECTRAL REMOTE SENSING

A thesis presented in partial fulfilment of the requirements for the degree of

Doctor of Philosophy in Earth Science

At Massey University, Palmerston North, New Zealand

Rupsa Chakraborty

2022

Abstract

Preliminary steps of mineral exploration have traditionally included drilling and other destructive, expensive, and time-consuming techniques. To meet the ever-increasing demand for mineral resources pertaining to the increase in population and technological demand, it is very important to develop environmentally friendly, faster, and cheaper prospecting methods. In this study, we have targeted three known regions of mesothermal gold mineralisation in the South Island, New Zealand to develop hyperspectral remote sensing-based prospect models combined with biogeochemical data. The three study sites have geological similarities around the gold mineralisation including the major pathfinder elements. On the contrary the environmental settings, and other surficial and near-surface processes including the soil and groundwater interactions with the host rock, are vastly different. This led to a wide variation in the physico-chemical properties of the soil cover and the subsequent uptake by the overlying vegetation.

The *Pinus radiata* plantation at the Hyde-Macraes Shear Zone was the first study site to test the feasibility of using biogeochemical responses overlying the gold mineralisation through hyperspectral remote sensing for gold prospecting. *Pinus radiata* is known to be an accumulator of metals and metalloids with roots reaching as deep as the shear zone beneath it. The data showed a good spatial elemental trend along the shear zone for both the bark and the needle samples although the regression models performed much better with $R^2_{CV} > 0.7$ for the bark samples. After confirming the feasibility of utilising the vegetation cover as a medium, the second site in the Rise and Shine Shear Zone was examined to assess the limits of the airborne hyperspectral data over variably exposed soil. The potentially high As anomalies indicating the gold mineralisation were classified coupled with a thorough understanding of the soil cover and its relation to the lithology. The orthogonal total variation component analysis transformed data produced the best-performing models using random forest classification with an accuracy ~50% for the high concentration As zonation. Finally, the third study site in Reefton exhibited a multi-species natural forest overlying the gold mineralisation. Apart from varying elemental responses among the different species the Reefton study area also manifested regions contaminated by previous mining activity which likely impacted the elemental uptake in the overlying vegetation. The regression models performed poorly but the spatial predictions rendered some valid correlations based on ground knowledge from previous studies.

Acknowledgement

I would like to extend my sincere gratitude to all the people who helped me throughout my PhD journey.

First and foremost, I am extremely grateful to my supervisor, Gabor Kereszturi for giving me this PhD opportunity and for being such an amazing mentor throughout the journey. His exceptional passion for the subject and work ethic created a very positive work environment. I also thank co-supervisor Patricia Durance for her consistent follow up and help in documenting all the way from Perth. I also thank my co-supervisors Reddy Pullanagari, Chris Anderson and Salman Ashraf for their invaluable advice and constant support. I would also like to thank, Dave Craw (University of Otago) for his assistance with data, fieldwork and feedback on the write-up. I thank Tom Ritchie from Hardie Pacific Ltd., Kim Bunting from Matakanui Gold Ltd. and Oceana Gold Ltd. for their help with fieldwork, access to data and permissions related to publications. Many thanks to Raoul Solomon at Massey University's Manawatu Imaging Centre for his assistance with the SEM-EDS analysis and Mark Lawrence from GNS Lower Hutt, Avalon for his assistance with the pXRF analysis. I also thank Hyperceptions Ltd. for procuring the AisaFENIX airborne hyperspectral data for the study sites. I thank all the staff and students of the Volcanic Risk Solutions group at Massey University for their help during the course, especially Mathew Irwin and Kate Arentsen for their help with technical glitches and software arrangements. I am thankful to the Ministry of Business, Innovation and Employment (MBIE)- Endeavour Fund- Smart Ideas: Assessing New Zealand's environmental and mineral indicators for their financial support. I also thank the examiners for their invaluable and insightful comments on the thesis.

I would like to thank my friends in Palmy who made the PhD journey and my stay here so beautiful and memorable, including Cecilia Rodriguez Gomez, Nidhi Shrivastav, Charline Lormand, Boglarka Nemeth, Carlos Santa Cruz, Daniel Uhle, Bernhard Auer, Aylin Sen, Daniel Coulthard and Ling Hu.

I am thankful to Ma, Baba, and Bhai for being my constant support system and keeping me motivated and bearing with me through all the hard days. I also thank my grandparents for their love and blessings

always guiding me through life. I thank my best friends in the world, Moumita, Rituparna and Arunima for their support, encouragement and for being such an important part of my life through thick and thin.

Finally, I thank my fiancé Parth Naik, for being my “rock”. Thank you for identifying the researcher in me and encouraging me to pursue a PhD. Covid made our rather difficult long-distance relationship even harder but it's only with your constant love and support that I can dream and achieve.

Table of Contents

List of Figures

1 List of Tables

List of Acronyms

ANN- Artificial neural network

ATCOR- Atmospheric and topographic correction model

BAC- Biological absorption coefficient

BRDF- Bidirectional reflectance distribution function

BSE- Back-scatter electron

CLR- Centred log-ratio

CR- Continuum removed

DN- Digital Number

EDS- Energy dispersive X-ray spectroscopy

ESAM- Extended spectral angle mapper

FLAASH- Fast Line-of-sight atmospheric analysis of spectral hypercubes

FLC - Fuzzy logic classifier

FOSRP- First order spectral roughness penalty

FOV- Field of view

FWHM- Full width half maximum

HMSZ- Hyde Macraes Shear Zone

IBD- Integrated band depth

ICA- Independent component analysis

ICP-ES- Inductively coupled plasma emission spectroscopy

ICP-MS- Inductively coupled plasma mass spectroscopy

IFOV-	Instantaneous field of view
KPLSR-	Kernel partial least squares regression
LASSO-	Least shrinkage and selection operator
LOOCV-	Leave one out cross validation
LPP-	Locality preserving projection
LWIR-	Longwave infrared
MLPP-	Modified locality preserving projection
MNF-	Minimum noise fraction
MSAM-	Modified spectral angle mapper
MWIR-	Midwave infrared
NDVI-	Normalised difference vegetation index
NWFE-	Non-parametric weighted feature extraction
OOB-	Out of bag
OSAM-	Optimised spectral angle mapper
OTVCA-	Orthogonal total variation component analysis
PCA-	Principal component analysis
PLS-	Partial least squares
ppm-	Parts per million (µg/g)
ppb-	Parts per billion (ng/g)
REE-	Rare earth elements
RF-	Random Forest

RFE-	Recursive feature elimination
RGB-	Red green blue
RMSE-	Root mean square error
RSSZ-	Rise and Shine Shear Zone
SAM-	Spectral angle mapper
SDA-	Semi-supervised discriminant analysis
SEGL-	Semi-supervised graph learning
SELF-	Semi-supervised Local Fisher’s Discriminant Analysis
SEM-	Scanning electron microscope
SFF-	Spectral feature fitting
SID-	Spectral information divergence
SNR-	Signal to noise ratio
SVM-	Support vector machine
SWIR-	Shortwave infrared
VIS-	Visible
VNIR-	Visible near infrared
XRF-	X-ray fluorescence

Chapter 1. Introduction

1.1 Mineral Prospecting

The demand for metals is exponentially rising due to the increase in population, technological demand and higher standards of living (Krausmann et al., 2018). In order to meet such demands, the mining industry needs to develop towards more sustainable and less destructive preliminary approaches that can discover new mineral resources. Effective mineral prospecting should be affordable while it should also be environmentally friendly (Farjana et al., 2019). Innovative solutions should be targeted to resolve legacy mining contamination issues, such as heavy metal contamination problems affecting the soil, the vegetation and the environment as a whole even after the lifespan of a mine (Choe et al., 2008).

Mineral exploration approaches have been becoming inherently multidisciplinary utilising various geophysical methods, such as resistivity survey, electrical conductivity survey, aero-magnetic survey, proton-magnetometer survey, gravity and audio-frequency magneto telluric and optical remote sensing (Hubbert, 1934; Sato and Mooney, 1960; Strangway et al., 1973; Sabins, 1999; Xiong et al., 2007; Christie, 2016). Complementing geophysical approaches, geochemical and element prospecting on rock, soil and plant can also give additional directions to delineate and discover new ore deposits (Butt et al., 2000; Anand et al., 2007; Rincheval et al., 2019b; Cohen et al., 2021). Both geochemical and geophysical exploration methods are data-driven and empirical in nature.

Geological and structural mapping of an area is the key to delineating a mineral resource (Peters, 1987; Pirajno, 2012; Christie, 2016). Mineral bodies with spatial exposures (e.g., Cuprite) have been utilised to test numerous state-of-the-art remote sensing techniques (Goetz et al., 1985; Kruse et al., 1993; Meer, 1996; van der Meer and Bakker, 1997). Presently, such well-exposed mineral resources are on the verge of exhaustion, and it calls for more advanced, sustainable, and non-invasive approaches for mineral prospecting (Dunn, 2007). Geologically the mineralised zones are constantly being chemically and physically altered due to processes such as erosion, groundwater circulation and chemical weathering (Cohen et al., 1987; Abbaszadeh and Hezarkhani, 2013; Simpson and Christie, 2019; Frutuoso et al., 2021). These processes integrate realms of the earth which broadens the parameters for reconnaissance surveys. One such important parameter is the chemical breakdown (or alteration) of the host rock, leading to the redistribution of leached elements within the soil and plants (King, 1984; Christie et al., 2019; Dunn and Christie, 2020; Cohen et al., 2021). The interactions among the (ore-bearing) bedrock, soil and plants have long been recognised and explored to locate mineral deposits (Warren et al., 1968; Dunn, 1986; Cohen and Rotman, 2005; Rincheval et al., 2019a; Cohen et al., 2021). Furthermore, mineral exploration studies using hyperspectral remote sensing have been testing ideas in the laboratory (Gomez et al., 2008; Rathod et al., 2015) and under airborne conditions (Rencz, 1989; Robson et al., 2013; Rogge, 2014; Cui et al., 2019; Lhotáková et al., 2021).

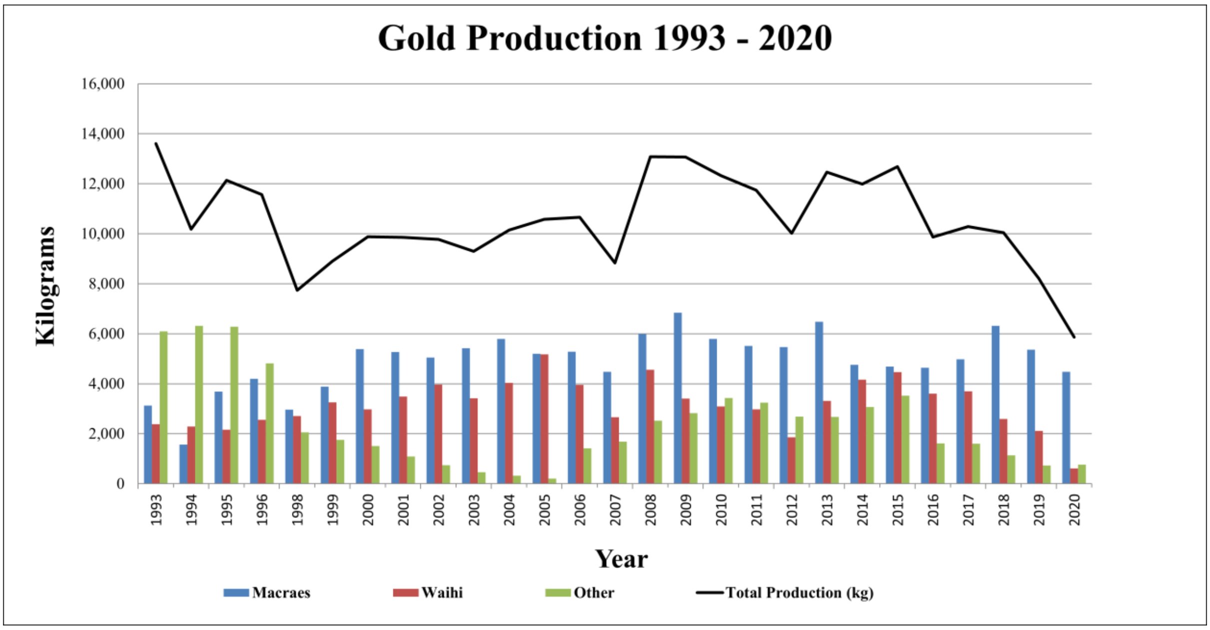

Figure 1.1: Gold production in New Zealand between 1993-2020. Source: New Zealand Petroleum and Minerals

Vegetation cover and rugged topography are the two main accessibility challenges obstructing gold exploration presently in New Zealand (Figure 1.1) (Christie, 2019), and also globally (Dunn, 1986; Ashton, 1989). This inflates the cost of exploration as well as can be intrusive to the environment (methods such as early drilling, and infrastructure development). Vegetation cover is the interference between the atmosphere and the lithosphere, and it resembles many properties of the underlying bedrock and soil (Brooks, 1979; Dunn, 1986; Kovalevsky, 1987; Haest, 2013; Cui et al., 2019; Dunn and Christie, 2020; Hedenquist and Arribas, 2021; McQueen et al., 2021). The elemental enrichments within the soil and the bedrock are subsequently accumulated by plants (Dunn, 1986; Dunn, 2007), representing a convenient medium to sample for mineral exploration. Thus, utilising the vegetation cover as a medium rather than considering it as a hindrance would bring a good balance to mineral exploration here and elsewhere (Cohen and Rotman, 2005). Biogeochemistry is a very important toolset that can help in bridging this gap (Cohen et al., 1987; Lintern et al., 2017). The source of water and nutrients for the plants come from the soil and the subsurface geology underneath which makes them an excellent on-surface accessible representation of the subsurface layers (Cohen et al., 1987; Rencz, 1989; Dunn, 2007). Mapping the important pathfinder elements defining the mineralisation halo through analysis of the covering vegetation using remote sensing can provide a versatile platform complementing existing mineral exploration methods (Cohen and Rotman, 2005; Anand et al., 2007; Dunn, 2007). In particular, hyperspectral remote sensing can be a powerful imaging platform to fully characterise vegetation cover.

1.2 Hyperspectral Remote Sensing

Remote sensing uses the electromagnetic spectrum and its various interactions with different objects, to gather information about the object without actual physical contact (Jensen, 1996). Multispectral, hyperspectral and LiDAR remote sensing, operates based on the reflective property of light. Multispectral remote sensing captures spectral information in discrete portions of the spectrum with a typical bandwidth of 30-100 nm (Habibi and Samulon, 1975; Habibi et al., 1993). On the contrary imaging spectroscopy, hyperspectral remote sensing, samples the electromagnetic spectrum in a large number of contiguous, narrow intervals, while the spectral bandwidth is often under 10 nm (Meyer et al., 2022). This imaging setup can generate large volumes of information (Kruse, 1998), making hyperspectral data a rich source of information (Figures 1.2 and 1.3). Many applications have been developed by harvesting the rich spectral information that hyperspectral data can capture, including environmental monitoring, mineral mapping, precision agriculture, food industry and ecological sciences (Huber et al., 2008; Pullanagari, 2012; Kopačková, 2014; Notesco et al., 2014a; Cheng and Sun, 2016; Lawley, 2016; Lorenz et al., 2021; Naik et al., 2021; Thiele et al., 2021a).

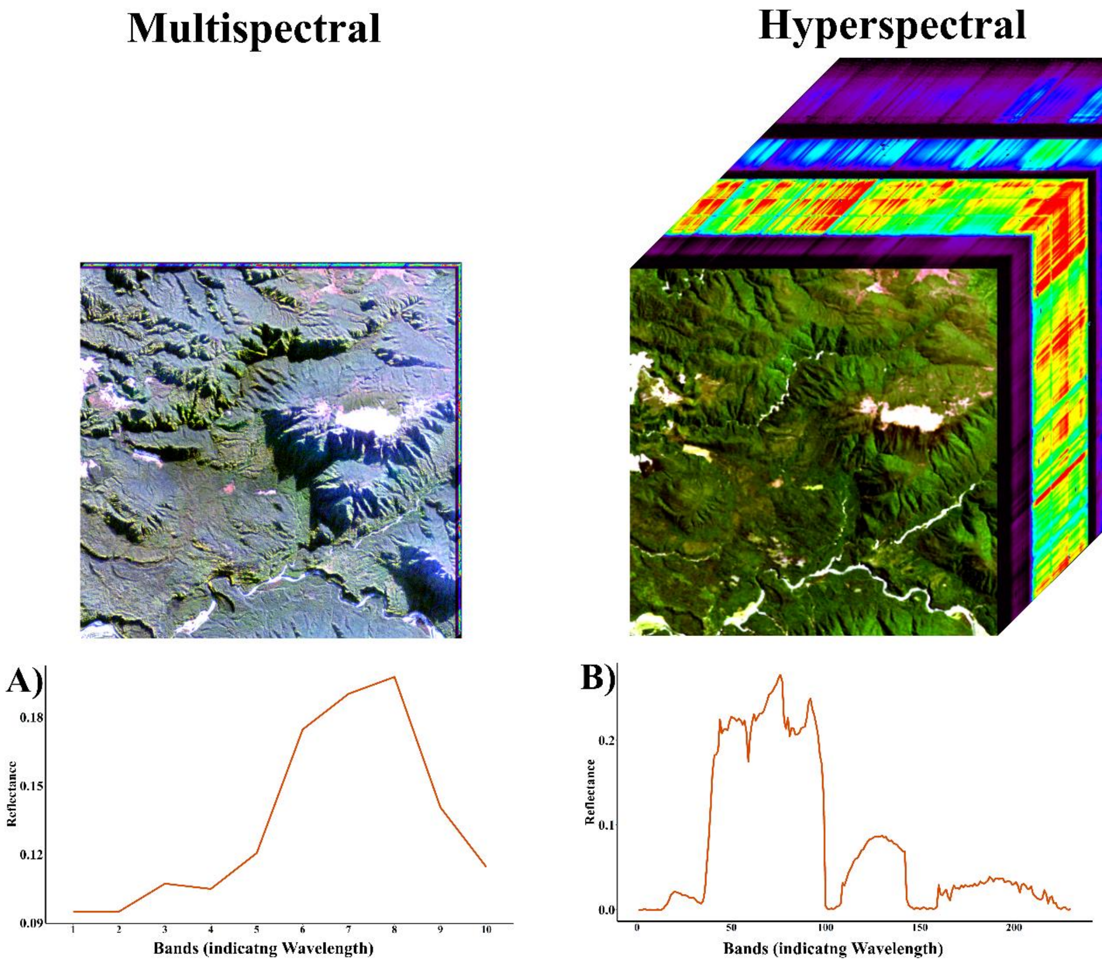

Figure 1.2: Multispectral (Sentinel 2A) image and hyperspectral (PRISMA) image compared against each other. A and B represent the vegetation spectra from multispectral data and hyperspectral data, respectively. Both the data expand over the same range (approximately 370-2500 nm), the multispectral covers the range in 10 bands and the hyperspectral in 239 bands, generating a more detailed spectral signature.

Electromagnetic radiation interacts uniquely with every object depending on the object's chemical structure/compositions and physical properties (e.g., grain size). The interaction of electromagnetic radiation with matter can principally, result in reflection, emission and scattering (Clark, 1999). Spectroscopy measures the electromagnetic radiation at often thousands of narrow and contiguous spectral bands, spanning from the visible and near-infrared (400-1000 nm; VNIR), shortwave infrared (1000-2500 nm; SWIR), mid-wave infrared (3000-7000 nm; TIR), and longwave infrared or thermal domains (7000-13000 nm) (van Ruitenbeek et al., 2005; Kriesel et al., 2011; Ullah et al., 2012; Notesco et al., 2014b; van der Meer, 2018; Laukamp et al., 2021a; Laukamp et al., 2021b). Objects, including minerals, are characterised by spectral reflectance that can be used to identify crystal lattice structure and chemical bonds (Figure 1.3). This can then be interpreted to identify typical mineral associations (Figure 1.3) (Hunt, 1982; Clark, 1999; Clark et al., 2003; Bishop, 2005; Ducart et al., 2006; Murchie et al., 2007; Chang et al., 2011; Chukanov, 2016; Kereszturi et al., 2020; Laukamp et al., 2021b). Furthermore, spectroscopy is also a fast (e.g., limited or no sample preparation required), versatile (e.g., both laboratory or field operational) and cheap (e.g., many measurements at a time) technique to recognize minerals in exploration geology and mining mediation identification (Chang, 2007; Kopačková, 2014; Notesco et al., 2014b; Chukanov, 2016; Cudahy et al., 2016). Fundamentally, light is absorbed in different wavelength position(s) depending on the chemistry of the substance, while the depth of this absorption features can relate to the abundance of the particular substance, purity and grain size (Hunt, 1982; Sabins, 1999; Clark et al., 2003; van der Meer, 2018). Moreover, the shape of the absorption feature (e.g., symmetric, skewed, or has multiple features) is also characteristic of identifying the mineral (van der Meer and Bakker, 1997; Cudahy et al., 2008; van Ruitenbeek et al., 2014; Laukamp et al., 2021a). The absorption features at the VNIR-SWIR region are mainly due to two general chemico-physical processes: electronic and vibrational within molecules (Clark, 1999). The VNIR region is mainly associated with absorption features due to electronic processes and helps identify transition metal ions (e.g., Fe, Cr). The SWIR region can be characteristic for some metals related to vibrational processes such as H_2O, OH^-, CO_3^{2-} etc (Hunt, 1982; Clark and Roush, 1984; Clark, 1999; Chukanov, 2016; Cudahy et al., 2016; van der Meer, 2018). The SWIR region is significant thus in mapping alteration mineral phases such as Al-OH bearing minerals (e.g., muscovite, kalinite, smectite), sulphates (e.g., jarosite and gypsum), Mg-OH bearing minerals (e.g., biotite, hornblende, phlogopite), and carbonate minerals (e.g., calcite, dolomite, ankerite and siderite) (King and Clark, 1989; Clark et al., 1990; Cudahy et al., 2008; Swayze et al., 2014). Spectral processing broadly refers to “the extraction of quantitative and/or qualitative information from remotely sensed reflectance (or emittance) spectra based on the albedo-, and wavelength-dependent properties of the material” (Mustard and Sunshine, 1999). The spectral analysis includes a diverse range of techniques, such as classification, and quantification of materials (Figure 1.4) (Chang, 2007; Khalili et al., 2015; Asadzadeh and de Souza Filho, 2016; Dalm et al., 2017; Pullanagari et al., 2017a; Kereszturi et al., 2018; Chang, 2021; Shrestha et al., 2022).

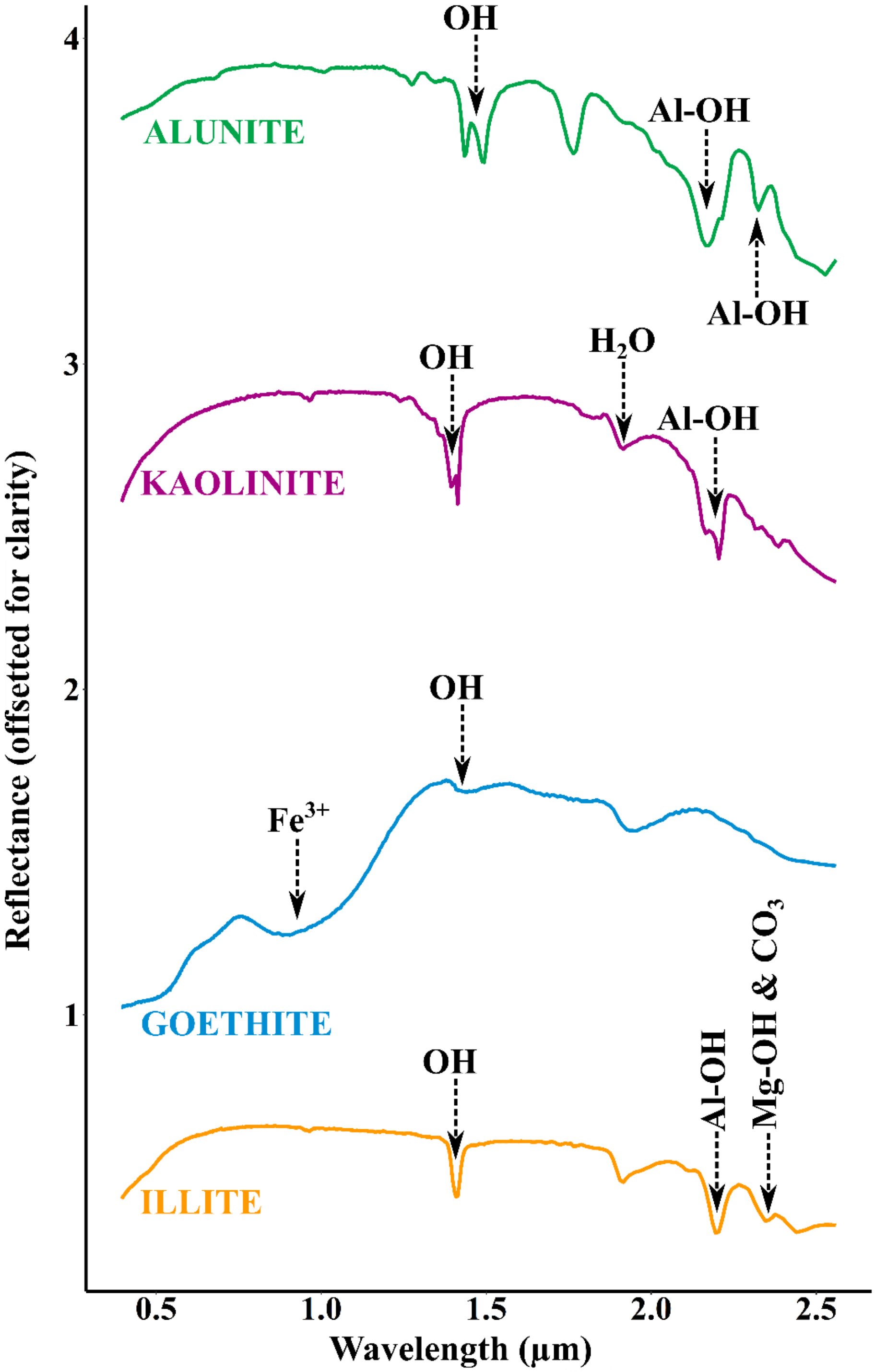

Figure 1.3: Signature spectra of common indicator minerals and their chemical characteristics driven absorptions.

The advances in machine learning and pattern recognition have made identifying the correlation between the hyperspectral data and the desired target variable, such as element concentration, alteration extent, biomass magnitude and water contamination, and providing robust results compared to many classical techniques (Ghamisi et al., 2017b; Ghamisi et al., 2021; Parsa, 2021; Thiele et al., 2021a; Booysen et al., 2022). Machine learning-based approaches are known for their robustness in handling variability in the ground truth and spectral data. Separate spectral analytical methods such as dimension reduction, spectral enhancement, spatial-spectral predictions, and band selection, can be integrated in a machine learning algorithm making it highly efficient. In mineral exploration, machine learning is being extensively used for spatial-spectral predictions and abundance mapping in challenging settings, such as rugged topography, accessibility complication due to vegetation cover or lack of outcrop exposure (Haest, 2013; Cracknell and Reading, 2014; Druzbicka and Craw, 2015; Laukamp et al., 2021a). Machine learning well accommodates multi-disciplinary approaches to current challenges making it invaluable. Although one of the major drawbacks of machine learning-based spectral analysis is that the models are highly data-driven. A particular hyperspectral image acquisition is subjected to various fluctuating and also developing factors such as the topography of the site, sensor/platform specifications and sensor technology. A collective sense of such specifications makes each data more unique than typical, making it highly data dependent and reducing its reproducibility (Ghamisi et al., 2017b; Ghamisi et al., 2021).

Hyperspectral imaging only detects surface objects, i.e., the signal does not penetrate the substrate and/or vegetation. Hyperspectral remote sensing has been used over the decades in mineral exploration for mineral and contamination mapping (Kruse, 1998; Kruse et al., 2003; Cudahy et al., 2008; Pour and Hashim, 2011; Rogge, 2014). However, when it comes to hyperspectral remote sensing being linked to biogeochemistry the spatial resolution of the most commonly used satellite-based hyperspectral data (~30 m) becomes a limitation. Biogeochemistry study is classically a point-based study (Dunn, 1986; Dunn and Ray, 1995) at a fine spatial level which made airborne hyperspectral data a better-suited tool over the satellite-based hyperspectral data with a much coarser spatial resolution (Cohen and Rotman, 2005). However, detailed studies aiming to prospect through vegetation using airborne hyperspectral remote sensing are very limited (Kalacska et al., 2007; Wei et al., 2020; Lhotáková et al., 2021).

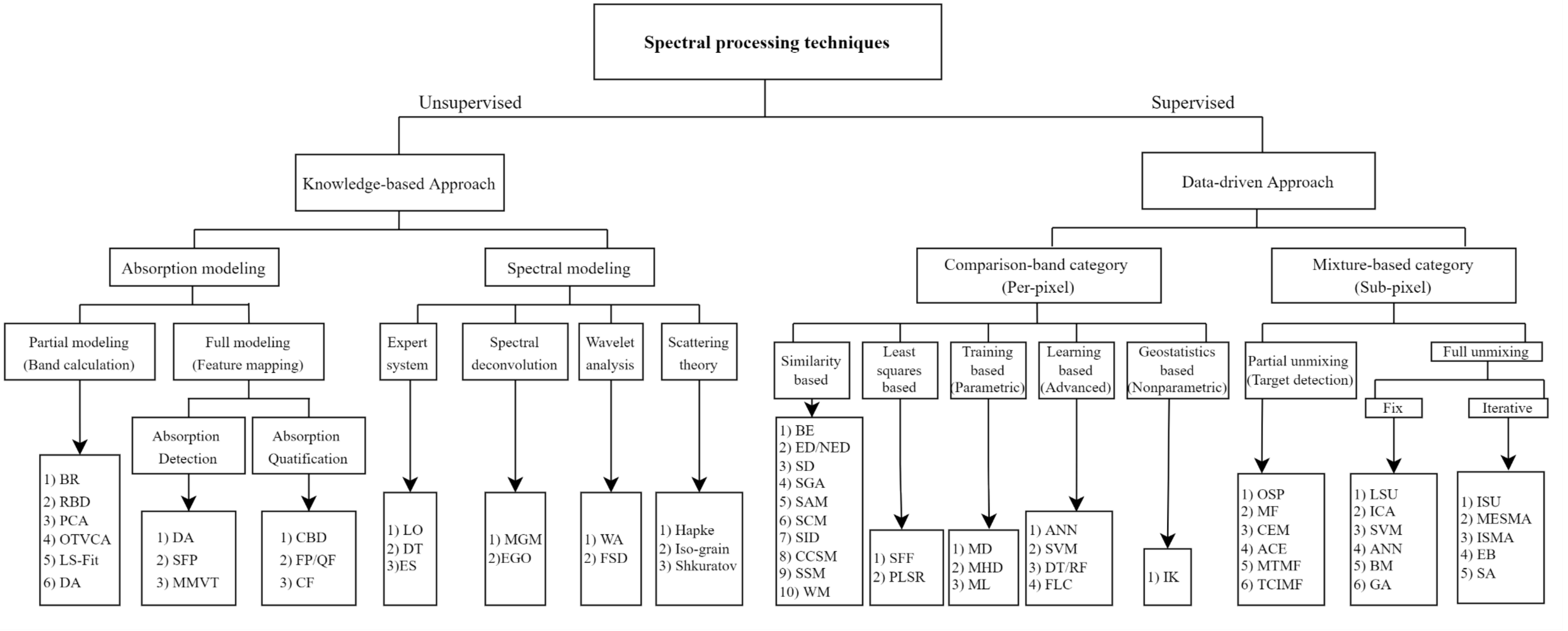

Figure 1.4: Taxonomic tree describing the spectral processing methods. The acronyms used in the tree and throughout the text are: BR: band ratio, RBD: relative absorption band depth, PCA: principal component analysis, OTVCA: orthogonal total (Martin et al., 2016) variation component analysis, LS-fit: least-square fitting, DA: derivative analysis, SFP: spectral fingerprints, MMWT: maximum modulus wavelet transform, CBD: continuum band-depth, FP: fitted polynomial, QF: quadratic fitting, CF: curve fitting, LO: logical operator, DT: decision tree, ES: expert systems, MGM: modified Gaussian model, EGO: exponential Gaussian optimization, WA: wavelet analysis, FSD: Fourier self-deconvolution, Hapke: Hapke (bidirectional) scattering theory, Iso-grain: Iso-grain scattering theory, Shkuratov: Shkuratov scattering theory, BE: binary encoding, ED: Euclidean distance, NED: normalised Euclidean distance, SD: spectral distance, SGA: spectral gradient angle, SAM: spectral angle mapper, SCM: spectral correlation mapper, SID: spectral information divergence, CCSM: cross-correlogram spectral match, SSM: spectral similarity mapper, WM: wavelength mapper, SFF: spectral feature fitting, PLSR: partial least square regression, MD: minimum distance, MHD: Mahalanobis distance ML: maximum likelihood, ANN: artificial neural network, SVM: support vector machines, DT: decision tree, RF: random forests, FLC: fuzzy logic classifier, IK: indicator kriging, OSP: orthogonal subspace projection, MF: matched filtering, CEM: constrained energy minimisation, ACE: adaptive coherence estimator, MTMF: mixture tuned matched filtering, TCIMF: target-constrained interference-minimised filter, LSU: linear spectral unmixing, ICA: independent component analysis, SVM: support vector machines, ANN: artificial neural network, BM: Bayesian model, GA: genetic algorithm, ISU: iterative spectral unmixing, MESMA: multiple endmember spectral mixture analysis, ISMA: iterative spectral mixture analysis, EB: endmember bundles, SA: simulated annealing. (Sourced from : Asadzadeh and de Souza Filho (2016))

1.3 Research gap and objectives

Previous research has identified the potential of quantifying metal stress in plants using laboratory experiments (Rathod et al., 2018; Wang, 2018). A change/shift in the red-edge is a commonly reported stress response in the vegetation spectra and can be used as an indirect element quantification “parameter” (Clark et al., 2003; Li et al., 2015; Rathod et al., 2015; Shin et al., 2019). Following the success of the controlled experiments, airborne and satellite-based retrieval of pathfinder elements and typical metal stress in plants are much less studied (Cohen and Rotman, 2005; Khalili et al., 2015; McQueen et al., 2021). Such previous studies both at laboratory and airborne/spaceborne levels indicate a clear relation between the biogeochemistry and the underlying lithology that can be extended to a spectral domain. A robust integration is yet to be developed that can at the same time overcome accessibility challenges, such as vegetation cover and undulated rugged topography while providing a mineral prospecting that is spatially seamless.

This research responds to this challenge by exploring advanced analytical methods combined with laboratory and airborne hyperspectral remote sensing, to better integrate such promising techniques into mineral exploration. In particular, this study aims to integrate precise laboratory determination of elemental concentration in plant tissue and soil samples that can be linked to the underlying rock formations using multivariate statistical analysis. The three main aims of this study are: -

- To test the feasibility of remote detection and quantification of biogeochemical signatures over a known gold mineralisation using laboratory-based spectroscopy and airborne hyperspectral imaging.
- To map potential As anomalies through surface manifestations of underlying gold mineralisation using airborne hyperspectral imagery over a partially to fully vegetation-covered region.
- To develop the framework and workflow for regional-scale mineralogical prospecting, using airborne hyperspectral remote sensing in a thick natural forest.

1.2 Thesis Structure

This thesis consists of six chapters which can be subdivided into three sections.

1. First Section – This section consists of the introductory chapter (**Chapter 1**), including the research objectives, and a brief background literature review (**Chapter 2**). Chapter 2 contains a brief review

of (1) the geological setting of the South Island, New Zealand covering the three test study sites; (2) hyperspectral remote sensing and associated data processing used for mineral exploration;(3) biogeochemistry and its role in mineral exploration.

2. Second section – This section consists of the main research chapters (Chapters 3-5). Each chapter addresses a research objective. Furthermore, each chapter is “self-contained”, with its specific introduction, methods and separate discussions easing the interpretations by the reader. **Chapter 3** is carried out at the Hyde Macraes Shear Zone (HMSZ) to test various machine learning algorithms for predicting biogeochemistry attributes using hyperspectral scanning and imaging. This chapter has already been published (Chakraborty et al., 2022). **Chapter 4** is carried out in the Rise and Shine Shear Zone (RSSZ), this chapter is to identify, link and utilise the effects of surface exposure to the geology of the area and map the potential As anomalies. Finally, **Chapter 5** is carried out in the Reefton goldfield. This chapter generalizes all the knowledge from the previous two chapters and aims to map gold-associated elemental anomalies in a natural forest to test the full potential of airborne hyperspectral imagery with real exploration data.
3. Third Section – To conclude the thesis, **Chapter 6** provides a broader discussion, covering the feasibility and role of hyperspectral remote sensing methods in different geological settings and the combination of analytical methods that can be used for mineral exploration. This section also formulates recommendations and identifies future research directions. Finally, **Chapter 7** summarises the key findings of the study and some potential future work directions.

Chapter 2. Background

2.1 Geological Setting

New Zealand is situated on the convergent and divergent plate boundaries between the Pacific and Australian plates (Mortimer et al., 2014). New Zealand contains two main islands, North Island (Te Ika-a-Māui in Te Reo) and South Island (Te Waipounamu in Te Reo). The South Island which hosts the target sites of this study is mostly made of Rakaia Terrane, Kaweka Terrane, Buller Terrane and Caples Terrane and they are partially overprinted by the Haast schist (Mortimer, 2004; Mortimer et al., 2014).

The Haast Schist is the most economically important formation in the South Island. It stretches over a length of 2000 km, from the Chatham Islands, through Otago, Wellington and into the central North Island (Figure 2.1). The Haast schist ranges from metamorphic pumpellyite-actinolite to amphibolite facies (Mortimer, 2004; Craw et al., 2005; Henne and Craw, 2012). Geographically, the Haast schist can be divided into many subregions, including Kaimanawa, Tairawhiti, Marlborough, Alpine, Otago and Chatham schists. The current thesis uses two study sites that are located within the Otago schist contained by the Haast schist. The overall regional metamorphism occurred between the Jurassic and early Cretaceous (Coombs et al., 1976; Mortimer, 2000, 2004) periods of crustal thickening as indicated by K-Ar and Ar-Ar dating studies (Little et al., 1999; Gray and Foster, 2004). Post the metamorphism event, extensive quartz veins associated with hydrothermal fluids intrusions were emplaced. Post metamorphism, in the late Cretaceous regional structural event (120 Ma), normal faults were formed which increased the host rocks' permeability and gave pathways for hydrothermal fluids. The gold mineralisation within the Otago schist is located in mineralised pockets that are associated with the formation of the normal faults (Teagle, 1990; Craw et al., 2005; Mackie et al., 2009; Allibone et al., 2018; Robinson, 2018).

The mineralization in the Otago schist is clustered in two broader areas:

1. The Hyde-Macraes Shear Zone (HMSZ) in East Otago. The HMSZ formed in the Early Cretaceous (140-135 Ma) based on K-Ar and Ar-Ar dating. Here, the mineralisation took place in the finer-

grained textural zone (Textural Zone III in Table 2.1), in the lower greenschist facies or the chlorite zone.

2. The Rise and Shine Shear Zone (RSSZ) located in Central Otago has a comparatively coarser grained textural zone (Textural Zone IV in Table 2.1). It formed, in the upper greenschist facies during mid-Cretaceous (112-110 Ma) based on K-Ar and Ar-Ar dating. Typically, the schist manifests garnet biotite-albite associations.

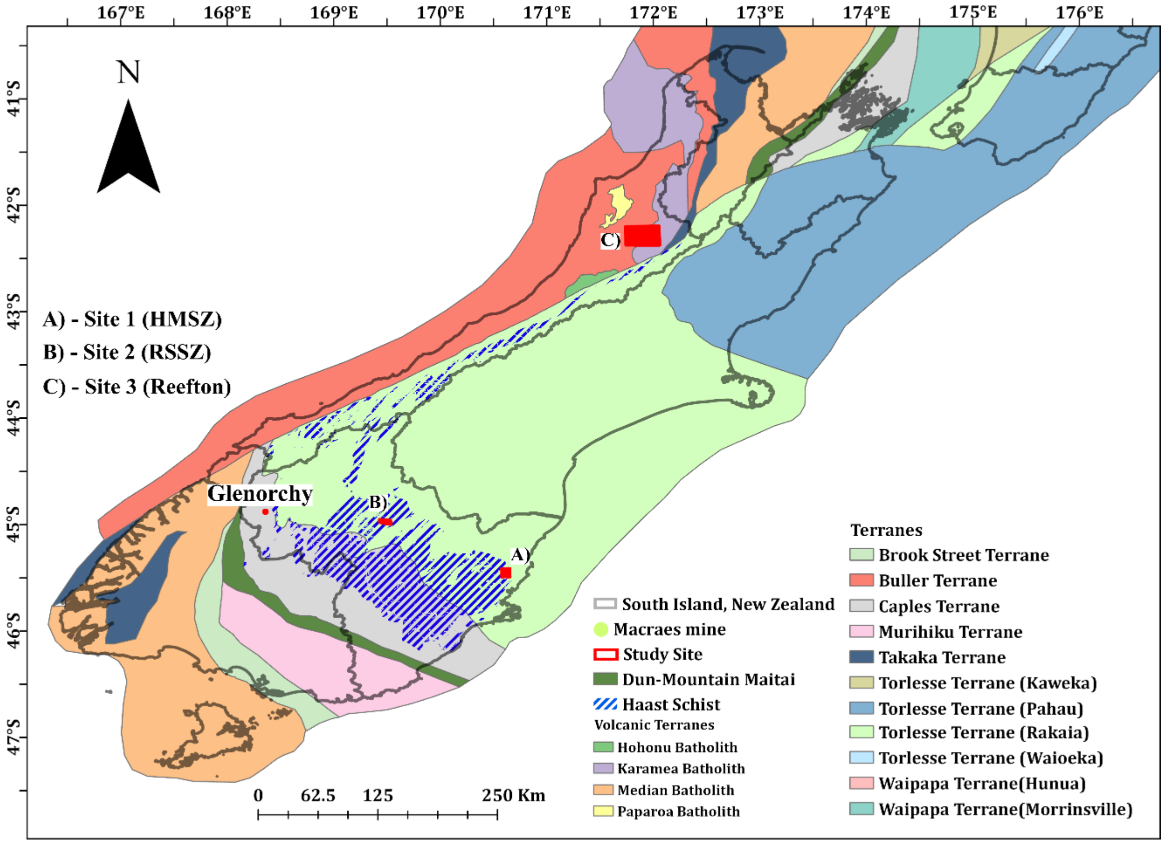

Figure 2.1: Basement terrains of South Island, New Zealand, adapted from GNS terrane map (Geological terrane data sourced from GNS Science 2020).

Structurally both HMSZ and RSSZ are characterised by compressional shear near the brittle-ductile transition zone which varies between 2-125 m depth (Teagle, 1990; Craw and Norris, 1991; Mortimer, 2000; Cox et al., 2006; MacKenzie et al., 2006; Mortimer et al., 2016; MacKenzie, 2017). Both the HMSZ and the RSSZ are truncated by low-angle normal faults (e.g., the Footwall Fault and the Thomson's Gorge fault respectively). In both cases, the normal fault, separates the mineralised from the non-mineralised lithologies (Deckert et al., 2002; Mortimer et al., 2016).

The gold mineralisation occurred in two pulses during the Cretaceous period, originating mainly from the prograde metamorphic dehydration at the greenschist-amphibole-biotite transition zone (Pitcairn et al., 2006; Mortensen et al., 2010). The early pulse was gold-tungsten rich and distributed along vein swarms continuously for over 10-15 m along the strike or downdip of the shear zone, each vein is up to 5 cm in width and about a meter long (Teagle, 1990; Craw et al., 1999). The gold enrichment from this pulse is more prominent in the Macraes region whereas the tungsten enrichment is more obvious in the Glenorchy area (Figure 2.1) (MacKenzie et al., 2006; Mortensen et al., 2010). In the second pulse, the gold is more associated with fracture-filling quartz veins formed precipitated from hydrothermal fluids of moderately acidic pH levels and at a temperature of <200°C (Ashley and Craw, 1995; Leach et al., 1997; Mackie et al., 2009). The gold mineralisation caused by both the pulses led to hydrothermal wall rock alteration in the greenschist facies host rock, forming recrystallised phyllosilicate, including kaolinite and illite accompanied by sulphide, most commonly, pyrite, arsenopyrite, chalcopyrite, galena, ullmannite and stibnite (Mortensen et al., 2010). In particular, the latter phase resulted in significant enrichment of, Au, Ag, As, Sb, Hg and Mo (Goldfarb et al., 2005; Pitcairn et al., 2006; Mortensen et al., 2010). Rock formation from this phase was targeted within the Otago schist for gold mining since 1990 (Christie, 2016).

The shist debris in the Otago schist is variably oxidised post-deposition by downward percolating groundwater forming the alteration zones (Craw, 1994; Craw and Rufaut, 2017). The near-surface oxidation mainly influenced by groundwater changes the ferrous iron-bearing minerals to form pre-dominantly iron oxyhydroxide (HFO). A portion of the HFO remains in situ to form pseudomorphs and the rest migrates to form a coating on adjacent rocks (Craw, 1994; Cudby et al., 2021). Arsenopyrite oxides to form scorodite which coats the fracture surfaces of the primary mineral grains (Craw et al., 2007b; Cudby et al., 2021). The clay altered and the variably oxidised schist marks the nearly 50 m thick basement unconformity between the Cretaceous and the Cenozoic sediments. Muscovite is preserved in all clay phases, although kaolinite is more dominant in oxidised schist whereas smectite and vermiculite are more common in unoxidised schist (Craw, 1994; Chamberlain et al., 1999). These features are commonly spotted on the surface across the region.

Table 2.1: Textural zone classification of the Otago schist. Adapted from (Turnbull et al., 2001).

Textural Zone	Metamorphic white mica, thickness, length, habit	Hand Specimen features	Thin section features	Applicable rock names
I	<5 µm thick; <75 µm long; coarse detrital micas	Spaced fracture cleavage; local quartz veins	Detrital textures without any orientation	Sandstone, mudstone, greywacke, argillite
IIA	<5 µm thick; <75 µm long; slaty matt black-coloured pelites.	Foliation features are weakly developed. Bedding still dominates cleavage; local quartz veins.	Detrital quartz grains showing undulose extinction; weakly oriented metamorphic micas.	Foliated greywacke, semi-schist, slate.
IIB	5-15 µm thick; <75 µm long; Black pelites with a distinct sheen; grey psammites.	Foliation features are strongly developed. Cleavage dominated bedding; flattened detrital grains with no foliation parallel segregation; local quartz veins cut foliation at an angle	Detrital quartz grains composed of sub-grains are still visible; mica is strongly oriented in anastomosing folia.	Psammitic or pelitic semi-schist, phyllite, slate.
III	15-25 µm thick; 75-125 µm long; silvery grey pelites and psammites.	Foliations are strong and undulating at a mm scale; psammitic-pelitic contacts are sharp at a mm scale; foliation parallel quartz lenses (<1mm thick) throughout the rock; mm-cm thick quartz veins.	Quartz and mica are almost equigranular and form sub-mm segregations.	Quartzo-feldspathic schist, grey schist.
IV	25-30 µm thick; 125-500 µm long; clearly visible mica grains	Foliations are strong and undulating in mm-cm scale; psammitic-pelitic contacts are blurred at mm scale but resolvable at cm scale; widespread quartz veins >1mm thick; poly-deformed quartz veins.	Adjacent quartz and mica grains merge to form segregations and foliations of variable length and thickness.	Quartzo-feldspathic schist, grey schist, gneiss

Besides the Otago schist, Reefton goldfield has a significant gold deposit, which formed within the Buller Terrane in the Greenland group of rocks (Figure 2.1). The metaturbidites and the Paleozoic granitoids are the main rock formations here (Laird and Shelley, 1974; Adams et al., 2007). The gold mineralisation is hosted in the Palaeozoic metasedimentary rocks, consisting of weakly metamorphosed alternating layers of turbiditic greywacke and argillites (Laird and Shelley, 1974; Christie et al., 2000; Rattenbury and Stewart, 2000; Druzbicka and Craw, 2015). The turbidite depositions took place between Cambrian and Ordovician periods, and metamorphosis occurred between Silurian and Devonian periods, dated back to 438 to 395 Ma based on K-Ar dating (Adams et al., 1975; Goldfarb et al., 2005; MacKenzie et al., 2014). The Reefton rocks typically manifest characteristic bedding parallel carbonate spots (mainly magnesian siderite, Christie et al. (2006)), these are flattened and lensoidal in shape. The carbonate spots are truncated by porphyroblasts of pyrite and arsenopyrite (MacKenzie et al., 2014).

The gold occurrence in the Reefton goldfield holds typical orogenic mesothermal gold characteristics and hence is fundamentally similar in form to that of the Otago goldfields such as HMSZ and RSSZ as mentioned previously (Table 2.2) (Craw and Norris, 1991; Christie et al., 2000; Bierlein et al., 2004). The gold in the Reefton goldfield is closely associated with quartz veins. The quartz veins here are late-metamorphic and post-metamorphic in nature (MacKenzie et al., 2014). The former is comprised of white quartz which is mostly associated with the gold occurrence in the area, and these veins are intensely sheared and disrupted unlike the quartz veins hosting the Otago gold deposits (MacKenzie et al., 2014). The post-metamorphic quartz veins majorly comprise of ankerite and massive stibnite veins (MacKenzie et al., 2014). The common sulphides which are pathfinder minerals to gold here are arsenopyrite, stibnite, ullmannite and boulangerite (Christie et al., 2001; Pirajno and Bentley, 2012; MacKenzie et al., 2014) occurring in quartz veins hosted at the shear zones (Christie and Brathwaite, 2003; Christie et al., 2010). The major pathfinder elements being As and Sb and minor pathfinder elements being Cu, Pb, Fe, Ti, Co, W and Ag (Bierlein et al., 2004).

Mining was targeted in the quartz veins or the lodes in the shear zones. The Reefton Goldfield consisted of numerous mines, out of which The Globe Progress, and Blackwater Waiuta mines are the most significant ones (Magner et al., 1997; Christie et al., 2006; Durance et al., 2015). The Globe progress mine had two lifespans initially as an underground hard rock mine, between 1879 and 1920, when it produced 418343 oz of gold. The mine was redeveloped as an open pit mine during its later phase which operated between 2007 and 2015 during which it produced 536494 oz of gold (Christie, 2016). At Globe progress, the main quartz veins are bordered by clay-rich breccia zones. The veins contain gold in native form alongside sulphides such as pyrite, arsenopyrite, stibnite and chalcopyrite. The wall rock hydrothermal alteration of the phyllosilicates led to the formation of secondary minerals like illite/sericite, pyrite and carbonates such as magnesian siderite and ankerite (Christie and Brathwaite, 2003; Christie et al., 2006). The proximal mineralised halo here extends up to 30 m which is unlike most other gold-bearing outcrops in the area which extends to a maximum of 20 m. The Blackwater Waiuta mine was the largest producer of gold in the Reefton goldfield during its time between 1909-1951, producing 732907 oz of gold. This mine was developed around the Birthday reef which is hosted in the biggest quartz vein. The mineralised zone here extended up to 10m here (MacKenzie et al., 2016).

Table 2.2: Characteristics of gold mineralisation in the three sites used in the study

	HMSZ	**RSSZ**	**Reefton**
Age	Early Cretaceous	Mid Cretaceous	Silurian to Devonian
Mineralization style	• Lode Shears • Disseminated sulphides and stockworks. • Quartz veins contain free grains of gold and in sulphides	• Disseminated sulphides • Shear hosted veins	• Brecciated quartz veins, • Disseminated sulphides • High-grade quartz lodes hosted
Host rock	Lower greenschist facies rock	Upper greenschist facies rock	Meta turbidites
Mineralization depth	10-12 km	5-10 km	1-5 km
Mineral halo	~100 m	~100 m	10-30 m
Pathfinder elements	As, Sb, W, Ag	As, Sb, Fe (ankerite)	As, Sb
Hydrothermal fluid temperature	300-400 °C	200-300 °C	200-300 °C

2.2 Hyperspectral Remote Sensing and its Role in Mineral Exploration

Imaging spectroscopy, or hyperspectral imaging, records the upwelling radiance from an object, as co-registered images, each corresponding to a narrow, and contiguous spectral band (Goetz et al., 1985). Each pixel can be characterised by its spatial location (i.e., X and Y principal directions) and the spectral signals are collected at every channel/band (e.g., Z axis). Furthermore, all the wavelength bands are spatially aligned and each pixel constitutes a vector that represents the spectral response (Figure 2.2.2). The imaging sensors, often mounted on ground-based tripods, low-flying aircrafts and space-borne satellites, perform the image acquisition in different imaging designs, including pushbroom, whiskbroom and full frame scanning (Jensen, 1996; Lillesand et al., 2015). The pushbroom scanners contain a series of linear detectors in the focal plane which images across the entire field of view while a whiskbroom scanner has multiple detectors on the focal plane oriented along the platform direction, thus collecting several rows of the image simultaneously (Chang, 2007). Lately, there are more and more sensors providing full-frame imaging solutions, such as Telops (Gagnon et al., 2015).

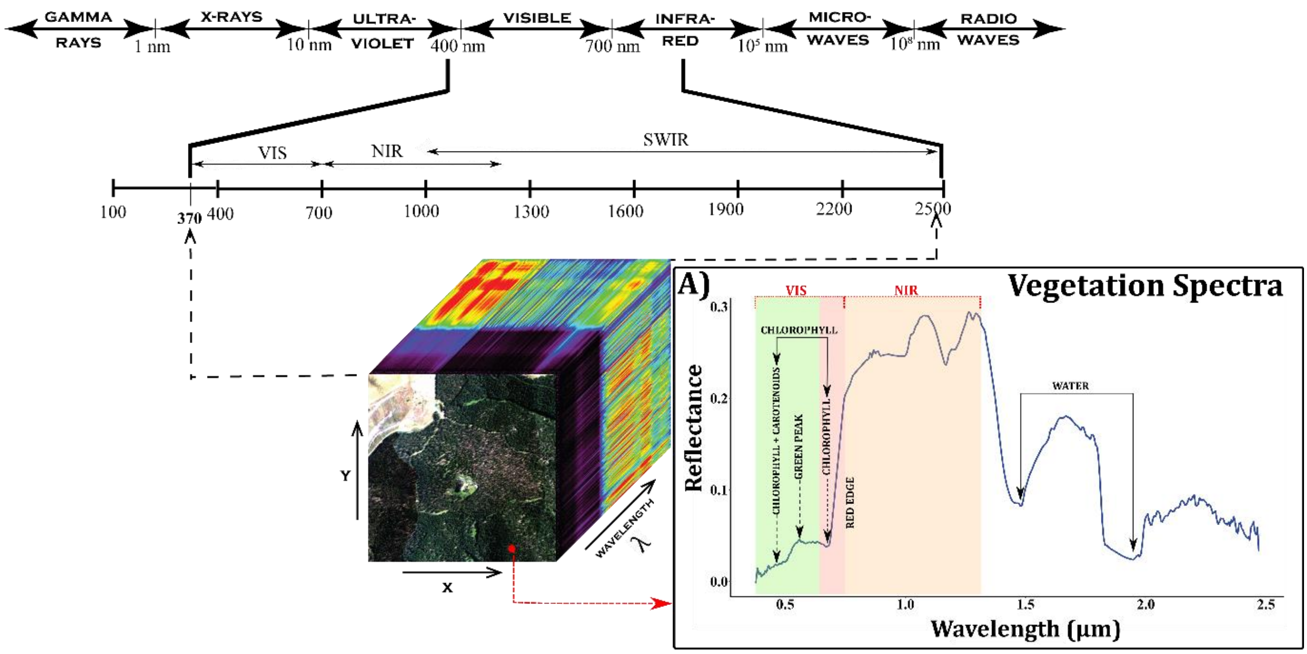

Figure 2.2 : Electromagnetic spectrum and a portion of the hypercube. A) vegetation spectra and the important sections characterising different parameters.

In the spectral domain, the bandwidth is an important factor (Notesco et al., 2014a), since he defines the width of an individual spectral channel. The narrower the bandwidth the narrower absorption feature a sensor can detect and resolve accurately (Notesco et al., 2014a; van der Meer, 2018). Furthermore, the spacing between two individual spectral bands (i.e., spectral sampling interval or sometimes called spectral resolution) is also an important characteristic of a spectral imaging sensor, defining the sensor's ability to sense fine wavelength intervals (Fig 2.3) (Sabins, 1999; van der Meer, 2018). In reflectance spectroscopy, a signal is the amount of light measured by the spectrometer, and the random variability of this signal is the noise.

Noise in hyperspectral data can originate from the atmosphere which is handled using atmospheric correction modules such as ATCOR and FLAASH which are part of the classical pre-processing workflow (Gao and Goetz, 1990a; Cooley et al., 2002; Gao et al., 2009). On the contrary different types of instrumental/sensor-induced noise can be ignored by the pre-processing steps and still remain in the data, such as quantization noise, shot (photon) noise and thermal noise which can cause various degrees of discrepancy in the spectral bands (Liu et al., 2011; Rasti et al., 2018). Hyperspectral data denoising algorithm models can be used as a pre-processing step to further improve the signal-to-noise ratio prior to further analysis. Denoising methods such as those based on Gaussian models (e.g., Low-Rank Matrix Recovery; HyRes- Hyperspectral Restoration) (Zhang et al., 2013b; Rasti et al., 2018) and 2D and 3D wavelet-based models (e.g., FOSRP- First Order Roughness Penalty) data (Othman and Qian, 2006; Rasti et al., 2013), have been used for many applications to deal with such noisy hyperspectral (Fan et al., 2018; Payet et al., 2020; Meng et al., 2021). The ratio between the desired signal and the noise is important to judge the efficiency of a sensor.

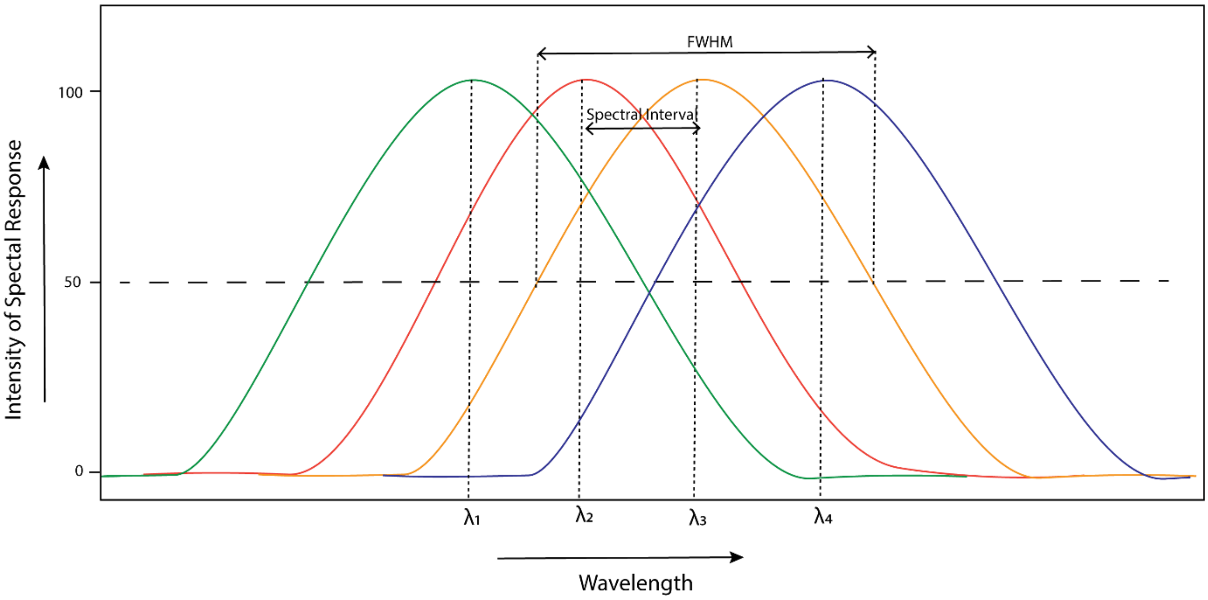

Figure 2.3: Schematic reference of a narrow bandwidth hyperspectral response function. Abbreviations: FWHM- Full width at half maximum, λ- central wavelength value (i.e., spectral wavelength)

2.2.1 Pre-processing and corrections

Spectral data is originally recorded by detectors sensitive to photons, such as digital number (DN). The actual DN depends on the sensor's sensitivity and fore-optic design. The DN needs to be calibrated properly and converted into radiometric quantities, such as radiance, which has the SI unit of W/m^2/str/nm. The image that is thus captured by these sensors is a flattened 2D representation of a 3D surface, leading to geometric distortion (Fred, 2018). Moreover, the sensor's viewing geometry and its motion, with respect to the rotation of the Earth can also appear to add to the geometric distortion (Green et al., 2000). Thus to link a point on the image to that on the ground, cartographic properties of a map are assigned to the image using ground reference points in geometric correction (Dave et al., 2015).

Geometrically corrected, radiance imagery shows the reflected radiation at a given wavelength from any object in the optical path, including both ground and the atmosphere. The atmosphere can induce issues owing to scattering due to dust, aerosols and molecules, absorption due to, trace gasses and water vapour, solar irradiation, atmospheric visibility and terrain effects (Itten and Meyer, 1993; Brunn et al., 2003; Gao et al., 2009; Amigo and Santos, 2020). Thus, the radiation at senor needs to be corrected for atmospheric effect, via atmospheric corrections (Vanonckelen et al., 2013; Dierssen, 2019; Richter and Schläpfer, 2019). The reflected proportion from the ground is called surface reflectance. The reflectance thus measured here is a ratio between the radiant exitance and the irradiance. The two main effects considered by an atmospheric correction model are referred to as “path radiance” and “adjacency” effects (Yuen et al., 2004). The path radiance refers to certain unaccounted radiation signals that reach the sensor due to various scattering effects in the atmosphere and the adjacency effect refers to the influence of the surrounding pixels on an individual pixel, these two effects lead to the loss of target clarity in the image (Yuen et al., 2004). Thus, taking into account all these factors, the process of atmospheric correction converts the measured radiance to absolute ground reflectance (Gao and Goetz, 1990b; Gao et al., 2009).

Although some topography-induced noise, such as a rugged hilly terrain will still show differences caused by the Sun’s illumination, resulting in variation of reflectance values even after the atmospheric correction (Vanonckelen et al., 2013). These effects can further be corrected using methods such as bidirectional reflectance distribution function (BRDF) which utilises the scan angle and the IFOV of the sensors to further reduce the anisotropic effects on the reflectance image (Dong et al., 2019). Some most popularly used post-processing data analytics in spectroscopic studies are signal smoothening and enhancing, where algorithms (e.g., moving average, Savitzky-Golay filtering, band ratio) are applied to increase the signal-to-noise ratio (SNR) and continuum removal, which normalizes the reflectance spectra and enables to compare the individual absorption features from a common baseline (Clark and Roush, 1984).

2.2.2 Post-processing and spectral enhancement methods

Hyperspectral data is theoretically co-linear, but the number of complexities, such as mixed pixels, atmospheric interference, and geometric distortion, makes it highly non-linear (Ghamisi et al., 2017b). Different methods have been subjected to trial and error, based on various applications of the hyperspectral data (Liu and Gu, 2017; Dierssen, 2019). The idea of all such post-processing algorithms is to extract maximum information by eliminating redundancies.

Hyperspectral data has hundreds of dimensions which often poses disparity in the number of spectral bands and training samples, so the initial approaches of post-processing mostly include dimension reduction (Ghamisi et al., 2017b). Several unsupervised methods have been developed for dimensionality reduction techniques, including Principal Component Analysis (PCA) which captures the maximum variance in the data in order to gather maximum information into a smaller dimension (Jolliffe, 1986). Independent Component Analysis (ICA) which maximises the statistical independencies and re-projects the spectral bands to a matrix to reduce the initial dimension (Hyvärinen et al., 2001) and finally Minimum Noise Fraction (MNF) (Green et al., 1988a). MNF transformation is a widely used data reduction technique in hyperspectral remote sensing (Frassy et al., 2013; Wu et al., 2013; Luo et al., 2016a). MNF transformation includes two rotations, the first calculates the noise covariance matrix and decorrelates the noise from the data, and the second rotation further transforms the noise-whitened data to generate principal components (Green et al., 1988b; Joseph, 1994). These dimension reduction algorithms are often followed by an inverse function which brings back the noise deducted data to the original image space (Luo et al., 2016a; Wang, 2016). More hyperspectral image-specific dimension reduction techniques have evolved over time and have given way to new and more effective algorithms. Recently developed, Orthogonal Total Variation Component Analysis (OTVCA), belongs to unsupervised methods, which focus on feature extraction, by optimising the total variation of a feature while controlling the spatial smoothness, (Rasti et al., 2016); Locality Preserving Projection (LPP), here a fundamental manifold structure reflection of a feature is projected in a lower dimension using nearest-neighbour, this algorithm is linear in nature which makes the application more user-friendly (Wang and He, 2011); Modified Locality Preserving Projection (MLPP), this algorithm extends on LPP by giving a weightage to the nearest neighbours, thus increasing the distance between the non-nearest neighbours while maintaining the feature space (Zhai et al., 2016).

Supervised dimensionality reduction techniques include Partial Least Squares (PLS), which adds the expert knowledge of the region to the model and adds a regularisation term to preserve certain properties of the data (Arenas-García and Camps-Valls, 2007; Yang et al., 2010). Non-parametric Weighted Feature Extraction (NWFE) is also popular in which weights are assigned to the samples and then the weighted mean is calculated to assign it to a non-parametric class (Kuo and Landgrebe, 2004). Some semi-supervised techniques include Semi-supervised Discriminant Analysis (SDA) (Cai et al., 2007); Semi-supervised Local Fisher's Discriminant Analysis (SELF) (Sugiyama et al., 2010) and Semi-supervised graph learning (SEGL) (Luo et al., 2016b).

Finally, there are some fusion-based techniques that integrate data-fusion and dimensionality reduction to deal with this problem (Debes et al., 2014; Liao et al., 2015) and kernel-based methods that integrate the spectral and spatial information in a lower dimension (Borhani and Ghassemian, 2015). Apart from these established techniques, different applications have different ways of dealing with the dimensionality of the hyperspectral data (Tsai and Philpot, 1998; Jinkai et al., 2004; Cohen and Rotman, 2005; Gomez et al., 2008; Ruffin et al., 2013).

2.2.3 Hyperspectral Image Classification

Image classification is the most commonly used and addressed topic in hyperspectral remote sensing applications Ghamisi et al. (2017b). Based on the type of user input (or training), classifications can be subdivided into, unsupervised, semi-supervised and supervised methods (Yang et al., 2010). In unsupervised classification, an image is classified into different inherent categories of the images without any actual labelling information (Villa et al., 2013), whereas a supervised classifier is completely reliant on the training data (e.g., labelled classes) (Dundar and Landgrebe, 2004). Finally, in a semi-supervised classification, the training dataset is a mixture of known and unknown endmember (Fujino et al., 2005). Furthermore, based on the fundamentals of the classification techniques, the most commonly used methods can be divided into 1) Spectral matching and mapping and 2) Advanced learning-based approaches.

1) Spectral Mapping and Matching Approaches

These techniques are based on spectral features (such as absorption features) and their location information to discriminate ground objects and assign them to a class.

Band selection, **band ratioing** and **PCA** are some of the earliest approaches to mineral mapping using remote sensing (Sheffield, 1985; Crosta and Moore, 1989). The bands showing maximum and minimum reflectance values for a particular target feature, along with a few other bands of known reflectance for example the NIR band (in the case of Multispectral data) that is considered to reflect vegetation are selected. PCA is then applied to these selected bands which transforms the data-based maximum variance into principal components (the number of principal components is equal to the selected number of bands). The target is likely to show up in one of the Principal Components. To select the component which contains the information, the eigenvector matrix is analysed for the maximum difference between bands which contains the information (as negative and positive loadings). An RGB composite of the subset of principal components is often used for mineral resource detection and mapping (Crosta and Moore, 1989; Crosta, 1989; Loughlin, 1991b). One of the major drawbacks of these techniques is that they are highly dependent on expert knowledge and thus the interpretations can be biased. Additionally, PCA is an effective tool for exploring data structure, but it has its limitations of being scale-invariant, and the highly correlated information may not be extracted, in the process of maximising the variance (Lever et al., 2017).

The **Spectral Angle Mapper (SAM),** calculates the spectral angular similarity between the reference spectra and the image spectra, by considering both the spectra as vectors (Kruse et al., 1993). The spectra collected from training sites in the image, field or lab spectra, or the spectral libraries can be used as the reference spectra here which are then compared to the spectra derived from the hyperspectral images. The pixels are thus classified based on the minimum included angle with the reference spectrum. This approach has been often applied in mineral exploration (Debba et al., 2005; Kruse, 2007; Bishop et al., 2011; Mielke et al., 2014; Notesco et al., 2014b; Notesco et al., 2015). The fundamentals of SAM have also been used to upgrade its performance, into models such as 1) modified SAM (MSAM) that compares both the spectral and the hyper angle between two spectra (Staenz et al., 1999); 2) optimised SAM (OSAM) that optimises a reference spectral library and compares the unlabelled spectra to it (Luc et al., 2005); and 3) extended SAM(ESAM) which uses SAM to remove the unwanted background information and then uses support vector model and vertex component analysis to extract pure pixels (Li et al., 2014). Such methods are still in use to date, and they are integrated into ENVI software for further ease of application and reach (Boardman et al., 1995; Clark, 1999; Kruse et al., 2003; Kruse, 2015).

The **Cross Correlogram** approach calculates the correlation coefficients of the spectral signature of the pixels to be classified to that of a reference spectrum at various matching positions (van der Meer and Bakker, 1997). A pixel is classified to a particular class when the correlogram takes the form of a parabola, i.e., when the coefficient is nearing 1, the extent of the match here is assessed by the skewness of the correlogram (van der Meer and Bakker, 1997; van der Meer, 2001). It has been applied and tested in the geoscience domain in studies such as Asadzadeh and de Souza Filho (2016) and Emery and Maleki (2019).

The **USGS Tetracorder System** (Clark et al., 2003) contains a set of algorithms, in a decision-making system, which compares the unknown spectra to a spectral library of reference spectra. The matching is based on diagnostic portions of the electromagnetic spectrum, which is driven by the physico-chemical properties of the target material. Finally, it uses the modified least squares shape-matching algorithm to map the material distribution (Clark et al., 2003; Dalton et al., 2004).

The **Spectral Information Divergence** (SID) method calculates the spectral similarity of a reference spectrum and the image spectrum in terms of the variations or amount of divergence between the two spectra, considering them as two vectors (Chang, 2000). SID has been successfully used in studies such as Zhang et al. (2013a) and Khaleghi et al. (2014) to map minerals.

Spectral Feature Fitting (SFF) classifies the target pixels by fitting the absorption features to the reference spectrum or the endmembers, this approach is efficient to extract target based information from hyperspectral images (Kruse et al., 1993; Xu, 2014). This is also included in the ENVI processing module. It has been extensively used in studies such as Abbaszadeh and Hezarkhani (2013) to map hydrothermal alteration zones and in Jain and Sharma (2018) to map mineral zones.

The **Integrated Band Depth** (IBD) method was first developed by (Mustard et al., 2011) for mapping minerals in a crater of the moon. IBD is a mineral indicator method formulated by capturing the significant mineralogical variations on the surface via summation of band depths of characteristic absorption features (Bhattacharya et al., 2019). It has been used extensively to map minerals in studies such as Banerjee et al. (2019) and also to map lunar mineralogy in studies such as Kusuma et al. (2012) and Kaur et al. (2013).

The **Wavelength Mapper** is another semi-automatic method by which the minerals are mapped based on their absorption feature characteristics (Figure 1.3). Firstly, the spectral region of interest is subsetted, from which the continuum is calculated and removed, it is then followed by identifying the deepest absorption feature and its wavelength position. The output of this method is a soft classified image, that can be differentiated based on various material properties (Bakker et al., 2011; van Ruitenbeek et al., 2014; van der Meer et al., 2018a; van der Meer et al., 2018b).

Table 2.3: Comparison of different spectral approaches used in the hyperspectral mapping. Partially adapted from (Shanmugam and Srinivasa Perumal, 2014)

Method	Advantages	Disadvantages	Citation
SAM	• It is not affected by scale or the Sun's position. • Simple and fast computation.	• The smallest unit of an endmember is a pixel, hence does not work with mixed pixel targets. • Not suitable for intra-class variations	(Clark et al., 1993; Kruse et al., 1993; Chang, 2007; Jiao et al., 2012; Asadzadeh and de Souza Filho, 2016)
Cross-Correlogram	• Compares materials of different albedos. • Can be easily automated. • Has a higher accuracy.	• Does not consider subtle spectral differences. • Does not work in mixed pixels.	(van der Meer and Bakker, 1997; van der Meer and Bakker, 1998)
USGS Tetracorder system	• The spectral library contains binary and ternary mineral compositions in both linear and non-linear scenarios.	• The residual errors of the radiative transfer models for atmospheric corrections hamper the output.	(Clark et al., 2003; Dalton et al., 2004; Asadzadeh and de Souza Filho, 2016)
SID	• Better quantifies the spectral similarity. • Accommodates high dimension data without redundancy approach.	• Works mainly for mixed pixels. • The accuracy decreases when subjected to compression processes.	(Chang, 2000; Nidamanuri and Zbell, 2010; Cerra et al., 2011; Vishnu et al., 2013)
SFF	• Allows accurate identification of absorption features. • Minimizes effects of grain size variation and sun illumination.	• Does not consider the full spectrum. • Might result in considering absorption features similar to noise.	(Clark et al., 1990; Warner et al., 2009)
IBD	• Highly accurate in mapping clay and carbonate minerals	• Expert knowledge-driven, making it prone to discrepancies. • Not suitable for other minerals with subtle absorption features.	(Mustard et al., 2011; Bhattacharya et al., 2019)
Wavelength Mapper	• Automated approach. • Maps subtle differences in mineral chemistry.	• Does not deal with noise separately, and thus may be confused with absorption.	(van der Meer et al., 2018a; van der Meer, 2018)

2) Learning-based approaches

The advent of machine learning algorithms and image mining approached broad concept of supervised classification and has reached new levels of efficiency and accuracy. The most common methods, that can be relevant to mineral/geological exploration, have been briefly overviewed below and summarised in Table 3.

Random Forest (RF) classifier is a decision tree-based logic-based model (Breiman, 2001; Abdel-Rahman et al., 2012). The model generates decision trees using random subsets of variables from the training data. Each decision tree further expands independently using the bagging method (Breiman, 1996). Every single full-grown decision tree casts a vote on the most popular class, and the final output classifier is based on the majority vote. Hyperparameter tuning is often used to refine extensive arrays of parameters RF models need, including the total number of trees, maximum depth of the tree, and the minimum number of samples in each split (Breiman, 2001; Cracknell and Reading, 2014). In the domain of mineral mapping, it is widely used, some successful examples being Kereszturi et al. (2020) for hydrothermal alteration mapping around a volcano.

Support Vector Machine (SVM) classifiers are used mainly for their ability to define non-linear decision boundaries within an n-dimensional feature space (Vapnik, 1998). In a non-linear dataset, the separable dataset containing points from two classes can have an infinite number of hyperplanes separating these two classes. SVM identifies the best-suited hyperplane that best differentiates the two classes using a small subset of training data which are called the support vectors. The maximum distance (maximal margin) between two support vectors is identified as the optimal decision boundary (Karatzoglou et al., 2006; Yu et al., 2012). The main tuning parameters in the SVM module are C and gamma. C is the regularizing parameter which regulates the balance between minimising the error and maximising the margin of the decision function. The parameter gamma defines how far a single training sample can influence the hyperplane (Vapnik, 1998; Karatzoglou et al., 2006). Studies such as Yousefi et al. (2021), Wang et al. (2014) and Abedi et al. (2012) have used SVM to successfully map mineral phases.

Fuzzy Logic Classifier (FLC) is a soft classifier. FLC is used where the difference between two classes is not abruptly definable at an earth imagery scale and/or has multiple classes with very close/overlapping spectral signatures. This makes it for the conventional hard classifiers to define a boundary between two classes. The fuzzy classifiers assign a degree of similarity to all classes for a single pixel (Bárdossy and Samaniego, 2002; Lu and Weng, 2007). It has been utilised in studies such as Kamenev et al. (2017) and Senesi et al. (2018) to identify and map minerals with a specific absorption feature.

Artificial Neural Network (ANN) classifier comprises a network of primitive functions that contains multiple weighted inputs which are evaluated in terms of their ability to differentiate the classes with the training data. Each combination of the networks creates an individual model. While training the connection weights are adjusted in case of error between the separation inputs. The convergence process of the networks continues until the errors reach a decay threshold (Rojas, 2013; Cracknell and Reading, 2014). Studies such as Jiang et al. (2019), Deng et al. (2021) and Liu et al. (2021) and many more are using a neural network to map minerals using various parameters and layers specific to the objectives of the study.

2.2.4 Regression and Quantification Approaches

Regression in statistics broadly means to establish a relation between a dependent variable (or target variable) to one or multiple independent variables (or predictor variables). Regression has widely been used for applications in remote sensing, to predict various in-situ parameters from the hyperspectral data in geosciences such as geochemical parameters including elemental concentration, and soil properties (Gomez et al., 2008; Pandit et al., 2010; Chabrillat et al., 2014; Pullanagari et al., 2018; Jeong et al., 2021), also in various other domains such as forestry and agriculture (Shi et al., 2016; Pullanagari et al., 2017b; Naik et al., 2021).

The most commonly used regression approaches in geological applications are either least square-based regression models, such as Partial Least Squares regression (PLSR) and kernel-based PLSR as well as many other learning-based models documented in Table 4. PLSR is a linear multivariate model which is widely used in chemometrics (Wold et al., 2001). Its ability to deal with high collinearity makes it ideal for the hyperspectral dataset (Gomez et al., 2008; Cheng and Sun, 2016; Pullanagari et al., 2016). PLSR decompose the two parts of the data, i.e., the predictor variable and target variable in latent variables. The maximum number of latent variables is defined by the user (Rosipal and Trejo, 2001; Li et al., 2014). Conventional linear models such as PLSR often fail in dealing with complex data (e.g., X). On the contrary, KPLSR iteratively estimates the orthogonal components from the input variables in a higher dimensional feature space, until the model reaches an optimal dimension (Arenas-García and Camps-Valls, 2007; Pullanagari et al., 2016). This help to deal with the inherent non-linearity in data which the standard PLSR model fails to deal with.

RF, SVM and ANN can also be used as regression methods (Abdel-Rahman et al., 2012; Cheng and Sun, 2016; Roshanravan et al., 2021), while their learning-based regression approaches are based on the same fundamental concepts (Table 4). The main difference lies in the target variables. In the case of regression, the target variable is either continuous in nature or a real value whereas in classification it is a discrete value.

Table 2.4: Comparison of different advanced learning-based models for both regression and classification.

Methods	Advantages	Disadvantages	Citation
Random Forest/ Decision Tree	• Often outperforms SVM and ANN in geological applications, such as lithology classification and mineral detection. • Deals with multicollinearity and random distribution proficiently. • Reduces potential overfitting	• Unable to extrapolate beyond the range of training data.	(Gislason et al., 2006; Cracknell and Reading, 2014; Belgiu and Drăguţ, 2016; Su et al., 2017; Kereszturi et al., 2018; Demarchi et al., 2020)
Support Vector Machine	• Requires comparatively fewer training points at the class boundary.	• Parameter assignment and training can be extensive. • Often shows high convergence error.	(Dundar and Landgrebe, 2004; Melgani and Bruzzone, 2004; Cracknell and Reading, 2014; Pullanagari et al., 2017a)
Fuzzy Logic Classifier	• Accommodates a range of class membership values for a single pixel.	• At a broader scale and highly mixed pixel level, it is hard to find the correct set of membership rules. • Requires thorough field training.	(Bárdossy and Samaniego, 2002; Lu and Weng, 2007; Naik and Kumar, 2021)
Artificial Neural Network	• It is independent of distribution assumptions. • Ability to generalise and procure information even in noisy environments. • Works in both linear and non-linear datasets.	• The training process is extensive. • Works best with ample sets of examples and training.	(Lu and Weng, 2007; Mas and Flores, 2008; Licciardi and Del Frate, 2011)
Partial Least-Squares	• It is a multivariate linear model which simplistic in nature and easy to implement. • The least-square regularization helps it handle with noisy and high collinearity of the data	• The model renders unbiased components, but the variance is too large • Fails to deal with multicollinearity in data	(Wold et al., 2001; Arenas-García and Camps-Valls, 2007; Cheng and Sun, 2016)

2.3 Biogeochemistry

2.3.1 Overview of relevant factors

Biogeochemistry utilises elemental concentrations of plant tissues as a reflection of the soil and host-rock chemistry and mineralogy (Dunn, 1986; Kovalevsky, 1987; Farago, 2008; Lintern et al., 2017). Biogeochemical methods have been used earlier in Canada, Australia and even New Zealand for prospecting mineral deposits such as porphyry Cu-deposits and gold and also to map transported regolith (Dunn, 1986; Cohen et al., 1987; Rencz, 1989; Dunn, 2007; Lintern et al., 2017).

Some elements, such as N, P, K, Fe and S, are critical for plant health and growth (Table 5) (Brooks, 1979; Farago, 2008), while other elements, such as As, Cd can be toxic (Arnon and Stout, 1939; Ashton, 1989). Based on the element mobility and species (Cohen et al., 1987; Kovalevsky, 1987; Dunn, 2007; Farago, 2008), plants can unanimously uptake elements both useful and toxic elements that can introduce change to their physical (e.g., leaf area index, canopy structure) and chemical properties (e.g., chlorophyll content, hyperaccumulator plants). Factors including plant species, underlying mineralogy, ionic size, and element mobility govern the occurrence of various elements in different parts of the plant (King, 1984; Dunn, 2007). Most of the heavy elements are not used by the plants for their survival processes while some result in morphological anomalies, such as stunted growth and discolouration (Bech et al., 1997; Pratas et al., 2005; Santos-Jallath et al., 2012; Doronila et al., 2014). Elements can impact plants differently which is tabulated in Table 2.5. Elements such as Au, Ag, and W are usually absorbed by the plants passively along with the water and occur as background trace amounts when a plant is grown on such mineralised soil (Brooks, 1979; Dunn, 2007). Other than the elemental uptake through water by the roots, metal and metalloids can also be found in leaves by the process of foliar transport (Farago, 2008). In this case, elements and contamination can accumulate via the aeolian process and heavy metal deposition, often due to proximity to industrial areas and urban settlement (Tomašević et al., 2005; Uzu et al., 2010; Shahid et al., 2017; Li et al., 2022).

Table 2.5: Different elements used by plants for different life processes. Adapted from Brooks (1979) and Dunn (2007)

Elements	Plant Processes
Al	Used to produce and sustain the colloidal properties of cells
B	Used in carbohydrate metabolism and flavonoid synthesis
Ca	Cell Walls production and N-metabolism
Cl	Function as enzymes, in osmotic functions and stomatal movement
Co	Helps as a coenzyme
Cu	Helps as an enzyme, coenzymes and in phosphorylation
F	Used in respiration
Fe	Chloroplasts, respiratory enzymes, phosphorylation
I	Protein function
K	Used in enzyme activity, osmotic regulation and stomatal movement
Li	Helps in salt metabolism
Mg	It is the central element in the chlorophyll molecule, used in enzyme production and phosphorylation
Mn	Helps in chlorophyll synthesis and acts as an enzyme activator
Mo	Helps in nitrogen metabolism, and enzymes
N	Amino acids, proteins, cell membranes, enzymes, chlorophyll synthesis, protein synthesis
Ni	Translocation of N
P	Nucleoproteins, phospholipids, high-energy phosphate bonds, energy transfer, phosphorylation
Rb	Partial analogue for potassium (K)
S	Amino acids, proteins, coenzymes, phosphorylation
Si	Cell walls
Sr	Partial Analogue for calcium (Ca)
Ti	Nitrogen Fixation
V	Nitrogen Metabolism
Zn	Enzyme hormone synthesis

Plant tissue sampling is a critical aspect of biogeochemistry, typically to avoid contamination as it already has a low concentration of elements, the total observation points in a typical biogeochemical survey can range from tens to a few hundred (Dunn, 2007). Elements are typically distributed heterogeneously within plants, with a decreasing concentration from the root to the leaves (Cohen et al., 2021; McQueen et al., 2021). However, the actual concentration levels can widely vary during the growth and life span of plants

(Kovalevsky, 1987; Dunn, 2007). For example, seasonal changes can play a role (such as autumn) when many plants transfer the nutrients from the leaves to the twigs (Dunn, 2007). Furthermore, previous studies have also reported spring to be an ideal season to study gold in the trees, while for some elements a recurring sampling is suggested for all seasons (Dunn, 1986; Cohen et al., 1987; Stednick et al., 1987). Different tree species have different abilities to collect, store, use and also discard toxic elements (Kovalevsky, 1987), allowing detection of the anomalous areas using different analytical processes.

The analytical processes for biogeochemical samples in recent times mostly include, X-ray Fluorescence (XRF), Inductively Coupled Plasma Emission Spectroscopy (ICP-ES) and Inductively Coupled Plasma Mass Spectrometry (ICP-MS) (Liang et al., 2005; Frommer et al., 2011; Gault-Ringold et al., 2012; Durães et al., 2015; Christie, 2016; Rincheval et al., 2019a). ICP-MS is a widely used technique for elemental analysis, it is often preferred over other elemental analysis techniques, because of its simpler spectra (Dunn, 2007). The detection limit here ranges from 0.01 to 0.1 ppb for many elements (Hall et al., 1990) which makes it highly suitable to measure low concentrations of elements in plant tissues such as in this study, although in the case of soil samples the detection limits are similar to that of XRF analysis. Moreover, it can also be used to quantify element concentrations as well as isotopes and has comparatively lesser spectral interference than all other methods (Olesik, 1991; Eggins et al., 1998; Thomas, 2013). A major limitation of ICPMS is polyatomic interference, where two or more elements conjugate to form the same mass (Dunn, 2007). The detectors and the instruments manufactured for this approach thus consider this limitation and include an understanding of the polyatomic interferences for different analytes to avoid poor results (May and Wiedmeyer, 1998).

Globally biogeochemistry has been used in quite a few places as a mineral exploration tool. Cohen et al. (1987) have used biogeochemistry for gold exploration in the Canadian shield. The study reported anomalous concentration of pathfinder elements, Mo, Ba and Sb in *Alnus rugosa*, *A. crispa* corresponding to the gold concentration in soil (B-horizon) overlaying a gold mineralisation. Cohen et al. (2021) further extended biogeochemical orientation toolset to explore Cu mineralisation in Cyprus. This study analysed 476 samples of *Pinus brutia* needles and *O. europaea* leaves. Cu by itself being an important element for the plant processes rendered less prominent correlation (Table 2.5), although REE, Zn and Sr manifested correlated trends both in the plant and soil chemistry. Lintern et al. (2013) reported native gold particles in Eucalyptus leaves in Australia and mark their potential to prospect buried gold deposits.

2.3.2 Biogeochemical orientation surveys in New Zealand.

Applications of biogeochemistry and geobotany have been implemented in New Zealand since 1960, commenced by the Late Professor Robert Brooks. The most significantly successful biogeochemistry surveys carried out in New Zealand are mentioned below chronologically.

- The Riwaka Complex in Nelson in the South Island, New Zealand is an igneous complex hosting Ni-Cu and a platinum group of elements (Bates, 1989). Biogeochemical orientation surveys were carried out here by Timperley et al. (1970) and Timperley (1971). The study used samples from 12 locations, across four plant species, namely, *Nothofagus fusca*, *Nothofagus manziesii*, *Quintinia actufolia* and *Weinmannia racemose* along with some soil samples analysed for Cu, Ni and Zn. The study reported a strong correlation for Cu and Ni concentration in the plant tissue and soil but no correlation for Zn concentration.
- Whitehead et al. (1971) have reported high concentrations of U in aquatic bryophytes, which is a type of moss in the Buller Gorge which hosts uranium mineralisation. This study was not used for mineral exploration purposes.
- Brooks et al. (1973) reported elevated concentrations of Cu in aquatic bryophytes which are present in the Coppermine Island near Whangarei, Northland which hosts porphyry copper style mineralisation. This study was also not oriented toward mineral exploration.
- There have been many studies focusing on gold uptake by various plant species in New Zealand, with a special interest in pines such as *Pinus radiata* and *Doughlas fir* which are considered accumulators of metals and metalloids (Ward and Brooks, 1978; Dunn et al., 2012a; Dunn and Christie, 2014; Dunn and Christie, 2020). Studies such as Anderson et al. (1998) and Anderson et al. (1999) report how different species of crops such as *Brassica juncea* accumulates a significant amount of gold when grown in auriferous soil.
- The Coromandel Volcanic Zone contains several epithermal quartz veins that occur in the Miocene andesites hosting gold mineralisation (Briggs and Fulton, 1990; Gregg et al., 1990;

Christie et al., 2007). Samples from plants over the Martha Hill and the Union Hill including samples from *Pinus radiata* were analysed. Significant high correlations between the soil chemistry and the Plant tissue chemistry for Cr, Ni, Na and even gold concentrations were reported (Ward and Brooks, 1978; Goff et al., 1985; Gregg et al., 1990).

- The Taupo Volcanic Zone hosts many geothermal complexes which are known to contain important metals such as gold and silver. Studies such as Dunn (2007) and Dunn and Christie (2020) have reported correlations between the soil chemistry and the plant tissue chemistry of the Kanuka shrub (*Kunzea ericoides*) which wildly grows in the region and withstands high heat and accumulates high proportions of metals from the soil.

The orientation studies above have rendered both success and failure in New Zealand. Similarly, other studies globally have been proven to be successful to different degrees, signalling the importance of geologically and biological factors being unique to each location.

Chapter 3. Mineral Prospecting from Biogeochemical and Geological Information using Hyperspectral Remote Sensing- Feasibility and Challenges

3.1 Introduction

Ore deposits are becoming scarce, leading to urgency in efforts for both metal exploration and metal recycling (Northey et al., 2017; Jowitt et al., 2018; Li et al., 2018). Exploration for new ore deposits to satisfy global current and future needs pushes exploration into evermore challenging environments such as dense vegetation rendering deposits blind to ‘traditional’ remote sensing methods. Not only are these terrains more difficult to explore, but they typically lack detailed geological and drill data for assessment prior to undertaking field activities. Therefore, new concepts are required to be used as first-order reconnaissance remote sensing, to test geological concepts arguing for the presence of mineral deposits in these terrains in a cost-effective, socially and environmentally sensitive way. Geochemical alteration patterns in surface and near-surface material (e.g., gossan, regolith, soil samples, stream sediment samples) provide evidence for ore deposit proxies that develop as a result of metamorphism, hydrothermal alteration, and chemical and physical weathering. These geochemical alteration patterns have distinctive elemental signatures, and these elements are, referred to as pathfinder elements as they define a path that is proximal to distal in relation to the location of the ore deposit. Biogeochemical studies show that most of these pathfinder elements can and do find their way into and onto a wide range of plant species (Lintern et al., 2017; Cindrić, 2018), thus potentially inducing changes to the plants that can be observed through remote spectroscopic analysis (Rathod et al., 2018; Cui et al., 2019; Zhang et al., 2021).

Biogeochemistry is focused on studying the inorganic chemical composition of plant tissues as a proxy to understand the geochemistry of the underlying soil and country rock (Brooks, 1979). Elements taken up by plants along with water and nutrients from the surrounding soil/rock boundary create an opportunity for, plants to be a viable sampling medium for mineral exploration, particularly in heavily vegetated regions (Dunn, 1986; Dunn and Ray, 1995; Anderson et al., 1999). Major and trace elements in plant tissues can be either absorbed (Lintern et al., 2017) or adsorbed (e.g. airborne dust particles) (Shahid et al., 2017). Moreover, deep-rooted plants, such as trees that reach the rock-soil interface are especially good for uptaking metals, metalloids and other pathfinder elements originating from the bedrock, which is then translocated and redeposited in bark and leaf tissues (Dunn, 1986; Kovalevsky, 1987; Dunn and Ray, 1995; Dunn, 2007). However, like other types of geochemical sampling, biogeochemical surveys are point-based and rely on statistical spatial handling over larger areas of interest (e.g., extrapolation, interpolation, and kriging) to impute over areas without data. There is usually a trade-off between increasing the density of sampling sites to provide more certainty in analysing variations of elemental distribution across a large area and allocating exploration investment across different projects (Dunn, 1986; Dunn, 2007; Gomez and Coulouma, 2018).

There is currently a dearth of exploration methods that provide spatially continuous high-resolution geochemical and mineralogical data. Satellite and airborne hyperspectral remote sensing supported by laboratory-based hyperspectral data can however provide a spatially continuous and rich data to map lithological changes and indicator minerals that are exposed at the surface as bare rocks (Kratt et al., 2006; Choe et al., 2008; Rogge, 2014; Boesche et al., 2015; Kruse, 2015; Notesco et al., 2015; Rodriguez-Gomez et al., 2021). However, the utilization of hyperspectral remote sensing for mineral prospecting in vegetated terrains remains untested. We hypothesise that prospect-to regional-scale hyperspectral data is suitable for detecting spectral changes in vegetation that may indicate the presence of an ore deposit and its associated pathfinder metals and metalloids found at depth. The concentration of these elements in plant tissue is usually at the low µg/g to ppb level, however, even at such low concentrations, these elements can still cause subtle changes in the spectral signature of the vegetation across the VNIR and SWIR regions (e.g., metal stress causing red edge shift in the vegetation spectra) (Rathod et al., 2015). Further, the effect of green and dry vegetation can be unmixed, delivering useful results even at up to 70% canopy cover (Cudahy et al., 2008; Haest, 2013; Huesca et al., 2016; Pullanagari et al., 2016; Pullanagari et al., 2017b; Wang, 2018). If proven this workflow could potentially make hyperspectral technology very suitable for orientation studies and reconnaissance surveys for mineral prospecting.

Hyperspectral remote sensing, or imaging spectroscopy measures radiated, emitted, and absorbed energy at hundreds of narrow and spectrally contiguous wavelengths. Hyperspectral remote sensing can span over different optical domains including the; visible (VIS; 400-700 nm), near-infrared (NIR; 700-1200 nm), shortwave infrared (SWIR; 1000-2500 nm), mid-wave infrared (MWIR; 3000-7000 nm), and longwave infrared or thermal domains (LWIR; 7000-13000 nm) (van Ruitenbeek et al., 2005; Kriesel et al., 2011; Kruse et al., 2012; Ullah et al., 2012; Notesco et al., 2014b; van der Meer, 2018; Simpson and Christie, 2019; Kereszturi et al., 2020). The VIS-SWIR regions of the electromagnetic spectrum make the detection and recognition of hydrated minerals possible (Hunt, 1982; van der Meer and Bakker, 1997; Sabins, 1999; Clark et al., 2003; van Ruitenbeek et al., 2014; van der Meer, 2018). A typical spectral response of vegetation in the VNIR-SWIR region is essentially a combination of morphological parameters such as canopy structure, leaf area and chemical properties such as water content, nutrients, chlorophyll, nitrogen concentration (Jensen et al., 2002; Townsend et al., 2003; Ferwerda and Skidmore, 2007; Wu et al., 2008).

The current study aims to bridge the gap between conventional biogeochemistry and hyperspectral remote sensing, by developing a novel workflow for exploration and reconnaissance mapping over a densely vegetated area. This study is carried out in a region of the mesothermal gold mineralisation in the Hyde Macraes Shear Zone (HMSZ) (Craw and Norris, 1991; Craw et al., 1999; Craw et al., 2007a; Mortimer et al., 2016; Allibone et al., 2017), in the South Island, New Zealand (Figure 3.1). The study integrates surface sampling of *Pinus radiata* (bark and needle) along with soil and rock samples with a hand-held spectroradiometer and airborne hyperspectral data. The main pathfinder element to gold here is As, along with some associated elements. (Table 3.1).

Table 3.1: Summary of the elements chosen for the study and their connection to the local geology in East Otago and their function in the plant system.

Pathfinder elements	Geological occurrence	Function in plants	Reference
As	Gold-bearing arsenopyrite and its alteration by-products	Easily taken up by plants due to high mobility and water solubility, often accumulates in plant parts.	(Dunn and Ray, 1995; Craw et al., 1999; Lombi and Nolan, 2004; Anke, 2005; Craw and MacKenzie, 2016)
Fe	Present in sulphides including arsenopyrite, pyrite, chalcopyrite, and pyrrhotite, as well as in their alteration products, such as goethite and clay minerals.	Essential in energy transfer for various plant cell processes, also a major constituent in chlorophyll and takes part in photosynthesis.	(Craw et al., 1999; Dunn, 2007; Craw et al., 2015a; Craw and MacKenzie, 2016)
Sb	Associated with As-bearing minerals (e.g. arsenopyrite with boulangerite).	Taken up in soluble forms, but non-essential for plant functions	(Ashley and Craw, 1995; Craw, 2002; Craw and MacKenzie, 2016)
Ti	In prograde metamorphism titanite ($CaTiSiO_5$) breaks down to form rutile (TiO_2). In retrograde metamorphism, rutile helps in mobilising W, which reacts with titanite to form disseminated scheelite ($CaWO_4$).	Leads to increased growth rate and chlorophyll productivity; it is also an important indication of airborne contamination (e.g., dust deposition).	(MacKenzie and Craw, 1993; Dunn, 2007; Craw and MacKenzie, 2016)
Co	The Co rich zone occurs along the edge of the high gold mineralisation zones	Tends to follow iron-rich organic compounds or Ni.	(Dunn, 2007)
W	Mostly present in form of scheelite in the quartz veins, also shows a weak positive correlation with gold occurring in quartz veins.	Rarely taken up by plants. Although they are reported in plants growing on mining areas.	(MacKenzie and Craw, 1993; Dunn, 2007; Craw and MacKenzie, 2016)
Ag	Minor mineral fraction but associated with Au	Mostly below the detection limit in plant tissues. Likely to show a spike Ag concentration when growing on Ag-rich soils.	(Dunn, 2007; Craw and MacKenzie, 2016)

3.2 Geological Settings

The South Island (Te Waipounamu in Te Reo) is mostly made of Rakaia, Kaweka and Caples Terranes which are partially overprinted by the Haast schist (Mortimer, 2004; Mortimer et al., 2014) (Figure 3.1). The Haast schist stretches over a length of 2000 km, from the Chatham Islands in the South Island, through Otago, Wellington and into the central North Island. The Haast Schist hosts orogenic and economically important mesothermal gold deposits (Craw and Norris, 1991; Turnbull et al., 2001; Christie, 2019). The sulphide-bearing rocks (rich in pyrite and arsenopyrite) at a near-surface red-ox boundary are often metastable and decompose due to atmospheric oxygen and water. This geochemical weathering facilitates the physical and chemical mobility of gold along with other associated or pathfinder elements in the system, such as As (Craw et al., 2015a; Weightman et al., 2021).

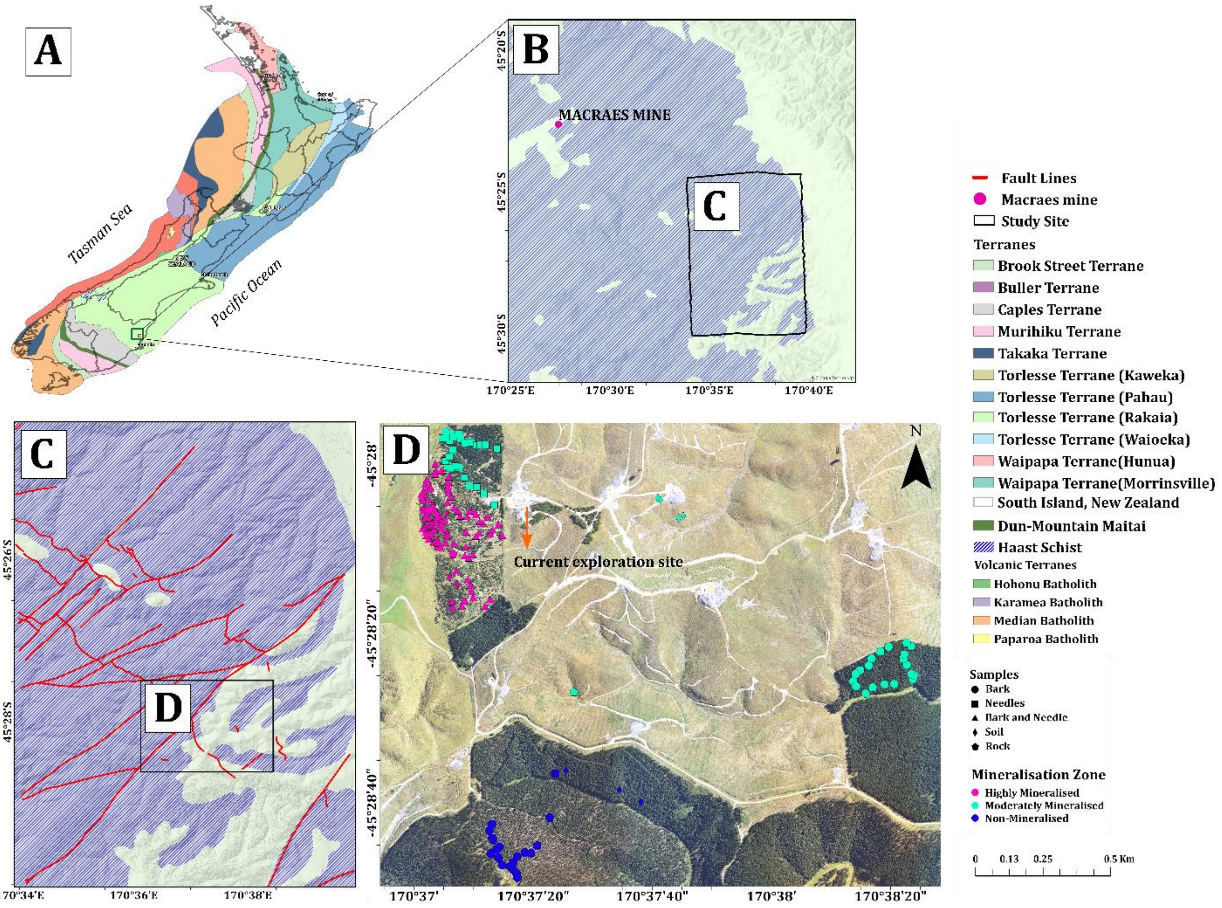

Figure 3.1: A) Overview map of the basement terrains of New Zealand, adapted from GNS terrane map (Geological terrane data sourced from GNS Science 20202) and QMap; B) The position of the Macraes mine with respect to the study site; C) The major fault lines present in the area; D) The sampling area and the distribution of samples, the basemap used here is the mosaic of the DSM digital photos.

The HMSZ is a regional structure in the Otago schist, that hosts the Macraes gold mine. The mineralised shear zone is contained in the lower greenschist facies rocks, where the schistose foliation runs sub-parallel to the shallow dipping thrust structure (Craw and MacKenzie, 2016). The HMSZ has evolved through the brittle-ductile transition (Winsor, 1991; Craw et al., 1999). The initiation of the shear zone started with a ductile deformation accompanied by hydrothermal alteration and gold mineralisation by infiltrating fluids (Craw et al., 1999; Craw, 2002; Allibone et al., 2018). While the hydrothermal alteration was taking place in the shear zone at shallower depths, the rocks underneath still experienced prograde reaction releasing metals and metalloid rich fluids (As, Sb, Au, W) (Craw, 2002; Craw and MacKenzie, 2016) (Figure 3.2). The structural deformation through shear zone development gave rise to more permeable brittle schist rocks which accommodate a larger volume of hydrothermal fluids, and this has in turn resulted in an increase in gold precipitation (Teagle, 1990; Craw et al., 1999)(Figure 3.2).

In the Otago schist, the graphite occurs simultaneously with gold and it has a hydrothermal origin (Craw et al., 2015b; Hu et al., 2015). The extent of the hydrothermal alteration ranges from a few meters to a few hundreds of meters beyond the ore-bearing rock (McKeag et al., 1989; Craw and MacKenzie, 2016; Mortimer et al., 2016; Allibone et al., 2017). A significant pathfinder for gold mineralisation is As which is mostly hosted by the sulphide mineral arsenopyrite (FeAsS). Surface processes commonly redistribute arsenopyrite and this results in a larger footprint for As than gold (Salama et al., 2016; MacKenzie, 2017; Blake et al., 2019; Weightman et al., 2021). In the case of HMSZ, orogenic sulphide minerals decomposed at the same time as the clay alteration along the basement unconformity (Craw et al., 2003; Craw and Lilly, 2016), leaching out As that has been redistributed by groundwater. Hence, the As concentration in the soil around the mineralised rock is much higher than in the rock itself (Blake et al., 2019). The majority of the As mobilisation took place at the Pleistocene-Holocene boundary (Blake et al., 2019).

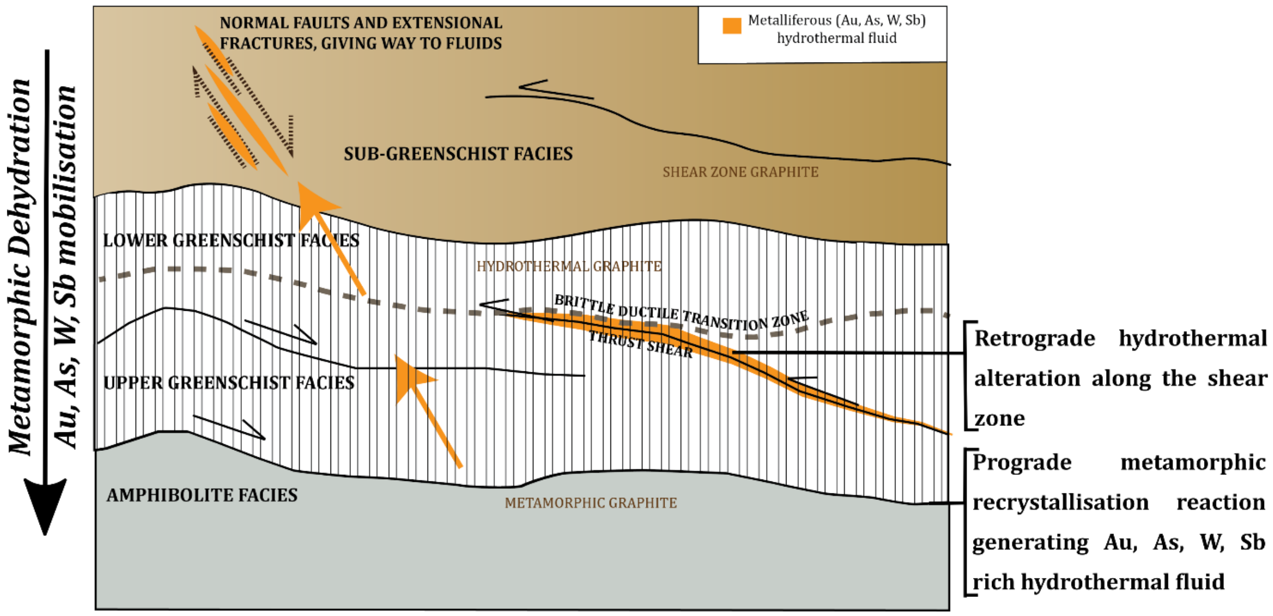

Figure 3.2: A conceptual model of the gold mineralisation that occurred at HMSZ in the Cretaceous period, adapted from Mortimer et al. (2016); Craw (2017)

The historical mining activity in the Otago area was driven by the supergene-enriched gold deposits, occurring at shallow depths. After most of the easy access surface gold deposits were exploited, the focus was deviated to the gold-bearing quartz veins which are related to the subsurface gold resources (Williams, 1974; Craw et al., 2015a; Allibone et al., 2017). The total production at the Macraes gold mine is 4 Moz since 1990 (Moore and Doyle, 2015), making up to 1/3rd of the total gold production New Zealand has produced (Christie, 2016). The maximum exploration took place in a 10 km radius along HMSZ. The main exploration was focused on drilling in the central parts of the geologically mapped mineralised structure (Martin et al., 2018).

3.3 Materials and Methods

3.3.1 Field Campaigns and Sampling

The study area is located approximately 11km east of the Macraes gold mine (Figure 3.1). Sampling sites were selected based on existing soil samples collected and analysed by the exploration company, Hardie Pacific Ltd., which indicated zones of potential mineralisation (Fig. 1). The geographical distribution of the samples aimed to capture the extent of known (or suspected) gold mineralization, moderately mineralised zones and non-mineralised zones thus maximising the total variation in pathfinder elements (Figure 3.1). The study site contains several *Pinus radiata* plantations which overlay a known gold-mineralised zone at a depth of 5-30 m based on drilling data (Ritchie, T. personal communication). The ground sampling includes rocks (where exposed), soil samples and bark and needle parts of the pine species.

The biogeochemical sampling of vegetation cover was confined to a single plant species, *Pinus radiata*, to avoid potentially complex interspecies biogeochemical differences. We collected two types of plant tissue from *Pinus radiata*; needles and bark. The bark of the tree often retains elements of higher magnitude than the leaves/needles (Brooks, 1979), although needle sampling here was also important, as it is a significant part of the trees that was captured through airborne hyperspectral remote sensing. A total of 104 bark and 111 needle samples were collected over multiple field campaigns in 2019 (Table 3.2). Trees of similar height were considered as a proxy of similar age groups while sampling the plant parts as older trees might have more adsorbed and/or accumulated metals as compared to the younger ones bringing in disparity during statistical analysis (Dunn, 2007).

Geological samples consisted of both rock and soil samples. Four rock samples were collected; three in and around the highly mineralised shear zone, targeting the greenschist host rock and the quartz veins which are likely to contain gold and one sample from an outcrop in the non-mineralised zone (Figure 3.1). Twenty-one soil samples were included in this study, 7 of which were collected during our field campaigns from seven different locations of high and low mineralised areas. An additional 14 soil samples were obtained from Hardie pacific Ltd. predominantly from the highly mineralised area (Table 3.2). The approximate depth of the topsoil cover in the sampling area varied from 10cm to ~ 1 m. In reference to the bark samples, gold concentration ranged up to 396 ppb in the highly mineralised zone and from 3 to 3.4 ppb in the non-mineralised zone (Table 3.2).

Table 3.2: Number of samples amongst different zones within the study area.

Category	**Number of samples**			
	Mineralised	**Moderately mineralised**	**Non-mineralised**	**Total**
Needles	84	27	-	111
Bark	65	20	19	104
Soil	13	4	4	21
Rock	3	-	1	4

3.3.2 Analytical Methods

The plant and the soil samples were oven-dried at 65°C for approximately 30 h. The spectral signatures of the dry samples were captured by an ASD FieldSpec 4 High-Resolution spectrometer. The ASD hyperspectral data was procured by direct spot measurements on the samples using a high-intensity contact probe (Kereszturi et al., 2018). The final spectral data has a spectral interval of 1nm, between 350 (VIS) to 2500 nm (SWIR). In total, three to five spot measurements were taken, each spot measurement was an average of 5 spectra recorded each as an average of ten measurements with an iteration time of 17 ms which were then averaged out. A Spectralon® white reference was used before measuring each sample. The total reflection of the white reflectance plate ensures that the spectroradiometer is optimised and the reflectance values across the spectrum are weighted the same (Figure 3.3).

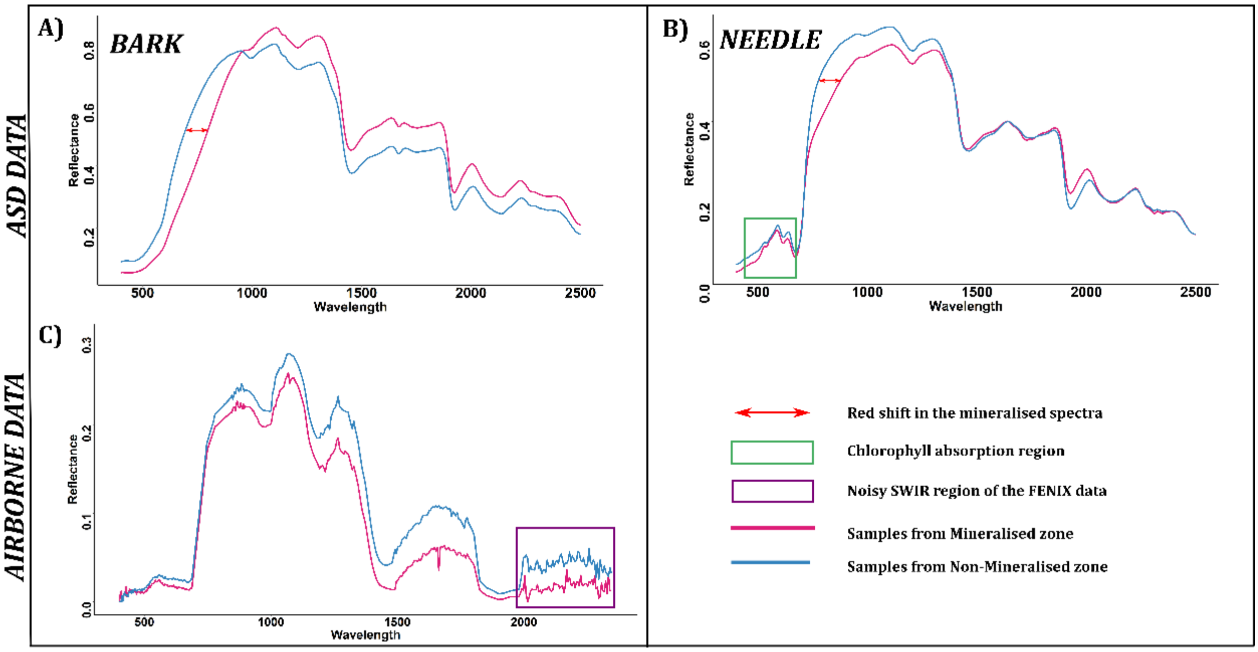

Figure 3.3: ASD and airborne hyperspectral spectra of bark and needle from mineralised and non-mineralised areas.

The samples were analysed by Inductively Coupled Plasma Mass Spectrometry (ICP-MS) for 37 elements, through ACME Analytical Laboratories, Vancouver, Canada. The detection limit here ranges from 0.01 to 0.1 ppb for many elements (Hall et al., 1990) which makes it highly suitable to measure low concentrations of elements in plant tissues such as in this study (Table 3.3). The dry equivalent weights of elemental concentration and values in 'ppm' were used for the regression models. This is the elemental concentration in the ash which is normalised based on the dry weight of the samples. Detailed quality analysis of the ICP-MS data analysis for the bark and needle samples is attached in Appendix 1A.

Table 3.3: Raw concentration of gold (Au) and other pathfinder elements in bark, needle and soil samples as analysed by ICP-MS. (BD- Below detection)

		As (ppm)	Fe (ppm)	Sb (ppm)	Ti (ppm)	Co (ppm)	W(ppm)	Ag(ppm)	Au(ppb)
Soil	Max	780.60	48900	1.99	1670	15.40	BD	0.06	327.20
	Min	4.50	4700	0.05	60	0.70	BD	0.01	0.20
	Median	14.4	21200	0.24	270	6.2	BD	0.02	15.8
Bark	Max	89.4	14500	15.63	581	61.5	11.9	0.801	396.3
	Min	3.6	1400	0.63	152	4.6	0.5	0.047	3.2
	Median	23.5	7050	6.285	326.5	17.3	3.15	0.21	23.7
Needles	Max	131.8	27400	29.5	408	53.3	2.5	2.778	111.7
	Min	1.5	1000	0.14	63	4	0.1	0.023	3.6
	Median	5.85	2300	1.29	236.5	16.8	0.9	0.352	13.3

A selected range of host rock was examined using Scanning Electron Microscope (SEM) equipped with energy-dispersive X-ray spectroscopy (EDS), for detailed mineralogical and compositional analysis. The rock samples were cut and mounted on glass slides, which were then grounded to achieve a thickness of ~0.6 to 0.8mm and then polished. The thick section slides were carbon-coated and imaged using ThermoFisher Scientific^{TM} FEI Quanta 200 Environmental Scanning Electron Microscope. The SEM was operated in Back-scattered electron (BSE) mode under an accelerating voltage of 20kV, with a working distance of 10 mm, at Massey University's Manawatu Imaging Centre.

3.3.3 Airborne Hyperspectral surveys and Data Processing

The airborne hyperspectral data was captured by the AisaFENIX push-broom full spectrum imaging sensor operated in conjunction with a Nikon D810 digital single-lens reflex camera, onboard a fixed-wing Cessna 185 aircraft. The platform speed was about 100 knots. The acquisition was designed in N-S-oriented lines with about 30% side-overlap. The field of view (FOV) and the instantaneous field of view (IFOV) of the sensor were 32.2° and 0.084° respectively. In order to georectify the final image, the sensor was operated along with an Oxford Survey^{+} inertia measurement unit and the Global Navigation Satellite System. The raw data was received in the digital number format which was then further pre-processed following the method of previous studies which have used this sensor (Pullanagari et al., 2016; Kereszturi et al., 2018). The workflow adapted for the processing is illustrated in Figure 3.4. The raw image data was initially converted from the DN values to the at-sensor radiances using CaliGeoPro (Yule et al., 2015; Pullanagari et al., 2016). The IMU and the GPS data were automatically matched with the image lines using the time stamp from the Oxford Survey+ system. The resulting radiance images were transformed into ground reflectance using Airborne Atmospheric and Topographic Correction Model, ATCOR algorithm using the ATCOR4 software (Richter and Schläpfer, 2002). The atmospherically corrected surface reflectance images were further corrected from the geometric inconsistencies, and georectified following the PARGE workflow (Schläpfer and Richter, 2002). After geocoding, the individual strips were mosaicked together using the ENVI ™ software.

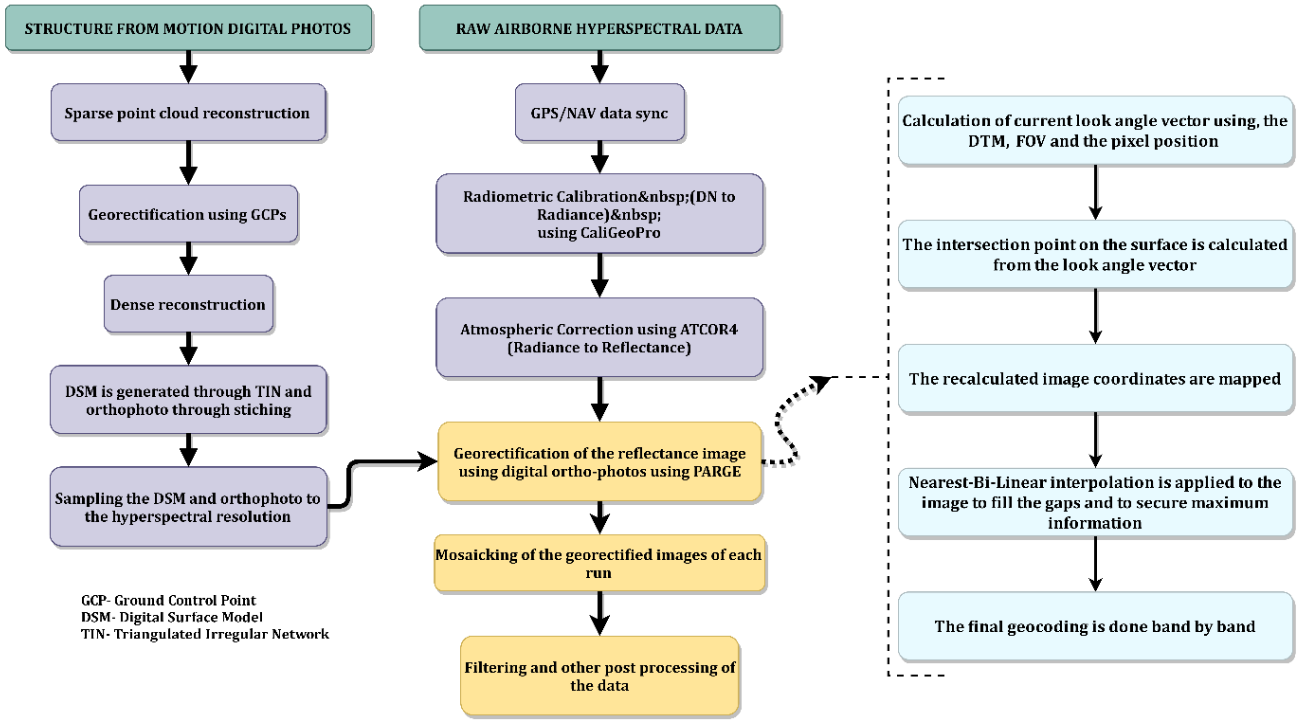

Figure 3.4: The workflow for pre-processing of the Airborne Hyperspectral data from DSM digital photos and Raw DN values to the georectified reflectance data.

3.3.4 Statistical Methods

Pearson’s correlation coefficient was used to assess first-order linear relationships between elemental concentration values from the ICP-MS analysis and the spectral reflectance from the laboratory-based hyperspectral data (Figure 3.3). Correlation requires normally distributed data, and normality was checked by plotting density distributions at wavelengths in both the VNIR and SWIR regions. The elemental data were normally distributed for most elements and log transformation was applied to those that were skewed (e.g., As, Sb etc). Intercorrelation among the variables was explored to remove redundant elements using PCA. Consideration of the correlation parameters and the results from the PCA allowed the identification of elements which were associated with gold mineralisation in the area.

Three commonly used multivariate regression models were applied to the datasets to formulate a relation between the elemental and the hyperspectral datasets. Partial Least Squares Regression (PLSR), Kernel Partial Least Squares Regression (KPLSR); and Random Forest Regression (RFR). A skewed or bimodal data distribution can often be unsuitable for such statistical models (Babish, 2000; Steinberg et al., 2016; Varmuza and Filzmoser, 2016). In this study centring and scaling arguments for the models or centred log-ratio transformation were used to satisfy input data assumptions for modelling depending on the input requirements of the model (Luo et al., 2016a; Varmuza and Filzmoser, 2016).

PLSR is a linear multivariate regression algorithm which is widely used in chemometrics. PLSR effectively deals with the noisy and high collinearity of data, such as hyperspectral data (Rosipal and Trejo, 2001; Gomez et al., 2008; van der Meer et al., 2012; Cheng and Sun, 2016; Pullanagari et al., 2016; Wei et al., 2020). The algorithm transforms the data into orthogonal components to maximise the covariance between the variables (Rosipal and Trejo, 2001). The decomposition also works simultaneously in which the first few components exhibit most of the variation in the input data. The derived orthogonal component in the current study was optimised through 15-fold cross-validation.

A conventional linear technique such as the PLSR results in an estimation of regression coefficients which is unbiased but shows high variance. The KPLSR iteratively estimates the desired components by transforming input variables to a higher dimensional feature space until the model reaches an optimal dimension. The linear PLSR algorithm operates in this higher dimensional feature space (Arenas-García and

Camps-Valls, 2007; Pullanagari et al., 2016). In both models, the orthogonal factors were optimised using 15-fold cross-validation.

RFR is a decision tree-based algorithm, where the decision trees form with random samples from the training data using Breiman's "bagging" approach (Breiman, 2001). A random subset of variables is selected at each node, this random subsetting helps in dealing with overfitting in case of high multicollinearity such as the hyperspectral data. Each decision tree keeps expanding until it reaches a user-defined maximum node where a random sample is replaced with data from the training data (Breiman, 2001). Typically, 64% of the training data is considered for in-bag data and the rest 36% is referred to as out-of-bag (OOB) data which is used for testing. A sequential mtry (i.e., number of variables within a decision tree) value from 1 to 150 was assigned for the tuning of the RFR models.

In both PLSR and KPLSR models, the maximum number of components was pre-defined, to be 20. The component with the lowest $RMSE_{cv}$ (Root Mean Square Error- Cross-validated) was chosen to be used for the prediction models. Typically, these were between the 3rd and the 7th component. In the case of RFR, the algorithm was trained using labelled training data and finally selects the best performing variables in a similar way based on R^2_{cv} (cross-validated R^2) and $RMSE_{cv}$ values (Pullanagari et al., 2018).

The input for all these models were the lab (350-2500 nm) or airborne spectral datasets (370-2490 nm) and the ICPMS-derived elemental dataset. This study experiments with various spectral pre-processing approaches including continuum removal, Savitzky-Golay filtering with first derivative (Savitzky and Golay, 1964; Tsai and Philpot, 1998; Gomez and Coulouma, 2018; Pullanagari et al., 2018; van der Meer et al., 2018b). In the Savitzky-Golay filter, the window was set at 9 for the airborne hyperspectral data and 25 for the ASD hyperspectral data. Finally, Centred Log-Ratio (CLR) was applied to the elemental concentration in some of the models, aiming at pre-processing on the compositional data to improve model performance (Montreuil et al., 2013; McKinley et al., 2016; de Caritat et al., 2017; Gazley et al., 2020).

3.4 Results

3.4.1 Host Rock Mineralogy, and Elemental Concentration Distribution

The SEM-EDS analysis of the sampled mineralised lower greenschist exhibited, the As-Fe rich, Ti-O_2 and Au-bearing phases along the quartz-dominated veins and veinlets following the foliation (Figure 3.5a). Most of the larger crystals (>200 μm) belonged to the Si-rich phases (silica polymorphs) and feldspar (albite) (#5 in Figure 3.5b). Samples from the quartz veins show disseminated sulphides, including arsenopyrite and rarely pyrite, along with fractures filled with sulphide precipitation (Figure 3.5c).

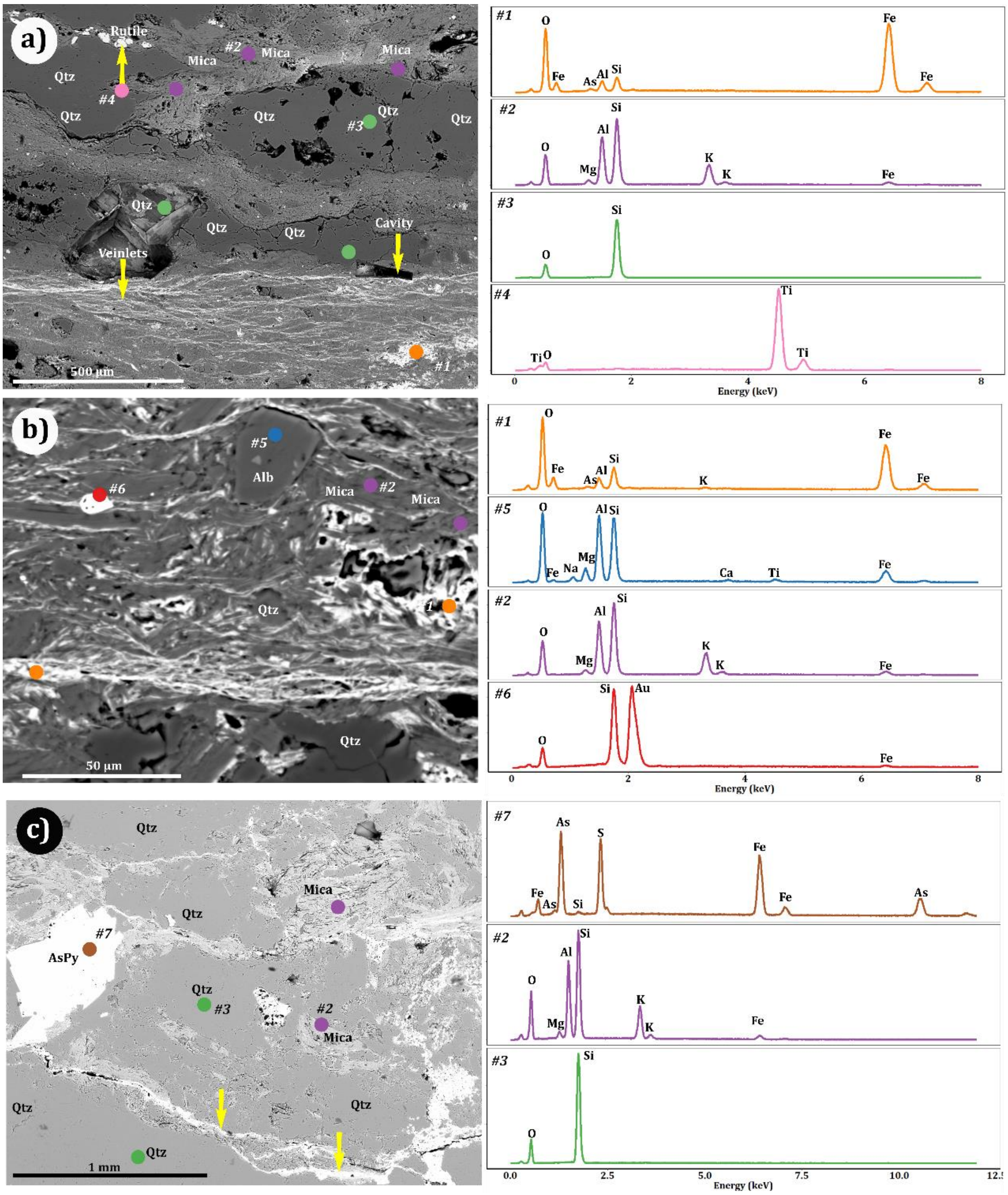

Figure 3.5: SEM images (left column) and EDS spectra (right column) of representative greenschist and quartz vein samples. The labelled EDS graphs are colour coded. A) Abundant quartz (Qtz), rutile, and mica, along with textural characteristics and orientation of the minerals along the foliation and cavities filled by quartz. B) Zoomed-in view of the schist with typical mineral phases, and gold is associated with pyrite (Py) and arsenopyrite (AsPy) phases; here #6 is a gold nugget. C) Shows both disseminated and euhedral arsenopyrite (AsPy) crystals along with fracture-infilling sulphide phases (yellow arrows).

3.4.2 Vegetation biogeochemistry

The correlation analysis of the hyperspectral and elemental concentration data identified seven trace metals which could be defined as pathfinder elements (As, Fe, Sb, W, Co, Ag, Ti) out of the total set of 37 elements (Appendix 1A). The elemental concentration spatial distribution from bark and needle samples matched closely to the inferred location of the high-grade mineralisation along the shear zone through structural mapping and target drilling data (Ritchie, T. personal communication) (Figure 3.6).

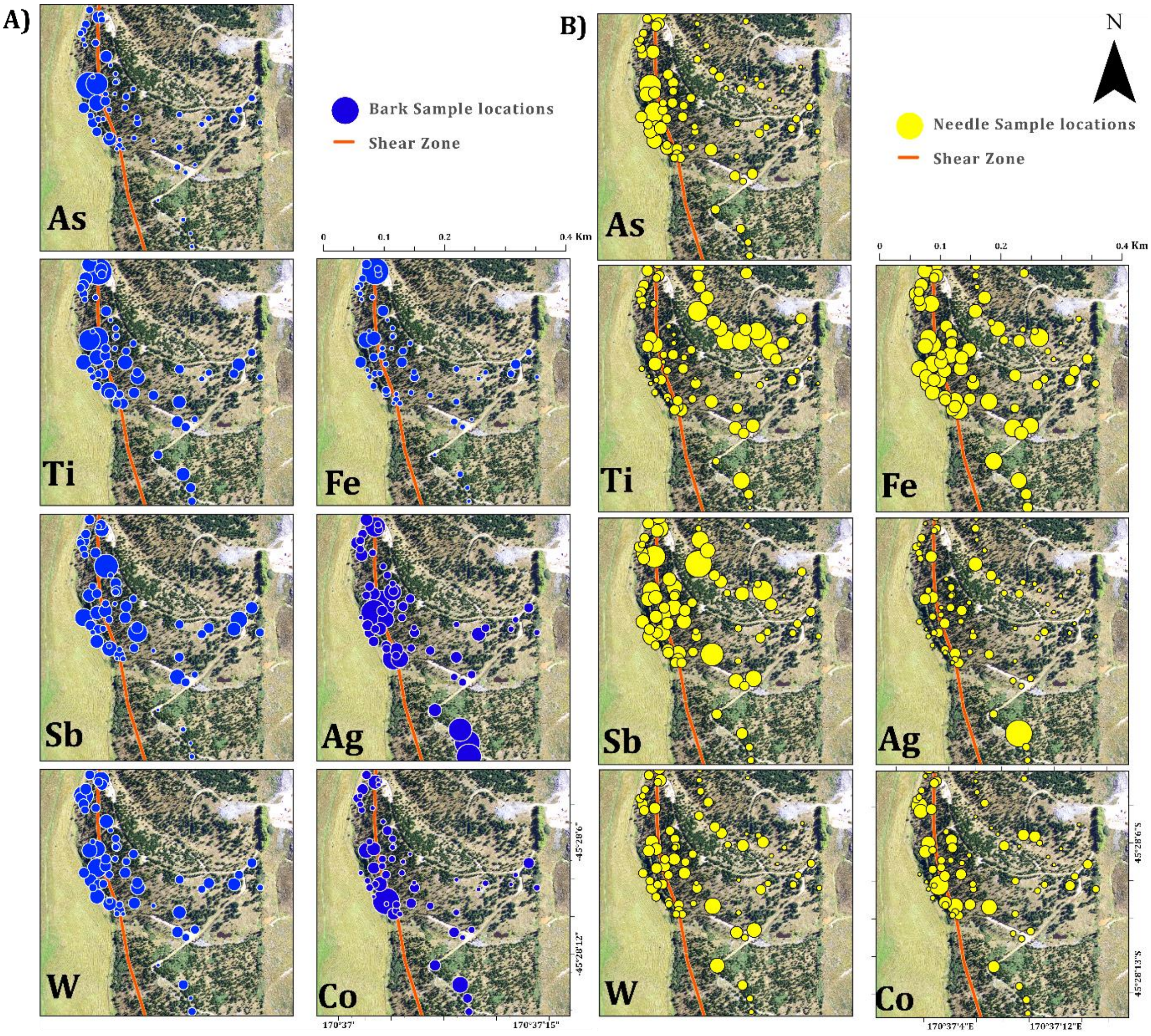

Figure 3.6: Proportional elemental concentration distribution of the samples around the shear zone which is located in the North-Western part of the sampling area; A- bark samples, B- needle samples.

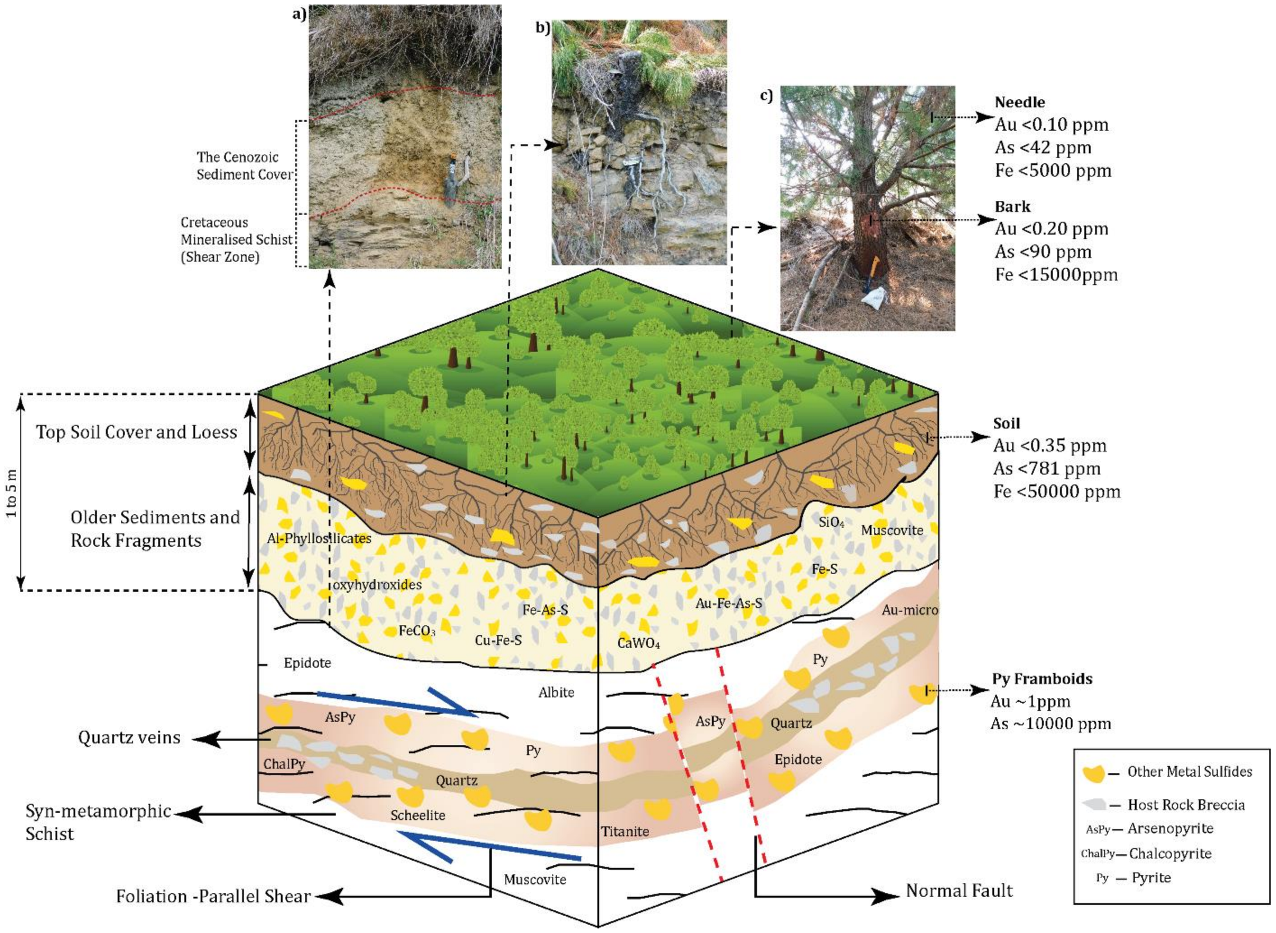

Figure 3.7: The block diagram shows the typical minerals and structural components of the region (after Craw and Norris (1991); Craw et al. (2007a)). a-b) Outcrop photo of the mineralised schist and tree roots reaching the surface of the mineralised zone along the shear zone; c) A tree that has been sampled for needles and bark. It also shows the typical raw concentration levels of gold (Au) and arsenic (As) within the host rock, soil and plant cover using the ICP-MS data.

The occurrence of these analysed rock samples and the general geology governing the manifestation of the mineralisation is compiled in the conceptual diagram for the HMSZ (Figure 3.7). The high-grade ore deposits occur along the shear zone as auriferous chalcopyrite, arsenopyrite and pyrite, along with albite, micas and rutile, and graphite based on previous studies (Henne and Craw, 2012; Blake et al., 2019). The location of the shear zone is exposed to the surface and atmospheric processes leading to supergene enrichment of gold at shallow depth and forming secondary mineral phases such as goethite, rutile, and K-mica (Cave et al., 2016). It is worth noting that the concentration drops by an order of magnitude lower between the host rock and the soil. Furthermore, the gold-bearing host rock is still remarkably superimposed onto the plant's biogeochemical data. Here, the bark samples show an order magnitude lower concentration (As<100 ppm, Fe< 20000 ppm) than those found in the soil samples, and typically double concentration than needles (Figure 3.7). The mapped vertical distribution of elemental concentration from host rock to plant can be used to formulate new approaches to bridge biogeochemistry with hyperspectral remote sensing approach to reveal potential coupling between shallow ore bodies and their impact on vegetation cover.

3.4.3 Correlation of pathfinder elements with hyperspectral signatures

The Pearson correlation coefficients for the chosen pathfinder elements in the bark samples were >0.4 (Figure 3.8). The correlation coefficients for needle samples exhibit a Pearson coefficient value <0.3 for all elements except for Ti and Fe.

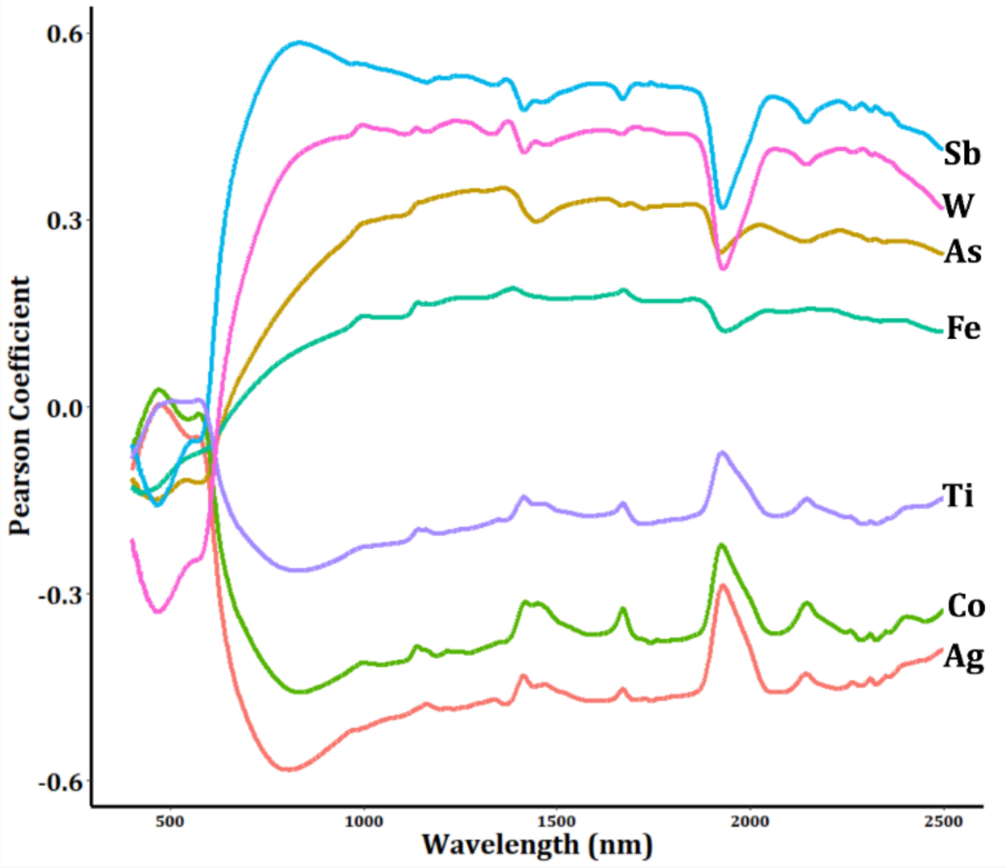

Figure 3.8: Laboratory-based spectrum to elemental concentration Pearson-type correlation coefficient curves for bark samples

Larger the concentration and range of the pathfinder element, the larger the feasibility that spectroscopic techniques can be applied to predict the concentrations (e.g., Pullanagari et al. (2016)). PCA was applied to explore the underlying structure of the elemental data. As shown in Figure 3.9, the majority of samples relevant to highly mineralised samples (green-coloured samples) are separated from the remaining samples. The loadings plots exhibit close associations of the elements in relation to the bedrock lithology. The As and Fe association is traced back to the common host-mineral arsenopyrite (Martin et al., 2018), Sb and W follow the immediate zone of arsenopyrite in the mineralising system, also sulphides of Pb and Cu, among others, have similar association and mobility which often brings them together in the system (Figure 3.9 and Table 3.1). The cluster of elements including Zn, Mg and P are important elements for plant processes. Although the concentration of Ag is very less in plants, yet it forms simultaneously with gold, which makes its PCA pull coinciding with the highly mineralised zones.

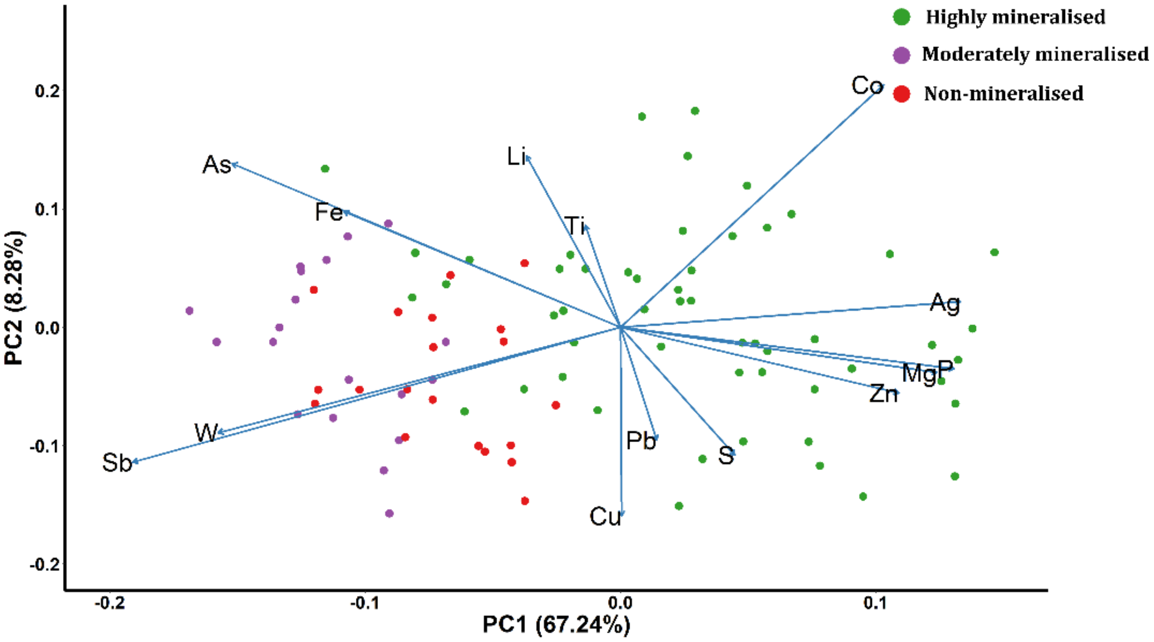

Figure 3.9: PCA biplot for an elemental dataset on bark samples. The first component is on the x-axis and the second component is on the y-axis.

3.4.4 Laboratory-based and Airborne Hyperspectral Prediction Models

3.4.4.1 Laboratory-based hyperspectral: The PLSR, KPLSR and the RFR model outputs significantly vary from bark to needles. The models trained from the bark samples have the best accuracy for Sb, which exhibits the best R^2_{cv} of 0.57 with elemental concentration values in ‘ppm’. The R^2_{cv} increases to 0.80 when transformed using CLR (Figure 3.10). Whereas the prediction models for needles show the best R^2_{cv} values for Ti, the highest with ‘ppm’ unit of elemental concentration is 0.71 which on CLR transformed elemental dataset shows a maximum R^2_{cv} of 0.54 (Figure 3.11).

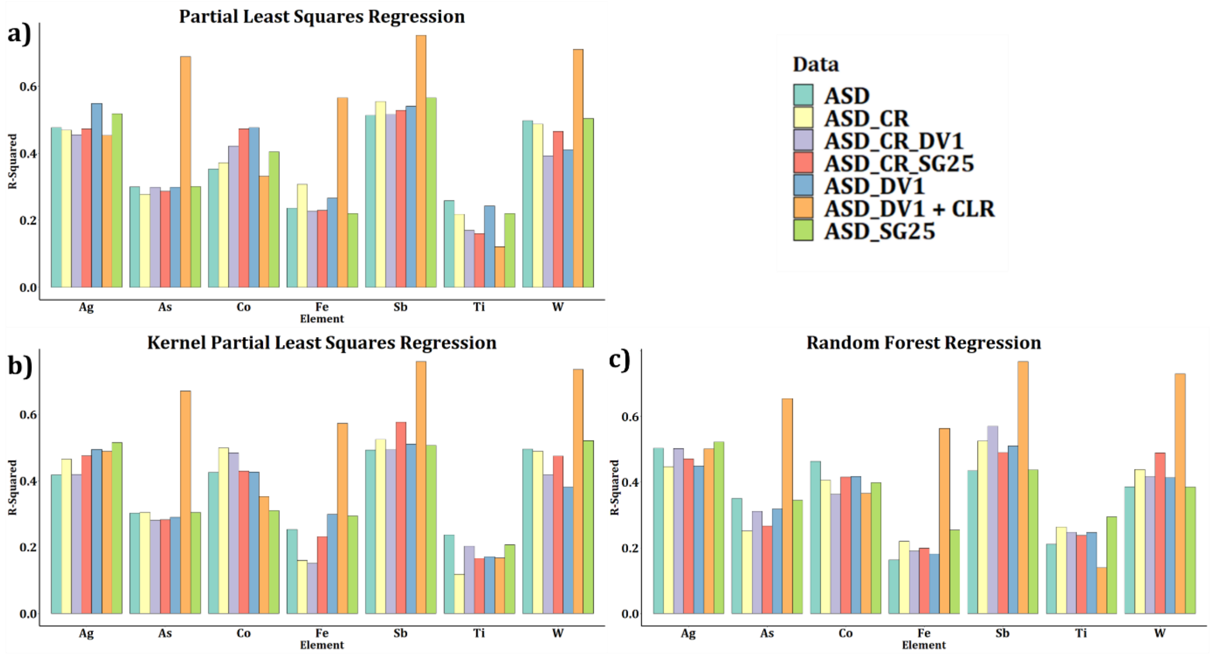

Figure 3.10: Bark samples-Bar plot showing performances of different regression models using lab hyperspectral data a) Partial least squares regression, b) Kernel-based partial least squares regression and c) Random forest regression. Different colours signify differently treated input dataset. CR, DV1, SG25 and CLR stand for continuum removed, first derivative, Savitzky-Golay filter with window size 25 and centred log-ratio transformation, respectively.

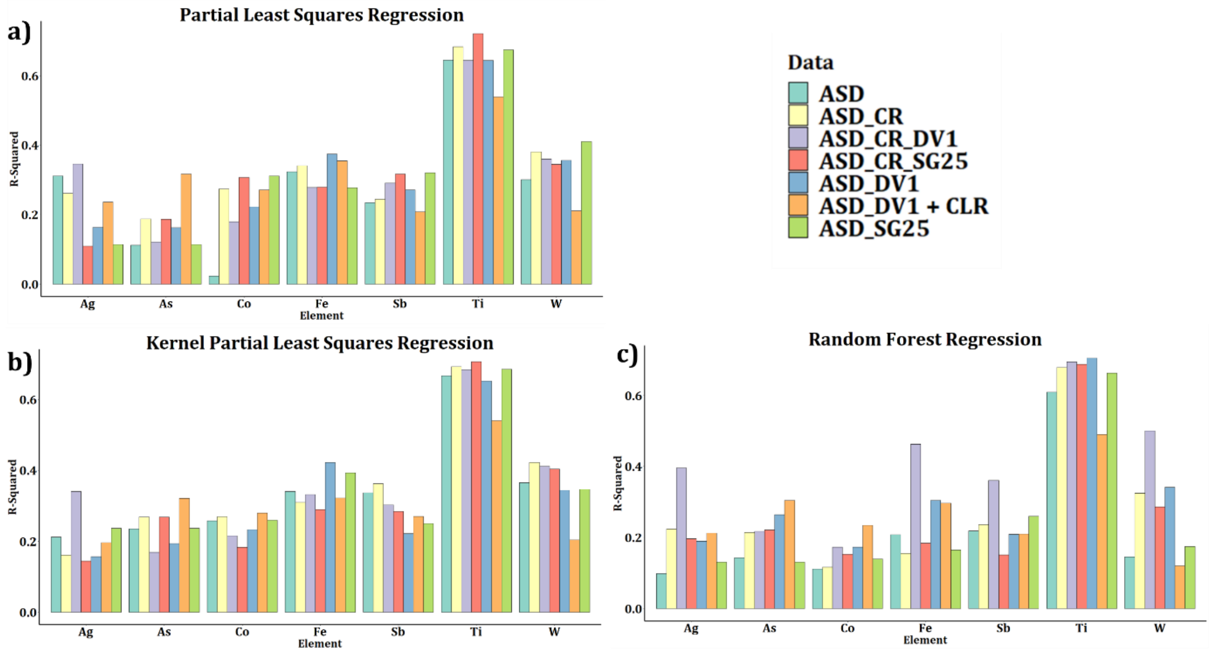

Figure 3.11: Needle samples- Bar plot showing performances of different regression models using lab hyperspectral data b) Kernel-based partial least squares regression and c) Random Forest regression. Different

colours signify differently treated input datasets. CR, DV1, SG25 and CLR stand for continuum removed, first derivative, Savitzky-Golay filter with window size 25 and centred log-ratio transformation respectively.

The model performances were also assessed using a scatter plot for predicted versus observed values for As and Sb (Figure 3.12). The predictions within the confidence interval (grey part in Figure 3.12) are higher for the models including bark samples compared to the needle samples. Although the difference between R^2_{cv} between the needle models is a mere 0.02 the model trained for Sb has more observation in the confidence interval as compared to As.

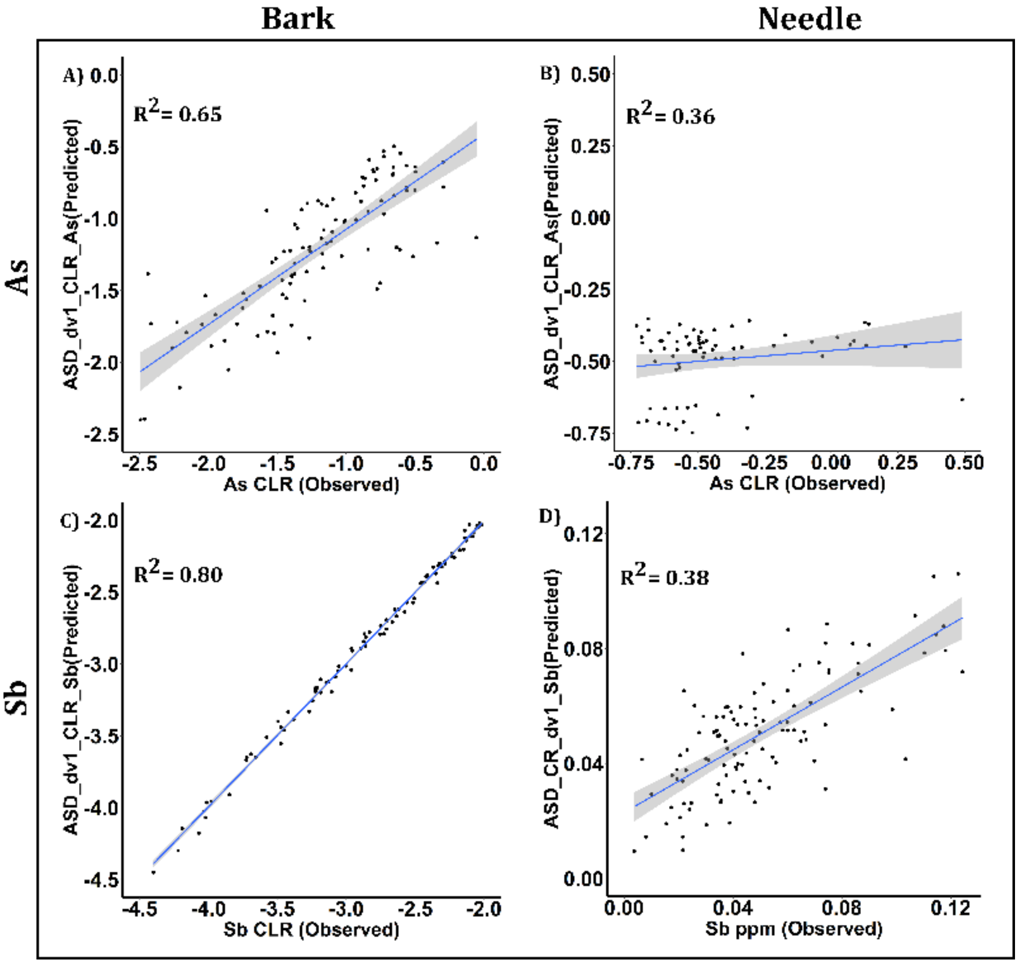

Figure 3.12: Scatter plot showing the observed vs predicted values for the best models of Bark and Needle for As and Sb. The grey area around the trendline illustrates the 95% confidence interval.

3.4.4.2 Airborne hyperspectral: The model outputs were poorer compared to the laboratory-based hyperspectral data when trained with the airborne hyperspectral data. Surprisingly, the models trained with the bark samples show the best accuracy for Ag and Sb. The best R^2 values for Ag were ~0.50 for almost all models, Sb shows the best R^2_{cv} value of 0.38 when trained with elemental concentration in 'ppm' which increased to 0.55 when CLR transformed. The models utilizing the needles were poorer compared to the bark-based models. Although like the other models utilising the needle sample data the Ti still shows the maximum R^2 value of 0.38 with CLR transformed data. The performances of all models are detailed in the SD2.

The best regression model for Sb is used to predict the potential Sb concentration anomalies that coincide with the distribution of the illustrated shear zone (Figure 3.13). The data of the model is trained using elemental concentration data from the bark samples and the airborne hyperspectral data. The model performance in this instance is moderate (R^2_{cv}=0.55) but shows the feasibility of the proposed methodology.

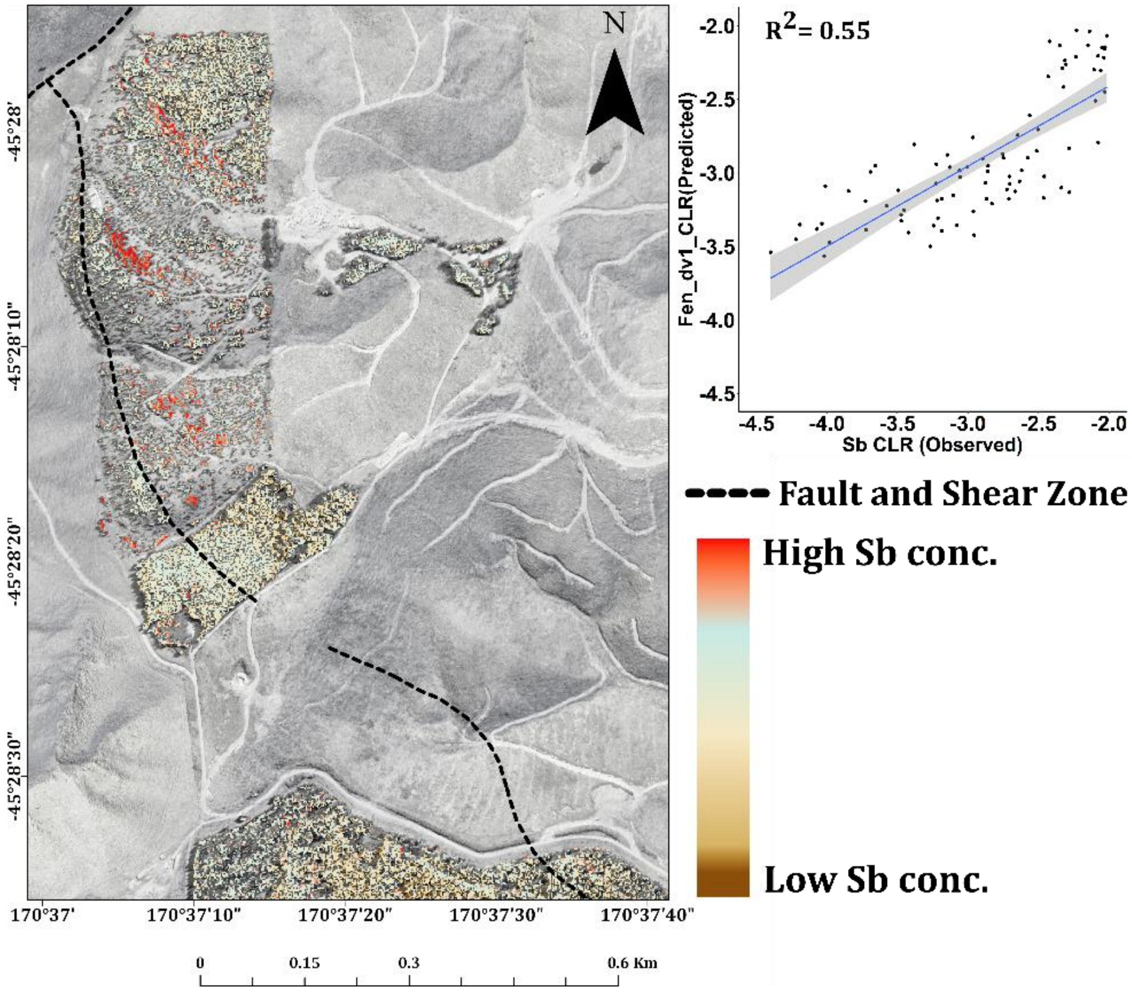

Figure 3.13: The results from the PLSR regression model using Sb concentration from the bark samples and the airborne hyperspectral data were used to predict Sb values on the plantation patch pixels from the airborne hyperspectral image.

3.4 Discussion

3.4.1 Occurrence of pathfinder elements and their mobility in plants

The rocks analysed through SEM-EDS exhibited gold-bearing arsenopyrite and pyrite. The disseminated gold-bearing phase often occurs along the foliation trend of the host rock. The surface breakdown and weathering help to release the major pathfinder element that this study was focused on. The concentration of As, the main pathfinder element for gold in Otago, decreases about an order of magnitude from ~1000 µg/g to 50-100 µg/g over mineralised areas from soil to bark. While, other elements, such as Sb, and Ag show the opposite trend of being enriched in the needles and bark of the trees (Table 3.3). The chemical breakdown of arsenopyrite at shallow depth leads to leaching of As into the groundwater due to its high water solubility of As. Water solubility can further decrease the retention of As concentration in the plant tissues (Ashton, 1989; Patinha et al., 2004). On the other hand, Fe is ubiquitous in the soil and plant system which makes it hard to link its occurrence to underground geology and mineralisation.

The observed element uptake and distribution within plants are influenced by the chemical association between elements in a mineral, ionic size and the presence or absence of ligands which control geochemical mobility and bioavailability (King, 1984; Dunn, 2007). Therefore, we interpret the observed trends in our data to be related to element mobility and water solubility since those trace metals and metalloids absorbed by the plants passively along with water and they are not considered essential for plant growth and may even be toxic (Brooks, 1979; Bech et al., 1997; Anderson et al., 1999; Dunn, 2007; Doronila et al., 2014). Our study shows a moderate to strong correlation between the biogeochemistry of *Pinus radiata* trees and underlying geology. This is in agreement with studies on other deep-rooted tree species such as Eucalyptus and *Douglas fir* (Dunn, 1986; Farago, 2008; Kovalevsky, 1987; Lintern et al., 2017). However, this correlation can be apparent at times as trees can collect, store, use and also discard toxicity induced by elements over a span of time (Dunn, 1986; Cohen et al., 1987; Stednick et al., 1987). This makes the soil and plant chemistry uncorrelated over time, as it alters the vegetation in elemental concentration in the plant compared to its surroundings, as seen from the ground samples (Figure 3.6). The implication here is that over time a geochemical-biogeochemical equilibrium is reached in mineralised regions that differ and can be distinguished from that in non-mineralised regions. These elements were used mostly in soil baseline exploration (Martin et al., 2016). Our study shows that the biogeochemical signature follows these lines, and they change with levels of mineralization in the host rock.

3.4.2 Feasibility of bridging hyperspectral data analysis with biogeochemistry

This study shows that the elemental concentration in the plant can be predicted using laboratory-based hyperspectral scanning. Our results are more consistent and robust for bark samples than for needle samples (Figures 3.10 and 3.11). This is due to the presence of a wide variability of elemental concentrations in the bark. The best regression models using laboratory-based hyperspectral data exhibit R^2_{cv} values between 0.6 and 0.8 after cross-validation for immediate pathfinder elements like As, Sb, and Ag. This was interpreted to be related to the sub-surface gold mineralisation in the area.

Interestingly, the prediction model for Ti yielded one of the best results among all the other models using the needle samples. However, this is likely to be related to airborne contamination, such as wind-blown dust (here, from a nearby new drill location) (Brooks, 1979; Shahid et al., 2017) as opposed to the uptake of Ti from the soil (Table 1). The model performances in Ti using bark samples yielded much poorer results, this was interpreted to be due to low mobility of Ti in the plant system thus decreasing its concentration range in the bark samples.

A quantitative approximation of elemental concentration through vegetation R^2_{cv} values through spectroscopy has been put forward based on controlled experiments (Farago, 2008; Rathod et al., 2015; Shi et al., 2016; Rathod et al., 2018; Zhou et al., 2018). A major concern with the interpretations in this domain with the hyperspectral sensor is that, even in the laboratory, the image signal is influenced by morphological and chemical properties of the plant canopy, such as leaf structure, undulation and water content (Wang, 2018). Our results indicate the feasibility of laboratory-based hyperspectral data as a potentially faster and cheaper tool to screen mineral resources, such as gold. However, trace elements, such as As and Sb, lack characteristic absorption features within the VNIR and SWIR range, and hence the prediction models need to be treated with care and used as secondary evidence of the correlation between the vegetation and underlying lithology/mineralisation. The use of portable spectroradiometer can also be used for in-situ measurements aiding exploration efforts (e.g., geochemical vectoring). The spectral data has a bandwidth of 1 nm and 2151 bands, while the airborne hyperspectral data has a bandwidth of 3.5-6.8 nm, and 448 bands instead. This makes the laboratory-based hyperspectral data capable of differentiating more subtle physico-chemical features in the spectra as compared to the airborne data. The lab data is still limited by its point-based data procurement. However, it can still reduce operation costs and time significantly compared to conventional biogeochemical exploration methods (e.g., ICP-MS). Therefore, it can provide a robust pre-screening method for reconnaissance surveys for mineral exploration in densely vegetated terranes.

Airborne hyperspectral imagery however manifests modest correlation as compared to the laboratory-based data. The prediction models for bark samples predicted higher accuracy (R^2_{cv} of 0.3–0.6) than needles (R^2_{cv} of 0.1–0.4). This could be attributed to the narrower variations in the elemental concentrations in needles (e.g., As, Fe, Sb in Appendix 1B). Additional factors could influence our prediction models including atmospheric interference such as differences in illumination, shadow effects and also absorption and scattering from atmospheric gases and dust particles (Itten and Meyer, 1993; Gao et al., 2009; Fred, 2018). The 2 m spatial resolution of the airborne hyperspectral image has also mixed pixels, dominated by crown leaf spectra, sun-lit and/or shadowed parts of the canopy, bare ground, spectral resolution, and bandwidth differences. This requires future studies and airborne data collection experiments to quantify the spatial resolution dependency of our prediction models.

The potential application of airborne hyperspectral imaging using such methods has been demonstrated in Figure 3.13. A major limitation in this model is that the canopy suppresses the bark spectral signature, regardless there is much potential in this technology. Future research must implement the proposed approach on higher resolution airborne data with a higher signal-to-noise ratio and a much larger training dataset. This provides a new opportunity to predict the element concentration in a vegetated area at a regional scale, opening a new first-order reconnaissance survey approach for mineral exploration.

3.4.3 Exploration with hyperspectral technology

The typically high-resolution airborne hyperspectral image data has already been employed to numerous quantitative and qualitative applications, including biogeochemical predictions and mineral mapping (van der Meer et al., 2012; Pullanagari et al., 2016; Ghamisi et al., 2017a; Pullanagari et al., 2017b; Kereszturi et al., 2018). In the near future, a new series of hyperspectral satellites will be put into orbit, including Environmental Mapping and Analysis Program (EnMAP) (Kaufmann et al., 2008), Hyperspectral Infrared Imager (HyspIRI)(Abrams and Hook, 2013; Lee et al., 2015), Hyperspectral Environment and Resource Observer (HERO)(Bergeron et al., 2008), HYPerspectral X Imagery (HYPXIM) (Carrere et al., 2013). In fact, the PRISMA mission was successfully launched and put on orbit and is providing new hyperspectral data on 29 days repeat cycle (Lopinto and Ananasso, 2020; Cogliati et al., 2021) with the potential to be utilised for mineral exploration purposes. It has a spectral resolution of <12 nm in both the VNIR and SWIR regions across a total of 237 bands ranging from 400 to 2505 nm, and a spatial resolution of 30 m. A major limitation to port this methodology to a satellite-based platform is the spectral and spatial resolution. All of these spaceborne sensors have larger spatial pixel, typically 30 m-50 m, which is very coarse at such plantation patch levels. The satellite-based sensors could be used in such applications of mineral mapping and biogeochemical explorations on mineral deposits on a larger spatial extent where the coarser pixel might not be a hindrance. These new datasets can provide new avenues for geochemical prospecting and mapping to support large, regional-scale prospects.

3.5 Conclusion

Delineating mineral resources in a densely vegetated area, which is the case in New Zealand and many places globally is highly challenging. Utilizing the technology of hyperspectral remote sensing in this domain could make the process more sustainable and time efficient. The three main exploration approaches, geophysical, geochemical and geological, in congruence are likely to formulate a faster and cheaper reconnaissance survey. This study trailed three regression approaches to link biogeochemistry data to underground mineralization through new laboratory-based and airborne hyperspectral data. The results of the multivariate regression models show that the laboratory-based hyperspectral data is suitable as an early prospecting tool and thus proving its feasibility in geochemical exploration.

The airborne hyperspectral data cover a larger footprint, the crown leaf spectra dominating the majority of the pixels and are subjected to atmospheric gas/particle absorption. This has resulted in poor performances of the models when trained using airborne hyperspectral data. The variation in the R^2 values with respect to the pathfinder elements was still consistent to that of the laboratory-based data but in a much lower range, highlighting the feasibility of airborne hyperspectral data with improved signal-to-noise enhancement and instrumentation (e.g., increasing spectral sampling frequency).

The physiological function of the pathfinder elements in the plants governs their occurrence and/or magnitude of concentration in the various plant tissues. This was reflected in bark and needle samples, which showed significantly different model performances. The workflow developed in this study is suited to the mono-species (*Pinus radiata*) areas. We may expect a different behaviour for ecosystems with different types of vegetation cover which would require new training models to be developed.

The future work to minimise the effects caused by such disparities and formulate better prediction models can make this approach applicable for extended airborne datasets and satellite-based hyperspectral data. This improvement can provide a new and quick tool for reconnaissance surveys to locate economic resources in inaccessible areas using hyperspectral remote sensing.

3.6 Acknowledgement

This study was supported by the Ministry of Business, Innovation and Employment (MBIE)-Endeavour Fund- Smart Ideas: Assessing New Zealand’s environmental and mineral indicators (contract number: MAUX1802). The authors are also grateful for the support from Hardie Pacific Ltd., with logistics, ground access and data interpretation and Colin Dunn Consulting Inc. with ICP-MS elemental analysis. Field assistance from Ildikó Soós is greatly appreciated. The authors are also thankful to Raoul Solomon (Massey University’s Manawatu Imaging Centre) for his help in operating the SEM-EDS machine. The authors are grateful to the Journal Editor and the three anonymous reviewers for their constructive comments.

Chapter 4. Mapping arsenic anomalies indirectly using airborne hyperspectral imaging- Implication for gold prospecting along the Rise and Shine Shear Zone in New Zealand

4.1 Introduction

Hyperspectral imaging measures reflected and emitted energy from the Earth’s surface at hundreds of contiguous spectral bands. Hyperspectral data can span over multiple parts of the electromagnetic spectrum, including the; visible (VIS; 400-700 nm), near-infrared (NIR; 700-1200 nm), shortwave infrared (SWIR; 1000-2500 nm), mid-wave infrared (MWIR; 3000-7000 nm), and longwave infrared or thermal domains (LWIR; 7000-13000 nm) (van Ruitenbeek et al., 2005; Kriesel et al., 2011; Kruse et al., 2012; Ullah et al., 2012; Notesco et al., 2014b; van der Meer, 2018; Simpson and Christie, 2019; Kereszturi et al., 2020; Laukamp et al., 2021b; Tripathi and Garg, 2021). Hyperspectral data can deliver spectrally ‘rich’ information due to its narrow and contiguous spectral band design. However, it comes at an expense of higher dimensionality and increased noise, such as instrumental and atmospheric among others, compared to broadband multispectral imaging (Mielke et al., 2014; Ghamisi et al., 2017b; Laukamp et al., 2021b). Overcoming the complexity of data processing has led to many applications, including agriculture, planetary studies (Kusuma et al., 2012; Chauhan, 2015), ecology, water/coastal studies, geology (van der Meer et al., 2018a; van der Meer, 2018), geothermal exploration (Rodriguez-Gomez et al., 2021), and soil science (Wei et al., 2020).

Mineral exploration can benefit from hyperspectral remote sensing due to its capacity to spatially map minerals by measuring absorption due to molecular-bond and vibrational processes. Furthermore, reconnaissance survey using airborne and satellite-based hyperspectral data is also a fast and cheap method for vectoring in mineralised zones (Cloutier et al., 2021). For instance, the SWIR region has potential to detect phyllosilicates, sulphates, Fe-rich oxides, carbonates, chlorites and many other alteration minerals (Hunt, 1982; van der Meer and Bakker, 1997; Sabins, 1999; Clark et al., 2003; van Ruitenbeek et al., 2014; van der Meer, 2018). Previous studies have been utilising hyperspectral imaging for mapping indicator minerals using ‘direct’ information, such as wavelength position and depth. In a standard hyperspectral imaging mapping workflow, the reflectance data is initially put through minimum noise fraction (MNF) for dimensionality reduction. MNF includes two levels of rotation, the first separate the noise from the information and in the second rotation, the noise-whitened data is further transformed to capture the maximum variance in the data (Wu et al., 2013). This is followed by identifying the pure pixels indices that are then used for selecting the endmembers to form the training subset. These endmembers are finally used in mapping algorithms for generating abundance maps (Clark et al., 1993; Boardman et al., 1995; Kruse et al., 2003; Kruse, 2007; Kruse et al., 2012). This is a powerful approach when the targeted exploration site is well-exposed, such as the famous Cuprite dataset (van der Meer and Bakker, 1997; Swayze et al., 2014). However, Cuprite and other similar sites with well-exposed exploration targets (i.e., none to sparse vegetation, thin regolith cover) represent a minor percentage of the current mineral prospect globally, demanding new approaches that can handle partial to full vegetation cover.

The opportunity can rise to capitalise on the complexity of the hyperspectral data by integrating advance statistical methods, such as machine learning (Ghamisi et al., 2017b). The advent of machine learning in hyperspectral remote sensing has brought many effective algorithms (e.g., random forest, support vector machine, neural networks, advanced spectral unmixing methods), to tackle the complexity of the data and extended many solutions to the inherent challenges (Cheng and Sun, 2016; Ghamisi et al., 2017a; Pullanagari et al., 2017a; Naik et al., 2021; Rodriguez-Gomez et al., 2021). One of the major advances in the recent hyperspectral sensors is the finer spectral resolution which leads to hundreds and even thousands of bands/variables, increasing computation demand. Thus, variable selection methods, such as least absolute shrinkage and selection operator (LASSO), stepwise selection, and recursive feature elimination (RFE) have been utilised to improve computation time, costs, and applicability of the resultant statistics (Guyon and Elisseeff, 2003; Zou, 2006; Paul et al., 2008; Kursa et al., 2010; Zhou et al., 2014; Han et al., 2016; Demarchi et al., 2020; Lotfollahi et al., 2020).

The present study aims to explore the information captured by hyperspectral data for mineral exploration using a mineral prospect from New Zealand with partial to full vegetation cover (i.e., ‘less optimal’ for hyperspectral data). This study, therefore, develops an alternative approach that can build on indirect interference to locate mineral resources underground. This study is based on the Rise and Shine shear zone (RSSZ) in South Island, New Zealand (Figure 4.1A), which hosts mesothermal gold mineralisation in the upper greenschist facies rock (Craw and MacKenzie, 2007; MacKenzie and Craw, 2007). It is a highly rugged terrain showing a diverse range of exposed soil (5-80%), and sparse grass and tussock vegetation cover (Figure 4.1B). Using a 2 m spatial resolution airborne hyperspectral data, this study allows to depict the complexities of the reflectance signals, including exposure fraction and influences of vegetation, while developing a new screening method to locate underground gold mineralisation. Utilising arsenic (As) as the main pathfinder element through certain surface manifestations (Table 4.1) caused mostly by the leaching of arsenopyrite and scorodite which are the main pathfinder minerals to gold in the RSSZ.

Table 4.1: Theoretical parameters differentiating non-mineralised to mineralised and the corresponding hyperspectral signals driving the study. (Veg-vegetation)

Attribute	Non-mineralised	Weakly mineralised	Strongly mineralised
Shear zone features at the surface			
Gold	Below detection	<0.5 ppm; rare veg	>1 ppm; rare veg
Arsenic	<30 ppm	>50 ppm	>1000 ppm
Shear zone trace	Sharp boundary to NE (Thomsons Gorge Fault) Diffuse boundary to SW	Strong feature, NW strike, 20 m wide at the surface	Strong feature, NW strike, wider surface zone, to 100 m
Outcrop structure	Foliation dominated	Foliation and shears	Foliation and shears
Carbonate	Minor calcite	Minor calcite, ankerite	Abundant ankerite
Hydrothermal alteration	None altered	Alteration of chlorite to ankerite	Ankerite completely replaces chlorite
Kaolinite	Minor alterations from the Cenozoic era	Minor from Cenozoic alteration; some hydrothermal	Minor Cenozoic alteration; abundant hydrothermal alteration
Ferric oxyhydroxide	Minor alterations from the Cenozoic era	Abundant from sulphides and ankerite	Abundant from sulphides and ankerite
Surface	Outcrops, colluvium	Abundant scree from sheared rock	Abundant scree from sheared rock
Expected hyperspectral signals at the surface			
Surface features	Mostly vegetated	Abundant bare ground	Abundant bare ground
Chlorite	Strong Mg-OH signal	Weak Mg-OH signal	No Mg-OH signal
Kaolinite	Weak Al-OH signal	Moderate Al-OH signal	Strong Al-OH signal
Ferric oxyhydroxide	Weak Fe-OH signal	Moderate Fe-OH signal	Strong Fe-OH signal
Carbonate	Weak CO_3 signal	Moderate CO_3 signal	Moderate CO_3 signal

4.2 Geological settings

The RSSZ is part of the Otago Schist and is exposed as a ~50-100 m wide zone that strikes northwest across the Dunstan Range. The schists were pervasively recrystallised and foliated during metamorphism and now consist of highly segregated quartz-albite and chlorite-phengitic muscovite laminations at the centimetre scale. The shear zone is hosted in upper greenschist facies schists that have been juxtaposed against lower greenschist facies schist. The shear zone dips gently (~15-20°) to the northeast in the footwall of the Thomson’s Gorge Fault, post mineralisation normal fault (MacKenzie and Craw, 2007). Fresh mineralised schist contains disseminated arsenopyrite in foliation-parallel shears and breccias, and gold is closely associated with this arsenopyrite (Figure 4.1) (Mortimer, 2000; Craw et al., 2005; Christie, 2016; Cudby et al., 2021). Metamorphic chlorite was extensively altered to hydrothermal Fe-Mg-Ca carbonate (ankerite) during mineralisation. Oxidation of the mineralised zone has caused abundant ferric oxyhydroxide to form during the decomposition of arsenopyrite and ankerite. The ferric oxyhydroxide has variable amounts of adsorbed and intergrown As, and both Fe and As have been extensively remobilised on to fractures and foliation surfaces.

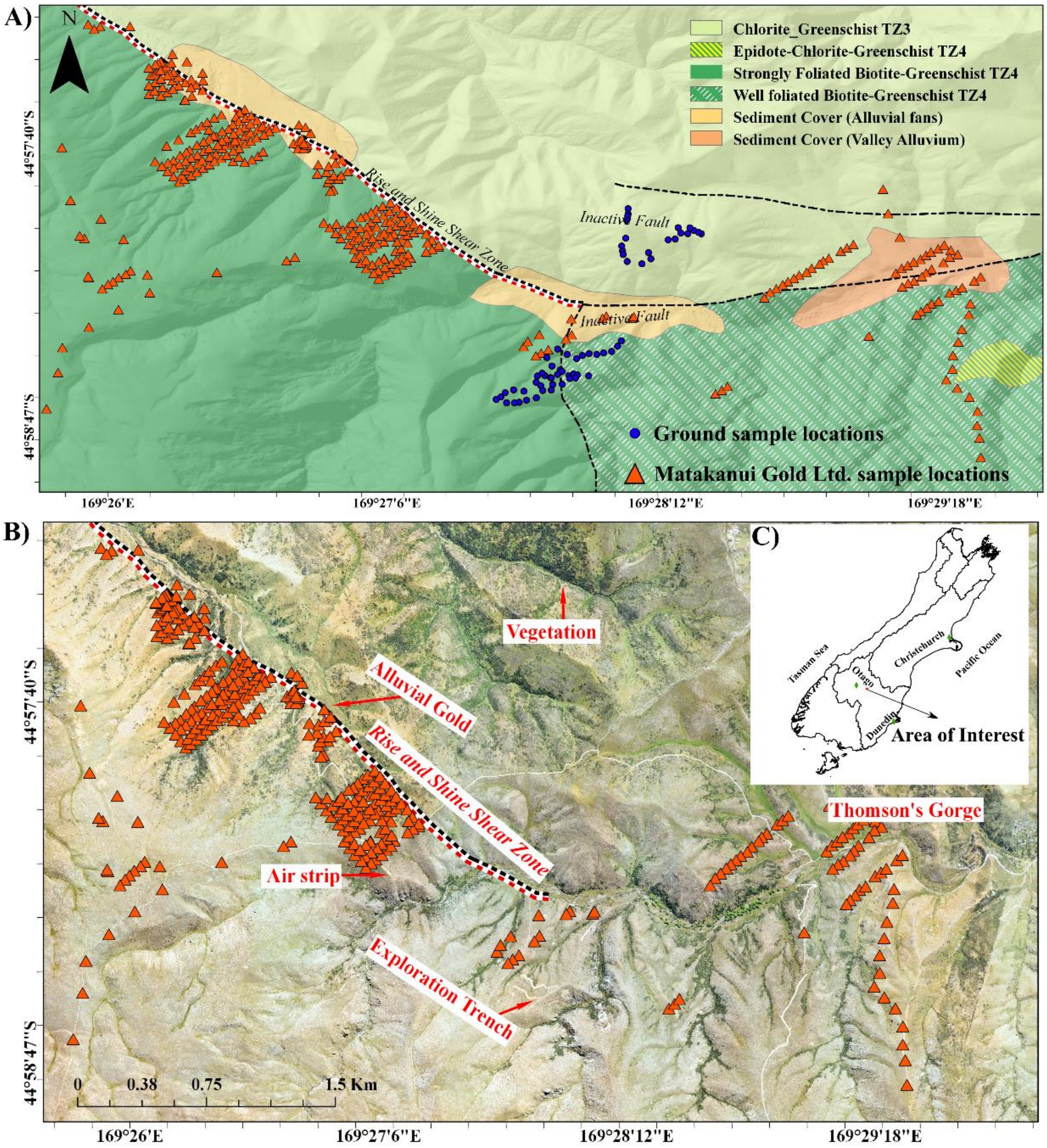

Figure 4.1: A) Simplified geological map of the Upper Thomson Gorge, overlaid by the sampling locations (blue dots) and geochemical vectoring data provided by Matakanui Gold Ltd. (orange triangles). B) RGB orthophoto of the same area, representing the ruggedness of the terrain and the grass/tussock cover. C) On a map of South Island, New Zealand, the key places and the study area are marked for a broader idea of the location.

Gold occurrence here is often signalled by elevated As concentration due to supergene breakdown of arsenopyrite, forming As-rich halos around the ore bodies. The Ca- poor ankerite alteration phase is also a characteristic indicator mineral for gold mineralisation along the RSSZ. The precipitation of ankerite through decomposition of metamorphic chlorite released Fe, triggering the formation of arsenopyrite and other sulphide minerals. This leads to sulphur depletion in the hydrothermal fluid destabilising the Au-S complexes and causing disseminated gold deposition (MacKenzie et al., 2006; Craw and MacKenzie, 2007).

The soil along the RSSZ is strongly controlled by the ore-bearing schistose parental material, which is in turn controlling its bulk soil geochemistry and weathering (Martin et al., 2016). Soil overlying biotite, chlorite-rich greenschist facies rocks show elevated As concentration in both A (0-30 cm) and B (50-70 cm) horizons, while on the contrary, soil developed on lower-grade metamorphic basement rocks show baseline concentrations. Recently, soils of Southland and Otago have been analysed by Inductively Coupled Plasma Mass Spectrometry (ICPMS) and XRF for multiple elements, including As (Martin et al., 2016; Martin et al., 2018). The sampling has been carried out at a regular 8 km grid spacing that can provide an adequate As baseline information for the RSSZ.

4.3 Materials and methods

4.3.1 Field campaigns, sampling, and rock analysis

The field sampling sites were selected based on a pXRF soil analysis dataset previously collected by the Matakanui Gold Ltd. and the geological knowledge of the area (Cox et al., 2006; Craw and MacKenzie, 2007). The sampling was targeted to incorporate the potential zones of mineralised and non-mineralised zones (Figure 4.1). In total 63 soil samples were collected, covering a range of exposure conditions (Figure 4.2). The soil exposure percentage was quantified based on 100 random point counts from near-nadir hand-held digital photos (Figure 4.2A-C). The details of all the 63 sample locations are provided in Appendix 2A.

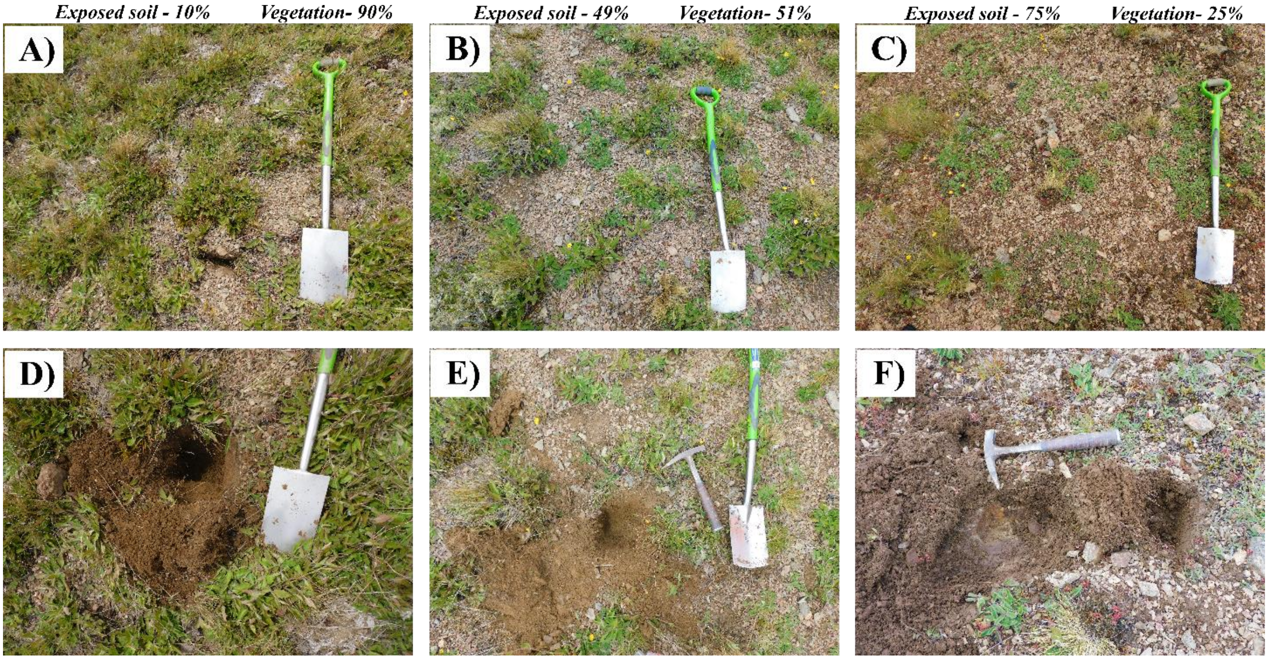

Figure 4.2: The soil exposure in the sampling sites varied approximately from 10 to 80%. The figure shows three different levels of soil exposures encountered in the sampling sites. The spade and hammer are ca. 100 cm and 30 cm long, respectively.

The field soil samples were collected from A-depth, 5-20 cm immediately beneath the vegetation cover (Figure 4.2 D-F). The rock fragments encountered typically at the interface of the soil and rock were also sampled. Forty-two soil samples were collected from the mineralised zone and the remaining 21 samples were collected from the non-mineralised zone for training purposes. This data was used for the band selection purpose and in the “direct” mapping workflow elaborated later in the chapter.

An additional 309 samples out of an extensive dataset of 1500 samples were also used. This database was developed through multi-year field campaigns and analysis using pXRF on the surface soil for As by Matakanui Gold Ltd. (Figure 4.1). These 309 samples were grouped into three classes to represent the previously established geochemical baseline (i.e., <20 ppm; Martin et al. (2016)), medium (20-100 ppm) and high As (>100 pm) that is indicative of underlying gold deposits.

A selected range of rock samples from both the mineralised and non-mineralised regions along with a scorodite-bearing schist rock sampled by Cudby et al. (2021) was examined using Scanning Electron Microscope (SEM) which was equipped with energy-dispersive X-ray spectroscopy (EDS), for detailed mineralogical and compositional analysis. Thick (~0.6 to ~0.8 mm) sections of the rock were mounted on glass slides. The thick sections were then carbon coated and imaged using ThermoFisher Scientific™ FEI Quanta 200 Environmental Scanning Electron Microscope. The SEM was operated in Back-scattered electron (BSE) mode under an accelerating voltage of 20kV, at the wondering distance of 10 mm. The EDS on the same thick section was operated at an accelerating voltage of 25 kV.

4.3.2 Airborne hyperspectral surveys and data processing

The airborne hyperspectral data was captured by a push-broom AisaFENIX sensor, operated jointly with a Nikon D810 digital single-lens reflex camera. The airborne survey was designed to capture hyperspectral images at a 2 m spatial resolution with 30% side overlap. The airborne experiment was carried out at local noon on the 11th of February 2020. The details of the sensor specifications area tabulated in Table 4.2 and pre-processing workflow can be found in Chakraborty et al. (2022).

Table 4.2: AisaFENIX specifications

	VNIR	SWIR
Field of View	32.2°	
Instantaneous Field of View	0.084°	
Full-Width-Half-Maximum	3.2-12.2 nm	
Spectral Bandwidth	~3.3 nm	~5.7 nm
Number of Bands	177	272
Spectral Range	0.3773-0.9775 µm	0.9831-2.4918 µm

4.3.2.1 Reflectance spectroscopy and pXRF analysis

The 63 field soil samples were oven dried at ~65°C for about two days. The samples were then coarsely grinded and sieved before acquiring VIS-SWIR reflectance using an ASD FieldSpec 4 High-Resolution spectrometer at Massey University. This instrument collects light reflectance from 350 nm to 2500 nm with a spectral interval of 1 nm. A small portion of the soil sample was transferred on a petri dish with a black background, the data was then obtained by direct spot measurements in 5 different spots, using a high-intensity contact probe. Before each measurement, white reference calibration was performed with a Spectralon® reference. The individual spot measurements were averaged for each sample and splice corrected before further analysis.

The 63 field soil samples were also analysed for elemental content using an Olympus Innov-X Delta series portable X-Ray Fluorescence (pXRF) machine, at GNS Science, Lower Hutt. The pXRF data of the samples were captured both in ‘GeoChem’ and ‘Soils’ mode. The elements of interest (As, Ca, Fe, Sb) were later analysed based on the detection error. The pXRF was calibrated before-, midway-, and after the soil, measurements using two standardised calibration samples provided by Olympus (Durance et al., 2014).

4.3.3 Absorption depth mapping and band ratios – “Direct” methods

In this study, the wavelength mapper algorithm (van der Meer et al., 2018b) was used to map absorption features through partial exposure. Wavelength mapper is based on a similar principal, to calculate the location and depth of the maximum absorption feature of the target material using expert knowledge (van der Meer et al., 2018b). The deeper the absorption feature the more abundant the targeted material (van Ruitenbeek et al., 2014; Dalm et al., 2017; van der Meer et al., 2018b; van der Meer, 2018). Here, we used two wavelength regions: 450-550 nm and 2250-2360 nm to map the Fe^{3+} and the chlorite absorption depth, respectively. The difference in the absorption depth at these ranges between mineralised and non-mineralised samples were validated by laboratory hyperspectral data (Figures 4.7A and D).

4.3.4 Proposed Workflow- “Indirect” method

We propose a novel workflow to classify the surface manifestations of arsenopyrite-bearing host rock and to eventually locate As anomalies that can be used for gold prospecting (Figure 4.3). In the hyperspectral data processing, the first two and the last three bands were excluded from analysis due to their extremely high sensor-induced noise proportion, reducing the total number of bands to 444. This data was smoothed by the Savitzky-Golay filter (filter window of 3 bands and degree of a polynomial of 2) and then continuum removed (Pullanagari et al., 2017b; Rathod et al., 2018; Chakraborty et al., 2022). The hyperspectral data was further masked by using a normalised difference vegetation index (NDVI >0.6), and also areas within 4 m around dirt/gravel roads. The buffer of 4 m was chosen to incorporate the maximum training data possible.

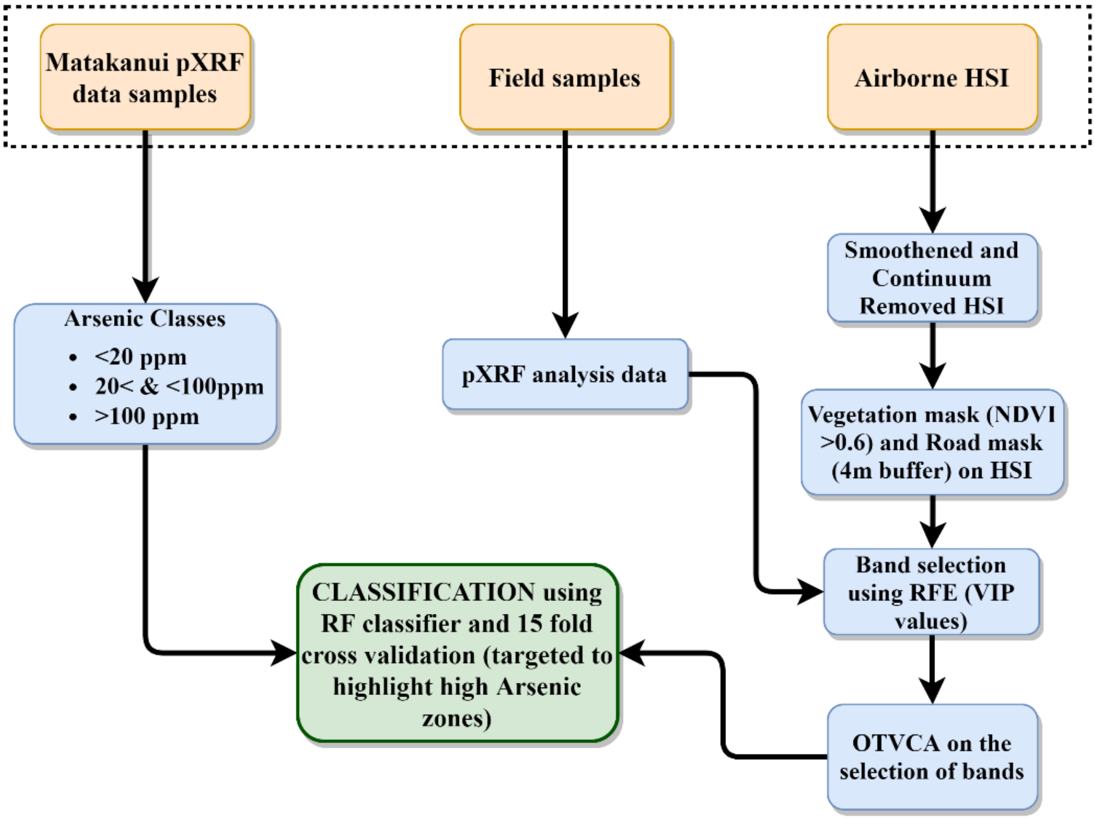

Figure 4.3: Proposed workflow for potential As zonation. Abbreviations; HSI- hyperspectral imagery, VIP- variable of importance.

Band selection was carried out using RFE on airborne hyperspectral data and the As relative concentration indicated by counts at 10.54keV from the pXRF spectra of the 63 laboratory-based samples (Figure 4.4). RFE generates a relevant set of important bands to map the corresponding to surficial differences in the mineralised and non-mineralised zones and eventually vectoring towards potential As anomalies. RFE is based on a feature ranking technique. It initiates from a complete set of predictor variables and discards the least relevant variable one by one by ranking them according to their importance (Zhou et al., 2014; Pullanagari et al., 2018; Demarchi et al., 2020). The selected bands using the RFE were further validated using Pearson type correlation coefficient that was calculated between the counts received at 10.54 keV from the pXRF spectra and the normalised continuum removed from the laboratory-based VNIR-SWIR reflectance spectra.

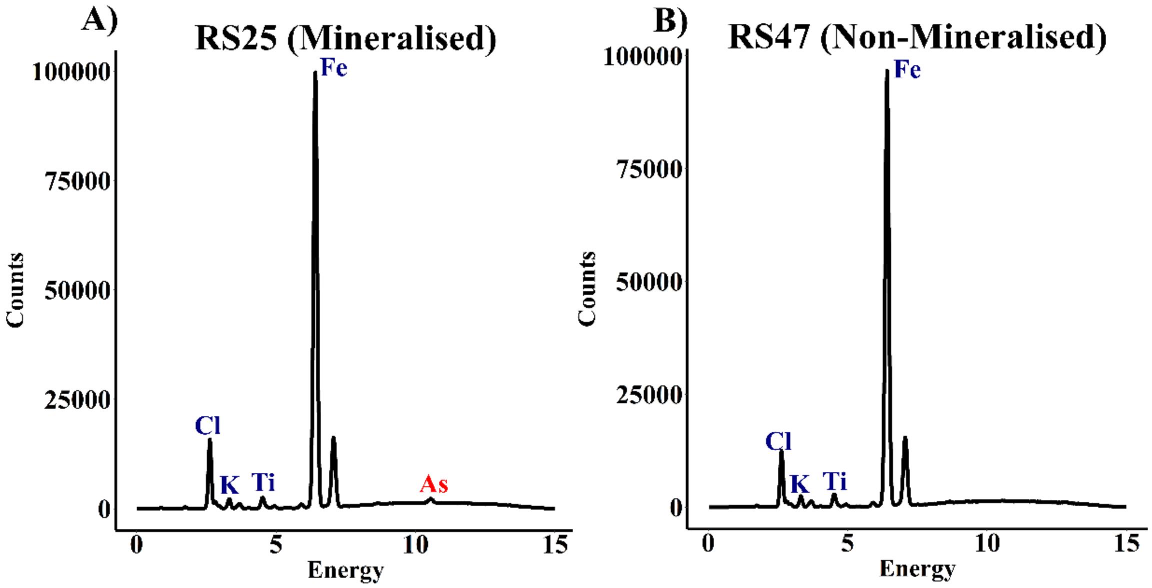

Figure 4.4: A and B are pXRF spectra of a representative mineralised and non-mineralised field sample. The mineralised samples show a characteristic As peak at 10.54 keV. Chlorine peaks are artefacts of sample mounting resin.

The selected 85 bands using RFE in the airborne hyperspectral data were further reduced using an unsupervised orthogonal total variation component analysis (OTVCA) for dimension reduction. OTVCA uses orthogonal feature transformation to find the maximum variance while it also considers the spatial information of the neighbouring pixels using a total variation penalty factor (Fauvel et al., 2012; Rasti et al., 2016; Ghamisi et al., 2017b). OTVCA reduces the dimension by optimising the cost function to find the best representation of the hyperspectral dataset in a lower dimensional feature space. The output is also optimised for spatial smoothness by using a total variation regularisation. The total variation regularisation enables piecewise smoothness on the initially extracted features which secure the pixel neighbourhood information that is crucial for further classification (Rasti et al., 2016). To prevent OTVCA from over smoothening the hyperspectral data, the selection of the TV regularisation tuning parameter (λ) is set to one percent of the maximum reflectance of the area of interest (Rasti et al., 2020). In this study, it was calculated based on the reflectance values of the ground sampling points. The maximum continuum removed reflectance value was 1 and the λ was set at 0.01. The OTVCA was operated in MATLAB^{TM}

The OTVCA transformed hyperspectral data was used as a predictor variable while the grouped Matakanui Gold Ltd. dataset into low, medium and high As concentration classes as target classes, implemented in a Random Forest (RF) classifier. The RF classifier was chosen due to its ability to deal with multicollinearity and random distribution of variables. RF is known for its lack of ability to extrapolate beyond the input data range (Hengl et al., 2018). However, given the training data encompasses 0 (background) to 1000 µg/g (extremely high), this limitation has a negligible impact on our results.

RF generates decision trees using the subset of training data and variables. Each of the decision tree grows independently to a maximum extent using the bagging method (Breiman, 2001; Pullanagari et al., 2017a). Each tree casts a vote for the most popular class at the input subset, and the final output of the classifier is based on majority vote of the trees (Gislason et al., 2006). In this study the total number of trees (ntree) was set at 500, to provide enough generalisation of the model, which generates the trees with high variance and minimal bias (Belgiu and Drăguţ, 2016). The number of splits at each node (mtry) was selected using a sequential expand grid from 1 to 100. The model was validated using Leave one out cross-validation (LOOCV). The classifier performance was assessed based on overall accuracy, along with the user's and producer's accuracy (Liu et al., 2007). This was considered as a suitable measure as relative differences and accuracies in between classes have been analysed for the final interpretation.

4.4 Results and interpretations

4.4.1 Host rock analysis

The SEM-BSE analysis was executed on selected rock samples based on analysis of VIS-SWIR reflectance spectra and some from active exploration sites. The scorodite and arsenopyrite bearing Otago schist rock, sampled by Cudby et al. (2021) mark the most confined halo of the gold mineralisation in the RSSZ. This rock type falls in the upper greenschist facies and is depleted of white mica. The scorodite-bearing schist is the parent host rock for gold in the RSSZ setting (Figure 4.5a) (Craw and Lilly, 2016; Craw, 2017; Cudby et al., 2021). The surface indicator of this confined mineral phase is ferric oxyhydroxide containing adsorbed As. This is generally amorphous and has variable compositions with Fe/As>1 (Figure 4.5b) (Cudby et al., 2021). The rock sample (Figure 4.5b) is derived from a separate location outside the type locality, which falls under the coverage of the airborne hyperspectral image and shows patches of elevated As concentration.

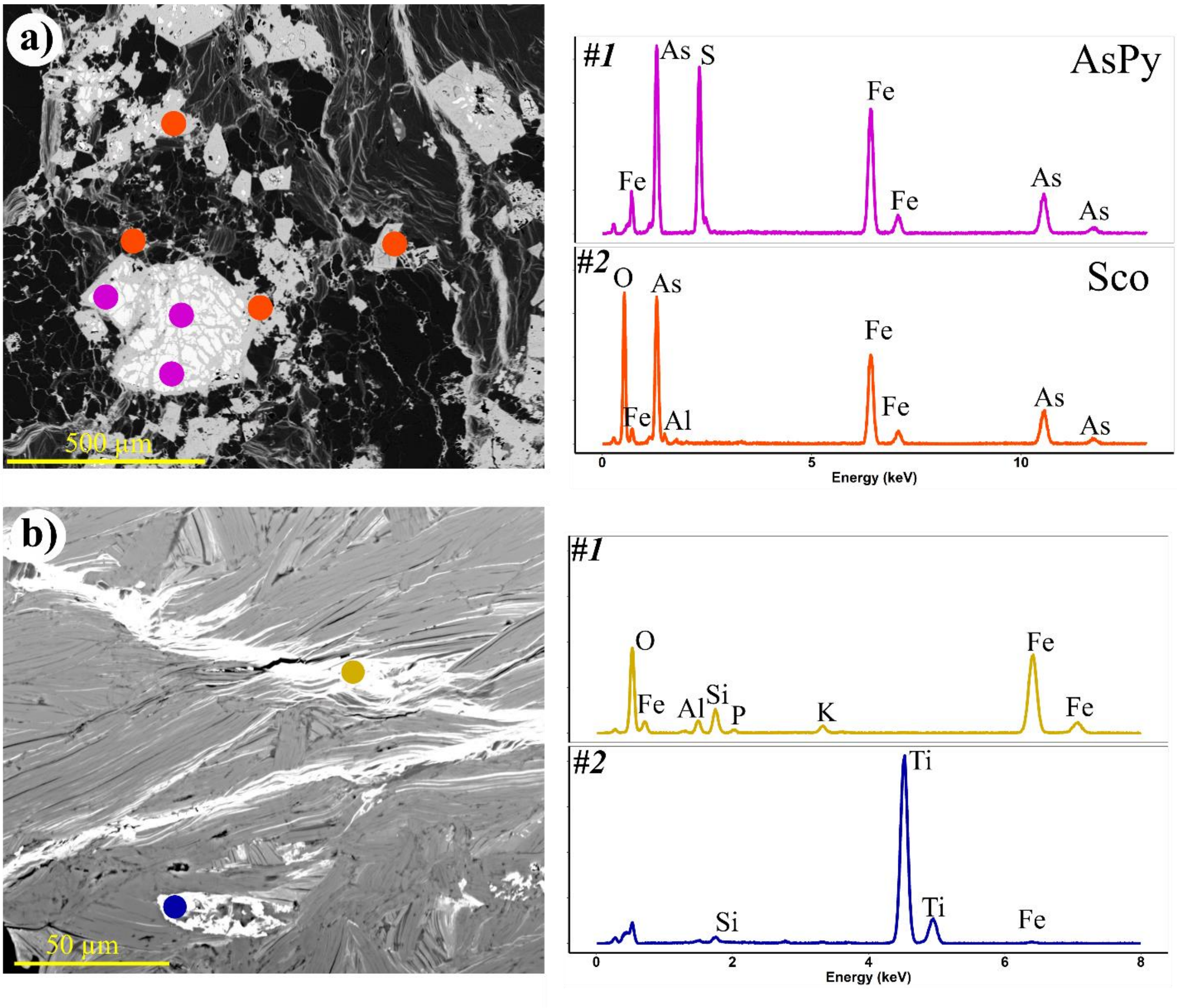

Figure 4.5. SEM-BSE images (left column) and EDS spectra (right column) of representative scorodite bearing schist, mineralised upper greenschist, and non-mineralised lower greenschist samples (top to bottom). a) The bigger scorodite (Sco #2) grains host smaller brecciated arsenopyrite (AsPy #1). b) The mineralised rock sample exhibits an elevated concentration of secondary ferric oxyhydroxide mobilised along shears and schist foliation (#1) and hydrothermal rutile (#2).

4.4.2 Direct absorption mapping and classification

The ground samples show a range of abundance and depletion of ferric hydroxide and chlorite detected at 450-550 nm and at 2250-2360 nm, respectively. The Mg-OH absorption in chlorites tend to shift to the larger end of the SWIR region over 2300 nm due to the variation in Fe-OH in the rocks, which was observed here (Cloutier et al., 2021; Krzesińska et al., 2021). The Mg-OH absorption here was observed at 2347 nm (Figure 4.8 A). The deeper the absorption feature the higher is the mineral abundance (Clark, 1999; van der Meer et al., 2018b). The absorption depth mapping results using airborne hyperspectral image were here thresholded to provide individualised distribution of ferric hydroxide and chlorite minerals (Figure 4.7). The mineralised schist is typically depleted of chlorite and exhibits an abundance of ferric hydroxide-bearing minerals. The depleted chlorite area band depth <0.06 covers an area of 1.45 km^2 and the ferric hydroxide abundant area (considering band depth >0.5) covers an area of 3.56 km^2.

The map distribution represents little value for mineral prospecting. The absorption in the SWIR range targeted to map the iron-bearing chlorite depletion has overlapping absorption wavelengths with the clay minerals present there such as, biotite, illite and smectite which also have similarly strong absorption in the SWIR range (Abweny et al., 2016; Laukamp et al., 2021a; Laukamp et al., 2021b). This renders the direct abundance mapping of chlorite even more ineffective in such a scenario. The strong signal difference in mineral phases at a subsurface level dissipates when it comes to surface mapping where more prominent surficial parameters such as vegetation cover, soil moisture, water solubility and distribution mask the well-defined mineralogical boundaries.

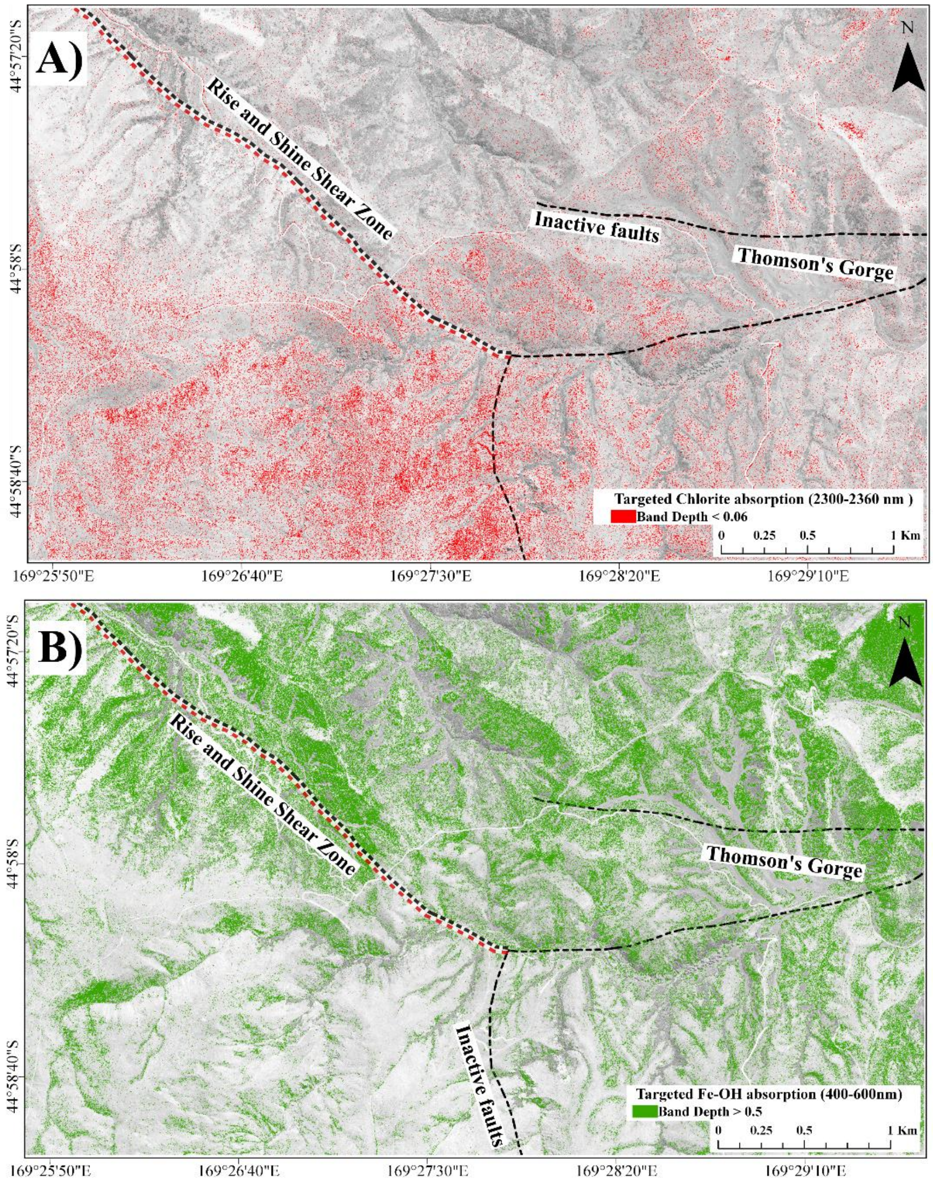

Figure 4.6: Band depth mapping results targeting A) chlorite absorption feature, where theoretically more chlorite was expected to the north of the RSSZ in the lower green schist facies region but is mixed with biotite and surface features and shows no clear demarcation and B) ferric hydroxide absorption feature, more of the green was expected to the south of the shear zone in the mineralised upper green schist facies region, but is very mixed with the vegetation cover and does not show a clear boundary. Highlighted areas in both maps correspond to the mineralised area returned by the band depth mapping approach. The underlying geological units are shown in Figure 4.1A.

The absorption band shape shows only weak differences between mineralised and non-mineralised samples of chlorite at both laboratory-based and airborne levels (Figures 4.7A, B and C). The subtle change in depth for the chlorite-related absorption feature can be indirectly vectored at potential As-enrichment zones and consequent chlorite depletion in the host rock (Craw and MacKenzie, 2007). On the other hand, ferric hydroxide-related absorption shows no related demarcation in absorption depth at laboratory-scale, while only showing a vague trend at the airborne scales. Despite being ubiquitous along the RSSZ and characterised by a very strong spectral response, the ferric hydroxide absorption feature at 450-600 nm appears to be of limited use for vectoring for gold. The lack of trend can further be linked to atmospheric and topographic effects (Richter and Schläpfer, 2010; Leifer et al., 2012; Vanonckelen et al., 2013). The visible domain is further affected by the strong absorption of chlorophyll in vegetation (Haboudane et al., 2008; Moses et al., 2012), and potentially to the "exposed soil fraction".

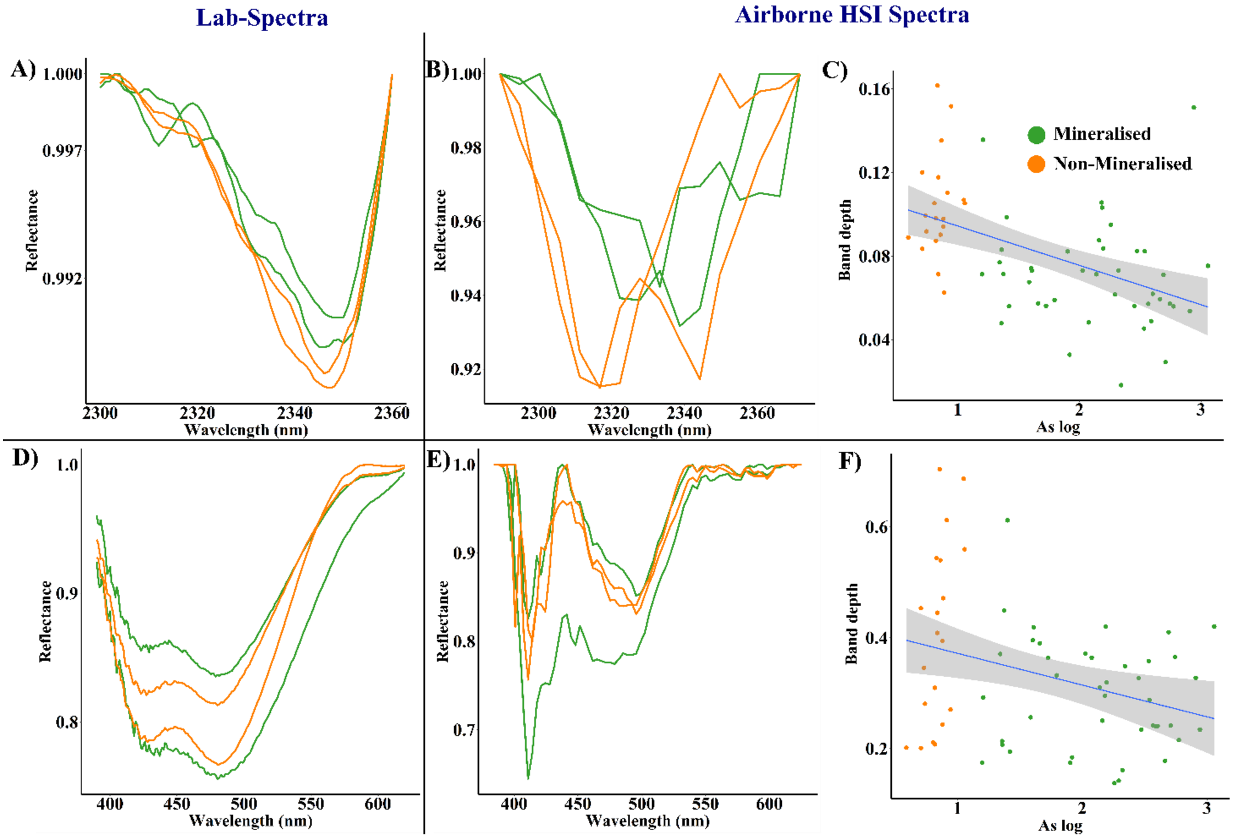

Figure 4.7: Lab and airborne absorption depth analysis of chlorite (A-C) and ferric-hydroxide (D-F). C and F images show correlation between the corresponding absorption depths and log of As ppm. The field samples RSS1 and RSS23 were representative of mineralised samples and; RSS54 and RSS62 were representative of non-mineralised samples.

4.4.3 Band Selection and spectral correlations

The airborne dataset was analysed through RFE to subset spectral bands with the largest contribution to the targeted As concentration (Figure 4.8A). The important bands are scattered throughout the spectrum, while many bands are selected from the SWIR. This can be due to the decreasing co-linearity of the input bands located further apart from each other, and/or due to less reflectance interference from chlorophyll in partial vegetation fraction cover. To further validate the bands selected by the RFE model, a Pearson-type correlation analysis between the laboratory-based reflectance spectra and As concentration represented by the pXRF counts at 10.54 keV from the 63 field samples was performed. Wavelengths that showed >0.2 coefficient that corresponds well with the expected absorption feature indicating chlorite-bearing rocks between 2240 to 2360 nm depending on the concentration of Fe and Mg (Neal et al., 2018; Cloutier et al., 2021) (Figure 4.8B). Another spectral region that shows higher linear correlation includes 1450-1500 nm and 1900-2000 nm. A resultant set of 85 bands were selected which coincided with both the correlation analysis and the RFE output bands were then used for the rest of the workflow. The corresponding wavelengths of the 85 bands are provided in Appendix 2B. The selected 85 bands still possess information regarding lithology, including mineralisation, topography, shadow and atmospheric effects and sensor noise. OTVCA was run to maximise spatially coherent variance in the input spectral data. Out of the first 10 components, 2 components were discarded which only consisted of sensor noise and scene boundaries. The remaining 8 components were used to create potential zonation of As anomalies through image classification using an RF classifier.

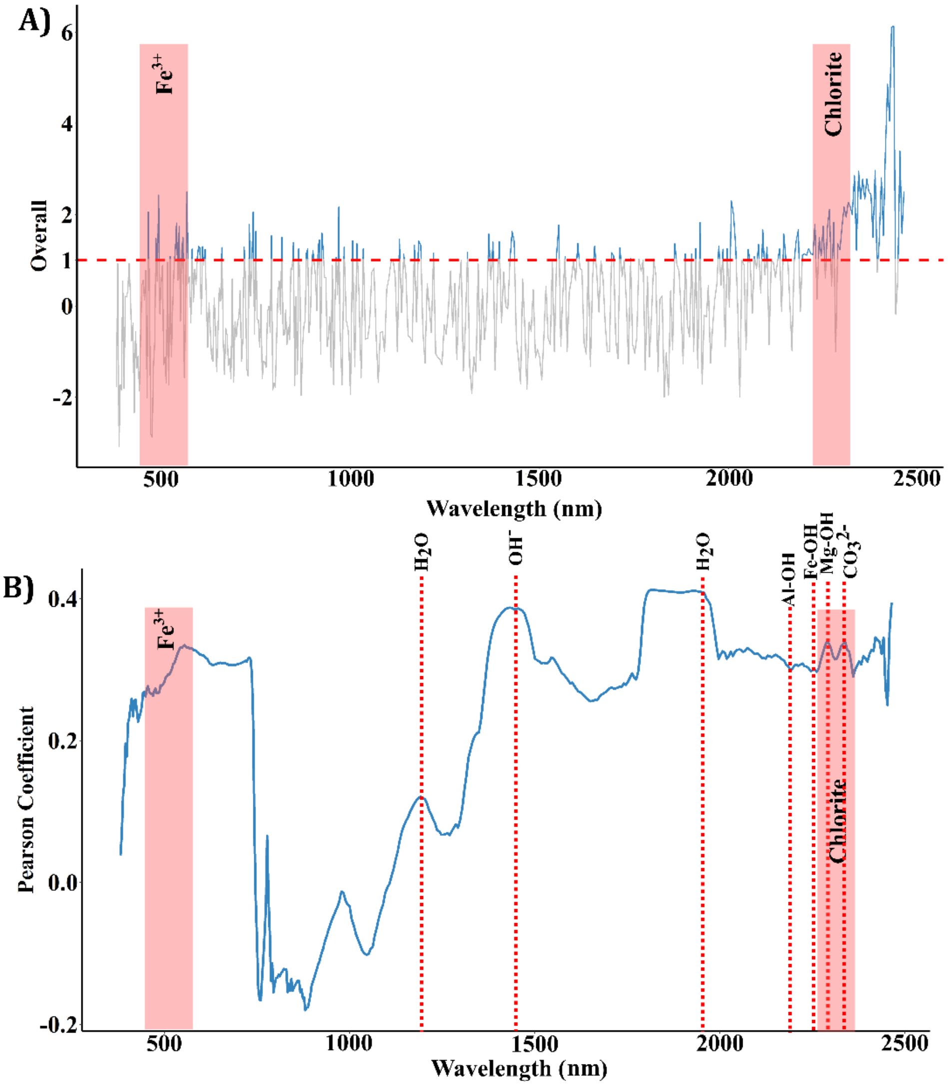

Figure 4.8: The graphs illustrate A) the overall importance across the airborne hyperspectral data as an output from the RFE band selection method and B) the correlation across the laboratory-based hyperspectral data to the target As concentration. The highlighted red regions are the spectral ranges used in the "direct mapping" workflow.

4.4.4 Indirect mineralisation mapping and classification

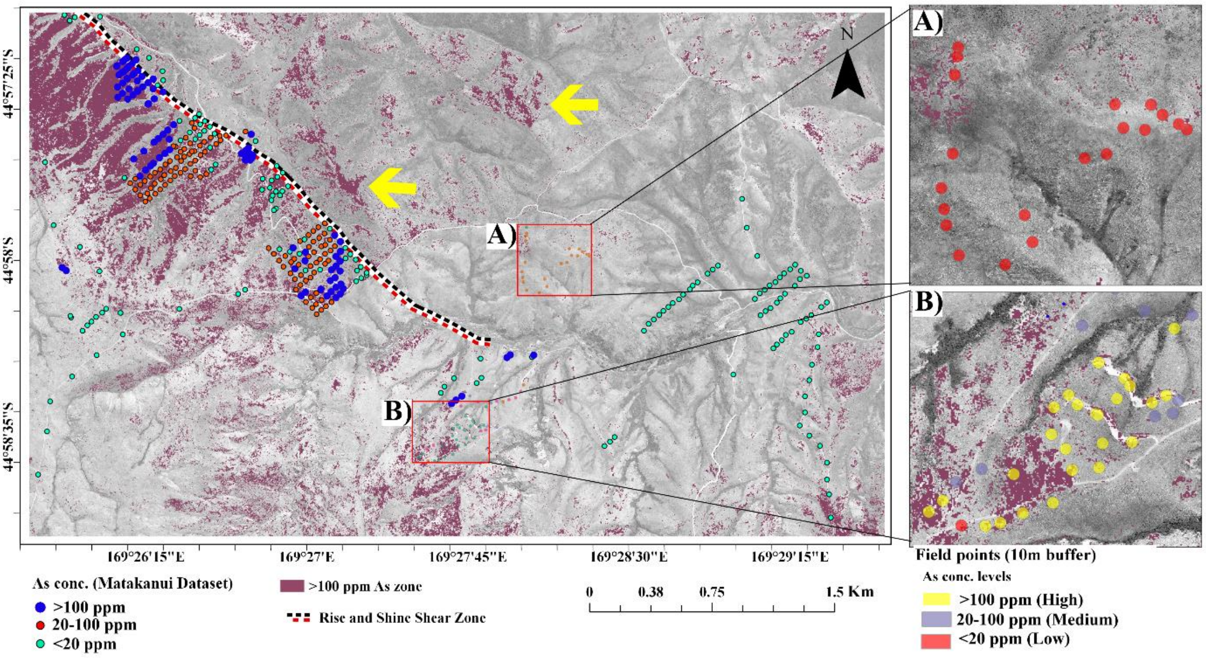

Figure 4.9: Potential As zonation map showing "High" concentration As (magenta) spatially extrapolated through Random Forest classifier using known ground points. The image has been overlayed by all the ground points collected in the study and the Matakanui Gold Ltd. dataset. The insets show details of the non-mineralised (A) and the mineralised (B) sections respectively. The yellow arrows show misclassified patches of "High" As concentration in topographic valleys within the lower greenschist facies.

The training data contains 87,97 and 123 observations from high (>100 ppm), medium (20-100 ppm), and low (<20 ppm) As concentration zones respectively. The overall accuracy of the classification is 0.58 (Table 4.3). The error matrix shows an ample number of misclassifications, among all three classes. A significant percentage of the misclassification was accountable to topographical and varying soil exposure fraction which was mixed in the training data as well. The highest class-wise accuracy is for the low concentration As class, which is 72% and 66% for producer's accuracy and user's accuracy (Table 4.4). This class has made up most of the study area, totalling to a 9.2 km^2. On the other hand, the lowest accuracy is reported for the high concentration As class, presumed to be related to underlying mineralisation. The total area classified under "High" As concentration zone was 1.84 km^2 (Figure 4.9).

The areas classified under "High" As concentration is based on the training data which contained As µg/g concentrations at 307 field locations (Figure 4.1). Although, the results show strong regional trends matching with the geology. The surface manifestations of the arsenopyrite and scorodite-bearing rocks can also be impacted by surficial processes such as leaching and mainly represents ferric oxyhydroxide with different levels of adsorbed As (Figure 4.5b).

Table 4.3: Error matrix of the random forest image classification using the independent validation data (columns) against the image classification results (row). The bold values show the correctly classified pixels.

	REFERENCE			
PREDICTION	**High**	**Medium**	**Low**	**Total**
High	**42**	25	16	83
Med	24	**49**	19	92
Low	23	23	**88**	134
Sum	89	97	123	309

Table 4.4: Area statistics and Image classification accuracy by image classes

Classes	User's Accuracy (%)	Producer's Accuracy (%)	Total area (pixel)	Total area (km^2)
High	51	48	460820	1.84
Medium	53	51	756242	3.02
Low	66	72	2430621	9.72

4.5 Discussion

4.5.1 Arsenic as a pathfinder to gold and its spectral importance

Geochemically, As anomalies are an established and globally used pathfinder to gold deposits (Kovalev et al., 2011; Large et al., 2012; Blake et al., 2019). The gold mineralisation in Central Otago is mostly hosted by arsenopyrite in association with other sulphide minerals, such as chalcopyrite and stibnite (Craw and MacKenzie, 2007; Craw et al., 2007a). With an increasing demand for gold, currently, there is more emphasis on exploring lower-grade gold deposits. The signal to these deeper-seated deposits is often shadowed by redistributed As halos due to supergene weathering and, leaching through groundwater circulation at a meter scale (Goldfarb et al., 2005; Blake et al., 2019; Jasiak et al., 2021). The lower greenschist facies zone at the RSSZ is less lithified and has more clay proportion thus enhancing the redistribution of As and increasing the amount of clay.

The supergene leaching facilitates enlarged alteration halos and can pose a major drawback in mapping As anomalies to target gold at a regional scale. Other pathfinder elements to gold in the Otago RSSZ setting, such as Sb, can also be plausible alternatives because of their co-occurrence with As and gold (MacKenzie and Craw, 2007; Chakraborty et al., 2022). Sb and As are released into the environment in concurrent breakdown of stibnite and arsenopyrite respectively. Sb oxidises and can get precipitated nearer to the target gold-bearing host rock; on contrary, As remains in solution and gets redistributed forming a larger As footprint (Ashley et al., 2003).

The mineralised samples exhibited a peak at 10.54 keV in the pXRF spectra signalling the presence of As in the mineralised field samples, whereas there was no such signal in the non-mineralised samples (Figure 4.4). It is important to note here As bearing rocks and minerals often have no particular absorption wavelength contributing to As variation within the VNIR-SWIR regions. The RFE band selection was run on the airborne hyperspectral data (predictor variable) against the raw pXRF counts at 10.54 keV (target variable) to select the most important bands contributing to this As variation (Figure 4.4). However, the important bands in the SWIR range signals the consistent depletion of chlorite in the mineralised samples and nearly ubiquitous presence of muscovite, and carbonate minerals (e.g., dolomite, ankerite), all of which have their significant absorption features in the SWIR (Figure 4.8). This shift in mineralogy coincides with the depletion of As-bearing minerals and therefore represent an avenue to detect and quantify As with VNIR-SWIR hyperspectral data. Furthermore, the important bands in the VNIR region are attributed to the comparative abundance of ferric hydroxide-bearing minerals in the mineralised schist and the varied vegetation cover in the zone. The subtle changes and shifts in these absorption features in indirect correspondence to As concentration in the samples fits the vectoring signals to the characteristics of the mineralised schist.

4.5.2 Band ratio vs multivariate data analysis for potential As zonation

Band ratio and direct wavelength mapping methods (e.g., Spectral Angle Mapper and Wavelength mapper) are inherently limited to capture variation of a single mineral group using its characteristic absorption feature caused by the chemical bonds and bulk compositions (Clark et al., 1990; van der Meer and Bakker, 1998; Clark, 1999; van Ruitenbeek et al., 2014; van der Meer, 2018; Shrestha et al., 2022). This can easily fall apart in a more challenging environment where >90% of the pixels are impure/mixed and have overlapping absorption ranges. This effect shows in the mapping results where the direct mapping gets confused a lot more with undulated topography and the creek whereas the indirect map renders much less confusion around the topography (Figure 4.10). In such a scenario, interpretation of band ratio must require expert knowledge to be used to portray the regional geology. Furthermore, the spectral signature of vegetation is stronger than most mineral signatures and can pose difficulty in analysing subtle shifts in mineral absorption when both has overlapping important wavelengths (Crippen and Blom, 1999).

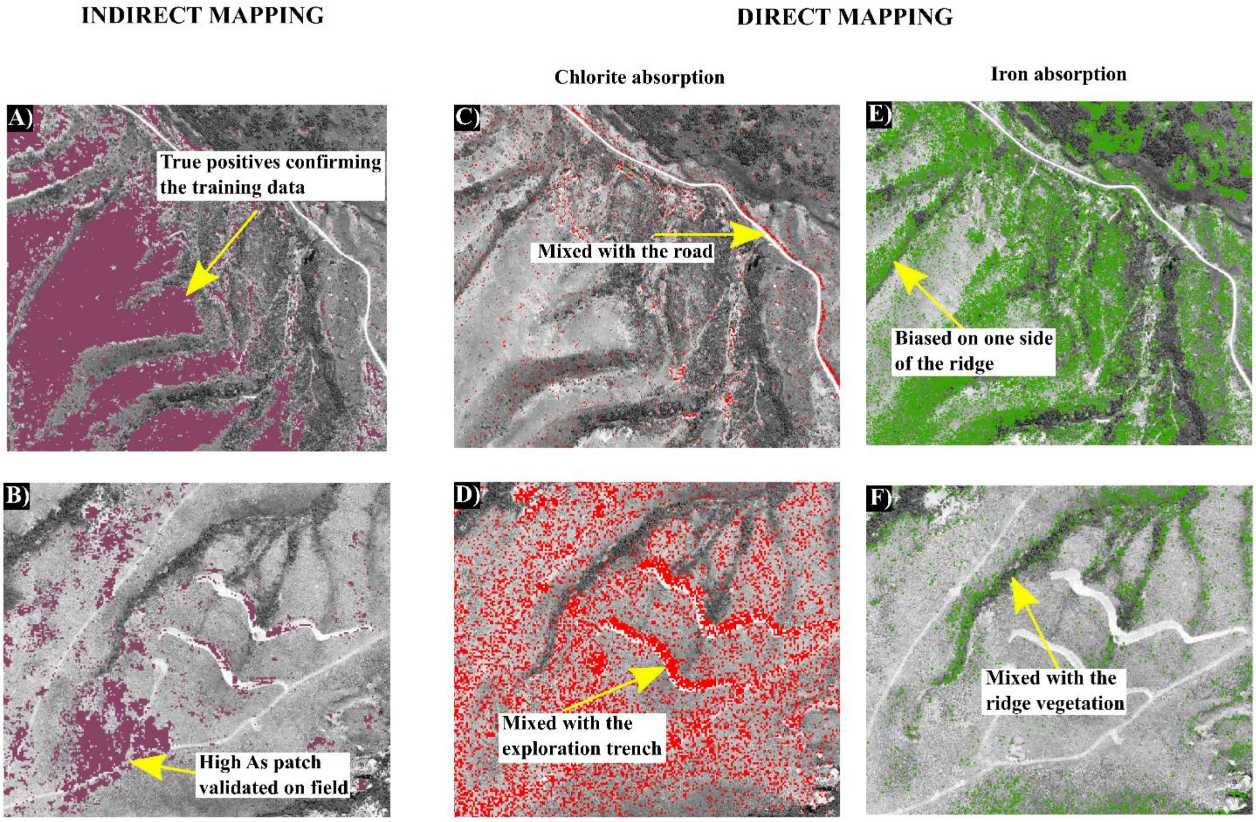

Figure 4.10: A comparison showing the topographic effects impacting the direct wavelength mapping results more than the proposed indirect workflow. Arrows indicate major on-surface differences in the two methods

High toxic levels of As leads to stunted plant growth and leaf colouration among others (Brooks, 1979; Farago, 2008) which are comparatively easier to detect using hyperspectral and even multispectral data. Although in a more subtle level when the effect of As is more at a molecular and at chemical stage than apparent physical changes, integrated knowledge of chemical associations are thus preferred and here-in proposed as indirect zonation of As (Rathod et al., 2015; Shi et al., 2016; Shin et al., 2019; Chakraborty et al., 2022). Our study area offers a great test ground for lithological mapping and chemical zonation due to its highly variable soil exposures between 5 and 85% on a known mineralisation. The proposed supervised classification approach can outperform any direct mapping methods due its ability to tune the data through maximising correlation between target (pXRF measurement on the ground) and predictor variables (airborne hyperspectral data). The multivariate classification model can therefore pick up and relate with subtle spectral changes associated with underground mineralisation which cannot be associated with mapping absorption features of individual mineral phases alone. Thus, this approach not only can capture the underlying lithology, but it can also shed light on expected mineralisation levels. Indirect mapping can increase the feasibility of mapping using hyperspectral remote sensing.

4.5.3 Connecting band selection and data transformation with the underlying geology

Despite an extensive legacy of geological remote sensing, there are still considerable gaps in utilising remote sensing to mineral prospecting on complex terrains without or only partial soil/rock exposure and/or target minerals without a unique absorption feature. Our novel workflow combining RFE with OTVCA shows promise to tackle natural complexity and can provide a new tool to utilize in mineral prospecting and improved land-surface mapping. The iterative elimination process implemented in the RFE using internal RF classifiers can help in reducing dimensionality and to deal with non-linear data (Su et al., 2017; Pullanagari et al., 2018; Demarchi et al., 2020). The RFE shows most bands across the VNIR-SWIR spectrum with large amounts of bands form the SWIR corresponding to characteristic absorption bands of chlorite. Chlorite is geologically linked to As-concentration (depletion when As is present in the RSSZ setting) that the dimensionality reduction maximised in the input hyperspectral data to link with the most. Our mapping results benefits using OTVCA that can further enhance geological features by increasing the inherent spatial coherence. This is particularly useful in investigating geological system, such as the gold mineralisation and lithological changes with high spatial autocorrelation (Warner and Shank, 1997). OTVCA is a spatially constrained data transformation technique that can maximise and generalise geological information explicitly. Consequently, the mineral prospecting classification results become more independent of the soil exposure fraction compared to non-transformed data and makes it more generalised/smoothed.

4.6 Conclusion

Potential arsenic zonation to locate a concealed gold mineralisation is challenging using remote sensing. Firstly, As lacks any unique absorption feature in the VNIR-SWIR spectral range, based on which most hyperspectral mapping techniques are tailored. Furthermore, As halo covers a large footprint than the target mineralisation due to leaching and transport by groundwater.

The topography and the varying soil exposure can add a significant percentage of information captured by hyperspectral imaging. Therefore, even if the characteristic absorption features exist for any target minerals, the lack of pure pixels can hamper wavelength-based approaches for image classification. Variable selection can help reducing bands, maximising relevant information and the prediction accuracy. The selected variables contain dominant target information and an essentially smaller percentage of background information. The band reduction via RFE and data transformation via OTVCA can simplify the information in the selected set of bands improving image classification accuracy. As mineral deposits are patchy geological systems the spatial correlation of the As halos to the gold mineralisation was maximised using OTVCA.

Compared to direct mapping using a single characteristic absorption feature, or the information of a single band, this proposed indirect mapping workflow manifested much better results. The future work in this study would be to minimise the topographic effects further by using sub-pixel-based training and/or pixel-based membership value which would potentially improve the classification. This can also facilitate in extending the workflow to satellite data where the spatial resolution is a limitation.

4.7 Acknowledgement

This study was supported by Ministry of Business, Innovation and Employment (MBIE) Endeavour Fund – Smart Ideas: Assessing New Zealand’s environmental and mineral indicators (contract number: MAUX1802). The authors are grateful for the support and access to exploration datasets carried out by from

Matakanui Gold Ltd and Matakanui Station for the land access and for digging us out from the mud. The authors are also grateful to Daniel Coulthard and Raoul Solomon at Massey University's Manawatu Imaging Centre for their assistance in the SEM-EDS analysis.

Chapter 5: Upscaling hyperspectral-based mineral prospecting in a multispecies natural forest in the Reefton goldfield, New Zealand

5.1 Introduction

The scarcity of ground exposure to map mineralisation is not restricted to New Zealand but is a global challenge which calls for more advanced, mineral exploration methods. The inherent spatially distributed nature of mineral deposits (e.g., ore-bearing veins) makes remote sensing an ideal toolset for exploration. Multispectral remote sensing has been used for decades to map gossan and alteration minerals, and soils using band ratioing, principal component analysis (PCA) and spectral angle mapper (SAM) (Crosta, 1989; Loughlin, 1991a; Kruse, 2007; Pour and Hashim, 2011). Satellite images from Landsat series, ASTER, SPOT, more recently Sentinel-2 have been intensively used to map spectrally detectable minerals at a regional scale (Bruno et al., 2021; Frutuoso et al., 2021; Souza et al., 2021; Imran et al., 2022). Expansion of hyperspectral remote sensing through ground-based (Bhattacharya et al., 2019; Cloutier et al., 2021; Thiele et al., 2021b), airborne and spaceborne (Gomez et al., 2008; Pullanagari et al., 2018; Cogliati et al., 2021) can add new geological applications, including mineral exploration. Hundreds of narrow and contiguous bands allow a quantitative study of physical and chemical characterisation of the Earth's surface, including grain size analysis, lithology and mineral mapping and using band depth (Kruse, 1998; Bioucas-Dias et al., 2012; Pullanagari, 2012; van der Meer et al., 2012; van Ruitenbeek et al., 2014; Chauhan, 2015; Kereszturi et al., 2021) which could be beyond the scope of multispectral remote sensing. Mineral exploration has been a key driving application for hyperspectral sensor development (e.g., Gao et al. (2009). Despite early intense development, most applications are focused on bare grounds (Swayze et al., 2014; Kereszturi et al., 2020; Cloutier et al., 2021; Laukamp et al., 2021b). Therefore, application of hyperspectral imaging to partially to fully vegetated terrain in a geologically significant area has remained poorly understood and explored.

Plants take up elements and nutrients from soil which forms as a product of climatic, parental material, topographic and microorganism effects over time (e.g., Jenny (1994)). The role of mineralised rocks and its influences on soil can be transposed to plant cover, making biogeochemistry an expanding tool in mineral exploration (Kovalevsky, 1987; Anderson et al., 1999; Pratas et al., 2005; Dunn, 2007; Kovalev et al., 2011). Soil-plant interactions and the uptake of toxic elements has been explored via pot-based experiments under controlled condition (Rathod et al., 2018), in point-based classical biogeochemistry surveys (Dunn and Ray, 1995; Dunn, 2007) and also at a fairly regional scale around the globe (Cohen and Rotman, 2005; Lintern et al., 2013; Beyer et al., 2021; Cohen et al., 2021). Similar results have been found between *Pinus radiata* bark elemental concentration and laboratory-based hyperspectral data in the HMSZ in New Zealand (Chakraborty et al., 2022). This emphasises the fact that remote sensing techniques can be used to map mineralisation-related anomalies using plants as a proxy media. However, extending laboratory-based observation to airborne and even to satellite data is challenging and requires data integration (Kereszturi et al., 2018; Lorenz et al., 2021) and innovative use of advanced data processing and analysis (Pullanagari et al., 2016; Lorenz et al., 2021; Parsa, 2021). Further studies at the Rise and Shine Shear Zone (RSSZ) have indicated data processing, including orthogonal total variation component analysis (OTVCA) and Random Forest (RF) can be used to enhance subtle anomalies present in hyperspectral data to infer and locate new mineral deposits underground where the surface is covered partially to fully with tussock grass.

Pathfinder elements, such as As and Sb are closely associated to gold mineralisation in South Island, New Zealand, across rock types and settings (Gazley et al., 2020), as well as globally (Nude et al., 2012; Korshunova and Charykova, 2019). The typically host minerals for these elements are sulphides, including arsenopyrite, pyrite, stibnite and their near-surface oxides such as scorodite (MacKenzie et al., 2007; Druzbicka and Craw, 2015; Allibone et al., 2018; Blake et al., 2019). Previous work at HMSZ established that the elemental trend of Sb and As pathfinder elements are retained from host rock through soil to plant tissue even though the concentration drops from 1000 µg/g to 10 µg/g approximately (Craw et al., 2007a; Chakraborty et al., 2022). Thus, the present study aims to explore the feasibility of airborne hyperspectral imaging to apply similar analytical and conceptual models at a regional scale for mapping mineralisation-related anomalies. However, its capability remains untested in a natural forest landcover (with multiple species). To test this idea, we have utilised a ground exploration database from Oceana Gold Ltd. with

~4000 soil samples collected adjacent to the Globe Progress mine and the Waiuta mine tailings around Reefton, New Zealand (Figure 5.1). The study area is located in the Victoria national park and provides an excellent opportunity to test whether hyperspectral imaging can be used as a screening tool over such multi-species forest landcover.

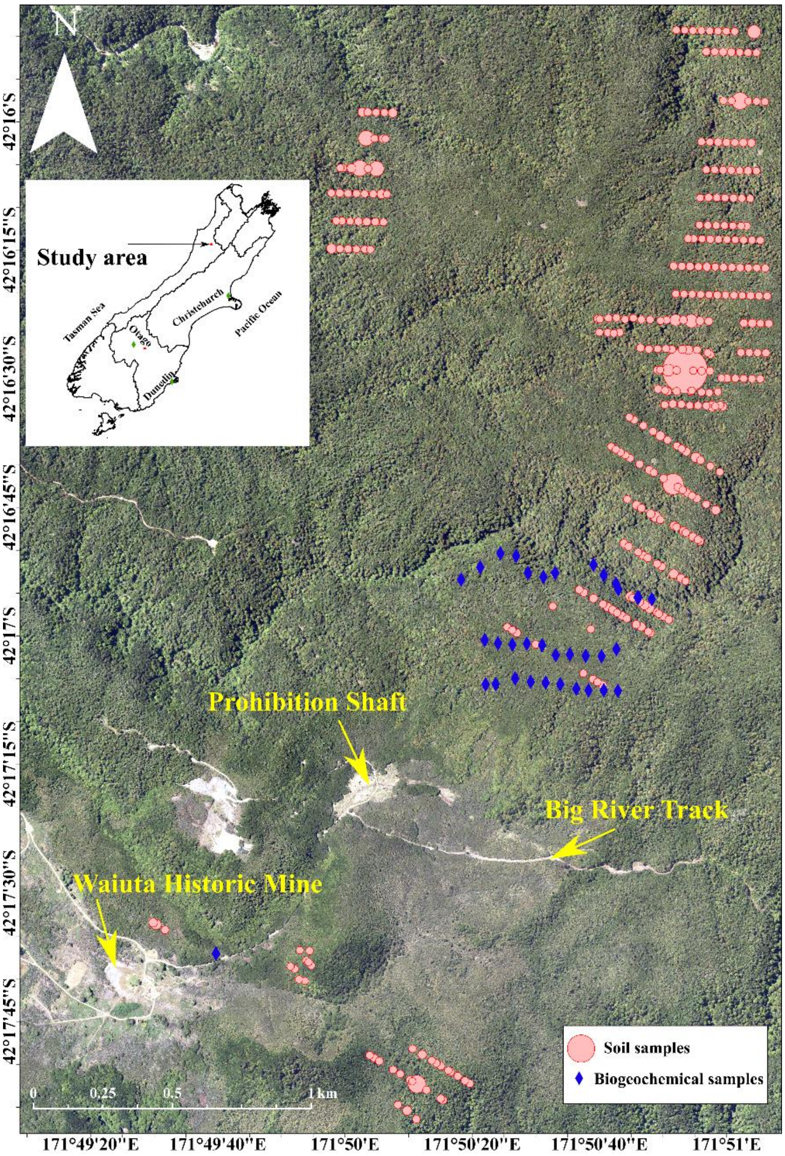

Figure 5.1: Overview map of the study area in the Reefton goldfield with the biogeochemistry (blue diamonds) and soil samples (pink circles). The size of the soil samples is proportional to the gold concentration.

5.2 Geological Setting

The Reefton goldfield is situated to the west of the Alpine Fault in the South Island, within the Buller terrane in the Cambrian-Ordovician Greenland Group (Laird and Shelley, 1974; Brathwaite and Pirajno, 1993; Mortimer, 2004). The Buller terrane is mostly comprised of variably metamorphosed siliciclastic sandstones and mudstones (lower greenschist facies), which were subjected to multiple hydrothermal alteration events and the deposition of quartz lodes (Christie and Brathwaite, 2003; Hamisi et al., 2017). The gold mineralisation is hosted in transgressive shear zones within weakly metamorphosed turbidites (Christie et al., 2000). The gold mineralisation here has an orogenic mesothermal origin and formed in two phases. Firstly, arsenopyrite, gold and quartz were introduced in an earlier ductile phase which was further overprinted with a brittle phase of the same minerals along stibnite (Christie and Brathwaite, 2003; Milham and Craw, 2009). The gold-bearing quartz veins are hosted by the metamorphosed sandstone units that have been dated Late Ordovician (Laird and Shelley, 1974; Rattenbury and Stewart, 2000; Christie et al., 2010; Druzbicka and Craw, 2015). The quartz veins were emplaced in two phases with thickness ranging from 1 to 3 m (MacKenzie et al., 2014). The first phase took place in the later stage of metamorphism and the second phase was a post-metamorphism event. The former quartz vein phase is more closely associated with gold mineralisation and has been intensely sheared. The latter phase of emplacement was associated with ankerite and also introduced massive stibnite veins along with quartz. In places this latter phase also filled the fractures in the quartz veins from the former phase (MacKenzie et al., 2014). The association of stibnite in the assemblage indicates that the second phase of mineralisation took place during or post the uplift of the Greenland Group (Silurian period) as the precipitates from this phase are found at comparatively shallower levels (Ashley and Craw, 2004; Craw et al., 2009).

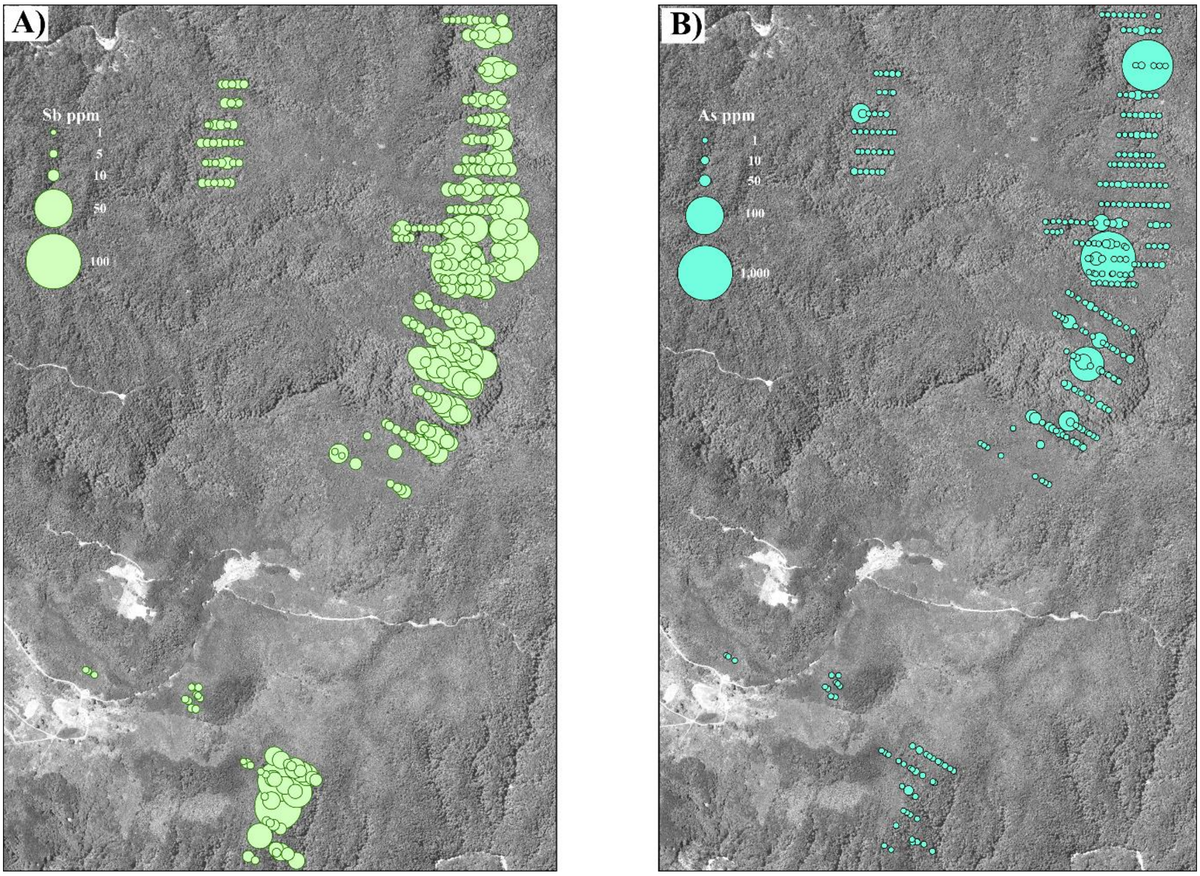

Figure 5.2: Field samples and log distribution of As (A) and Sb (B) concentration

The gold occurrence in the Reefton goldfield is typically related to quartz veins in association with sulphides, such as pyrite, arsenopyrite and stibnite. A minor fraction of the gold occurs in native form. The mineral assemblage related to hydrothermal alteration of the sandstones include K-mica, carbonates (e.g., dolomite and ankerite), pyrite and arsenopyrite with abundant chlorite (Christie and Brathwaite, 2003). The common pathfinder minerals to gold here are arsenopyrite, stibnite and boulangerite, and the main pathfinder elements for disseminated gold are As and Sb (Figure 5.2) (Christie et al., 2001; Pirajno and Bentley, 2012). The occurrence of arsenopyrite grains occur as porphyroblasts along with sulphides such as chalcopyrite and galena (Hamisi et al., 2017). Stibnite is common in quartz lodes; its occurrence is attributed to a later stage in mineralisation that filled the fractures in the quartz breccia (Christie and Brathwaite, 2003; Hamisi, 2016). The stibnite veins can range up to 1-5 cm^3 in volume (Milham and Craw, 2009). The background levels of As and Sb typically ranges from 5-15 µg/g and 1-2 µg/g respectively. The most prominent As and Sb halos extend up to 10 to 20 m from the mineralised quartz vein (Hamisi et al., 2017) (Figure 5.3).

The Reefton goldfield consisted of 84 mines and produced 2M oz of gold between 1872 and 1951 (Dunn et al., 2012b). The Globe-Progress and the Blackwaters mine at Waiuta are the two major gold mines (Leach et al., 1997; Magner et al., 1997; Rattenbury and Stewart, 2000). The Globe Progress mine covers the western flank of the Globe hill which is situated to the north of the target area in this study (Figure 5.1). The Globe Progress mine had two lifespans, first as an underground hard rock mine (1879-1920) which was then further redeveloped as an open pit mine between 2007 and 2015 (Christie, 2016). The quartz vein mined here exhibit a clay-rich border, and the gold occurs in native form as well as disseminated along the sulphides such as arsenopyrite and stibnite (Christie and Brathwaite, 2003; Christie et al., 2006). The mineralised halo for the Globe Progress mineralisation extends up to 30 m compared to the rest of the region where it extends to a maximum of 20 m (Figure 5.3). The Blackwater mine at Waiuta is located in the Birthday Reef quartz vein system, operated from 1905 to 1951 which was the largest Reefton mine during its time (Hamisi et al., 2017). The proximal mineralised halo here extends to a maximum of 10m. The area otherwise is a vast natural forest containing a range of plant species potentially covering a significant area of gold mineralisation hosted by meta-sedimentary rocks as opposed to greenschist facies metamorphic rocks hosting similar orogenic mesothermal gold mines in the Otago region (Craw and Norris, 1991; Ashley and Craw, 1995; Rattenbury and Stewart, 2000; Christie and Brathwaite, 2003).

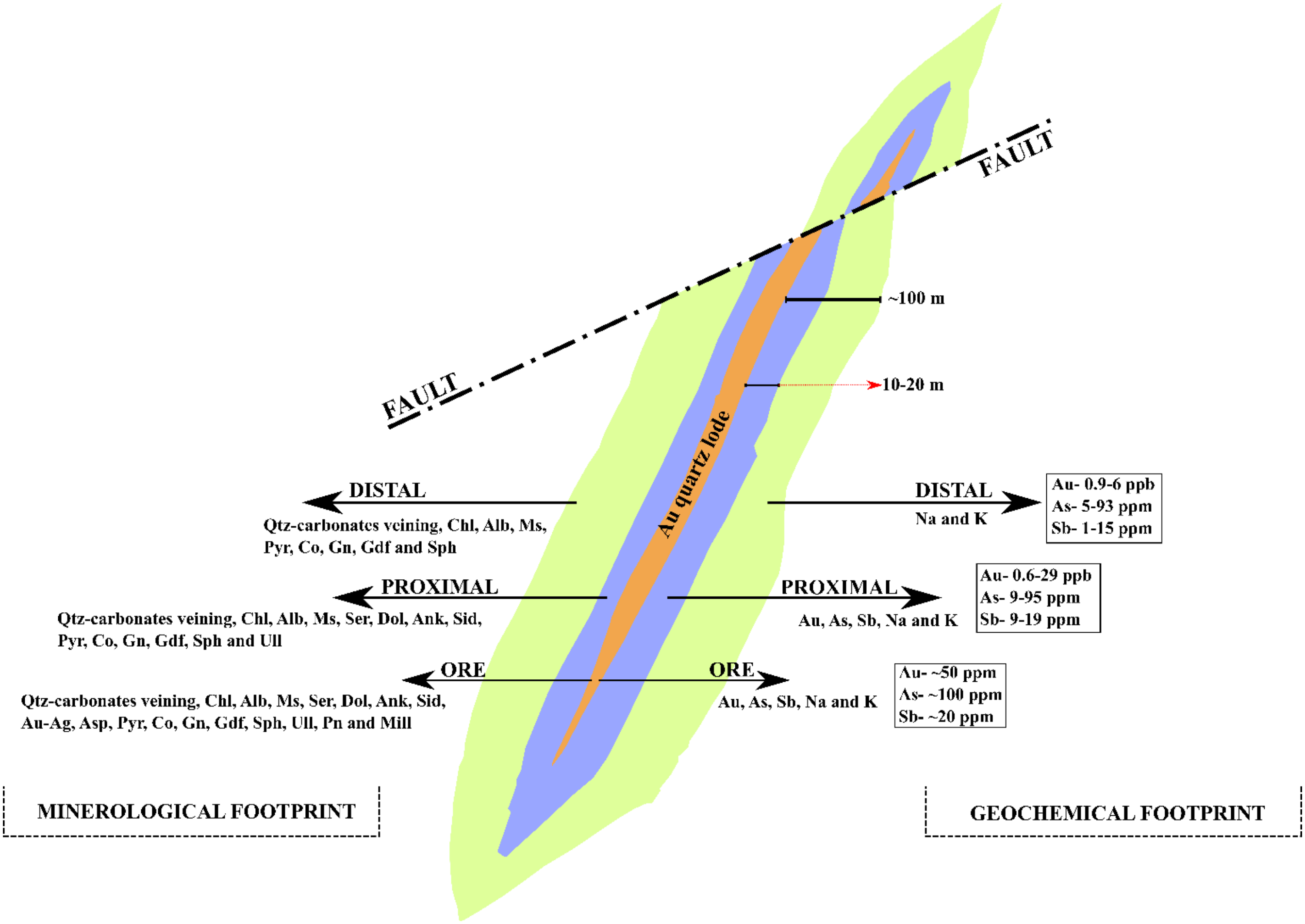

Figure 5.3 : Conceptual model of the mineralogical and geochemical footprint of the Reefton goldfield, adapted from Hamisi (2016). The abbreviations used here are: - Chl: Chlorite; Alb: Albite; Ms: Muscovite; Ser: Sericite; Dol: Dolomite; Ank: Ankerite; Sid: Siderite; Pyr: Pyrite; Co: Cobaltite; Gn: Galena; Gdf: Gersdorffite; Sph: Sphalerite; Ull: Ullmannite; Asp: Arsenopyrite; Pn: Pentlandite; Mlr: Millerite.

5.3 Materials and Methods

5.3.1 Ground samples

The soil sample dataset provided by Oceana Gold Ltd. consists of 3918 sampling locations, with corresponding As and Sb measurements using a portable XRF (Madambi and Moore, 2013). Of the total dataset 3358 samples fall under the regional baseline (in South Island) concentration of As and Sb within 5-15 and 1-2 µg/g respectively. The training dataset has been selected from this large dataset based on the availability of the hyperspectral image (Figures 5.1 and 5.2). In total, 325 data points were selected for further analysis.

The biogeochemistry dataset was collected during a biogeochemical orientation survey conducted by GNS Science; the data and its analysis can be found in Dunn et al. (2012b). The primary plants targeted for the survey included Westland quintinia (Quintinia acutifolia) which is ubiquitous in the region and three species of beech, commonly known as black, red and silver beech (*Nothofagus solandri*, *Nothofagus fusca* and *Nothofagus menziesii* respectively). Multi-element analysis was executed on the plant samples using Inductively Coupled Plasma Mass Spectrometry (ICP-MS). A subset of plant samples, quintinia (n=34) and beech (n=22) samples were used for further validation.

5.3.2 Hyperspectral image and data processing

The airborne hyperspectral data was captured using a AisaFENIX sensor (for specifications see Table 5.1), flown at 500-600 m above ground, resulting in a 1 m resolution image. The survey was flown close to Solar noon (e.g., Solar elevation > 63°) on 3rd February 2021 in between 12:35 pm and 1:05 pm (New Zealand Standard Time). Standard GPS and navigation data were captured by an Oxford Survey$^+$ GPS and inertial measurement unit, without any post-processing. For this study, we have applied post-processing data analytics to the hyperspectral data with different levels of processing: (1) raw radiance data, (2) surface reflectance with nadir normalisation and Bidirectional reflectance distribution function (BRDF) correction, (3) denoising using First Order Spectral Roughness Penalty (FOSRP), and (4) OTVCA on the denoised image.

Table 5.1: AisaFENIX sensor specifications and data survey settings

	VNIR	SWIR
Field of View	32.2°	
Flying height	500-600 m above the ground	
Instantaneous Field of View	0.084°	
Speed	100 knots	
Spatial resolution	1 m	
Full-Width-Half-Maximum	3.2-12.2 nm	
Spectral Bandwidth	~3.3 nm	~5.7 nm
Number of Bands	177	272
Spectral Range	0.3773-0.9775 µm	0.9831-2.4918 µm

(1) Radiance and (2) surface reflectance data: The data-processing follows Chakraborty et al. (2022), including radiometric and atmospheric corrections using CaliGeoPro and ATCOR 4 (Schläpfer and Richter, 2002). Outputs from CaligeoPro provide the input for the radiance data in units of Wm^{-2}sr^{-1}. The radiance image has been processed using flat-terrain atmospheric correction in ATCOR 4 (Richter and Schläpfer, 2011), using water retrieval band at 825 nm at a 50 km visibility. ATCOR-4 determines the aerosol and the water vapour map using the image itself and also removes low altitude haze (Dong et al., 2019; Richter and Schläpfer, 2019). The dataset showed illumination imbalances between the North to South (South heading) and the South to North (North heading) runs despite of being captured at Solar noon at 2-3 minutes intervals between consecutive runs (Figure 5.4).

Atmospheric correction models such ATCOR are based on MODTRAN 5.3 radiative transfer algorithm (Richter and Schläpfer, 2019). To reduce anisotropic effects on reflectance data, the atmospherically corrected data was further put through BRDF and nadir normalisation using ATCOR 4. The module used instantaneous field of view at each scene to calculate the BRDF and nadir normalised reflectance (Dong et al., 2019). The resultant data was finally georectified in ENVI 5.5.

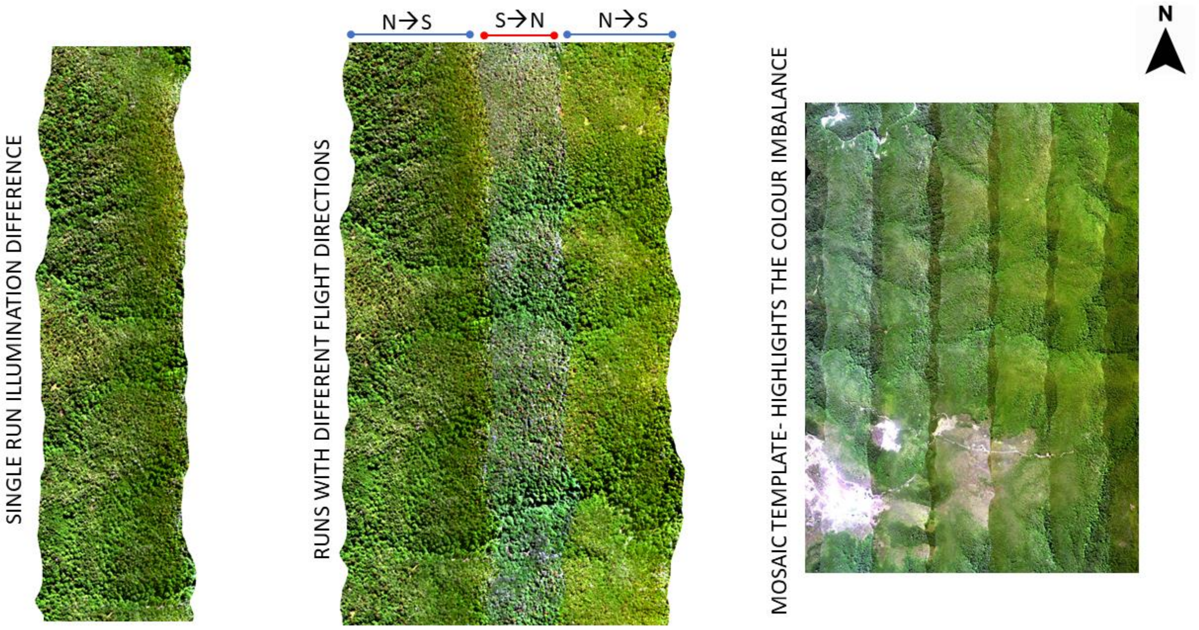

Figure 5.4: Colour/Illumination imbalance between the two directions of runs

(3) The first band and the last four bands were noisy and were deducted. The remaining 444 bands were put to further processing. The BRDF corrected surface reflectance data has been denoised using FOSRP. Hyperspectral data inherently contains a large percentage of noise caused by the sensor, atmospheric interference, among others (Zhuang and Ng, 2020; Chang, 2021; Dao et al., 2021), which can compromise further analysis. The degraded signal can be reconstructed using denoising techniques (Ghamisi et al., 2017b). FOSRP can reduce the sensor-induced noise affecting the spectral data. The FOSRP denoising technique has been used here which operates at a wavelet domain. FOSRP considers the high correlation in the spectral bands in a hyperspectral data and calculates penalised least squares using a first-order spectral roughness penalty for restoration. This method further uses the Stein's unbiased risk estimator to automatically select the tuning parameters based on the spectral intervals which are established on the step values provided by the user (start interval= [0,0,0,0], step size= [.001,.01,.1,1], end interval=[.01,.1,1,10]) (Rasti et al., 2013). Visually, the AisaFENIX data has more prominent noise in SWIR region (Figure 5.5), than in the VNIR region and also, they are captured by two separate detectors with different bandwidths (Table 5.1). Thus, denoising was run separately on the VNIR (0.37- 0.97 µm) and the SWIR (0.972-2.47 µm).

(4) OTVCA on denoised data: OTVCA stands out for its capacity to consider spatial information of the neighbouring pixels using the total variation penalty factor along with maximum variance in input reflectance (Rasti et al., 2016). OTVCA thus potentially conserves spectral and spatial information from a hyperspectral image better than the most commonly used PCA or Minimum Noise Fraction (Rasti et al., 2016; Rasti et al., 2020). The denoised hyperspectral imagery data was transformed into 15 OTVCA components, beyond 15 the components the data was mostly noise on visual interpretation. These were then used as predictor variables for the final set of regression models.

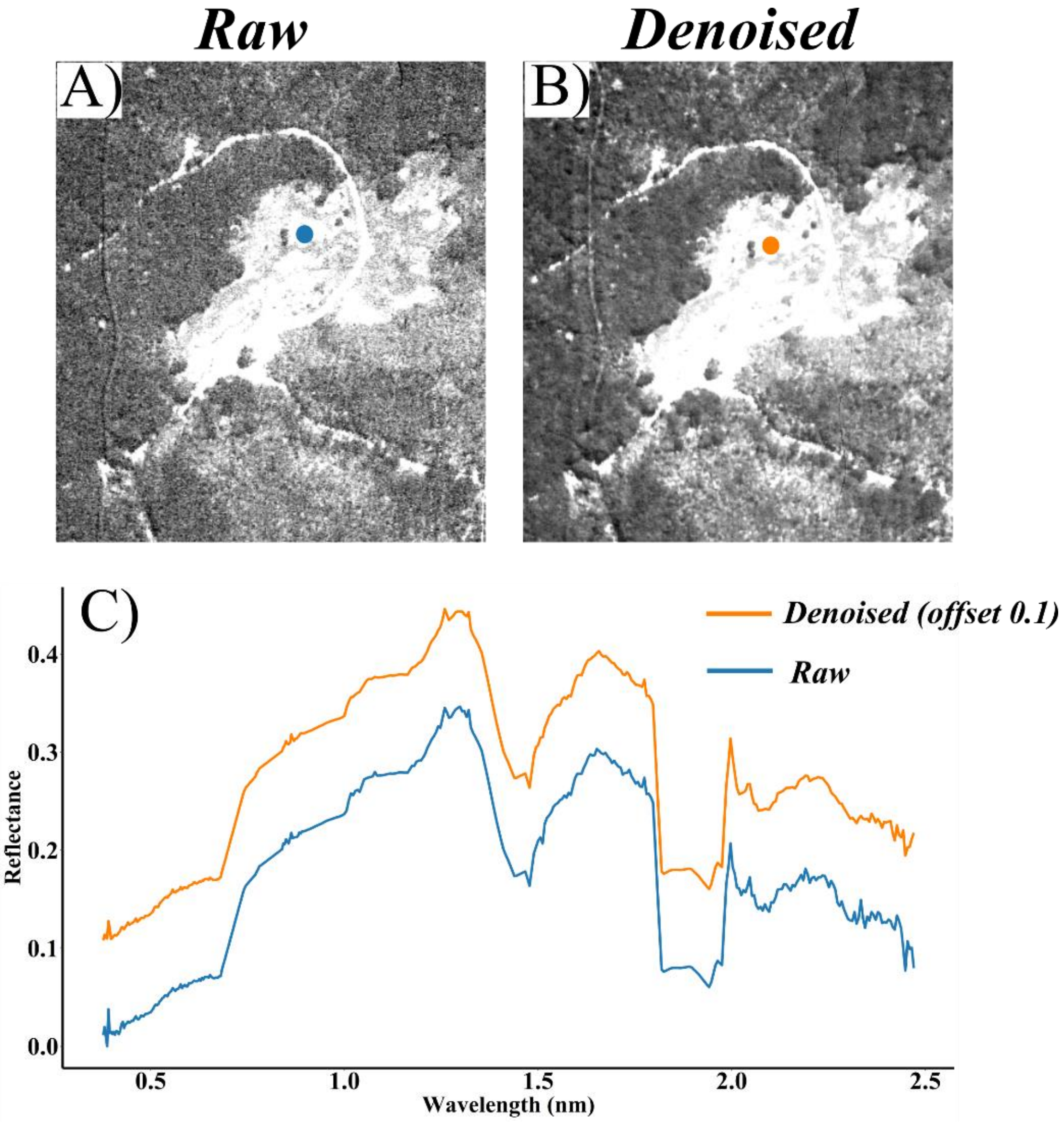

Figure 5.5 : Differences between the raw and denoised data visually and spectrally.

5.3.3 Prediction models using regression analysis

The separately denoised VNIR and SWIR spectral subsets were merged for all the runs. The denoised 444 band hyperspectral data for each run was then trained using Random Forest Regression (RFR). RFR was chosen for its ability to deal with multicollinearity like in the hyperspectral data. RFR also does not extrapolate the values beyond the training data which perfectly fits the objective, as the training data cover the range of concentration for both As and Sb in the region (Breiman, 2001; Belgiu and Drăguţ, 2016).

The South heading and the North heading runs were separately trained for the regression to minimise effect of viewing geometry on the results (e.g., Figure 5.4). This step was crucial as the models are presumed to be trained on subtle spectral differences across the VNIR-SWIR spectral range that correlate with As and

Sb concentration as they do not have a spectral signature in this region (Li et al., 2015; Rathod et al., 2018). A total of 187 and 237 training data points were used from North and South heading runs respectively. Out of those 98 common sampling locations has been used in North and South heading runs due to the 30% side-overlap between neighbouring image strips.

The total number of trees (ntree) in the RFR was 500 and was kept constant throughout the experiment, to provide adequate generalisation to the model, and reduce the bias by imposing greater variance (Abdel-Rahman et al., 2012; Li et al., 2015). The number of splits at each node (mtry) was set to a sequential grid from 1 to 150 and was optimised using a 15-fold cross-validation. The training and prediction were run on input data from processing levels 1-4, and each model were assessed based on R^2 and Root Mean Square Error (RMSE).

5.4 Results and Interpretations

The regression models show generally low to moderate accuracies for both As and Sb with maximum R^2 of 0.39 (Table 5.2). The models show a consistent improvement (e.g., reduction in RMSE and increase in R^2) with each step of pre and post-processing (Table 5.2). Notably the denoised data and the OTVCA transformed data models show a significant improvement with R^2 reaching as high as 0.39 with RMSE of 0.64. The largest change in R^2 was reported in the Sb-based models, which increased by 0.27 from radiance (processing #1) to OTVCA (processing #4) (Figure 5.6).

Table 5.2: Model error metrics

Predictor Inputs		**As**		**Sb**	
		R^2	**RMSE**	**R^2**	**RMSE**
Raw radiance data	N heading	0.07	0.57	0.11	0.76
	S heading	0.06	0.54	0.17	0.73
BRDF and Nadir treated reflectance data	N heading	0.1	0.58	0.18	0.71
	S heading	0.08	0.53	0.21	0.72
Denoised (reflectance data)	N heading	0.12	0.59	0.27	0.72
	S heading	0.05	0.55	0.24	0.71
OTVCA (on Denoised data)	N heading	0.17	0.55	0.39	0.66
	S heading	0.14	0.51	0.38	0.64

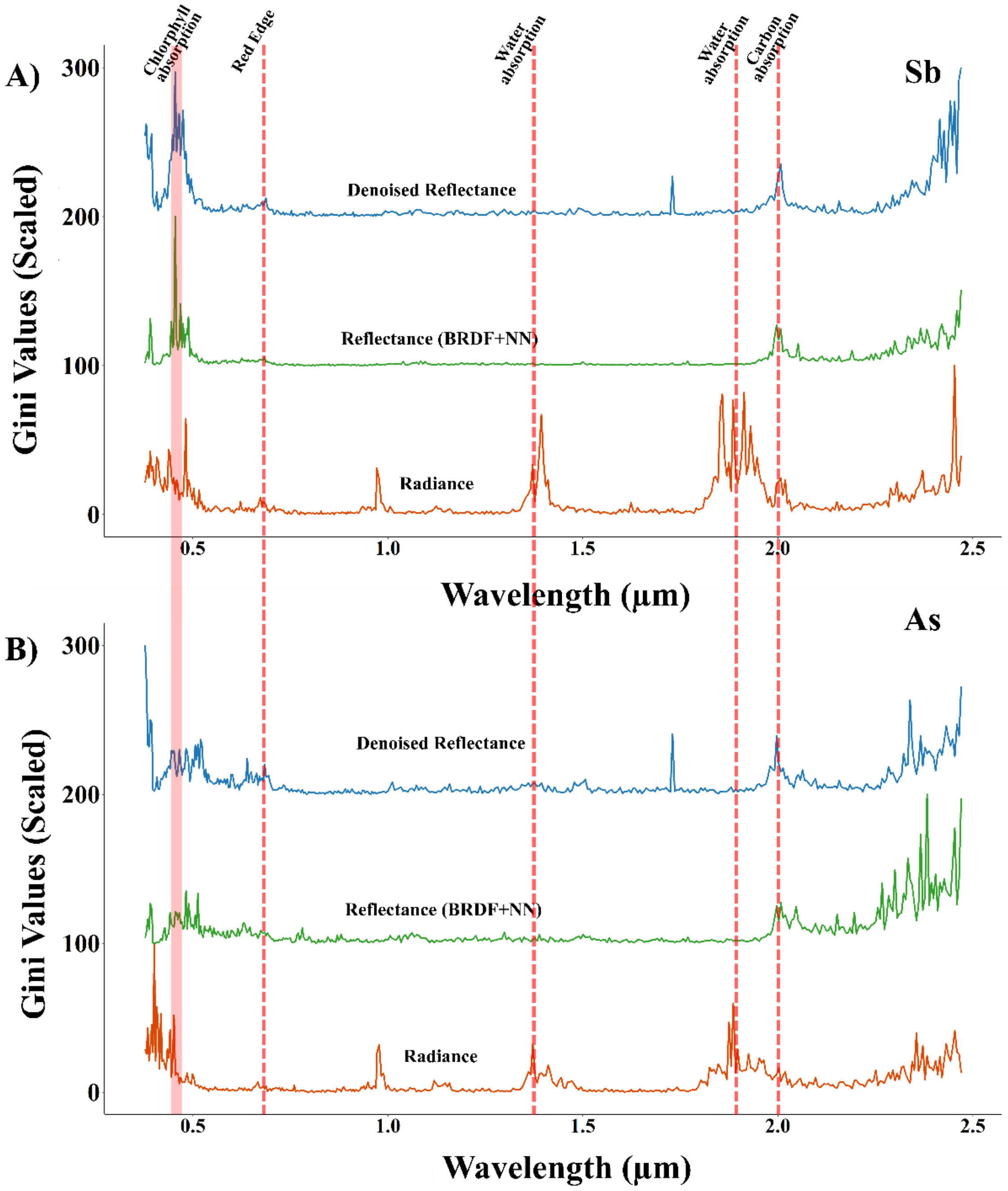

Figure 5.6: Graph showing the Gini values across the VIS-SWIR spectrum for models trained for As (A) and Sb (B).

The Gini value measures the permutation variable importance and facilitates in the splitting of nodes in a random forest tree (Breiman, 2001). Plotting the Gini impurity as a function of the wavelength highlights some differences between the Sb and As prediction models (Figure 5.6). Firstly, the chlorophyll absorption spectral region (0.45 to 0.47 µm, in Figure 5.6) is found to be important for both Sb and As prediction models, although it is more prominent for Sb models compared to As models. Other noted regions of higher importance for both As and Sb include 1.4 and 1.9 µm, which is absorption associated with atmospheric water. These spectral ranges have been eliminated by atmospheric corrections.

The scatter plot on analysis for the best models using OTVCA as input predictor variables for Sb-based models show about 16 ground points in the North heading model and 22 in the south heading with residuals error less than 0.1. Essentially these are the points with the highest prediction accuracy. The spatial distribution of these 38 points is illustrated in Figure 5.7C. The concentration of Sb in µg/g for these points range from 5.77 to 21.3 µg/g in training data (Figure 5.7).

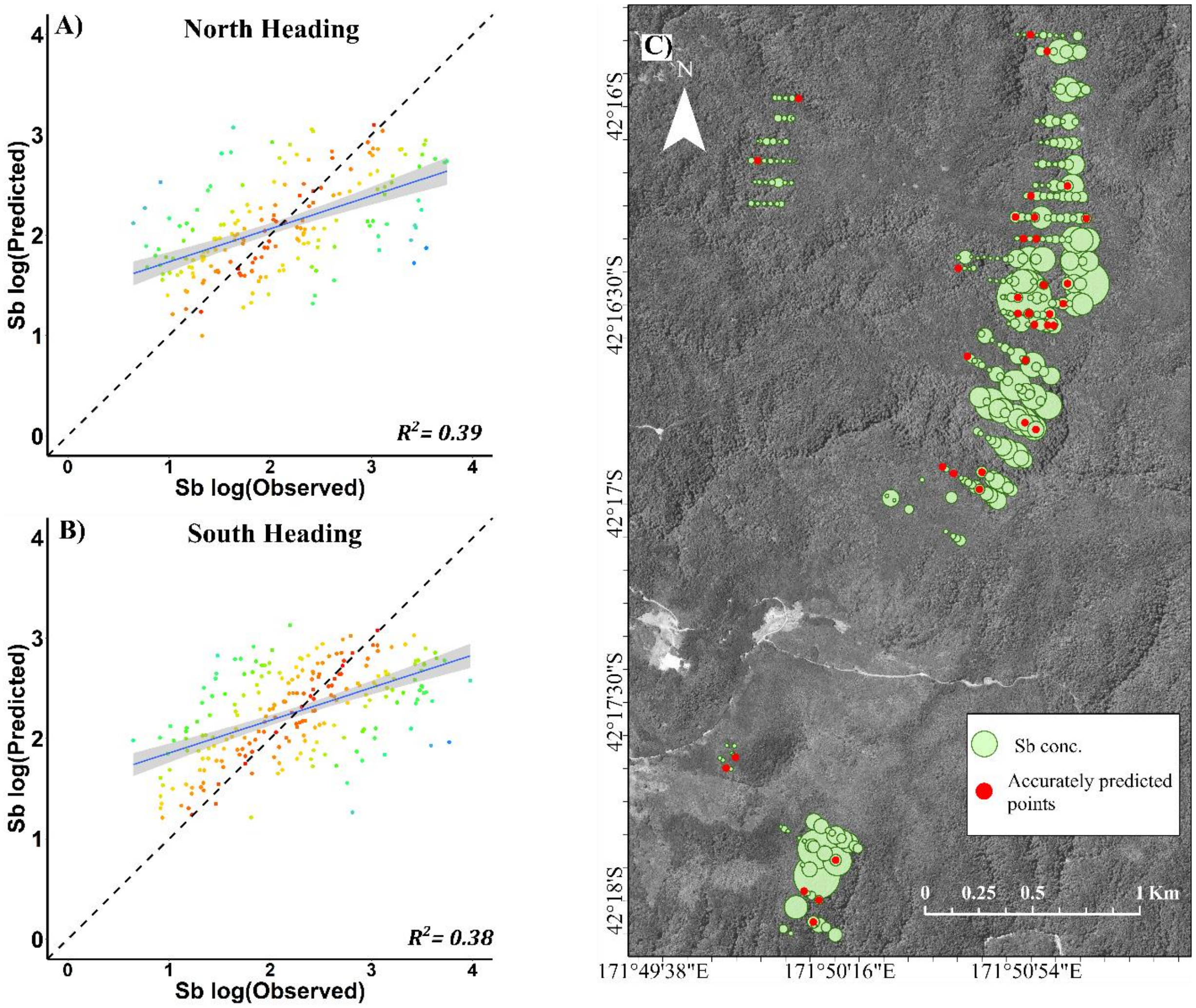

Figure 5.7: Scatter plot showing the observed vs predicted values for OTVCA-based models for Sb. The grey area around the trendline marks the 95% confidence interval. (Abs= absolute)

The spatial map showed Sb anomalies north of the Big River Track (Figure 5.8A) and also around the Waiuta mine tailings (Figure 5.8B). The former region is however, located closely with the training data while Waiuta had no training data (Figure 5.7B), but it is known for its mining-related As and Sb contamination (Haffert and Craw, 2009; Druzbicka and Craw, 2015; Tay et al., 2021).

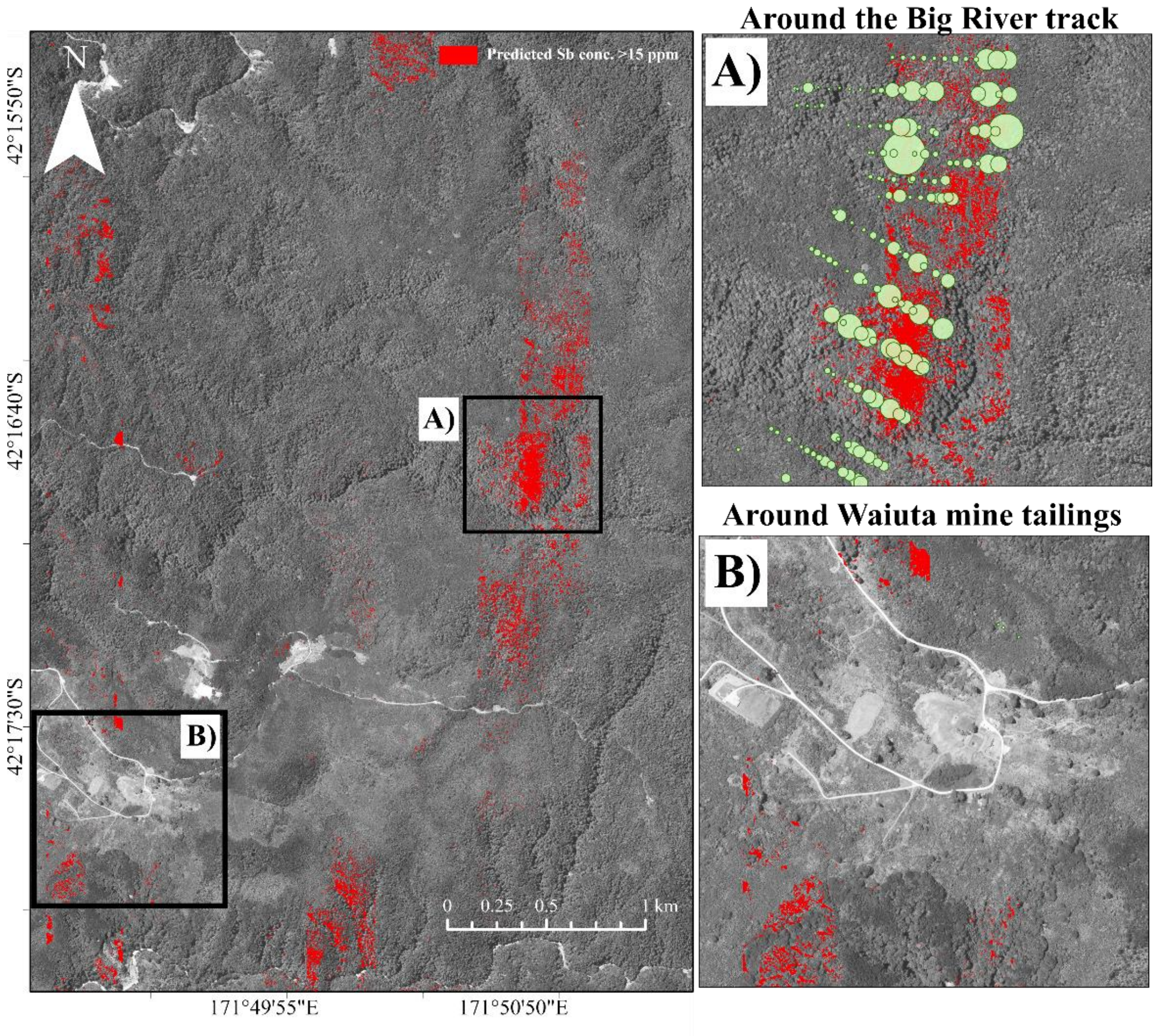

Figure 5.8: Predicted Sb anomalies that are above the background level and more than 15 µg/g (in red). Insets show the Sb anomalies at Big River track (A) and the Waiuta mine tailings (B). In A, green dots show the proportional Sb concentrations in the soil samples.

The Sb prediction were further validated against the biogeochemical samples, which show background values corresponding to the distal geochemical footprint (Table 5.3 and Figure 5.3). The predicted Sb (in ppm) fall mostly below 15 ppm, except for one location which is ~19 ppm, thus manifesting the range of Sb beyond the proximal mineralisation halo in soil. Therefore, the findings of the biogeochemistry orientation study (Dunn et al., 2012b) aligns well with our Sb anomaly predictions using hyperspectral imagery.

Table 5.3: Sb concentration in *Quintinia* and beech species compared to predicted Sb values in the soil.

Lat	Long	Sb (ppm) in Quintinia	Sb (ppm) in Beech	Type of Beech	Sb (ppm) in soil as predicted
-42.2849	171.8451	0.03	0.06	Black	19.05
-42.2849	171.8444	0.05	0.05	Black	7.46
-42.2849	171.8438	0.04	0.06	Black	7.32
-42.2849	171.8432	0.06	0.06	Black	5.06
-42.2847	171.8425	0.06	0.06	Black	5.97
-42.2847	171.8419	0.03	-	-	7.13
-42.2847	171.8412	0.05	0.06	Black	7.82
-42.2846	171.8406	0.06	0.05	Black	7.01
-42.2847	171.8397	0.06	-	-	7.74
-42.2848	171.8393	0.04	0.04	Black	7.94
			0.08	Red	
-42.2833	171.8392	0.04	-	-	7.38
-42.2834	171.8398	0.04	0.06	Black	6.10
-42.2835	171.8404	0.05	0.04	Black	6.82
-42.2834	171.8411	0.07	0.09	Black	7.74
-42.2835	171.8417	0.04	0.05	Black	6.87
-42.2838	171.8423	0.06	0.04	Black	5.03
-42.2838	171.8429	0.06	0.04	Black	5.29
-42.2838	171.8436	0.12	-	-	6.15
-42.2838	171.8443	0.05	0.05	Black	7.05
-42.2836	171.845	0.06	0.06	Black	15.24
			0.1	Silver	
-42.2819	171.8465	0.06	0.07	Black	12.80
			0.09	Red	
-42.2819	171.8459	0.09	-	-	13.24
-42.2819	171.8459	0.07	-	-	12.44
-42.2816	171.845	0.04	-	-	16.14
-42.2815	171.8449	0.06	-	-	13.54
-42.2812	171.8444	0.12	-	-	13.32
-42.2808	171.8439	0.09	0.11	Silver	4.82
-42.2811	171.8423	0.09	-	-	7.47
-42.2813	171.8418	0.07	-	-	6.50
-42.2811	171.8411	0.09	-		6.14
-42.2806	171.8406	0.07	0.11	Silver	5.99
-42.2805	171.8399	0.06	-	-	5.58
-42.281	171.839	0.07	-	-	11.15
-42.2814	171.8382	0.08	-		10.59
-42.2936	171.8276	No data	0.06	Black	8.09

5.5 Discussion

5.5.1 Data enhancement methods and their potential

Hyperspectral data contains a plethora of spatial and spectral information (Kruse, 1998; Liu et al., 2011; Ghamisi et al., 2017b; He et al., 2017; Maxwell et al., 2018; Ghamisi et al., 2021), which sits alongside a significant amount of noise (Othman and Qian, 2006; Rasti et al., 2018). Noise can be sensor induced (e.g., thermal noise, photon noise, salt and pepper, pattern noise) and scene related (e.g., atmospheric interference, illumination scattering affecting neighbouring pixels). The ever-advancing pre- and post-processing techniques have always focused on eliminating the various types of noise while at the same time enhancing the signal (Othman and Qian, 2006; Gao et al., 2009; Liu et al., 2011; Rasti et al., 2013; Ghamisi et al., 2017b). Our study has shown the impact of pre- and post-processing techniques on the performance of regression methods using hyperspectral data for mapping Sb and As anomalies. Overall, the regression models performed moderately at best, however, data post-processing has significantly improved the model performance (Table 5.2). The calculated Gini values can highlight underlying structure of the prediction models that can be conceptualised. This study shows that the important bands contributing to prediction models are situated well within the atmospheric absorption zones for radiance image, indicating the lack of proper information that is apparent to the regression models in the data. Atmospheric correction and denoising reduced atmospheric influences and improved the signal-to-noise ratio of the hyperspectral data which returned narrow but important spectral features located at 0.45-0.47 µm (Figure 5.6). This region at 0.45-0.47 µm is due to plant chlorophyll absorption (Gao and Goetz, 1990b), which has been documented to correspond with metal stress (Zengin and Munzuroglu, 2005; Li et al., 2015). Excessive absorption of metals in the plants induces stress which influences the chlorophyll absorption features causing effects such as red edge shift in the vegetation spectra (Pullanagari et al., 2018), and may also result in an overall decrease in canopy chlorophyll content which is also manifested in the vegetation spectra (Zengin and Munzuroglu, 2005; Li et al., 2015). This leverages the hyperspectral remote sensing toolset significantly for vegetation-based studies. Techniques, such as band ratio and NDVI have been designed and have utilised this spectral range extensively for various applications (Dalton et al., 2004; Cudahy et al., 2008; Pour and Hashim, 2011; Muriithi, 2015).

The results further indicate an increase in variable importance in the SWIR (>2.2 µm; Figure 5.6), potentially corresponding to the persistent noise that mimics the signal even after applying denoising. The sensor-induced noise in the SWIR spectral range of the AisaFENIX sensor is relatively high. This is, however, often taken as information when regression and classification models are developed on such noisy hyperspectral data. SWIR can be important to identify minerals, such as kaolinite and sulphates, such as gypsum, alunite, and carbonates, such as calcite, dolomite, and siderite, which are abundant within the Reefton goldfield (Clark and Roush, 1984; Clark, 1999; Hamisi, 2016; Hamisi et al., 2017).

5.5.2 Limits of hyperspectral imaging for biogeochemistry

The way vegetation reflects light can be exploited to map concealed mineralisation and this was proven in studies like, Chakraborty et al. (2022) using *Pinus radiata* along the HMSZ area to map elemental stress and using *Kunzea ericoides* in the geothermal area in Waiotapu (Rodriguez-Gomez et al., 2021). Biogeochemistry has also been used to map Cu mineralisation in Cyprus (Cohen et al., 2021), in Australia to map gold using Eucalyptus trees (Lintern et al., 2013), and in Canada to map uranium deposits using tree cores of Jack pine (Beyer et al., 2021). Each of these applications has resulted in varying ranges of both success and failure. In the context of New Zealand utilising biogeochemistry to map underlying gold mineralisation has previously failed in Reefton (Dunn et al., 2012a) while orientation studies have been successful in the Coromandel Peninsula (Dunn and Christie, 2014; Dunn and Christie, 2020). The failure in Reefton can be accounted to multiple reasons: -

1. In a natural forest ecosystem, equilibrium is often developed between the soil chemistry and plant chemistry over a long period of time which makes the elemental anomalies less obvious at a broader regional scale (Brooks, 1973; Dunn, 2007).
2. For a natural forest such as in the Reefton goldfield, there is usually a high proportion of decaying organic matter in the soil (Dunn, 2007). The decaying organic matter tends to remove the elements form the soil and binds onto themselves through microbial activity. This deprives the plants of elements from soil binding them through microbial assisted with organic complex. This deprives the plants of available elements in the soil and creates a higher degree of variability between plants growing on organic and inorganic soils (Anderson et al., 1999; Dunn, 2007).

3. Soil pH is also an important factor that can govern elemental uptake (Kovalevskii, 1969; Dunn, 2007). Acidic pH in the surrounding soil facilitates elemental uptake in plants whereas a near neutral pH lying between 5-6 which tends to restrict the elemental uptake (Dunn et al., 2012b).

The biological absorption coefficient (BAC) of a plant species can span a wide range in such a natural forest (Kovalevskii, 1969; Brooks, 1973). The parameter BAC is governed by the role of the element in the plant, age and health of the plant, and depth of the root system all of which are likely to vary across species as well as across individual plants of the same species (Brooks, 1973). Apart from the plant itself, the setting of a place including the topography (e.g., slope and aspect) can govern root development and the pH of the soil control the mobility of the targeted elements both chemically and mechanically (Kovalevskii, 1969; Kovalevsky, 1987). Such underlying diversity in a natural forest environment can lead to differences in metal stress manifestation in the vegetation spectra. In our prediction models, the Gini values indicate ample important bands at 450-500 nm coinciding with bio-chemical plant signatures (e.g., chlorophyll content) although the overall regression models have failed to generate reliable prediction models at regional scale. The low performance of the models is interpreted to be related to the previously mentioned factors affecting the multi-species flora variably. The resultant manifestation of metal stress in the spectra is very subtle. Although the model picks up relevant important wavelengths the subtlety and high variability of stress from species to species as well as from plant to plant renders poor model performance.

The insignificant model performance from a hyperspectral data perspective is interpreted due to low signal-to-noise ratio and 3-7 nm bandwidth of the airborne hyperspectral data. At the current technology (e.g., PRISMA and EnMAP with 30 m spatial resolutions), this finding also suggests that satellite hyperspectral imaging has limited potential to be used to explore regional-scale mineral distribution at the Reefton goldfield. Furthermore, the 30 m spatial resolution of hyperspectral satellites is further limited by the fact that quartz-hosted mineralised halos at the Reefton goldfield barely exceeds a distance of 10-20 m away from the mineralisation.

5.5.3 As versus Sb for pathfinder

The regression models in the current study were trained for pathfinder elements, such as As and Sb, which do not show any signature absorption in the VNIR-SWIR spectral range. This has not prevented hyperspectral application to be able to predict them in a controlled setting using laboratory hyperspectral data (Font et al., 2004; Gomez et al., 2008; Rathod et al., 2015; Shin et al., 2019; Shrestha et al., 2022) or airborne imaging (Rodriguez-Gomez et al., 2021; Chakraborty et al., 2022). The reason being many metals and metalloids can co-vary with other spectrally active constituents in both soils (e.g., presence or absence of associated elements such as Fe and Al, with signature absorption features and soil moisture) and plants (e.g., metal and water stress manifested in red edge shift and change in canopy chlorophyll manifested in the chlorophyll absorption feature).

The correlation between soil geochemistry and plant geochemistry is known to be area specific and plant-specific (Dunn, 2007; Dunn and Christie, 2020). Biogeochemistry is often preferred as an exploration tool compared to soil geochemistry as the deep roots of plants can integrate the geochemical signature of the entire soil horizon (Kovalevskii, 1969; Farago, 2008; Dunn and Christie, 2020). The migration of elements into the plant system is driven by elemental association in the minerals, ionic size and presence or absence of ligands (Brooks, 1973; King, 1984; Dunn, 2007). Biogeochemistry is also not affected by the dissipation of elemental concentrations such as those caused by groundwater-driven alteration and redistribution and chemical weathering which easily affect the soil geochemistry (King, 1984; Dunn, 2007; Dunn and Christie, 2020). On the contrary the magnitude of elemental concentration is much higher in soil than in the plant tissue which helps in the distribution of the target variable which often favours such regression-based analysis (Dunn and Ray, 1995).

Gold mineralisation in the Reefton goldfield is hosted in meta-sedimentary rocks where the magnitude of concentration of the pathfinder elements is significantly less compared to the dominantly hard-rock HMSZ and RSSZ where the gold mineralisation is hosted by the greenschist facies metamorphic rocks (MacKenzie and Craw, 2007; Craw, 2017). Furthermore, As mobility in the soil had also been accelerated at the Reefton goldfield by previous mining activities (Druzbicka and Craw, 2015). The ore processing methods such as roasting led to As separation from arsenopyrite (FeAsS) which then remobilised As, often through groundwater or even mine waters and oxidised to form scorodite ($FeAsO_4.2H_2O$) (Haffert and Craw, 2009). The leached-out elements, such as As and Sb, then gets transported and settle to form As and Sb-based oxyanions ($H_2AsO_4^-$, $HAsO_4^{2-}$, and SbO_3^-) further away in a less mobile region with acidic pH near the acidic mine draining areas. Furthermore, the presence of kaolinite at the pH of 2-3 around the Big River area (affected by acid mine drainage; out of the study area to the east) can, however, facilitate retention of As and Sb, as it gets adsorbed to the positively charged clay particles (Xi et al., 2010; Druzbicka and Craw, 2015). Altogether the leaching and the retention processes render the overall As and Sb footprints “blurry” and enlarged (Hamisi et al., 2017).

Arsenic already is known for its high mobility in a favourable environment (Boyle and Jonasson, 1973; Garcia-Sanchez and Alvarez-Ayuso, 2003), Sb is relatively less mobile. Consequently, Sb has proven to be a more reliable element in Reefton (Hamisi et al., 2017), as well as in East Otago (Chakraborty et al., 2022) for its vectoring capabilities for gold. The fact that the soil geochemistry signals are only mildly correlated with the underlying gold mineralisation has also impacted our prediction models, highlighting the importance to develop conceptual models for plant uptake before application of hyperspectral imaging. Such conceptual model should be formulated using laboratory-based measurements (e.g., using high signal-to-noise ratio data), prior to the airborne hyperspectral surveys and model-development. The laboratory-based models, therefore, can represent the best-case scenarios for each geological environments to apply any airborne hyperspectral imaging. This gives an idea regarding the maximum capacity of the hyperspectral data to predict the targeted variable.

5.6 Conclusion

Exploration of concealed gold mineralisation using pathfinder elements, such as As and Sb, through light reflective properties of a multi-species natural forest is highly complicated and challenging. Our study explored the interplay between rock-soil and plant interference to track and map the distribution of As and Sb anomalies that might be signalling gold mineralisation. Remote detection of such anomalies in plants is complicated as those elements are spectrally “featureless” and their concentration is in the lower/trace levels. Any remote detection is driven by the degree of plant stress induced by the underlying metal deposits. Our results indicate that the regression models highlighted regions spanning a narrow wavelength range between 0.45-0.47 µm corresponding to chlorophyll content in the canopy which is indicative of metal stress.

The best performing models have only reached moderate accuracies, although each step of pre- and post-processing lead to improvement in the R^2. The best model was achieved using the OTVCA components as predictor inputs with an R^2 of 0.39 for Sb. On spatially predicting the results, some clusters of the anomalies could be validated using previous studies and training point knowledge in the area (Figure 5.8) (Haffert and Craw, 2009). Although the models show some relevance it is tricky to confirm the anomalies without good laboratory based analysis of the biogeochemical samples at this level.

Conceptually and theoretically, the link between imaging and biogeochemistry is plausible, however, it seems that this relationship cannot be generalised. Based on this study, it seems individual conceptual models and sampling approaches must be developed separately for each prospect site. At Reefton, the poor to moderate performance of the prediction model for As and Sb is interpreted to be due to the poor rate of uptake of pathfinder elements from the rock to plants. Furthermore, the mineral halos can also be enlarged by the high mobility of As (e.g., anthropogenic As contamination due to ore processing), while this is less true for Sb (Figure 5.3), our results still poorly explain the spatial distribution of such pathfinder elements in relation to the underlying gold-bearing deposits.

Natural vegetative cover with a large variety of plant species can lead to considerable spatial variation elemental uptake, storage and finally ways to discard toxic elements across a forest canopy. This diversity can result in complexity in the spectral data that cannot be simplified through a regression model. This is in contrast with a plantation in which a single species is dominant. In case of plantation canopy, processes can be easier to understand by chemometric methods. For example, in the HMSZ chapter (Chapter 3) the pine species *Pinus radiata* is known for being a significant accumulator of metals and metalloids (Dunn, 2007; Farago, 2008; Dunn and Christie, 2020) which can (somewhat) simplify the modelling approach. The complexity of a natural vegetation cover therefore remains challenging to biogeochemical prospecting, and ongoing research will be needed to advance more robust exploration techniques that use trees.

5.7 Acknowledgement

The study was supported by the Ministry of Business, Innovation and Employment (MBIE) Endeavour Fund- Smart Ideas: Assessing New Zealand’s environmental and mineral indicators (contract number:

MAUX1802). The authors are grateful to OceanaGold Ltd for support and access to their extensive exploration dataset. The authors would also like to thank Dr. Colin Dunn for sharing biogeochemical data the from his previous study along with GNS Science.

Chapter 6. Integrated Discussion

6.1 Redistribution of elements in soil and plants

6.1.1 Gold redistribution and mobility in soil and plants

Mineralised shear zones within the Otago schist are often overlain by unconsolidated Quaternary sediments. These loose sediments are easily eroded by surficial processes bringing the ore bodies closer to the surface. The erosion of the overlaid sediments makes the mineralised shear zone prone to oxidation caused by groundwater and atmosphere along with supergene enrichment (Craw, 1994; Craw et al., 2015a). The sulphide-bearing minerals from the mineralised schist (e.g., pyrite and arsenopyrite) at near-surface atmospheric conditions are metastable and can easily decompose by oxidation forming metal hydroxides (e.g., iron-hydroxide formed by the transformation of arsenopyrite). Near-surface oxidation and weathering further result in an environment which facilitates physical and chemical mobility for gold and associated metal hydroxides (Blake et al., 2019; Beyer et al., 2021; Cudby et al., 2021). Gold in its free form is adsorbed by these metal hydroxides to form gold nuggets, which are subjected to surficial processes. The size of the gold nugget depends on the distance travelled by these gold adsorbed metal hydroxides. Once the nugget reaches a certain threshold of size and roundness which can be subjected to the effects of physical weathering, it may lead to further travel and eventually lose traceable characteristics such as pathfinder element association (Craw et al., 2015a; Craw, 2017; Cudby et al., 2021) (Figure 6.1). This phenomenon has been reported in the Otago gold mineralisation areas, with an extensive emphasis on the RSSZ (Craw et al., 2015a; Craw, 2017).

Hydrothermal alteration processes at shallower depths weaken the mineralised host rock which eventually forms weakly cemented authigenic clays (Craw and Lilly, 2016; Craw, 2017; Cudby et al., 2021). The authigenic clays are then prone to redistribution by physical surficial processes such as erosion (Chamberlain et al., 1999; Blake et al., 2019). The gold in this habitation is more likely to be released as soluble ions and taken up by plants (Lintern et al., 2013), especially in dry and arid environmental conditions that promote the availability of ligands for gold dissolution (Boyle and Jonasson, 1973; Lintern et al., 2017; McQueen et al., 2021).

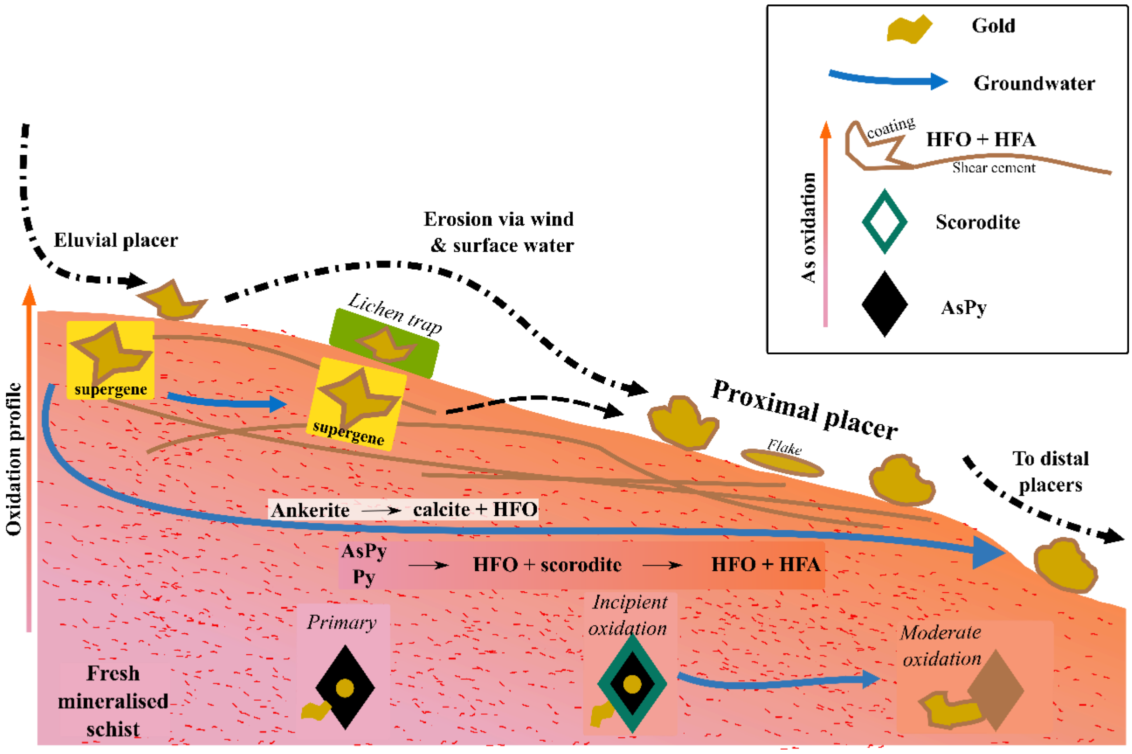

Figure 6.1: Distribution and redistribution of gold, caused by principal geochemical and physical processes (Modified from Cudby et al. (2021)). The minerals mentioned here are key to the gold mineralisation in the Rise and Shine area, although the supergene enrichment leading to the gold nugget formation and its movement is a generalised concept. AsPy- Arsenopyrite; Py- Pyrite; HFO- Fe-oxyhydroxide; HFA- arsenic bearing HFO.

The earliest study of gold uptake in plants was reported by Nemec et al. (1936) in *Equisetum palsustre*. Since then, many studies have been conducted to study the uptake of gold and attempts have been made to utilise the gold uptake as an orientation tool for mapping gold mineralisation (Lakin et al., 1974; Ward and Brooks, 1978; Dunn, 1986; Ashton, 1989; Anderson et al., 1999; Dunn, 2007; Nude et al., 2012; Lintern et al., 2013; Chakraborty et al., 2022). Many biogeochemical surveys have however reported gold uptake to be merely a "nugget" effect (i.e., outlier), with very poor reproducibility (Dunn, 2007). Gold anomalies in biogeochemical samples, therefore, need to substantially be validated using pathfinder elements such as As and Sb.

Lintern et al. (2013) provide a contrasting view and reported consistent levels of adsorbed native gold particles in all parts of Eucalyptus trees growing over an authigenic soil, including litter, bark, twigs and leaves. The nearly homogeneous distribution of the gold throughout the tree, in this case, was explained by the relatively high concentration of gold in the soil, which was intercepted by roots. There is an assumption that gold, being toxic to plants, is pushed to leaves from where it can easily shed through abscission (Farago, 2008). Lintern et al.'s study showed a greater mobility of gold in the plants compared to previous studies. This can be linked back to the basalt and shale host rock and the fact that it is classified as a supergene sub-economic gold deposit, indicating the presence of higher amounts of gold in free form which enters the soil and the plant parts with less chemical resistance (Eilu and Groves, 2001; Lintern et al., 2013).

Two main factors make analysing gold directly in plant tissue challenging. Firstly, gold uptake in plants is typically in very trace quantities making detection a limitation in the analysis. While ICP-MS analysis has a detection limit of 0.2 ppb for gold, pXRF has a limit of 20 ppb (Kovalevsky, 1987; Dunn, 2007). The biogeochemical orientation study by Dunn et al. (2012b) reported below the detection limit for gold in most of their samples even with ICPMS analysis. Thus, a good range and distribution of gold data for a vast spatial extent is hard to achieve, which is important in machine learning. Secondly, gold has a well-known nugget effect in environment settings that facilitate supergene enrichment, and this can lead to the very sporadic distribution of gold in soil and subsequent uptake in plants. This nugget effect is essentially an outlier in the data and renders the data analysis non-reproducible. This reinstates the fact that it should always be validated using associated pathfinder elements.

6.1.2 Redistribution of arsenic and antimony

The success of biogeochemical methods lies in the fact that gold and its pathfinder elements are spatially correlated (Nude et al., 2012; Korshunova and Charykova, 2019; Gazley et al., 2020), however, it is often not the case. Arsenic in the soil is mobilised by natural processes such as erosion and microbial activity (Bhattacharya et al., 2007; Malloch et al., 2017). This mobilisation is further enhanced by mining activities which can potentially increase the local pH of the soil and groundwater affecting the mobilisation and redistribution of As (Bech et al., 1997; Garcia-Sanchez and Alvarez-Ayuso, 2003; Patinha et al., 2004; Drahota and Filippi, 2009). The main source of As in soil in New Zealand and also globally is the breakdown of arsenopyrite and scorodite (Garcia-Sanchez and Alvarez-Ayuso, 2003). Decomposition of arsenopyrite along with other sulphides (e.g., stibnite, chalcopyrite and galena) releases SO_4^{2-} which decreases the pH (i.e., more acidic) of the soil. Arsenic released from the breakdown of arsenopyrite and scorodite is majorly adsorbed by iron-oxyhydroxide and adsorption is most effective for a pH range of 3-5 (Goldberg and

Glaubig, 1988; Singh et al., 1996; Manning and Goldberg, 1997; Smith, 1998). The overall decrease in soil pH associated with the chemical breakdown of As bearing minerals also facilitates improved elemental uptake by plants (Casado et al., 2007; Farago, 2008; Feng et al., 2013). Mining activity can disrupt these natural dynamics of As in soil changing its mobilisation, distribution and plant uptake (Lombi and Nolan, 2004; Anke, 2005; Casado et al., 2007). The increase of pH in mining-affected soils (around mine tailings) can have an adverse impact on elemental uptake by vegetation. This has been extensively reported in studies such as Casado et al. (2007) who showed that mining affected areas with an increase in soil pH reducing elemental uptake by the plants, including a reduction in As and Sb uptake. Furthermore, Sb and As behave similarly in plants (Feng et al., 2013) and soil (Wilson et al., 2010). They are often released from similar mineral associations, such as sulphide minerals like arsenopyrite and stibnite. Dissolved Sb adsorbs to iron-oxyhydroxides in a similar manner to As, although As preferentially adsorbs to displace Sb when both As and Sb are present (McComb et al., 2007; Muller et al., 2015).

Antimony and As are not essential for plants' survival and are mostly taken up passively through phosphorous uptake channels (Feng et al., 2013). This has been validated through controlled experiments which have reported an increase in uptake of Sb and As on addition of phosphate to the substrate (Spuller et al., 2007). Studies have also shown that the presence of elevated amounts of As in substrate can result in increased uptake of Sb (Müller et al., 2013). Due to their similar chemical association and similar chemical properties in the soil, the uptake of Sb and As is also similar in the plant system (Feng et al., 2011; Feng et al., 2013). Therefore, both elements co-vary under a variety of physico-chemical environments (Feng et al., 2013; Shahid et al., 2017). However, Dunn (2007) described the mobility rate of As in a plant as "medium" whereas that of Sb was categorised as "low". This often leads to varying correlations of As and Sb concentrations in different plant parts. Pratas et al. (2005) reported that species such as *C. vulgaris, C. tridentatum* and *P. pinaster* which are classified as hyper-accumulators for both As and Sb, manifest higher concentrations of As in the needles, leaves and mostly aerial parts whereas the bark and stem tissues exhibit higher concentration of Sb.

6.1.3 The pH effect

Elemental redistribution as well as plant uptake can be impacted by soil pH along with many other soil and environmental factors (Arnon and Stout, 1939; Anderson et al., 1999; Anand et al., 2007). Soil pH in Otago broadly lies between 6-8 (Craw and Rufaut, 2017), whereas that of Reefton lies between 5-6 (Hewlett et al., 2005; Haffert and Craw, 2009) (Figure 6.2). However, local variations in soil and plant types can further change the susceptibility of the plant cover to mimic the underlying geology and ore deposits. Our soil samples from the HMSZ indicate a pH of 4.5 under *Pinus radiata*, while a pH 6.5 is returned form samples outside of the plantation area. Therefore, *Pinus radiata* can create its own acidic micro-environment which facilitates more elemental uptake (Giddens et al., 1997; Burgess-Conforti et al., 2019), promoting *Pinus radiata* as an accumulator (e.g., Farago (2008) and Goff et al. (1985)). This makes the *Pinus radiata* biomass an excellent media for mineral prospecting using combined biogeochemistry and hyperspectral methods.

In the case of the natural forest in Reefton, Dunn et al. (2012b), described the primary vegetation to not include any of the pine species. Thus, the pH here is expected to be between 5-6, with a locally higher pH >7 around the mine tailings. Areas around the Waiuta mine tailings and the Prohibition Shaft are affected by significant mining-related contamination. The pH around Waiuta mine tailings is reported to be 7.6 (Haffert and Craw, 2009), and at such levels, elemental uptake is significantly lower. In such a scenario the elemental uptake by the overlying mixed vegetation is expected to be less compared to the HMSZ study site which contains only *Pinus radiata* species. This altogether facilitates a higher relatability between the soil and the plant chemistry in HMSZ (Chapter 3) than at Reefton with higher pH and multi-species habitat (Chapter 5).

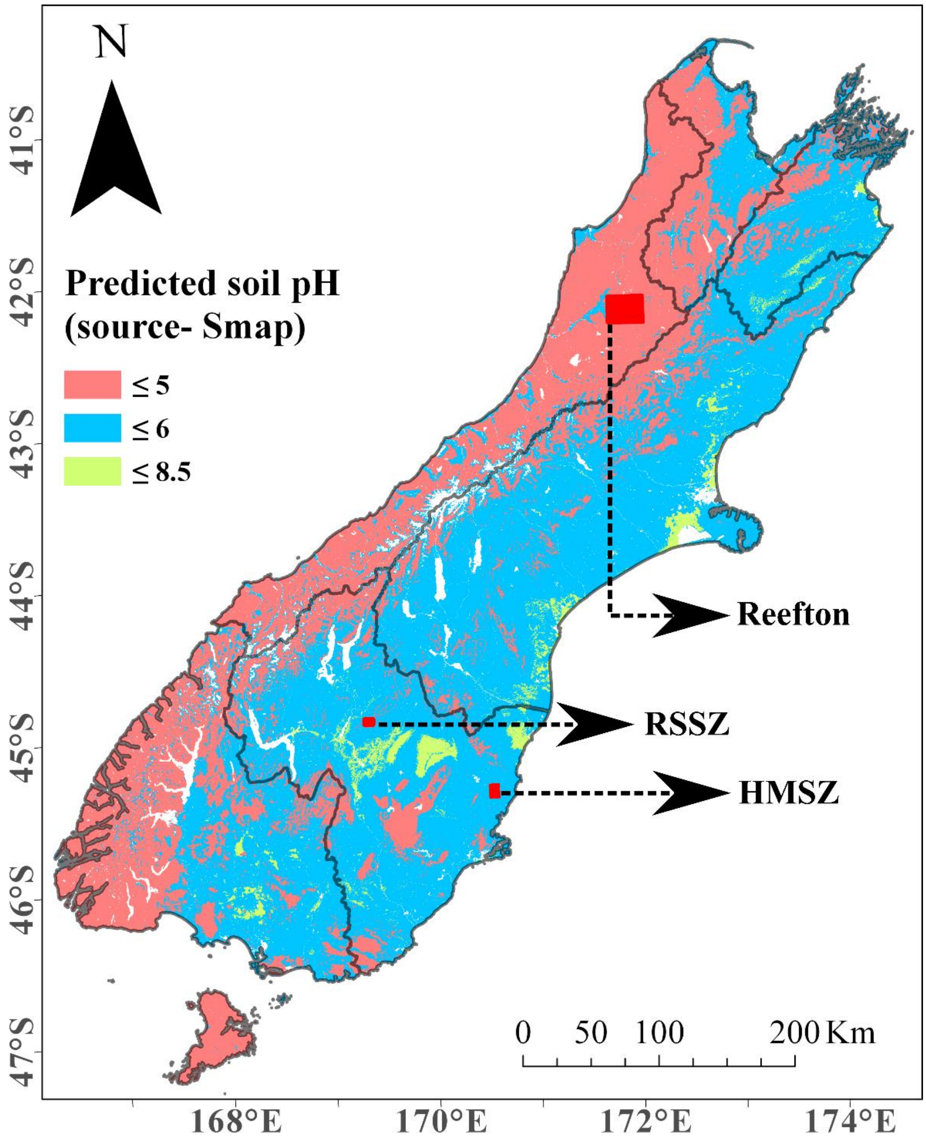

Figure 6.2: Predicted soil pH across South Island at a 100 m spatial resolution adopted from Roudier et al. (2020).

Our study is in good agreement with previous studies which have found a generally good correlation between low pH (~4 which is very acidic in soil pH scale) and success of biogeochemical orientation surveys among other factors (Table 6.1). Acidic soil pH, between 3-5 along with supporting factors such as surface charge, and soil biomass playing an additional role, is associated with a direct correlation to solubility and uptake of elements such as As and Sb by plants, (Table 6.1). The same is observed between the HMSZ and the Reefton study sites, where the pH in HMSZ inside the plantation area is ~4.5 and that of Reefton is between 5-6. The consistent deep root system of the *Pinus radiata* plantation also plays an important role in the magnitude of elemental uptake in the HMSZ study site apart from the acidic soil pH (Figure 6.4). In a more dynamic setting like the geothermal setting of the Taupo Volcanic Zone although the pH is 5.5 around the Champagne Pool with temperatures as high as 250-170°C (Dunn, 2007; Christie, 2016). The uptake of elements like As, Sb and gold in the *Kunzea ericoides* is reported to be quite high, and the high temperatures here facilitate the solubility and hence the uptake of these and metalloids ((Dunn, 2007; Dunn and Christie, 2020) and Rodriguez-Gomez, 2022 unpublished data).

6.1.4 Remote detection of plant response to underlying ore deposits

Neither gold nor any of the main pathfinder elements, such as As and Sb, show any unique absorption feature in the soil/plant spectra in the VNIR-SWIR region which can be directly used to infer their presence or absence. Any statistical prediction model, therefore, associates the elemental concentration with other physico-chemical features apparent in the VNIR-SWIR reflectance spectroscopy. Often such spectral features, such as red-edge shift (Chapter 3), responses related to soil moisture, vegetation cover and surface exposure (Chapter 4) and greenness of plants (Chapter 5), can co-vary with pathfinder elements of interest. Utilising the vegetation cover, and its plant chemistry increases the level of complexity for mineral prospecting in a setting by several orders of magnitude.

Even with the neutral pH and low uptake environments (mining contaminated pH) described here, the Sb concentration in soil is relatively high at the Reefton goldfield on account of the massive stibnite veins, and thus vegetation is likely to uptake Sb from the soil (Figure 6.4). On the other hand, Sb has low mobility in plants (Dunn, 2007), which has been confirmed by Chapter 3, showing high accumulation in bark and stem tissues as compared to the aerial parts which are usually visible to airborne hyperspectral sensors. This can mean that the vegetation stress caused by Sb is not apparent in the leaves and the aerial parts, limiting its remote detection using hyperspectral sensors. This explains why the most common metal stress in the red edge region of the vegetation spectrum is not captured by our models using the airborne sensor at both HMSZ and Reefton (Figure 6.3A). In contrast, the models trained using laboratory-based hyperspectral data of bark samples for Sb exhibited significantly high Gini values in the red edge region of the spectrum (700-800 nm) (Figure 6.3B).

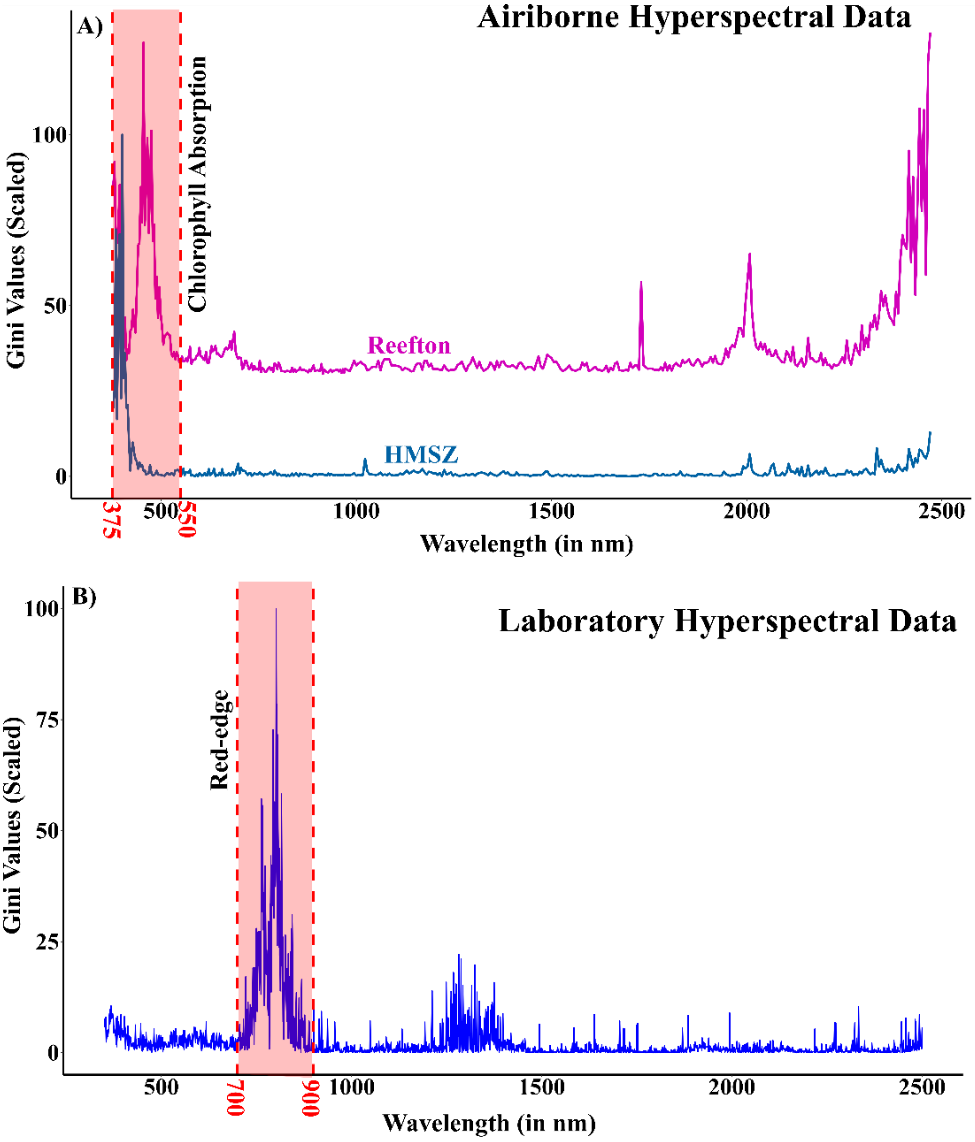

Figure 6.3: Comparison of important bands using Gini impurity values from Random Forest regression models as a function of wavelength. Target variables are Sb while the predictor variables are airborne hyperspectral data (A) and laboratory-based hyperspectral data (B). Note that the pixels of the airborne hyperspectral sensor is mixed (e.g., containing leaves, needle and shadow) while the laboratory hyperspectral data only captured bark.

Table 6.1: Comparison of biogeochemical orientation studies from New Zealand and some selected case studies for gold prospecting. (VHMS- Volcanic-hosted Massive Sulphide deposits)

Reference	Location	Mineralization type	plant species	Sample No.	pH	Remarks
Akçay et al. (1998)	Kanköy deposit, Trabzon, Turkey	Sulphide deposit (Cu, Zn and Pb anomaly)	*Corylus avellana* *Rhododendron luteum*	67	6-7.5	A strong negative correlation for Pb was reported between soil and plant species The orientation failed for Zn and Cu
Timperley et al. (1970) and Timperley (1971)	Riwaka Complex, Nelson, New Zealand	Ni-Cu and PGE	*Nothofagus fusca;* *Nothofagus manziesii;* *Quintinia actufolia;* *Weinmannia racemose*	147	5	Partial success for Cu and Ni but not Zn
Ward and Brooks (1978)	Coromandel Volcanic Zone	Epithermal orogenic gold mineralisation	*Pinus radiata* *Douglas fir*	20	4-5	Successful correlation between gold concentration in plants and soil
Dunn (2007) and Dunn and Christie (2020)	Taupo Volcanic Zone, New Zealand	Epithermal related to active geothermal activity	*Kunzea ericoides*	-	5.5	Uptake here is more correlated to temperature. Along the Champagne Pool with higher temperatures, there is more elemental uptake
Dunn (1986)	Saskatchewan, Canada	Mesothermal Gold, Platinum and Palladium Mineralisation	*Alnus crispa* *Alnus rugosa*	20	5-5.3	Successful Target elements are found more in the bark than leaves and in native form
Dunn et al. (2012b) Chapter 5	Reefton Goldfield, New Zealand	Orogenic mesothermal gold mineralisation	Quintinia, Beech (Red, Black and Silver), Rimu, Ferns (*Blechnum spp*.)	241	5-6	Unsuccessful for most elements
Leavitt and Goodell (1979)	Appalachian Piedmont, Virginia, USA	Sulphide deposits (Analysed for Ag, Cd, Cu, Pb and Zn)	*Lyriodendron tulipifera L.; Cornus florida L.; Quercus alba L.; Vaccinium vacillans Torr.*	17	3.6-4.6	Promising correlation for Zn and Cd. Poor to moderate correlation for Cu, Ag and Pb
Chapter 3	HMSZ, Otago, New	Mesothermal gold	*Pinus radiata*	114	<4.5	Promising correlation for Sb

	Zealand	deposits hosted in lower greenschist rocks				
Cohen et al. (1987)	Hemlo area, Ontario, Canada	Stratabound gold mineralization is characterised by felsic to intermediate volcanics and tuffs. (Analysed for Mo, Sb, Ba, As)	Spruce, alder, balsam fir, birch and mountain maple	~20 samples from each plant part across all the species	7.7-9.6	The results were highly varying across species and seasons with partial success. The highly anomalous gold concentration in samples were supported by high concentrations of associated elements.
Cohen et al. (2021)	Cyprus	VHMS Cu-deposits	*Pinus brutia* *Olea europaea*	114	5-6	Poor correlation for Cu concentration.
Lintern et al. (2013)	Yilgarn Craton, Western Australia	Gold deposits are hosted in Basalt and shale.	Eucalyptus	20 samples each from leaves, bark and twigs	Neutral pH	Consistent and very strong relation among all the plant parts, litter, and soil. Supergene.

6.2 Challenges of a generalised biogeochemical model

6.2.1 Being Unique

Anomalous pathfinder element concentrations can be used to define a proximal mineralisation halo and this is the key to mineral prospecting using biogeochemistry (Ashley and Craw, 2004; Hamisi et al., 2017; Laukamp et al., 2021a). The lateral extent of the proximal mineralisation halo related to orogenic gold mineralisation can vary from place to place. For example, in Yilgarn Craton in Western Australia, it extends over 200 m (Eilu and Groves, 2001), in Mali, West Africa, the characteristic ankerite and the sulphide anomalies extend up to 2 km (Lawrence et al., 2013) while in the Minas Azules in Argentina it lies between 70-100 m (Rodríguez and Bierlein, 2003). The extent of the proximal mineralisation halo in the South Island, New Zealand varies from ~10 to ~100 m. At HMSZ the mineralisation halo extends up to 100 m with As concentrations going as high as 780 µg/g in the soil whereas in the Reefton setting the proximal halo is extended only up to 20 m with As concentrations reaching a maximum of 100 µg/g in the soil (Christie and Brathwaite, 2003; Craw and MacKenzie, 2016; Hamisi et al., 2017; Cudby et al., 2021) (Figure 6.4). Other than the magnitude of pathfinder element concentration defining mineralisation, the halo is also subjected to variation in lithology, surface topography and soil moisture. A combination of all these factors makes every setting unique and eventually poses a major drawback in generalising a remote sensing-based approach for mineral prospecting suitable to all settings.

A highly anomalous mineralised halo like in the HMSZ, overlaid by known accumulators such as *Pinus radiata* makes integration between biogeochemistry and geology more feasible as compared to the Reefton goldfield which is overlaid by multispecies natural forest and has a lower magnitude pathfinder anomaly (Figure 6.4). The deep roots of *Pinus radiata* often reach the soil/rock boundary indicating access to a higher concentration of metals and metalloids (Chapter 3) unlike the multi-species natural forest at Reefton with variable canopy structure and variable access to elements of the bedrock (Chapter 5). This difference in access and uptake can produce contrasting results in the vegetation spectra (Chapter 5).

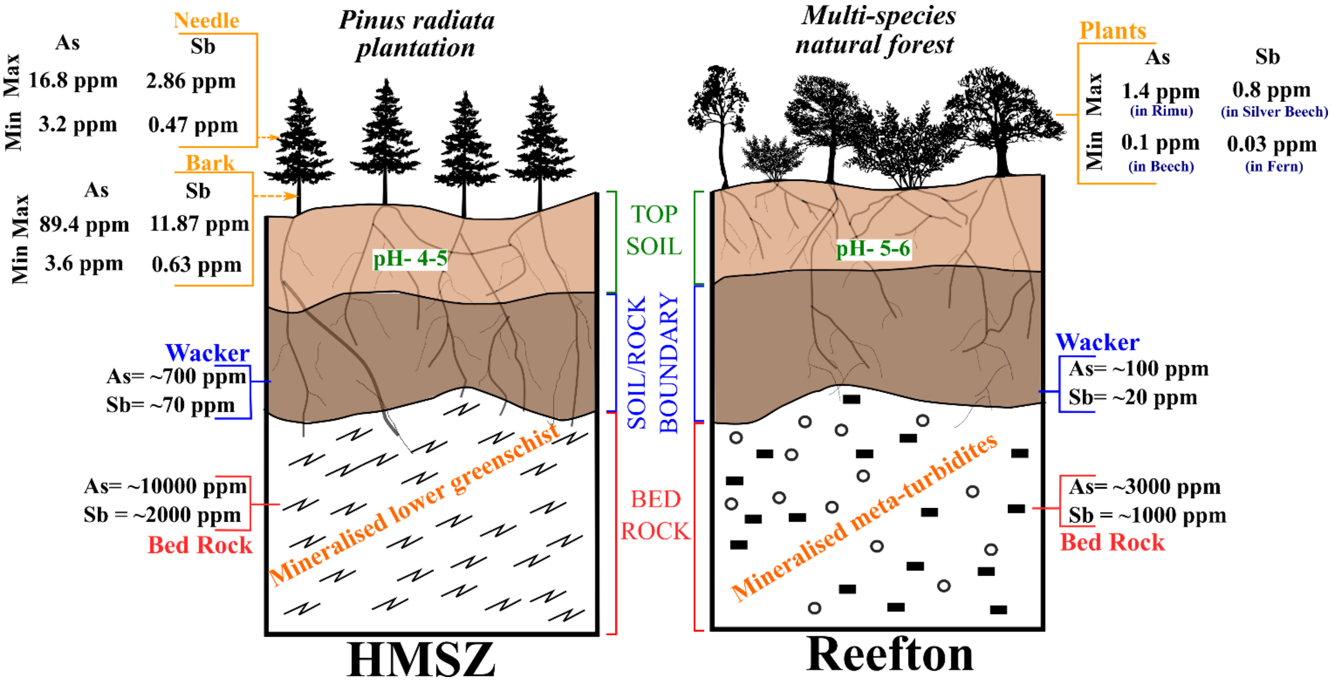

Figure 6.4: Conceptual vertical section comparison between the HMSZ and Reefton setting. The biogeochemical concentrations are based on ground field data from this study for HMSZ and from Dunn et al. (2012b) for Reefton goldfield based on samples collected around the known mineralisation surrounding the Globe progress mine which is to the north of the target area in Reefton. Not to scale.

Element uptake and storage are also species-dependent, adding considerable complexity to any generalised plant response signature. The migration of elements through a plant system occurs, through diffusion, bacterial movements, electrochemical cells and even seismic pumping (Dunn, 2007; Dunn and Christie, 2020). All of these factors are specific to plant species along with local environmental settings (e.g., soil type, climate and soil pH) and can often be specific to an individual plant depending on its age and health (Farago, 2008; Li et al., 2015; Lawley, 2016). Most of the pathfinder elements for mineral prospecting are classified as “non-essential” and/or “toxic” for the plants by Dunn (2007) including As, Sb and gold hence they are eventually discarded by the plants (Timperley, 1971; Dunn, 2007; Dunn and Christie, 2020). The plant’s internal processes aim to move it to the extreme aerial parts, such as the leaves, from where it is removed (Timperley, 1971; Dunn, 2007; Lintern et al., 2013; Dunn and Christie, 2020). Even once the elements are in the plant system, uptake by the roots and distribution into other plant organs is further governed by factors such as the presence of ligands with control on geochemical mobility, bioavailability and ionic size (King, 1984; Dunn, 2007). These biogeochemical factors strongly govern the elemental concentration in the plants and how far the elements can reach and deposits in a plant anatomy accounting for the observed differences in elemental concentration in different organs of the same plant (Brooks, 1973; Brooks, 1979; Kovalevsky, 1987; Dunn, 2007). The unique elemental and plant species behaviour is confirmed for the HMSZ where the performances varied among elements, plant tissues and between the laboratory and the airborne sensor-based models which captures different parts of the plant (Chapter 3).

6.2.2 Impact of hyperspectral data sensitivity on models

The models trained on the laboratory-based hyperspectral data as the predictor variable produced substantially better results than all the airborne hyperspectral-based models (e.g., Chapter 3). As discussed previously throughout this study, the laboratory hyperspectral data has a better signal-to-noise ratio than the airborne or satellite-based hyperspectral data with the least amount of spectral mixing (i.e., smallest sensor footprint). Furthermore, the laboratory captured data is not influenced by atmospheric interferences, nor by band saturation which is mitigated by performing white reference calibration before measuring each sample. All these factors make the models trained on airborne data perform much worse than laboratory-based data. Supporting this argument, the Gini plot for the models using the ASD data further shows contributing bands from the “red” and “red-edge” regions which are altogether known to be associated with chlorophyll absorption and can indicate metal stress (Figure 6.3) (Zuzana et al., 2013; Rathod et al., 2015; Shin et al., 2019; Lhotáková et al., 2021). Whereas the best models using the airborne data rely extensively on the greenness of the vegetation, which can be heavily impacted by heterogenic atmospheric parameters like water absorption, aerosol optical depth and BRDF (Chapter 5).

Chlorophyll absorption in the red and the blue regions of the electromagnetic spectrum (450-675 nm) dominates the spectral reflectance curves for vegetation. Most prediction models in this study show increased importance that coincides with chlorophyll absorption (Figures 6.3 and 6.6). It has been reported that an increase in metal stress decreases chlorophyll content in the canopy (Dunn, 2007; Wu et al., 2008; Dao et al., 2019; Shin et al., 2019; Naik et al., 2021) and this change is likely to be picked up in the models based on airborne hyperspectral data. However, this region of chlorophyll absorption often overlaps with the absorption of other carotenoids (between 400-500 nm), which are responsible for pigmentation in plants (Andersson et al., 1991; Jeevarajan et al., 1996; Sims and Gamon, 2002). Carotenoids are essential structures that help in quenching light and protect the cell from abiotic stress (Wu et al., 2008). It has also been extensively reported that this absorption region tends to face band saturation at low chlorophyll levels and eventually decreases the sensitivity of the high chlorophyll pixels (Sims and Gamon, 2002; Wu et al., 2008). Machine learning models in which the chlorophyll absorption region ends up being the sole contributor compared to the rest of the spectra can face this band saturation problem which leads to challenges in validation and reproducibility (Sims and Gamon, 2002; Wu et al., 2008). Although overall chlorophyll content is a manifestation of metal stress, in a multi-species natural forest, it can be seasonal and simply be a variation among species. Thus, it always needs to be validated by a supporting absorption region such as the "red-edge" or clean and targeted laboratory-based hyperspectral data. The chlorophyll absorption in the red region of the spectrum, followed by the "red-edge" region is the more reliable region in such quantitative model-based analysis. This also indicates that although Sb is good potential as a pathfinder element in soil and plant, the plant part samples for a study, and the part being captured by the hyperspectral sensor, is crucial for the integration of the hyperspectral data.

6.2.3 Adaptive post-processing

Given the unique behaviour of each geological setting (e.g., host mineralogy, gangue minerals, ore type and pathfinder elements) and associated environmental variables (e.g., plant species, soil pH, topography) along with sensing complications (e.g., mixed pixels, FWHM, band saturation) this study has explored some analytical methods that can improve model performance.

6.2.3.1 Data transformation

The most obvious underlying assumption is the input data distribution, which has a significant impact on model performances for all the datasets used in the study. The decision tree-based algorithm, random forest, is known to proficiently handle random non-normal data distribution (Table 2.4), but all chemometric regression and classification methods perform better on normally distributed data (Pullanagari et al., 2016; Varmuza and Filzmoser, 2016). The target variable (i.e., the elemental concentration here) in the training data which was normally distributed in the raw form (in µg/g values) did not exhibit a large variation in model performance on log-based transformation or CLR. On the other hand, in cases where the raw data in µg/g showed a skewed or bimodal distribution, a significant difference in model performance on both log and CLR transformations is demonstrated (Chapters 3 and 5). In the HMSZ study area the chemometric data span over a large range incorporating elemental concentration overlaying a completely non-mineralised host rock (the basalt dome area) to highly mineralised host rock (next to the mineralised shear zone) across ~100 samples with comparatively more data points from the mineralised area. The centring of the CLR transformation here has proven to be the best way to handle such distribution and produced the best regression models (Chapter 3). However, in the Reefton dataset, the range of elemental concentration was not as elaborate and was spread across ~320 data points and the model performance did not change much between the log transformation and CLR (Chapter 5). Furthermore, reversing the CLR data to µg/g is quite challenging due to the data centring which is irreversible to the real µg/g range, in contrast to log transformation. Thus, log transformation should be preferred if absolute µg/g values are desired. If only spatial patterns of high and low concentrations are in question CLR can be used to improve the accuracy of the prediction model.

6.2.3.2 Spatial resolution and spectral mixing effects on data enhancement methods

A 2 m spatial resolution of the hyperspectral image can also include bare ground, tree shadows and/or access roads along with topographic undulations (Figure 3.1). This makes the cumulative spectra of the “vegetation” at a particular pixel highly contaminated (Figures 6.5A and B). Even with comparatively higher levels of accuracy ($R^2 = 0.55$) in the spatial prediction map (Figure 3.13), substantial interference of topography is manifested. On the contrary, the training points in the Reefton study area lie in a natural forest, in which 1 m resolution retains the overall signature of vegetation spectra (Figures 6.5 E and F). However, it still contains highly mixed spectral signatures, containing both variation in species and response to metal stress. The airborne hyperspectral data in the RSSZ region on the other hand has tussock/grass cover, ranging from 20 to 80% which dominates the spectra over the “exposed” soil in a 2 m resolution. These differences across locations call for different processing approaches to extract the targeted information from the unwanted noise. Data enhancement techniques have proven beneficial to tackle the spatial-spectral variability of the data although there still is not one algorithm that would fit all.

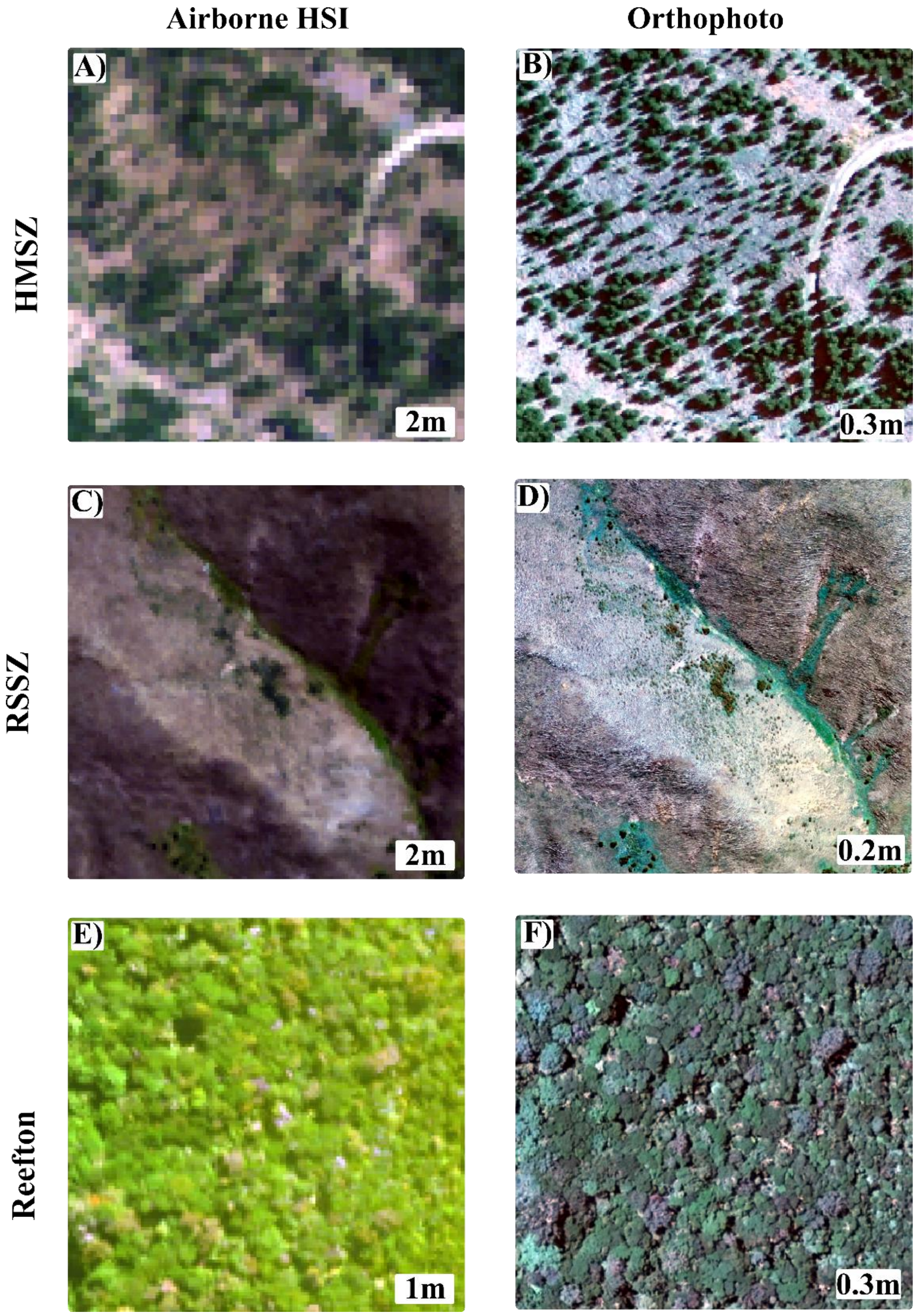

Figure 6.5: Visual comparison of airborne hyperspectral data acquired by AisaFENIX and high-resolution orthophoto of all the three study areas, i.e., HMSZ (A-B), RSSZ (C-D) and Reefton (E-F).

Orthogonal total variation component analysis (OTVCA) which proved to be beneficial for the model performances in the case of RSSZ and the Reefton study areas (Chapters 4 and 5) but does not have the same effect on the models based on the HMSZ area (Chapter 3). OTVCA incorporates spatial information into the transformed data using a user-defined total variation regularisation tuning parameter (λ) (Rasti et al., 2016; Lorenz et al., 2021). This utilises the pixel neighbourhood information to redefine the targeted pixel. In the case of RSSZ and Reefton data this neighbourhood pixel information helps in enhancing the identity of a particular pixel (Figure 6.5 C to F). For example, in RSSZ, there is a strong correlation between the soil moisture and vegetation cover (e.g., plant associations) to the potential As anomalies indirectly vectoring to the gold mineralisation. These factors have inherently impacted the classification results positively. Whereas, HMSZ has discrete tree canopies of the *Pinus radiata* pines with sharp boundaries (Figures 6.5 A and B); consequently, the neighbourhood pixel information does not add relevant information, failing to enhance regression and classification accuracies. Thus, OTVCA transformed hyperspectral data cannot provide good generalisation when the target is surrounded by mixed pixels.

Denoising has also been actively used to improve the performance of regression (Rasti et al., 2013; Shanmugam and Srinivasa Perumal, 2014) and classification problems on hyperspectral data (Rasti et al., 2018; Fu et al., 2019; Rasti et al., 2020; Ghamisi et al., 2021; Rasti et al., 2021). The effect of applying denoising to the hyperspectral data only reflects in the multivariate statistical model performance depending on how much the raw data is originally affected by various sensor-induced noise and background noise (Wang and He, 2011; Rasti et al., 2018). The effect on the model performance further depends on which part of the electromagnetic spectrum is contributing the most to the models. To maintain consistency in comparison, the airborne hyperspectral data captured in the HMSZ was put through the FOSRP denoising algorithm identical to the Reefton dataset. The random forest regression on the earlier reported "better" performing models, using Sb, W and Ag concentration in the *Pinus radiata* bark samples, from the HMSZ dataset were tested using the denoised reflectance (Figure 6.6).

Sensor-induced noise in the SWIR region is much higher in the Reefton dataset compared to the HMSZ dataset. Denoising visually and computationally improves this region to some extent in the Reefton dataset (Figure 5.5), but it continues to drive the regression models significantly with Gini values in the upper 10% of the range (Figure 5.6). Whereas the noise in the SWIR for the HMSZ data is low enough not to override the other important sections of the spectrum. This makes the effect of denoising on the HMSZ data very different from that of the Reefton data, impacting the target variable predictions. On training the models for W and Sb concentration, it is seen that the chlorophyll absorption in the blue section (350-500 nm) is contributing the most to the models (Figures 6.5A and B). The model performances improve (Figure 6.5) from reflectance to denoised reflectance but do not outperform the performance using other enhancement techniques (Figure 3.10).

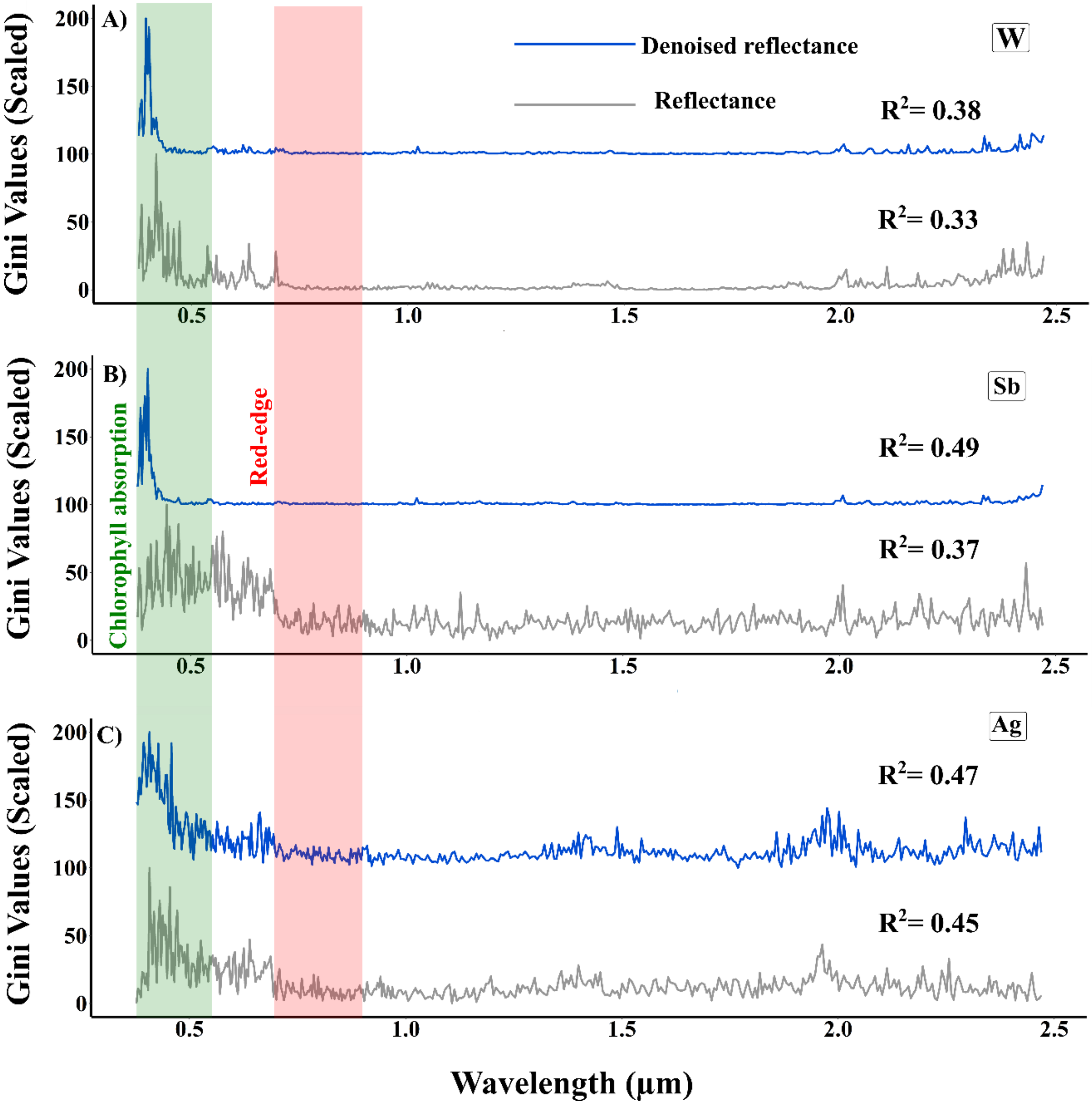

Figure 6.6: Effect of denoising on the HMSZ data for W, Sb and Ag concentrations in the *Pinus radiata* bark samples. Gini values shown in blue are offset by 100 for clarity.

The regression models for all the elements show higher Gini values in the chlorophyll absorption region, indicating maximum contribution to the models (Figure 6.5). In the denoised reflectance-based models, the noise fluctuations across the spectrum diminish and manifests clearer contributing wavelengths facilitating the model performances (Figure 6.5). The Gini values across the spectrum for Sb and W suggest that there are some factors in the chlorophyll absorption region which contribute to the model’s performance more than any other region. Both Sb and W are very closely associated with the gold mineralisation in the HMSZ area (Table 3.1). Ag has consistently shown a strong correlation in the dataset, both in the laboratory hyperspectral data-based Pearson-type correlation analysis (Figure 3.8) and in the PCA of the elemental dataset (Figure 3.9). The enhancement techniques previously improved the Ag-based models up to an R^2 of 0.43 whereas the denoise data increased it to 0.47 (Figure 6.5C). Although the model has comparatively higher Gini values in chlorophyll absorption ranging up to 700 nm it fluctuates across the rest of the spectrum. The model based on RFR has provided consistent performance which means less influenced by sensor noise. These differences in responses across models and settings reinstate that each setting is to be approached differently with a detailed knowledge of the setting and its noise/background elements.

Chapter 7. Conclusion

7.1 Key findings

The main takeaway message from the present study is that setting is key. A multi-disciplinary approach, such as this, for mineral exploration, takes into account parameters in terms of interactions between the physico-chemical environment that covary to form what the current setting exhibits. These interactions and the combination of interactions among all the "layers" are unique to every mineral prospect and eventually, they depend on a combination of factors, including, 1) bedrock chemistry, 2) the chemical associations leading to mineral breakdown, 3) the chemical breakdowns governing soil and groundwater pH, 4) the groundwater interactions with the soil layers and bedrock, 5) soil moisture, 6) surficial processes, such as erosion, weathering and anthropogenic activities 7) surface cover, such as natural forest, plantations and agricultural fields, and 8) vegetation behaviour and responses to the physical and chemical environment among others.

Considering mineral exploration as the main objective, understanding the bedrock geology is crucial as it primarily defines all the layers above it. The targeted mineralisation is characterised by the proximal mineralisation halo which manifests the geochemical anomalies vectoring towards the mineralisation and is the key to mineral prospecting. The extent of the mineralisation halo highly varies ranging from a few meters to a few kilometres depending on the type of mineralisation and the environment. The subtle differences between the mineralisation halo and the background are often manifested in the soil spectra (e.g., presence or absence of specific elements or minerals) and the metal stress in the vegetation spectra (e.g., changes in the chlorophyll absorption and red-edge features). These spectral features are expected to be captured by a hyperspectral image. However, spatial and spectral resolution plays a major role in sensing these subtle spectral differences. For example, if the bandwidth of the hyperspectral data is wider than the targeted absorption feature. Similarly, if the mineralisation halo is less than the spatial resolution of the hyperspectral data, the changes within the mineralisation halo and the background would be at a sub-pixel level making it hard to differentiate without a referenced pure pixel, which is also scarce.

Airborne hyperspectral remote sensing analysis is targeted to the prospect of a particular location and is thus supposed to be designed with a detailed understanding of the information as well as the background/noise. In this study as well, different approaches proved to be suitable for different settings. The relation between the targeted information and the noise/background is an important factor to be considered in setting up the airborne hyperspectral data analysis workflow.

Laboratory-based hyperspectral data is highly centred on the samples with no background or atmospheric influence and rendered the best and the most relevant models. The laboratory-based hyperspectral data is also important to understand and filter specific information captured by airborne hyperspectral data. Thus, remote detection and quantification over biogeochemical signals and surface indicators are feasible but need to be substantially supported by laboratory-based data analysis.

All three sites (HMSZ, RSSZ and Reefton), despite their quite similar geological setting, widely differ in all other soil and surface parameters. All three sites are mesothermal gold mineralisation settings with similar major pathfinder elements defining the geochemical footprint of the proximal mineralisation halo (e.g., As and Sb). However, soil and its interaction with plant behaviour strongly indicate a site-dependent element uptake pattern. To resolve such natural diversity, our study conceptualises mineral prospecting for gold through a combination of biogeochemistry and hyperspectral imaging as a flowchart (Figure 7.1).

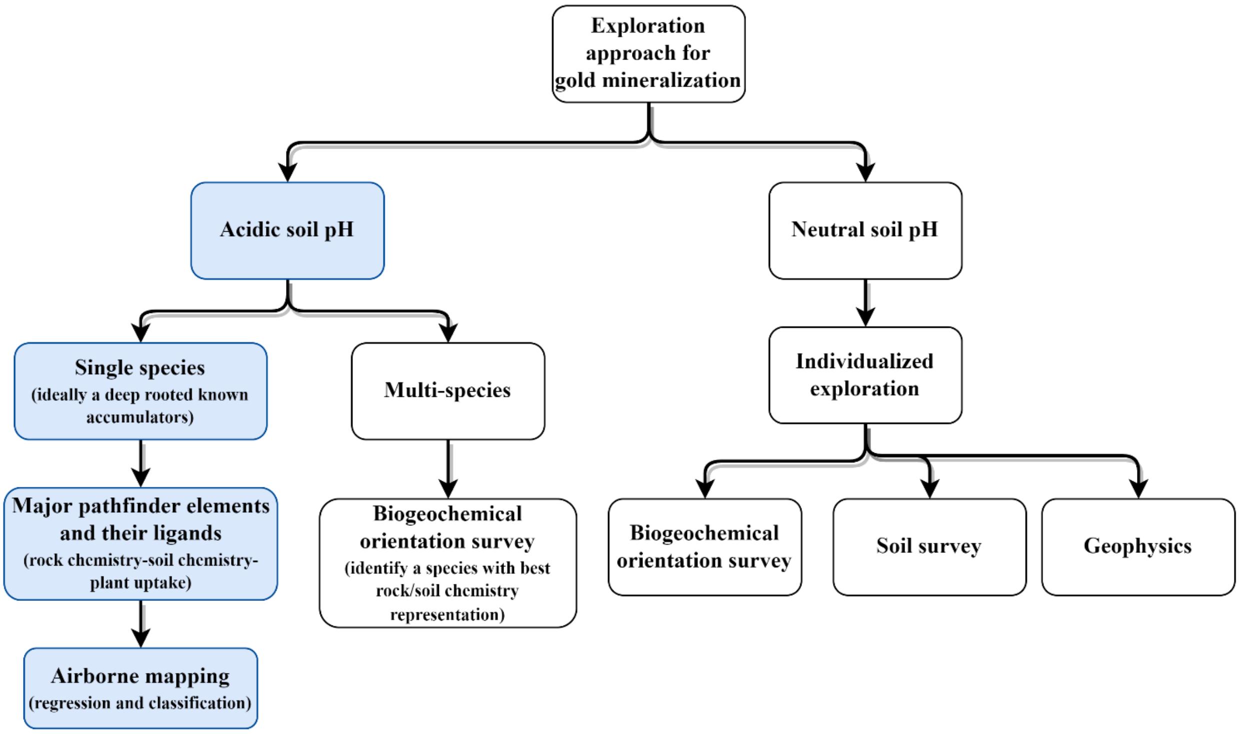

Figure 7.1: Flowchart showing the likely ways to mineral exploration approaches. The flowline marked in blue has proven to be the most ideal in this study.

7.2 Future Work

There are several directions to extend the study for mineral exploration using a multidisciplinary approach. One major leap in this domain would be to use space-borne hyperspectral data, such as PRISMA (Lopinto and Ananasso, 2020; Cogliati et al., 2021) and EnMAP (Chabrillat et al., 2014; Rogge, 2014). The space-borne hyperspectral data is much cheaper and has temporal availability but is limited by coarse spatial resolution. In this study, we analysed the prospect around known mineralisation, which required a finer spatial resolution, but at a broader scale, the mineral system is spatially much bigger (Hagemann et al., 2016; Durance et al., 2018). The larger mineral system can extend across terranes that span hundreds of kilometres which makes the space-borne hyperspectral data a suitable choice for large regional or terrane coverage at a consistent and spatial resolution (currently up to 30 m). The mapped broader region can further be narrowed down using airborne hyperspectral data of a finer spatial resolution to indicate the proximal mineralisation halo vectoring of the targeted ore body.

The limitation of spatial resolution in the case of space-borne hyperspectral data could be handled with various data fusion techniques (on theories like component substitution, multiresolution analysis, spectral unmixing and Bayesian probability) (Liu, 2000; Aiazzi et al., 2007; Bendoumi et al., 2014; Wei et al., 2015), which can potentially enrich such multidisciplinary exploration whilst maintaining the faster and cost-effective nature of the study. Currently, spaceborne multispectral data is available at a spatial resolution of a few meters (e.g., IKONOS- 3.3 m, RapidEye- 5 m and Planet- 3 m). If these datasets could be coupled with the hyperspectral data for spatial/spectral analysis, the machine learning models could pick up more subtle spatial-spectral differences correlating to the mineralisation (Yokoya et al., 2017).

Apart from coupling hyperspectral data with multispectral data, the integration of sensors covering the MWIR and TIR spectral ranges could also potentially improve model accuracies. Many minerals such as quartz, feldspar and pyroxene, are known to have characteristic absorption features in the MWIR and TIR regions (Chukanov, 2016). Clay minerals (e.g., kaolinite), and iron-bearing minerals (e.g., hematite, goethite) show additional absorption features in these spectral ranges (Clark, 1999; Chukanov, 2016; Laukamp et al., 2021a). The additional information that this range provides in identifying hydroxylated silicates, sulphates and carbonates would enrich the information of content and variability and potentially improve the model accuracies (Laukamp et al., 2021a; Laukamp et al., 2021b). On the other hand, adding several in-situ parameters (e.g., soil data parameters), geophysical data (e.g., magnetic or electric) and LiDAR data (e.g., as topography or derived parameters such as vegetation height) could add more effective variables to the machine learning algorithms to better understand the setting, but would also increase the cost of the study.

The future of a multidisciplinary approach to a rather specific problem such as mineral exploration is extensive and ever-evolving. The newer satellite-based platforms such as EnMAP and PRISMA have a much better spectral resolution (EnMAP- 6.5 nm for VNIR and 10 nm for SWIR, PRISMA- <12 nm) with more bands in the SWIR region. This makes them more suitable for such geological and soil studies with better capabilities of mineral identification at a larger scale. This opens a range of opportunities to extend and expand mineral exploration toolkits using hyperspectral remote sensing.

8. References

Abbaszadeh, M., Hezarkhani, A., 2013. Enhancement of hydrothermal alteration zones using the spectral feature fitting method in Rabor area, Kerman, Iran. Arabian Journal of Geosciences 6, 1957-1964.

Abdel-Rahman, E.M., Ahmed, F.B., Ismail, R., 2012. Random forest regression and spectral band selection for estimating sugarcane leaf nitrogen concentration using EO-1 Hyperion hyperspectral data. International Journal of Remote Sensing 34, 712-728.

Abedi, M., Norouzi, G.-H., Bahroudi, A., 2012. Support vector machine for multi-classification of mineral prospectivity areas. Computers & Geosciences 46, 272-283.

Abrams, M.J., Hook, S.J., 2013. NASA’s hyperspectral infrared imager (HyspIRI), Thermal infrared remote sensing. Springer, pp. 117-130.

Abweny, M.S., van Ruitenbeek, F.J., de Smeth, B., Woldai, T., van der Meer, F.D., Cudahy, T., Zegers, T., Blom, J.-K., Thuss, B., 2016. Short-Wavelength Infrared (SWIR) spectroscopy of low-grade metamorphic volcanic rocks of the Pilbara Craton. Journal of African earth sciences 117, 124-134.

Adams, C., Campbell, H., Griffin, W., 2007. Provenance comparisons of Permian to Jurassic tectonostratigraphic terranes in New Zealand: perspectives from detrital zircon age patterns. Geological Magazine 144, 701-729.

Adams, C., Harper, C.T., Laird, M., 1975. K-Ar ages of low grade metasediments of the Greenland and Waiuta Groups in Westland and Buller, New Zealand. New Zealand journal of geology and geophysics 18, 39-48.

Aiazzi, B., Baronti, S., Selva, M., 2007. Improving component substitution pansharpening through multivariate regression of MS $+ $ Pan data. IEEE Transactions on Geoscience and Remote Sensing 45, 3230-3239.

Akçay, M., Lermı, A., Van, A., 1998. Biogeochemical exploration for massive sulphide deposits in areas of dense vegetation: an orientation survey around the Kanköy Deposit (Trabzon, northeastern Turkey). Journal of Geochemical Exploration 63, 173-187.

Allibone, A., Jones, P., Blakemore, H., Craw, D., MacKenzie, D., Moore, J., 2018. Structural Setting of Gold Mineralization within the Hyde-Macraes Shear Zone, Southern New Zealand. Economic Geology 113, 347-375.

Allibone, A., Jones, P., Moore, J., Craw, D., MacKenzie, D., Blakemore, H., 2017. Kilometre-scale structural setting of ore shoots in the Frasers gold deposit, Macraes mine, New Zealand. Ore Geology Reviews 89, 1107-1121.

Amigo, J.M., Santos, C., 2020. Preprocessing of hyperspectral and multispectral images, Data handling in science and technology. Elsevier, pp. 37-53.

Anand, R., Cornelius, M., Phang, C., 2007. Use of vegetation and soil in mineral exploration in areas of transported overburden, Yilgarn Craton, Western Australia: a contribution towards understanding metal transportation processes. Journal of Geochemistry: Exploration, Environment, Analysis 7, 267-288.

Anderson, C.W., Brooks, R.R., Stewart, R.B., Simcock, R., 1998. Harvesting a crop of gold in plants. Nature 395, 553-554.

Anderson, C.W., Brooks, R.R., Stewart, R.B., Simcock, R., 1999. Gold uptake by plants. Gold Bulletin 32, 48-52.

Andersson, P.O., Gillbro, T., Ferguson, L., Cogdell, R.J., 1991. Absorption spectral shifts of carotenoids related to medium polarizability. Photochemistry and photobiology 54, 353-360.

Anke, M., 2005. Arsenic in plants, soils and some foodstuffs. Trace and Ultratrace Elements in Plants and Soil.

Arenas-García, J., Camps-Valls, G., 2007. Feature extraction from remote sensing data using Kernel Orthonormalized PLS, 2007 IEEE International Geoscience and Remote Sensing Symposium. IEEE, pp. 258-261.

Arnon, D.I., Stout, P., 1939. The essentiality of certain elements in minute quantity for plants with special reference to copper. Journal of Plant Physiology 14, 371.

Asadzadeh, S., de Souza Filho, C.R., 2016. A review on spectral processing methods for geological remote sensing. International Journal of Applied Earth Observation and Geoinformation 47, 69-90.

Ashley, P., Craw, D., 1995. Carrick Range Au and Sb mineralisation in Caples Terrane, Otago Schist, Central Otago, New Zealand. New Zealand Journal of Geology 38, 137-149.

Ashley, P., Craw, D., 2004. Structural controls on hydrothermal alteration and gold–antimony mineralisation in the Hillgrove area, NSW, Australia. Mineralium Deposita 39, 223-239.

Ashley, P., Craw, D., Graham, B.P., Chappell, D., 2003. Environmental mobility of antimony around mesothermal stibnite deposits, New South Wales, Australia and southern New Zealand. Journal of Geochemical Exploration 77, 1-14.

Ashton, L.W.R., W.C., 1989. Seasonal variation of gold and arsenic in biogeochemical samples from a disseminated gold deposit in the Northern Cordillera. Journal of Geochemical Exploration 31, 171-184.

Babish, G., 2000. Geostatistics without tears- A practical guide to Geostatictics, Variograms and kriging, 4.60 ed.

Bakker, W., van Ruitenbeek, F., van der Werff, H., 2011. Hyperspectral image mapping by automatic color coding of absorption features.

Banerjee, K., Jain, M.K., Panda, S., Jeyaseelan, A., 2019. Landsat 8 OLI data for identification of hydrothermal alteration zone in Singhbhum Shear Zone using successive band depth difference technique-a new image processing approach. Current Science (00113891) 116.

Bárdossy, A., Samaniego, L., 2002. Fuzzy rule-based classification of remotely sensed imagery. IEEE transactions on geoscience and remote sensing 40, 362-374.

Bates, T., 1989. Copper and nickel mineralisation in the Riwaka Complex, Northwest Nelson. Mineral Deposits of New Zealand, Australasian Institute of Mining and Metallurgy monograph 13, 119-123.

Bech, J., Poschenrieder, C., Llugany, M., Barceló, J., Tume, P., Tobias, F., Barranzuela, J., Vásquez, E., 1997. Arsenic and heavy metal contamination of soil and vegetation around a copper mine in Northern Peru. Journal of the Total Environment 203, 83-91.

Belgiu, M., Drăguţ, L., 2016. Random forest in remote sensing: A review of applications and future directions. ISPRS journal of photogrammetry and remote sensing 114, 24-31.

Bendoumi, M.A., He, M., Mei, S., 2014. Hyperspectral image resolution enhancement using high-resolution multispectral image based on spectral unmixing. IEEE Transactions on Geoscience and Remote Sensing 52, 6574-6583.

Bergeron, M., Hollinger, A., Staenz, K., Maszkiewicz, M., Neville, R.A., Qian, S.-E., Goodenough, D.G., 2008. Hyperspectral environment and resource observer (HERO) mission. Canadian Journal of Remote Sensing 34, S1-S11.

Beyer, S.R., Kyser, K., Kotzer, T.G., Ansdell, K., Quirt, D., 2021. Exploration geochemistry of surficial media over the high-grade McArthur River uranium deposit, Saskatchewan, Canada. The Canadian Mineralogist 59, 913-945.

Bhattacharya, P., Welch, A.H., Stollenwerk, K.G., McLaughlin, M.J., Bundschuh, J., Panaullah, G., 2007. Arsenic in the environment: biology and chemistry. Elsevier, pp. 109-120.

Bhattacharya, S., Kumar, H., Guha, A., Dagar, A.K., Pathak, S., Rani, K., Mondal, S., Kumar, K.V., Farrand, W., Chatterjee, S., Ravi, S., Sharma, A.K., Rajawat, A.S., 2019. Potential of airborne hyperspetral data for geo-exploration over parts of different geological/metallogenic provinces in INdia based on AVIRIS-NG observations. Current Science 116, 1143-1156.

Bierlein, F., Christie, A., Smith, P., 2004. A comparison of orogenic gold mineralisation in central Victoria (AUS), western South Island (NZ) and Nova Scotia (CAN): implications for variations in the endowment of Palaeozoic metamorphic terrains. Ore Geology Reviews 25, 125-168.

Bioucas-Dias, J.M., Plaza, A., Dobigeon, N., Parente, M., Du, Q., Gader, P., Chanussot, J., 2012. Hyperspectral Unmixing Overview: Geometrical, Statistical, and Sparse Regression-Based Approaches. IEEE Journal of Selected Topics in Applied Earth Observations and Remote Sensing 5, 354-379.

Bishop, C.A., Liu, J.G., Mason, P.J., 2011. Hyperspectral remote sensing for mineral exploration in Pulang, Yunnan Province, China. International Journal of Remote Sensing 32, 2409-2426.

Bishop, J.L., 2005. The visible and infrared spectral properties of jarosite and alunite. American Mineralogist 90, 1100-1107.

Blake, F., Grant, K., MacKenzie, D., Scott, J., Craw, D., 2019. Surficial arsenic redistribution above gold-mineralised zones in East Otago, New Zealand. New Zealand Journal of Geology and Geophysics, 1-15.

Boardman, J.W., Kruse, F.A., Green, R.O., 1995. Mapping Target Signatures via Partial Unmixing of AVIRIS Data.

Boesche, N., Rogass, C., Lubitz, C., Brell, M., Herrmann, S., Mielke, C., Tonn, S., Appelt, O., Altenberger, U., Kaufmann, H., 2015. Hyperspectral REE (Rare Earth Element) Mapping of Outcrops—Applications for Neodymium Detection. Remote Sensing 7, 5160-5186.

Booysen, R., Lorenz, S., Thiele, S.T., Fuchsloch, W.C., Marais, T., Nex, P.A., Gloaguen, R., 2022. Accurate hyperspectral imaging of mineralised outcrops: An example from lithium-bearing pegmatites at Uis, Namibia. Remote Sensing of Environment 269, 112790.

Borhani, M., Ghassemian, H., 2015. Kernel multivariate spectral–spatial analysis of hyperspectral data. Journal of Selected Topics in Applied Earth Observations and Remote Sensing 8, 2418-2426.

Boyle, R., Jonasson, I.R., 1973. The geochemistry of arsenic and its use as an indicator element in geochemical prospecting. Journal of Geochemical Exploration 2, 251-296.

Brathwaite, R., Pirajno, F., 1993. Metallogenic map of New Zealand: Monograph 3. Institute of Geological & Nuclear Sciences, Lower Hutt 215.

Breiman, L., 1996. Bagging predictors. Machine learning 24, 123-140.

Breiman, L., 2001. Random forests. Machine learning 45, 5-32.

Briggs, R., Fulton, B., 1990. Volcanism, structure, and petrology of the Whiritoa-Whangamata coastal section, Coromandel Volcanic Zone, New Zealand: facies model evidence for the Tunaiti caldera. New Zealand journal of geology and geophysics 33, 623-633.

Brooks, R., 1973. Biogeochemical parameters and their significance for mineral exploration. Journal of Applied Ecology, 825-836.

Brooks, R., Yates, T., Ogden, J., 1973. Copper in bryophytes from Coppermine Island, hen and chickens group, New Zealand. New Zealand Journal of Botany 11, 443-448.

Brooks, R.R., 1979. Indicator Plants for Mineral Prospecting - A Critique. Journal of Geophysical Research 12, 67-78.

Brunn, A., Fischer, C., Dittmann, C., Richter, R., 2003. Quality Assessment, Atmospheric and geometric correction of airborne hyperspectral Hymap data, Proceedings of the 3rd EARSeL Workshop on Imaging Spectroscopy. Citeseer, pp. 72-81.

Bruno, R., Kasmaeeyazdi, S., Tinti, F., Mandanici, E., Balomenos, E., 2021. Spatial Component Analysis to Improve Mineral Estimation Using Sentinel-2 Band Ratio: Application to a Greek Bauxite Residue. Minerals 11, 549.

Burgess-Conforti, J.R., Moore, P.A., Owens, P.R., Miller, D.M., Ashworth, A.J., Hays, P.D., Evans-White, M.A., Anderson, K.R., 2019. Are soils beneath coniferous tree stands more acidic than soils beneath deciduous tree stands? Environmental Science and Pollution Research 26, 14920-14929.

Butt, C., Lintern, M., Anand, R., 2000. Evolution of regoliths and landscapes in deeply weathered terrain—implications for geochemical exploration. Ore Geology Reviews 16, 167-183.

Cai, D., X.F.He, Han, J.W., 2007. Semi-supervised Learning Literature Survey, in: IEEE (Ed.), International Conference of Computer Vision, pp. 1-7.

Carrere, V., Briottet, X., Jacquemoud, S., Marion, R., Bourguignon, A., Chami, M., Dumont, M., Minghelli-Roman, A., Weber, C., Lefevre-Fonollosa, M.-J., 2013. HYPXIM: a second generation high spatial resolution hyperspectral satellite for dual applications, 2013 5th Workshop on Hyperspectral Image and Signal Processing: Evolution in Remote Sensing (WHISPERS). IEEE, pp. 1-4.

Casado, M., Anawar, H.M., Garcia-Sanchez, A., Santa Regina, I., 2007. Antimony and Arsenic Uptake by Plants in an Abandoned Mining Area. Communications in Soil Science and Plant Analysis 38, 1255-1275.

Cave, B.J., Pitcairn, I.K., Craw, D., Large, R.R., Thompson, J.M., Johnson, S.C., 2016. A metamorphic mineral source for tungsten in the turbidite-hosted orogenic gold deposits of the Otago Schist, New Zealand. Mineralium Deposita 52, 515-537.

Cerra, D., Bieniarz, J., Avbelj, J., Reinartz, P., Mueller, R., EOC, E.O.C., 2011. Spectral Matching through Data Compression. International Archives of the Photogrammetry, Remote Sensing, Spatial Information Sciences 38.

Chabrillat, S., Foerster, S., Steinberg, A., Segl, K., 2014. Prediction of Common Surface Soil Properties Using Airborne and Simulated EnMAP Hyperspectral Images: Impact of Soil Algorithm and Sensor Charactericitic, in: IEEE (Ed.), IGARSS.

Chakraborty, R., Kereszturi, G., Pullanagari, R., Durance, P., Ashraf, S., Anderson, C., 2022. Mineral prospecting from biogeochemical and geological information using hyperspectral remote sensing-Feasibility and challenges. Journal of Geochemical Exploration, 106900.

Chamberlain, C., Poage, M., Craw, D., Reynolds, R., 1999. Topographic development of the Southern Alps recorded by the isotopic composition of authigenic clay minerals, South Island, New Zealand. Chemical Geology 155, 279-294.

Chang, C.-I., 2000. An Information-Theoretic Approach to SpectralVariability, Similarity, and Discrimination for Hyperspectral Image Analysis. IEEE Transactions on Information Theory 46, 1927-1932.

Chang, C.-I., 2007. Hyperspectral data Exploitations. Theory and Applications. Wiley.

Chang, C.-I., 2021. Hyperspectral Target Detection: Hypothesis Testing, Signal-to-Noise Ratio, and Spectral Angle Theories. IEEE Transactions on Geoscience and Remote Sensing 60, 1-23.

Chang, Z., Hedenquist, J.W., White, N.C., Cooke, D.R., Roach, M., Deyell, C.L., Garcia, J., Gemmell, J.B., McKnight, S., Cuison, A.L., 2011. Exploration Tools for Linked Porphyry and Epithermal Deposits:

Example from the Mankayan Intrusion-Centered Cu-Au District, Luzon, Philippines*. Economic Geology 106, 1365-1398.

Chauhan, P.K.P.S., N.; Sinha, Rishitosh K.; Jain, Nirmala.; Murty, S.V.S.;, 2015. Hyperspectral remote sensing of planetary surfaces: an insight into composition of inner planets and samall bodies in the solar system. Current Science 108, 915-924.

Cheng, J.-H., Sun, D.-W., 2016. Partial Least Squares Regression (PLSR) Applied to NIR and HSI Spectral Data Modeling to Predict Chemical Properties of Fish Muscle. Food Engineering Reviews 9, 36-49.

Choe, E., van der Meer, F., van Ruitenbeek, F., van der Werff, H., de Smeth, B., Kim, K.-W., 2008. Mapping of heavy metal pollution in stream sediments using combined geochemistry, field spectroscopy, and hyperspectral remote sensing: A case study of the Rodalquilar mining area, SE Spain. Remote Sensing of Environment 112, 3222-3233.

Christie, A., 2016. Mineral Deposits of New Zealand: Exploration and Research. Australasian Institute of Mining and Metallurgy.

Christie, A., Barker, R.G., Brathwaite, R., 2010. Mineral resource assessment of the West Coast region, New Zealand. GNS Science Lower Hutt, New Zealand.

Christie, A., Corner, N., Bierlein, F.P., Smith, P., Ryan, B., Arne, D., 2000. Disseminated gold in turbidite-hosted gold deposits of Reefton (South Islan, New Zealand, Victoria (Australia) and Nova Scotia (Canada), 2000 New Zealand Minerals & Mining Conference. Publicity Unit, Ministry of Economic Development, pp. 105-117.

Christie, A., Corner, N.G., Bierlein, F.P., Smith, P., Ryan, R.J., Arne, D.C., 2001. Disseminated gold at Reefton, South Isand, New Zealand, compared with similar occurrences in Victoria, Australia and Nova Scotia, Canada. New Zealand Mining 28, 14-24.

Christie, A., Cox, S., Rattenbury, M., Brathwaite, R., Whetter, N., 2006. Orogenic (mesothermal) gold deposits of the Reefton Goldfield, West Coast: review of exploration and geology. Geology and Exploration of New Zealand Mineral Deposits, 255-262.

Christie, A.B., 2019. Introduction to New Zealand hard rock gold deposits and their exploration models. New Zealand Journal of Geology and Geophysics 62, 394-413.

Christie, A.B., Brathwaite, R.L., 2003. Hydrothermal alteration in metasedimentary rock-hosted orogenic gold deposits, Reefton goldfield, South Island, New Zealand. Mineralium Deposita 38, 87-107.

Christie, A.B., Simpson, M.P., Barker, R.G., Brathwaite, R.L., 2019. Exploration for epithermal Au–Ag deposits in New Zealand: history and strategy. New Zealand Journal of Geology and Geophysics 62, 414-441.

Christie, A.B., Simpson, M.P., Brathwaite, R.L., Mauk, J.L., Simmons, S.F., 2007. Epithermal Au-Ag and related deposits of the Hauraki goldfield, Coromandel volcanic zone, New Zealand. Economic Geology 102, 785-816.

Chukanov, N.V.C., Alexandr D., 2016. Infrared Spectroscopy of Minerals and Related Compounds. Springer.

Cindrić, I.J.Z., M.; Starčević, A.; Stingeder,G., 2018. Metals in pine needles: characterisation of bio-indicators depending on species. International Journal for Environmental Science and Technology 16, 4339-4346.

Clark, R.N., 1999. Spectroscopy of Rocks and Minerals and Principles of Spectroscopy, Remote Sensing for the Earth Sciences: Manual of Remote Sensing.

Clark, R.N., King, T.V., Klejwa, M., Swayze, G.A., Vergo, N., 1990. High spectral resolution reflectance spectroscopy of minerals. Journal of Geophysical Research 95.

Clark, R.N., Roush, T.L., 1984. Reflectance spectroscopy: Quantitative analysis techniques for remote sensing applications. Journal of Geophysical Research: Solid Earth 89, 6329-6340.

Clark, R.N., Swayze, G., Boardman, J., Kruse, F., 1993. Comparison of three methods for materials identification and mapping with imaging spectroscopy.

Clark, R.N., Swayze, G.A., Livo, K.E., Kokaly, R.F., Sutley, S.J., Dalton, J.B., McDougal, R.R., Gent, C.A., 2003. Imaging spectroscopy: Earth and planetary remote sensing with the USGS Tetracorder and expert systems. Journal of Geophysical Research: Planets 108.

Cloutier, J., Piercey, S.J., Huntington, J., 2021. Mineralogy, Mineral Chemistry and SWIR Spectral Reflectance of Chlorite and White Mica. Minerals 11, 471.

Cogliati, S., Sarti, F., Chiarantini, L., Cosi, M., Lorusso, R., Lopinto, E., Miglietta, F., Genesio, L., Guanter, L., Damm, A., Pérez-López, S., Scheffler, D., Tagliabue, G., Panigada, C., Rascher, U., Dowling, T.P.F., Giardino, C., Colombo, R., 2021. The PRISMA imaging spectroscopy mission: overview and first performance analysis. Remote Sensing of Environment 262.

Cohen, D.R., Hoffman, E., Nichol, I., 1987. Biogeochemistry: A geochemical method for gold exploration in the Canadian Shield. Journal of Geochemical Exploration 29, 49-73.

Cohen, D.R., Zissimos, A.M., Schifano, J.A., Rutherford, N.F., 2021. Biogeochemical response of Pinus brutia and Olea europaea to lithological variations and Cu mineralisation in Cyprus. Science of The Total Environment 759, 143434.

Cohen, Y., Rotman, S., 2005. Spatial-spectral filtering for the detection of point targets in multi-and hyperspectral data, Algorithms and Technologies for Multispectral, Hyperspectral, and Ultraspectral Imagery XI. International Society for Optics and Photonics, pp. 47-55.

Cooley, T., Anderson, G.P., Felde, G.W., Hoke, M.L., Ratkowski, A.J., Chetwynd, J.H., Gardner, J.A., Adler-Golden, S.M., Matthew, M.W., Berk, A., 2002. FLAASH, a MODTRAN4-based atmospheric correction algorithm, its application and validation, IEEE international geoscience and remote sensing symposium. IEEE, pp. 1414-1418.

Coombs, D., Landis, C., Norris, R., Sinton, J., Borns, D., Craw, D., 1976. The Dun Mountain ophiolite belt, New Zealand, its tectonic setting, constitution, and origin, with special reference to the southern portion. American journal of science 276, 561-603.

Cox, L., Mackenzie, D.J., Craw, D., Norris, R.J., Frew, R., 2006. Structure and geochemistry of the Rise & Shine Shear Zone mesothermal gold system, Otago Schist, New Zealand. New Zealand Journal of Geology and Geophysics 49, 429-442.

Cracknell, M.J., Reading, A.M., 2014. Geological mapping using remote sensing data: A comparison of five machine learning algorithms, their response to variations in the spatial distribution of training data and the use of explicit spatial information. Computers & Geosciences 63, 22-33.

Craw, D., 1994. Contrasting alteration mineralogy at an unconformity beneath auriferous terrestrial sediments, central Otago, New Zealand. Sedimentary Geology 92, 17-30.

Craw, D., 2002. Geochemistry of late metamorphic hydrothermal alteration and graphitisation of host rock, Macraes gold mine, Otago Schist, New Zealand. Chemical Geology 191, 257-275.

Craw, D., 2017. Placer gold and associated supergene mineralogy at Macraes Flat, East Otago, New Zealand. New Zealand Journal of Geology and Geophysics 60, 353-367.

Craw, D., Falconer, D., Youngson, J.H., 2003. Environmental arsenopyrite stability and dissolution: theory, experiment, and field observations. Chemical Geology 199, 71-82.

Craw, D., Lilly, K., 2016. Gold nugget morphology and geochemical environments of nugget formation, southern New Zealand. Ore Geology Reviews 79, 301-315.

Craw, D., MacKenzie, D., 2007. Disseminated gold in ankeritic alteration zones, Rise & Shine and Shotover, Otago Schist.

Craw, D., MacKenzie, D., 2016. Macraes Orogenic Gold Deposit (New Zealand), Origin and Development of a World Class Gold Mine.

Craw, D., MacKenzie, D., Grieve, P., 2015a. Supergene gold mobility in orogenic gold deposits, Otago Schist, New Zealand. New Zealand Journal of Geology and Geophysics 58, 123-136.

Craw, D., MacKenzie, D., Pitcairn, I., Teagle, D., Norris, R., 2007a. Geochemical signatures of mesothermal Au-mineralized late-metamorphic deformation zones, Otago Schist, New Zealand. Journal of Geochemistry: exploration, environment, analysis 7, 225-232.

Craw, D., Mackenzie, D.J., Begbie, M., Norris, R.J., 2005. Late metamorphic structural zones in the Otago Schist: prospective hosts for gold mineralisation, NZ Minerals Conference: Realising New Zealand's mineral potential, pp. 89-97.

Craw, D., Mortensen, J., Mackenzie, D., Pitcairn, I., 2015b. Contrasting geochemistry of orogenic gold deposits in Yukon, Canada and Otago, New Zealand. Journal of Geochemistry: exploration, environment, analysis 15, 150-166.

Craw, D., Norris, R.J., 1991. Metamorphogenic Au-W veins and regional tectonics: Mineralisation throughout the uplift history of the Haast Schist, New Zealand. New Zealand Journal of Geology and Geophysics 34, 373-383.

Craw, D., Rufaut, C., 2017. Geochemical and mineralogical controls on mine tailings rehabilitation and vegetation, Otago Schist, New Zealand. New Zealand Journal of Geology and Geophysics 60, 176-187.

Craw, D., Rufaut, C., Haffert, L., Paterson, L., 2007b. Plant colonization and arsenic uptake on high arsenic mine wastes, New Zealand. Water, air, and soil pollution 179, 351-364.

Craw, D., Upton, P., MacKenzie, D., 2009. Hydrothermal alteration styles in ancient and modern orogenic gold deposits, New Zealand. New Zealand Journal of Geology and Geophysics 52, 11-26.

Craw, D., Windle, S.J., Angus, P.V., 1999. Gold mineralization without quartz veins in a ductile-brittle shear zone, Macraes Mine, Otago Schist, New Zealand. Mineralium Deposita 34, 382-394.

Crippen, R., Blom, R., 1999. Unveiling the lithology of vegetated terrains in remotely sensed imagery.

Crosta, A.P., Moore, J.M., 1989. Geological mapping using Landsat Thematic Mapper imagery in Almeria Province, south-east Spain. International Journal of Remote Sensing 10, 505-514.

Crosta, A.P.a.M., J.M., 1989. Enhancement of LANDSAT Thematic Mapper Imagery for Residual Soil Mapping in SW Minas Gerais State Brazil: A Prospecting Case History in Greenstone Belt Terrain., Thematic Conference on remote Sensing for Exploration geology.

Cudahy, T., Caccetta, M., Thomas, M., Hewson, R., Abrams, M., Kato, M., Kashimura, O., Ninomiya, Y., Yamaguchi, Y., Collings, S., 2016. Satellite-derived mineral mapping and monitoring of weathering, deposition and erosion. Scientific reports 6, 1-12.

Cudahy, T., Jones, M., Thomas, M., Laukamp, C., Caccetta, M., Hewson, R., Rodger, A., Verrall, M., 2008. Next generation mineral mapping: Queensland airborne HyMap and satellite ASTER surveys 2006–2008. Perth, Publicly available report: P2007/364, 152.

Cudby, J., Scott, J.M., Craw, D., Hesson, M., Rufaut, C., 2021. Surficial redistribution of gold and arsenic from the Rise and Shine Shear Zone, Otago, New Zealand. New Zealand Journal of Geology and Geophysics, 1-15.

Cui, S., Ding, R., Zhou, K., 2019. A New Hyperspectral Index for Estimating Copper Content in an Indicative Plant for the Exploration of Copper Deposit. Journal of Plant Growth Regulation 38, 956-965.

Dalm, M., Buxton, M., van Ruitenbeek, F., 2017. Discriminating ore and waste in a porphyry copper deposit using short-wavelength infrared (SWIR) hyperspectral imagery. Minerals engineering 105, 10-18.

Dalton, J.B., Bove, D.J., Mladinich, C.S., Rockwell, B.W., 2004. Identification of spectrally similar materials using the USGS Tetracorder algorithm: The calcite–epidote–chlorite problem. Remote Sensing of Environment 89, 455-466.

Dao, P.D., He, Y., Lu, B., 2019. Maximizing the quantitative utility of airborne hyperspectral imagery for studying plant physiology: An optimal sensor exposure setting procedure and empirical line method for atmospheric correction. International Journal of Applied Earth Observation and Geoinformation 77, 140-150.

Dao, P.D., Mantripragada, K., He, Y., Qureshi, F.Z., 2021. Improving hyperspectral image segmentation by applying inverse noise weighting and outlier removal for optimal scale selection. ISPRS Journal of Photogrammetry and Remote Sensing 171, 348-366.

Dave, C.P., Joshi, R., Srivastava, S.S., 2015. A Survey on Geometric Correction of Satellite Imagery. International Journal of Computer Applications 116, 24-27.

de Caritat, P., Main, P., Grunsky, E., Mann, A., 2017. Recognition of geochemical footprints of mineral systems in the regolith at regional to continental scales. Australian Journal of Earth Sciences 64, 1033-1043.

Debba, P., van Ruitenbeek, F.J.A., van der Meer, F.D., Carranza, E.J.M., Stein, A., 2005. Optimal field sampling for targeting minerals using hyperspectral data. Remote Sensing of Environment 99, 373-386.

Debes, C., Merentitis, A., Heremans, R., Hahn, J., Frangiadakis, N., van Kasteren, T., Liao, W., Bellens, R., Pižurica, A., Gautama, S., 2014. Hyperspectral and LiDAR data fusion: Outcome of the 2013 GRSS data fusion contest. Journal of Selected Topics in Applied Earth Observations and Remote Sensing 7, 2405-2418.

Deckert, H., Ring, U., Mortimer, N., 2002. Tectonic significance of Cretaceous bivergent extensional shear zones in the Torlesse accretionary wedge, central Otago Schist, New Zealand. New Zealand Journal of Geology and Geophysics 45, 537-547.

Demarchi, L., Kania, A., Ciężkowski, W., Piórkowski, H., Oświecimska-Piasko, Z., Chormański, J., 2020. Recursive feature elimination and random forest classification of natura 2000 grasslands in lowland river valleys of poland based on airborne hyperspectral and LiDAR data fusion. Remote Sensing 12, 1842.

Deng, K., Zhao, H., Li, N., Wei, W., 2021. Identification of minerals in hyperspectral imagery based on the attenuation spectral absorption index vector using a multilayer perceptron. Remote Sensing Letters 12, 449-458.

Dierssen, H.M., 2019. Hyperspectral measurements, parameterizations, and atmospheric correction of whitecaps and foam from visible to shortwave infrared for ocean color remote sensing. Frontiers in Earth Science 7, 14.

Dong, X., Yan, B., Gan, F., Li, N., 2019. Progress and prospectives on engineering application of hyperspectral remote sensing for geology and mineral resources, Fifth Symposium on Novel Optoelectronic Detection Technology and Application. SPIE, pp. 754-765.

Doronila, A.I., Maddox, L.E., Reichman, S.M., King, D.J., Kolev, S.D., Woodrow, I.E., 2014. Vegetation response of Australian native grass species redgrass (Bothriochloa macra (Steudel) S.T. Blake) and spider grass (Enteropogon acicularis (Lindl.) Lazarides) in saline and arsenic contaminated gold mine tailings: A glasshouse study. Minerals Engineering 56, 61-69.

Drahota, P., Filippi, M., 2009. Secondary arsenic minerals in the environment: a review. Environ Int 35, 1243-1255.

Druzbicka, J., Craw, D., 2015. Metalloid attenuation from runoff waters at an historic orogenic gold mine, New Zealand. Mine Water and the Environment 34, 417-429.

Ducart, D.F., Crósta, A.P., Filho, C.R.S., Coniglio, J., 2006. Alteration mineralogy at the Cerro La Mina epithermal prospect, Patagonia, Argentina: Field mapping, short-wave infrared spectroscopy, and ASTER images. Economic Geology 101, 981-996.

Dundar, M.M., Landgrebe, D.A., 2004. Toward an Optimal Supervised Classifier for the Analysis of Hyperspectral Data. IEEE Transactions on Geoscience and Remote Sensing 42, 271-277.

Dunn, C., Christie, A., 2020. Tree ferns and tea trees in biogeochemical exploration for epithermal Au and Ag in New Zealand. Geochemistry: Exploration, Environment, Analysis 20, 299-314.

Dunn, C.E., 1986. Biogeochemistry as an aid to exploration for gold, platinum and palladium in the northern forests of Saskatchewan, Canada. Journal of Geochemical Exploration 25, 21-40.

Dunn, C.E., 2007. Biogeochemistry in Mineral Exploration. Handbook of Exploration and Environmental Geochemistry. Elsevier Amsterdam, The Netherlands.

Dunn, C.E., Christie, A., 2014. Biogeochemical orientation survey. Luck at last mine area Coromandel New Zealand, GNS Science report, pp. 1-112.

Dunn, C.E., Christie, A., Waldron, H.M., 2012a. Biogeochemical orientation surveys, Reefton, New Zealand, GNS Science report 2012, pp. 1-60.

Dunn, C.E., Christie, A., Waldron, H.M., 2012b. Biogeochemical Orientation Surveys, Reefton, New Zealand.

Dunn, C.E., Ray, G.E., 1995. A comparison of lithogeochemical and biogeochemical patterns associated with gold mineralization in mountainous terrain of southern British Columbia. Economic Geology 90, 2232-2243.

Durães, N., Bobos, I., Da Silva, E.F., Dekayir, A., 2015. Copper, zinc and lead biogeochemistry in aquatic and land plants from the Iberian Pyrite Belt (Portugal) and north of Morocco mining areas. Journal of Environmental Science Pollution Research 22, 2087-2105.

Durance, P., Hill, M., Turnbull, R., Morgenstern, R., Rattenbury, M., 2018. Nickel and cobalt mineral potential in New Zealand, Proceedings of the 50th annual conference, New Zealand Branch of the Australasian Institute of Mining and Metallurgy.

Durance, P., Jowitt, S., Bush, K., 2014. An assessment of portable X-ray fluorescence spectroscopy in mineral exploration, Kurnalpi Terrane, Eastern Goldfields Superterrane, Western Australia. Applied Earth Science 123, 150-163.

Durance, P.M.J., Christie, A., C;, M., M, C., 2015. The Composition of Disseminated,Gold-bearing Sulfides within the Three-dimensional Framework of Bulk Au, As and Sb in the Globe-Progress Orogenic Gold Deposit, Reefton Goldfield, New Zealand, PACRIM 2015 Congress.

Eggins, S.M., Kinsley, L., Shelley, J., 1998. Deposition and element fractionation processes during atmospheric pressure laser sampling for analysis by ICP-MS. Journal of Applied Surface Sciemce 127, 278-286.

Eilu, P., Groves, D., 2001. Primary alteration and geochemical dispersion haloes of Archaean orogenic gold deposits in the Yilgarn Craton: the pre-weathering scenario. Geochemistry: Exploration, Environment, Analysis 1, 183-200.

Emery, X., Maleki, M., 2019. Geostatistics in the presence of geological boundaries: Application to mineral resources modeling. Ore Geology Reviews 114, 103124.

Fan, H., Li, C., Guo, Y., Kuang, G., Ma, J., 2018. Spatial–spectral total variation regularized low-rank tensor decomposition for hyperspectral image denoising. IEEE Transactions on Geoscience and Remote Sensing 56, 6196-6213.

Farago, M.E., 2008. Plants and the chemical elements: biochemistry, uptake, tolerance and toxicity. John Wiley & Sons.

Farjana, S.H., Huda, N., Mahmud, M.P., Saidur, R., 2019. A review on the impact of mining and mineral processing industries through life cycle assessment. Journal of cleaner production 231, 1200-1217.

Fauvel, M., Tarabalka, Y., Benediktsson, J.A., Chanussot, J., Tilton, J.C., 2012. Advances in spectral-spatial classification of hyperspectral images. Proceedings of the IEEE 101, 652-675.

Feng, R., Wei, C., Tu, S., Ding, Y., Wang, R., Guo, J.J.E., botany, e., 2013. The uptake and detoxification of antimony by plants: a review. Journal of Environmental Experimental Botany 96, 28-34.

Feng, R., Wei, C., Tu, S., Tang, S., Wu, F., 2011. Simultaneous hyperaccumulation of arsenic and antimony in Cretan brake fern: evidence of plant uptake and subcellular distributions. Microchemical Journal 97, 38-43.

Ferwerda, J.G., Skidmore, A.K., 2007. Can nutrient status of four woody plant species be predicted using field spectrometry? ISPRS Journal of Photogrammetry and Remote Sensing 62, 406-414.

Font, R., Del Rio, M., Velez, D., Montoro, R., De Haro, A., 2004. Use of near-infrared spectroscopy for determining the total arsenic content in prostrate amaranth. Sci Total Environ 327, 93-104.

Frassy, F., Dalla Via, G., Maianti, P., Marchesi, A., Nodari, F.R., Gianinetto, M., 2013. Minimum noise fraction transform for improving the classification of airborne hyperspectral data: Two case studies, 2013 5th Workshop on Hyperspectral Image and Signal Processing: Evolution in Remote Sensing (WHISPERS). IEEE, pp. 1-4.

Fred, O., 2018. Hyperspectral Sensor Characteristics: Airborne, Spaceborne, Hand-Held and Truck-Mounted; Integration of Hyperspectral Data with LiDAR, in: Thenkabail, P.S.L., John G.; Huete Alfredo. (Ed.), Fundamentals, Sensor Systems, Spectral Libraries, and Data Mining for Vegetation.

Frommer, J., Voegelin, A., Dittmar, J., Marcus, M.A., Kretzschmar, R., 2011. Biogeochemical processes and arsenic enrichment around rice roots in paddy soil: results from micro-focused X-ray spectroscopy. European Journal of Soil Sciences 62, 305-317.

Frutuoso, R., Lima, A., Teodoro, A.C., 2021. Application of remote sensing data in gold exploration: Targeting hydrothermal alteration using Landsat 8 imagery in northern Portugal. Arabian Journal of Geosciences 14, 1-18.

Fu, P., Meacham-Hensold, K., Guan, K., Bernacchi, C.J.J.F.i.P.S., 2019. Hyperspectral leaf reflectance as proxy for photosynthetic capacities: An ensemble approach based on multiple machine learning algorithms. 10, 730.

Fujino, A., Ueda, N., Saito, K., 2005. A hybrid generative/discriminative approach to semi-supervised classifier design, Proceedings of the National Conference on Artificial Intelligence. Menlo Park, CA; Cambridge, MA; London; AAAI Press; MIT Press; 1999, p. 764.

Gagnon, M.-A., Tremblay, P., Savary, S., Duval, M., Farley, V., Lagueux, P., Guyot, E., Chamberland, M., 2015. Airborne Thermal Infrared Hyperspectral Imaging For Mineral Mapping, !3th International Workshop on Advanced Infrared Technology and Applications, PIsa, Italy.

Gao, B.-C., Goetz, A.F.H., 1990a. Column atmospheric water vapor and vegetation liquid water retrievals from Airborne Imaging Spectrometer data. Journal of Geophysical Research 95.

Gao, B.-C., Goetz, A.F.H., 1990b. Column Atmospheric Water vapour and Vegetation Liquid Water Retrievals From Airborne Imaging Spectrometer Data. Journal of Geophysical Research 95, 3549-3564.

Gao, B.-C., Montes, M.J., Davis, C.O., Goetz, A.F.H., 2009. Atmospheric correction algorithms for hyperspectral remote sensing data of land and ocean. Remote Sensing of Environment 113, S17-S24.

Garcia-Sanchez, A., Alvarez-Ayuso, E., 2003. Arsenic in soils and waters and its relation to geology and mining activities (Salamanca Province, Spain). Journal of Geochemical Exploration 80, 69-79.

Gault-Ringold, M., Adu, T., Stirling, C.H., Frew, R.D., Hunter, K.A., 2012. Anomalous biogeochemical behavior of cadmium in subantarctic surface waters: mechanistic constraints from cadmium isotopes. Earth and Planetary Science Letters 341, 94-103.

Gazley, M.F., Martin, A.P., Turnbull, R.E., Frontin-Rollet, G., Strong, D.T., 2020. Regional patterns in standardised and transformed pathfinder elements in soil related to orogenic-style mineralisation in southern New Zealand. Journal of Geochemical Exploration 217.

Ghamisi, P., Plaza, J., Chen, Y., Li, J., Plaza, A.J., 2017a. Advanced Spectral Classifiers for Hyperspectral Images: A review. IEEE Geoscience and Remote Sensing Magazine 5, 8-32.

Ghamisi, P., Shahi, K.R., Duan, P., Rasti, B., Lorenz, S., Booysen, R., Thiele, S., Contreras, I.C., Kirsch, M., Gloaguen, R., 2021. The Potential of Machine Learning for a More Responsible Sourcing of Critical Raw Materials. IEEE Journal of Selected Topics in Applied Earth Observations and Remote Sensing 14, 8971-8988.

Ghamisi, P., Yokoya, N., Li, J., Liao, W., Liu, S., Plaza, J., Rasti, B., Plaza, A., 2017b. Advances in Hyperspectral Image and Signal Processing: A Comprehensive Overview of the State of the Art. IEEE Geoscience and Remote Sensing Magazine 5, 37-78.

Giddens, K., Parfitt, R., Percival, H., 1997. Comparison of some soil properties under Pinus radiata and improved pasture. New Zealand Journal of Agricultural Research 40, 409-416.

Gislason, P.O., Benediktsson, J.A., Sveinsson, J.R., 2006. Random forests for land cover classification. Pattern recognition letters 27, 294-300.

Goetz, A.F.H., Vane, G., Solomon, J.E., Rock, B.N., 1985. Imaging Spectrometry for Earth Remote Sensing. Science 228, 1147-1153.

Goff, S., Brooks, R., Naidu, S., Coppard, E., 1985. Delineation of potentially auriferous quartz reefs by analysis of the bark of Pinus radiata (Monterey Pine). Journal of Geochemical Exploration 24, 273-280.

Goldberg, S., Glaubig, R., 1988. Anion sorption on a calcareous, montmorillonitic soil-selenium. Soil Science Society of America Journal 52, 954-958.

Goldfarb, R., Baker, T., Dube, B., Groves, D.I., Hart, C.J., Gosselin, P., 2005. Distribution, character and genesis of gold deposits in metamorphic terranes. Society of Economic Geologists.

Gomez, C., Coulouma, G., 2018. Importance of the spatial extent for using soil properties estimated by laboratory VNIR/SWIR spectroscopy: Examples of the clay and calcium carbonate content. Geoderma 330, 244-253.

Gomez, C., Lagacherie, P., Coulouma, G., 2008. Continuum removal versus PLSR method for clay and calcium carbonate content estimation from laboratory and airborne hyperspectral measurements. Geoderma 148, 141-148.

Gray, D., Foster, D., 2004. 40Ar/39Ar thermochronologic constraints on deformation, metamorphism and cooling/exhumation of a Mesozoic accretionary wedge, Otago Schist, New Zealand. Tectonophysics 385, 181-210.

Green, A.A., Berman, M., Switzer, P., Craig, M.D., 1988a. A Transformation for Ordering Multispectral Data in Terms of Image Quality with Implications for Noise Removal. IEEE Transactions on Geoscience and Remote Sensing 26.

Green, A.A., Berman, M., Switzer, P., Craig, M.D., 1988b. A transformation for ordering multispectral data in terms of image quality with implications for noise removal. IEEE Transactions on geoscience and remote sensing 26, 65-74.

Green, E.P., Mumby, P.J., Edwards, A.J., Clark, C.D., 2000. Geometric Correction of Satellite and Airborne Imagery, Remote Sensing Handbook for Tropical Coastal Management. United Nations Educational Scientific and Cultural Organization.

Gregg, P., Stewart, R., Stewart, G., 1990. Determination of a suitable plant growth medium on gold and silver mining waste, Martha Hill, Coromandel Peninsula [New Zealand]. Occasional Report-Fertilizer and Lime Research Centre (New Zealand).

Guyon, I., Elisseeff, A., 2003. An introduction to variable and feature selection. Journal of machine learning research 3, 1157-1182.

Habibi, A., Blyth, B., Andrews, C., 1993. Classification consistency for bandwidth compressed multispectral imagery, Proceedings of 27th Asilomar Conference on Signals, Systems and Computers. IEEE, pp. 1347-1351.

Habibi, A., Samulon, A., 1975. Bandwidth compression of multispectral data, Efficient Transmission of Pictorial Information. SPIE, pp. 23-35.

Haboudane, D., Tremblay, N., Miller, J.R., Vigneault, P., 2008. Remote estimation of crop chlorophyll content using spectral indices derived from hyperspectral data. IEEE Transactions on Geoscience and Remote Sensing 46, 423-437.

Haest, M.C., Thomas; Rodger, Andrew; Laukamp, Carsten; Martens Evelin; Caccetta, Mike;, 2013. Unmixing the effects of vegetation in airborne hyperspectral mineral maps over the Rocklea Dome iron-rich palaeochannel system (Western Australia). Remote Sensing of Environment 129, 17-31.

Haffert, L., Craw, D., 2009. Field quantification and characterisation of extreme arsenic concentrations at a historic mine processing site, Waiuta, New Zealand. New Zealand Journal of Geology and Geophysics 52, 261-272.

Hagemann, S.G., Lisitsin, V., Huston, D., 2016. Mineral system analysis: Quo vadis. Ore Geology Reviews 76, 504-522.

Hall, G., Pelchat, J.-C., Dunn, C., 1990. The determination of Au, Pd and Pt in ashed vegetation by ICP-mass spectrometry and graphite furnace atomic absorption spectrometry. Journal of Geochemical Exploration 37, 1-23.

Hamisi, J., 2016. Defining The Geochemical Footprint For Gold Mineralisation Around Birthday Reef. Reefton Goldfield, New Zealand.

Hamisi, J., MacKenzie, D., Pitcairn, I., Blakemore, H., Zack, T., Craw, D., 2017. Hydrothermal footprint of the Birthday Reef, Reefton goldfield, New Zealand. New Zealand Journal of Geology and Geophysics 60, 59-72.

Han, H., Guo, X., Yu, H., 2016. Variable selection using mean decrease accuracy and mean decrease gini based on random forest, 2016 7th ieee international conference on software engineering and service science (icsess). IEEE, pp. 219-224.

He, L., Li, J., Liu, C., Li, S., 2017. Recent advances on spectral–spatial hyperspectral image classification: An overview and new guidelines. IEEE Transactions on Geoscience and Remote Sensing 56, 1579-1597.

Hedenquist, J.W., Arribas, A., 2021. Exploration Implications of Multiple Formation Environments of Advanced Argillic Minerals. Economic Geology.

Hengl, T., Nussbaum, M., Wright, M., Heuvelink, G., Gräler, B., 2018. Random forest as a generic framework for predictive modeling of spatial and spatio-temporal variables, PeerJ, 6, e5518.

Henne, A., Craw, D., 2012. Synmetamorphic carbon mobility and graphite enrichment in metaturbidites as a precursor to orogenic gold mineralisation, Otago Schist, New Zealand. Mineralium Deposita 47, 781-797.

Hewlett, L., Craw, D., Black, A., 2005. Comparison of arsenic and trace metal contents of discharges from adjacent coal and gold mines, Reefton, New Zealand. Marine and Freshwater Research 56, 983-995.

Hu, S., Evans, K., Craw, D., Rempel, K., Bourdet, J., Dick, J., Grice, K., 2015. Raman characterization of carbonaceous material in the Macraes orogenic gold deposit and metasedimentary host rocks, New Zealand. 70, 80-95.

Hubbert, M.K., 1934. Results of earth resistivity survey on various geologic structures in Illinois. Transactions of AIME 110.

Huber, S., Kneubühler, M., Psomas, A., Itten, K., Zimmermann, N.E., 2008. Estimating foliar biochemistry from hyperspectral data in mixed forest canopy. Journal of Forest Ecology Management 256, 491-501.

Huesca, M., García, M., Roth, K.L., Casas, A., Ustin, S.L., 2016. Canopy structural attributes derived from AVIRIS imaging spectroscopy data in a mixed broadleaf/conifer forest. Remote Sensing of Environment 182, 208-226.

Hunt, G.R., 1982. Spectroscopic Properties of Rocks and Minerals, Handbook of Physical Properties of Rocks.

Hyvärinen, A., Karhunen, J., Oja, E., 2001. Independent component analysis. john willey & sons. Inc. New York.

Imran, M., Ahmad, S., Sattar, A., Tariq, A., 2022. Mapping sequences and mineral deposits in poorly exposed lithologies of inaccessible regions in Azad Jammu and Kashmir using SVM with ASTER satellite data. Arabian Journal of Geosciences 15, 1-13.

Itten, K.I., Meyer, P., 1993. Geometric and Radiometric Correction of TM Data of Mountainous Forested Areas. IEEE Transactions on Geoscience and Remote Sensing 31.

Jain, R., Sharma, R.U., 2018. Mapping of mineral zones using the spectral feature fitting method in Jahazpur belt, Rajasthan, India. Int. Res. J. Eng. Technol.(IRJET) 5, 562-567.

Jasiak, I., Wiklund, J., Leclerc, E., Telford, J., Couture, R., Venkiteswaran, J., Hall, R., Wolfe, B., 2021. Evaluating spatiotemporal patterns of arsenic, antimony, and lead deposition from legacy gold mine emissions using lake sediment records. Applied Geochemistry, 105053.

Jeevarajan, J., Wei, C., Jeevarajan, A., Kispert, L., 1996. Optical absorption spectra of dications of carotenoids. The Journal of Physical Chemistry 100, 5637-5641.

Jenny, H., 1994. Factors of soil formation: a system of quantitative pedology. Courier Corporation.

Jensen, J.R., 1996. Introductory digital image processing: a remote sensing perspective. Prentice-Hall Inc.

Jensen, J.R., Olson, G., Schill, S.R., Porter, D.E., Morris, J., 2002. Remote sensing of biomass, leaf-area-index, and chlorophyll a and b content in the ACE Basin National Estuarine Research Reserve using sub-meter digital camera imagery. Geocarto International 17, 27-36.

Jeong, Y., Yu, J., Wang, L., Lee, K.-J., 2021. Bulk scanning method of a heavy metal concentration in tailings of a gold mine using SWIR hyperspectral imaging system. International Journal of Applied Earth Observation and Geoinformation 102, 102382.

Jiang, G., Zhou, K., Wang, J., Cui, S., Zhou, S., Tang, C., 2019. Identification of iron-bearing minerals based on HySpex hyperspectral remote sensing data. Journal of Applied Remote Sensing 13, 047501.

Jiao, H., Zhong, Y., Zhang, L., 2012. Artificial DNA computing-based spectral encoding and matching algorithm for hyperspectral remote sensing data. IEEE Transactions on Geoscience and Remote Sensing 50, 4085-4104.

Jinkai, Z., Rivard, B., Sanchez-Azofeifa, A., 2004. Derivative spectral unmixing of hyperspectral data applied to mixtures of lichen and rock. IEEE Transactions on Geoscience and Remote Sensing 42, 1934-1940.

Jolliffe, I.T., 1986. Principal components in regression analysis, Principal component analysis. Springer, pp. 129-155.

Joseph, W., 1994. Automated spectral analysis: A geologic example using AVIRIS data, north Grapevine Mountains, Nevada, Proc. Tenth Thematic Conference on Geologic Remote Sensing, Environmental Research Institute of Michigan, pp. 1407-1418.

Jowitt, S.M., Werner, T.T., Weng, Z., Mudd, G.M., 2018. Recycling of the rare earth elements. Current Opinion in Green and Sustainable Chemistry 13, 1-7.

Kalacska, M., Sanchez-Azofeifa, G.A., Rivard, B., Caelli, T., White, H.P., Calvo-Alvarado, J.C., 2007. Ecological fingerprinting of ecosystem succession: Estimating secondary tropical dry forest structure and diversity using imaging spectroscopy. Journal of Remote Sensing of Environment 108, 82-96.

Kamenev, A., Pashchenko, F., Pashchenko, A., 2017. Neural-fuzzy model for gold minerals detection, 2017 IEEE 11th International Conference on Application of Information and Communication Technologies (AICT). IEEE, pp. 1-5.

Karatzoglou, A., Meyer, D., Hornik, K., 2006. Support vector machines in R. Journal of statistical software 15, 1-28.

Kaufmann, H., Segl, K., Guanter, L., Hofer, S., Foerster, K.-P., Stuffler, T., Mueller, A., Richter, R., Bach, H., Hostert, P., 2008. Environmental mapping and analysis program (EnMAP)-Recent advances and status, IGARSS 2008-2008 IEEE International Geoscience and Remote Sensing Symposium. IEEE, pp. IV-109-IV-112.

Kaur, P., Bhattacharya, S., Chauhan, P., Kumar, A.K., 2013. Mineralogy of Mare Serenitatis on the near side of the Moon based on Chandrayaan-1 Moon Mineralogy Mapper (M3) observations. Icarus 222, 137-148.

Kereszturi, G., Schaefer, L., Mead, S., Miller, C., Procter, J., Kennedy, B., 2021. Synthesis of hydrothermal alteration, rock mechanics and geophysical mapping to constrain failure and debris avalanche hazards at Mt. Ruapehu (New Zealand). New Zealand Journal of Geology and Geophysics, 1-22.

Kereszturi, G., Schaefer, L.N., Miller, C., Mead, S., 2020. Hydrothermal Alteration on Composite Volcanoes–Mineralogy, Hyperspectral Imaging and Aeromagnetic Study of Mt Ruapehu, New Zealand. Geochemistry, Geophysics, Geosystems, e2020GC009270.

Kereszturi, G., Schaefer, L.N., Schleiffarth, W.K., Procter, J., Pullanagari, R.R., Mead, S., Kennedy, B., 2018. Integrating airborne hyperspectral imagery and LiDAR for volcano mapping and monitoring through image classification. International Journal of Applied Earth Observation and Geoinformation 73, 323-339.

Khaleghi, M., Ranjbar, H., Shahabpour, J., Honarmand, M., 2014. Spectral angle mapping, spectral information divergence, and principal component analysis of the ASTER SWIR data for exploration of porphyry copper mineralization in the Sarduiyeh area, Kerman province, Iran. Applied Geomatics 6, 49-58.

Khalili, R., Anvari, S., Honarmand, M., 2015. Combination Of Biochemical And Hyperspectral Remote Sensing Methods For Detection Of Heavy Metal Pollutions In Eucalyptus Leaves (Case Study: The City Of Bam). Internal Archives of the Photogrammetry, Remote Sensinig Spatial Information Sciences 40.

King, H.D.C., Gary C.; Shacklette, Hansford T.;, 1984. Metal Uptake by Young Conifer Trees, in: USGS (Ed.), USUS Bulletin.

King, T.V., Clark, R.N., 1989. Spectral characteristics of chlorites and Mg-serpentines using high-resolution reflectance spectroscopy. Journal of Geophysical Research: Solid Earth 94, 13997-14008.

Kopačková, V., 2014. Using multiple spectral feature analysis for quantitative pH mapping in a mining environment. International Journal of Applied Earth Observation and Geoinformation 28, 28-42.

Korshunova, V.A., Charykova, M.V., 2019. Mobile forms of gold and pathfinder elements in surface sediments at the Novye Peski gold deposit and in the Piilola prospecting area (Karelia region). Minerals 9, 34.

Kovalev, K.R., Kalinin, Y.A., Naumov, E.A., Kolesnikova, M.K., Korolyuk, V.N., 2011. Gold-bearing arsenopyrite in eastern Kazakhstan gold-sulfide deposits. Russian geology and Geophysics 52, 178-192.

Kovalevskii, A., 1969. Some observations in biogeochemical parameters. Trudy Buryat Inst Estest Venn Nauk 2, 195-214.

Kovalevsky, A.L., 1987. Biogeochemical exploration for mineral deposits. VSP.

Kratt, C., Calvin, W., Coolbaugh, M., 2006. Geothermal exploration with Hymap hyperspectral data at Brady–Desert Peak, Nevada. Journal of Remote Sensing of Environment 104, 313-324.

Krausmann, F., Lauk, C., Haas, W., Wiedenhofer, D., 2018. From resource extraction to outflows of wastes and emissions: The socioeconomic metabolism of the global economy, 1900–2015. Global Environmental Change 52, 131-140.

Kriesel, J.M., Gat, N., Bernacki, B.E., Erikson, R.L., Cannon, B.D., Myers, T.L., Bledt, C.M., Harrington, J.A., 2011. Hollow core fiber optics for mid-wave and long-wave infrared spectroscopy, Chemical, Biological, Radiological, Nuclear, and Explosives (CBRNE) Sensing XII. International Society for Optics and Photonics, p. 80180V.

Kruse, F.A., 1998. Advances in Hyperspectral Remote Sensing for Geologic Mapping and Exploration.

Kruse, F.A., 2007. Identification and mapping of minerals in drill core using hyperspectral image analysis of infrared reflectance spectra. International Journal of Remote Sensing 17, 1623-1632.

Kruse, F.A., 2015. Integrated visible and near-infrared, shortwave infrared, and longwave infrared full-range hyperspectral data analysis for geologic mapping. Journal of Applied Remote Sensing 9, 096005.

Kruse, F.A., Bedell, R.L., Taranik, J.V., Peppin, W.A., Weatherbee, O., Calvin, W.M., 2012. Mapping alteration minerals at prospect, outcrop and drill core scales using imaging spectrometry. International Journal of Remote Sensing 33, 1780-1798.

Kruse, F.A., Boardman, J.W., Huntington, J.F., 2003. Comparison of airborne hyperspectral data and eo-1 hyperion for mineral mapping. IEEE Transactions on Geoscience and Remote Sensing 41, 1388-1400.

Kruse, F.A., Lefkoff, A.B., Boardman, J.W., Heidebrecht, K.B., Shapiro, A.T., Barloon, P.J., Goetz, A.F.H., 1993. The Spectral Image Processing System (SIPS) Interactive Visualization and Analysis of Imaging Spectrometer Data. Remote Sensing Environment.

Krzesińska, A.M., Bultel, B., Loizeau, D., Craw, D., April, R., Poulet, F., Werner, S.C., 2021. Mineralogical and Spectral (Near-Infrared) Characterization of Fe-Rich Vermiculite-Bearing Terrestrial Deposits and Constraints for Mineralogy of Oxia Planum, ExoMars 2022 Landing Site. Astrobiology 21, 997-1016.

Kuo, B.-C., Landgrebe, D.A., 2004. Nonparametric weighted feature extraction for classification. IEEE Transactions on Geoscience and Remote Sensing 42, 1096-1105.

Kursa, M.B., Jankowski, A., Rudnicki, W.R., 2010. Boruta–a system for feature selection. Fundamenta Informaticae 101, 271-285.

Kusuma, K., Sebastian, N., Murty, S., 2012. Geochemical and mineralogical analysis of Gruithuisen region on Moon using M3 and DIVINER images. Planetary and Space Science 67, 46-56.

Laird, M., Shelley, D., 1974. Sedimentation and early tectonic history of the Greenland Group, Reefton, New Zealand. New Zealand journal of geology and geophysics 17, 839-854.

Lakin, H.W., Curtin, G.C., Hubert, A.E., 1974. Geochemistry of Gold in the Weathering Cycle: A Study of the Solubilization of Gold by the Formation of Chloride, Bromide, Iodide, Thiosulfate, Thiocyanide, and Cyanide Gold Complexes and Related Topics. US Government Printing Office.

Large, R., Thomas, H., Craw, D., Henne, A., Henderson, S., 2012. Diagenetic pyrite as a source for metals in orogenic gold deposits, Otago Schist, New Zealand. New Zealand Journal of Geology and Geophysics 55, 137-149.

Laukamp, C., LeGras, M., Lau, I.C., 2021a. Hyperspectral Proximal Sensing Instruments and Their Applications for Exploration through Cover. Portable Spectroscopy and Spectrometry, 401-422.

Laukamp, C., Rodger, A., LeGras, M., Lampinen, H., Lau, I.C., Pejcic, B., Stromberg, J., Francis, N., Ramanaidou, E., 2021b. Mineral physicochemistry underlying feature-based extraction of mineral abundance and composition from shortwave, mid and thermal infrared reflectance spectra. Minerals 11, 347.

Lawley, V.L., M.; Clarke, K.; Ostendorf, B., 2016. Site-based and remote sensing methods for monitoring indicators of vegetation condition An Australian review. Ecological Indicators 60, 1273-1283.

Lawrence, D.M., Treloar, P.J., Rankin, A.H., Harbidge, P., Holliday, J., 2013. The geology and mineralogy of the Loulo mining district, Mali, West Africa: Evidence for two distinct styles of orogenic gold mineralization. Economic Geology 108, 199-227.

Leach, T., Corbett, G., Magner, P., McKenzie, M., 1997. A geological model for gold mineralisation at Reefton, New Zealand, The 1997 New Zealand Minerals and Mining Conference, Crown Minerals, Ministry of Commerce, pp. 159-165.

Leavitt, S.W., Goodell, H.G., 1979. Evaluation of biogeochemical prospecting methods in the search for sulfide deposits in the Appalachian Piedmont, Virginia, USA. Journal of Geochemical Exploration 11, 89-100.

Lee, C.M., Cable, M.L., Hook, S.J., Green, R.O., Ustin, S.L., Mandl, D.J., Middleton, E.M., 2015. An introduction to the NASA Hyperspectral InfraRed Imager (HyspIRI) mission and preparatory activities. Remote Sensing of Environment 167, 6-19.

Leifer, I., Tratt, D.M., Realmuto, V.J., Gerilowski, K., Burrows, J.P., 2012. Remote sensing atmospheric trace gases with infrared imaging spectroscopy. Eos, Transactions American Geophysical Union 93, 525-525.

Lever, J., Krzywinski, M., Altman, N., 2017. Principal component analysis. Nature Methods 14, 641-642.

Lhotáková, Z., Kopačková-Strnadová, V., Oulehle, F., Homolová, L., Neuwirthová, E., Švik, M., Janoutová, R., Albrechtová, J., 2021. Foliage Biophysical Trait Prediction from Laboratory Spectra in Norway Spruce Is More Affected by Needle Age Than by Site Soil Conditions. Remote Sensing 13, 391.

Li, C., Du, D., Gan, Y., Ji, S., Wang, L., Chang, M., Liu, J., 2022. Foliar dust as a reliable environmental monitor of heavy metal pollution in comparison to plant leaves and soil in urban areas. Chemosphere 287, 132341.

Li, H., Lee, W.S., Wang, K., Ehsani, R., Yang, C., 2014. 'Extended spectral angle mapping (ESAM)'for citrus greening disease detection using airborne hyperspectral imaging. Journal of Precision Agriculture 15, 162-183.

Li, J., Hitch, M., Power, I.M., Pan, Y., 2018. Integrated mineral carbonation of ultramafic mine deposits—A review. Minerals 8, 147.

Li, X., Liu, X., Liu, M., Wang, C., Xia, X., 2015. A hyperspectral index sensitive to subtle changes in the canopy chlorophyll content under arsenic stress. International Journal of Applied Earth Observation and Geoinformation 36, 41-53.

Liang, T., Zhang, S., Wang, L., Kung, H.-T., Wang, Y., Hu, A., Ding, S., 2005. Environmental biogeochemical behaviors of rare earth elements in soil–plant systems. Journal of Environmental Geochemistry and Health 27, 301-311.

Liao, W., Dalla Mura, M., Chanussot, J., Pižurica, A., 2015. Fusion of spectral and spatial information for classification of hyperspectral remote-sensed imagery by local graph. Journal of Selected Topics in Applied Earth Observations and Remote Sensing 9, 583-594.

Licciardi, G.A., Del Frate, F., 2011. Pixel unmixing in hyperspectral data by means of neural networks. IEEE transactions on Geoscience and remote sensing 49, 4163-4172.

Lillesand, T., Kiefer, R.W., Chipman, J., 2015. Remote sensing and image interpretation. John Wiley & Sons.

Lintern, M., Anand, R., Ryan, C., Paterson, D., 2013. Natural gold particles in Eucalyptus leaves and their relevance to exploration for buried gold deposits. Nature Communications 4, 2614.

Lintern, M.J., Ibrahimi, T., Pinchand, T., Cornelius, A., 2017. NW Biogeochemistry and Beyond Project, in: CSIRO (Ed.). Geological Survey of Western Australia.

Little, T.A., Mortimer, N., McWilliams, M., 1999. An episodic Cretaceous cooling model for the Otago-Marlborough Schist, New Zealand, based on 40Ar/39Ar white mica ages. New Zealand Journal of Geology and Geophysics 42, 305-325.

Liu, C., Frazier, P., Kumar, L., 2007. Comparative assessment of the measures of thematic classification accuracy. Remote sensing of environment 107, 606-616.

Liu, H., Wu, K., Xu, H., Xu, Y., 2021. Lithology classification using TASI thermal infrared hyperspectral data with convolutional neural networks. Remote Sensing 13, 3117.

Liu, J., 2000. Smoothing filter-based intensity modulation: A spectral preserve image fusion technique for improving spatial details. International Journal of Remote Sensing 21, 3461-3472.

Liu, S., Gu, G., 2017. Improving the impervious surface estimation from hyperspectral images using a spectral-spatial feature sparse representation and post-processing approach. Remote Sensing 9, 456.

Liu, X., Bourennane, S., Fossati, C., 2011. Nonwhite noise reduction in hyperspectral images. IEEE Geoscience and Remote Sensing Letters 9, 368-372.

Lombi, E., Nolan, A., 2004. Metal and arsenic bioavailability and uptake by hyperaccumulator plants. Wit Press.

Lopinto, E., Ananasso, C., 2020. The Prisma hyperspectral mission, Proceedings of the 33rd EARSeL Symposium, Towards Horizon.

Lorenz, S., Ghamisi, P., Kirsch, M., Jackisch, R., Rasti, B., Gloaguen, R., 2021. Feature extraction for hyperspectral mineral domain mapping: A test of conventional and innovative methods. Remote Sensing of Environment 252, 112129.

Lotfollahi, M., Tran, N., Berisha, S., Gajjela, C., Han, Z., Mayerich, D., Reddy, R., 2020. Adaptive Compressive Sampling for Mid-infrared Spectroscopic Imaging. arXiv preprint arXiv:2008.00566.

Loughlin, W., 1991a. Principal component analysis for alteration mapping. Photogrammetric Engineering and Remote Sensing 57, 1163-1169.

Loughlin, W.P., 1991b. Principal Component Analysis for Alteration Mapping. Photogrammetric Engineering and Remote Sensing 57, 1163-1169.

Lu, D., Weng, Q., 2007. A survey of image classification methods and techniques for improving classification performance. International journal of Remote sensing 28, 823-870.

Luc, B., Deronde, B., Kempeneers, P., Debruyn, W., Provoost, S., Sensing, R., Observation, E., 2005. Optimized Spectral Angle Mapper classification of spatially heterogeneous dynamic dune vegetation, a case study along the Belgian coastline, The 9th International Symposium on Physical Measurements and Signatures in Remote Sensing. ISPMSRS. Beijing. https://core. ac. uk/display/29279595.

Luo, G., Chen, G., Tian, L., Qin, K., Qian, S.-E., 2016a. Minimum noise fraction versus principal component analysis as a preprocessing step for hyperspectral imagery denoising. Canadian Journal of Remote Sensing 42, 106-116.

Luo, R., Liao, W., Zhang, H., Pi, Y., Philips, W., 2016b. Spectral-spatial classification of hyperspectral images with semi-supervised graph learning, Image and Signal Processing for Remote Sensing XXII. International Society for Optics and Photonics, p. 100040T.

MacKenzie, D., Blakemore, H., Craw, D., 2016. Paragenesis of orogenic mineralisation in the Reefton gold field, West Coast Region. Australasian Institute of Mining and Metallurgy Monograph 31, 125-132.

MacKenzie, D., Craw, D., 1993. Structural control of gold-scheelite mineralisation in a major normal fault system, Barewood, eastern Otago, New Zealand. Journal of Geology and Geophysics 36, 437-445.

MacKenzie, D., Craw, D., Blakemore, H., 2014. Multi-stage ore formation at the Reefton goldfield, New Zealand, Aust Inst Min Metall Conf, pp. 341-351.

MacKenzie, D.C., D, 2017. Geophysical Signals and Exploration for Orogenic Gold on the Low-grade Margins of the Otago Schist.

MacKenzie, D.J., Corner, N.G., Craw, D., 2006. Rise and Shine Shear Zone, Central Otago. Geology Exploration of New Zealand Mineral Deposits.

MacKenzie, D.J., Craw, D., 2007. Contrasting hydrothermal alteration mineralogy and gechemistry in the auriferous Rise & Shine Shear Zone, Otago New Zealand. New Zealand Journal of Geology and Geophysics 50, 67-69.

MacKenzie, D.J., Craw, D., Begbie, M., 2007. Mineralogy, geochemistry, and structural controls of a disseminated gold-bearing alteration halo around the schist-hosted Bullendale orogenic gold deposit, New Zealand. Journal of Geochemical Exploration 93, 160-176.

Mackie, C., Mackenzie, D.J., Craw, D., 2009. Structural and lithological controls on gold mineralisation at Oturehua on the northeastern margin of the Otago Schist, New Zealand. New Zealand Journal of Geology and Geophysics 52, 43-57.

Madambi, K., Moore, J., 2013. Technical Report for the Reefton Project. OceanaGold Corporation, Australia.

Magner, P., Dunphy, M., Silversmith, P., 1997. Wacker sampling as an effective gold exploration tool in the Reefton Goldfield, Greenland Group, West Coast, New Zealand, Proceedings, New Zealand Minerals and Mining Conference, Crown Minerals, Ministry of Commerce, pp. 105-109.

Malloch, K.R., Craw, D., Trumm, D., 2017. Arsenic mineralogy and distribution at the historic Alexander gold mine, Reefton goldfield, New Zealand. New Zealand Journal of Geology and Geophysics 60, 129-144.

Manning, B.A., Goldberg, S., 1997. Arsenic (III) and arsenic (V) adsorption on three California soils. Soil Science 162, 886-895.

Martin, A., Allibone, A., Blakemore, H., Blundell, C., Cox, S., Craw, D., Doyle, S., MacKenzie, D., Mortimer, N., Rattenbury, M., 2018. A new 1: 50 000 scale map and GIS dataset of the Hyde-Macraes Shear Zone.

Martin, A., Turnbull, R., Rattenbury, M., Cohen, D., Hoogewerff, J., Rogers, K., Baisden, W., Christie, A., 2016. The regional geochemical baseline soil survey of southern New Zealand: Design and initial interpretation. Journal of Geochemical Exploration 167, 70-82.

Mas, J.F., Flores, J.J., 2008. The application of artificial neural networks to the analysis of remotely sensed data. International Journal of Remote Sensing 29, 617-663.

Maxwell, A.E., Warner, T.A., Fang, F., 2018. Implementation of machine-learning classification in remote sensing: An applied review. International Journal of Remote Sensing 39, 2784-2817.

May, T.W., Wiedmeyer, R.H., 1998. A table of polyatomic interferences in ICP-MS. Journal of Atomic Spectroscopy 19, 150-155.

McComb, K.A., Craw, D., McQuillan, A.J., 2007. ATR-IR spectroscopic study of antimonate adsorption to iron oxide. Langmuir 23, 12125-12130.

McKeag, S., Craw, D., Norris, R., 1989. Origin and deposition of a graphitic schist-hosted metamorphogenic Au-W deposit, Macraes, East Otago, New Zealand. 24, 124-131.

McKinley, J.M., Hron, K., Grunsky, E.C., Reimann, C., de Caritat, P., Filzmoser, P., van den Boogaart, K.G., Tolosana-Delgado, R., 2016. The single component geochemical map: Fact or fiction? Journal of Geochemical Exploration 162, 16-28.

McQueen, K.G., Alorbi, A., Schifano, J.A., Cohen, D.R., 2021. Nickel Uptake by Cypress Pine (Callitris glaucophylla) in the Miandetta Area, Australia: Implications for Use in Biogeochemical Exploration. Minerals 11, 808.

Meer, F.v.d., 1996. Classification of remotely-sensed imagery using an indicator kriging approach: Application to the problem of calcite-dolomite mineral mapping. International Journal of Remote Sensing 17, 1233-1249.

Melgani, F., Bruzzone, L., 2004. Classification of hyperspectral remote sensing images with support vector machines. IEEE Transactions on Geoscience and Remote Sensing 42, 1778-1790.

Meng, X., Bao, Y., Ye, Q., Liu, H., Zhang, X., Tang, H., Zhang, X., 2021. Soil organic matter prediction model with satellite hyperspectral image based on optimized denoising method. Remote Sensing 13, 2273.

Meyer, J.M., Kokaly, R.F., Holley, E., 2022. Hyperspectral remote sensing of white mica: A review of imaging and point-based spectrometer studies for mineral resources, with spectrometer design considerations. Remote Sensing of Environment 275, 113000.

Mielke, C., Boesche, N., Rogass, C., Kaufmann, H., Gauert, C., de Wit, M., 2014. Spaceborne Mine Waste Mineralogy Monitoring in South Africa, Applications for Modern Push-Broom Missions: Hyperion/OLI and EnMAP/Sentinel-2. Remote Sensing 6, 6790-6816.

Milham, L., Craw, D., 2009. Two-stage structural development of a Paleozoic auriferous shear zone at the Globe-Progress deposit, Reefton, New Zealand. New Zealand Journal of Geology and Geophysics 52, 247-259.

Montreuil, J.-F., Corriveau, L., Grunsky, E.C., 2013. Compositional data analysis of hydrothermal alteration in IOCG systems, Great Bear magmatic zone, Canada: to each alteration type its own geochemical signature.

Moore, J., Doyle, S., 2015. Resource definition in the world-class Macraes gold mine, New Zealand, Proceedings, PACRIM Congress, AusIMM Publ Series, pp. 557-564.

Mortensen, J.K., Craw, D., MacKenzie, D.J., Gabites, J.E., Ulrich, T., 2010. Age and Origin of Orogenic Gold Mineralization in the Otago Schist Belt, South Island, New Zealand: Constraints from Lead Isotope and 40Ar/39Ar Dating Studies. Economic Geology 105, 77-793.

Mortimer, N., 2000. Metamorphic discontinuities in orogenic belts: example of the gernet-biotite-albite zone in the Otago Schist, New Zealand. International Journal of Earth Science 89, 295-306.

Mortimer, N., 2004. New Zealand's Geological Foundations. Gondwana Research 7, 261-272.

Mortimer, N., Craw, D., MacKenzie, D., Mortensen, J., Ring, U., Pitcairn, I., 2016. Cretaceous tectonics and gold mineralisation in the Otago Schist, New Zealand.

Mortimer, N., Rattenbury, M.S., King, P.R., Bland, K.J., Barrell, D.J.A., Bache, F., Begg, J.G., Campbell, H.J., Cox, S.C., Crampton, J.S., Edbrooke, S.W., Forsyth, P.J., Johnston, M.R., Jongens, R., Lee, J.M., Leonard, G.S., Raine, J.I., Skinner, D.N.B., Timm, C., Townsend, D.B., Tulloch, A.J., Turnbull, I.M., Turnbull, R.E., 2014. High-level stratigraphic scheme for New Zealand rocks. New Zealand Journal of Geology and Geophysics 57, 402-419.

Moses, W.J., Gitelson, A.A., Perk, R.L., Gurlin, D., Rundquist, D.C., Leavitt, B.C., Barrow, T.M., Brakhage, P., 2012. Estimation of chlorophyll-a concentration in turbid productive waters using airborne hyperspectral data. Water research 46, 993-1004.

Müller, K., Daus, B., Mattusch, J., Vetterlein, D., Merbach, I., Wennrich, R., 2013. Impact of arsenic on uptake and bio-accumulation of antimony by arsenic hyperaccumulator Pteris vittata. Environmental pollution 174, 128-133.

Muller, T., Craw, D., McQuillan, A.J., 2015. Arsenate and antimonate adsorption competition on 6-line ferrihydrite monitored by infrared spectroscopy. Applied Geochemistry 61, 224-232.

Murchie, S., Arvidson, R., Bedini, P., Beisser, K., Bibring, J.P., Bishop, J., Boldt, J., Cavender, P., Choo, T., Clancy, R.T., Darlington, E.H., Des Marais, D., Espiritu, R., Fort, D., Green, R., Guinness, E., Hayes, J., Hash, C., Heffernan, K., Hemmler, J., Heyler, G., Humm, D., Hutcheson, J., Izenberg, N., Lee, R., Lees, J., Lohr, D., Malaret, E., Martin, T., McGovern, J.A., McGuire, P., Morris, R., Mustard, J., Pelkey, S., Rhodes, E., Robinson, M., Roush, T., Schaefer, E., Seagrave, G., Seelos, F., Silverglate, P., Slavney, S., Smith, M., Shyong, W.J., Strohbehn, K., Taylor, H., Thompson, P., Tossman, B., Wirzburger, M., Wolff, M., 2007. Compact Reconnaissance Imaging Spectrometer for Mars (CRISM) on Mars Reconnaissance Orbiter (MRO). Journal of Geophysical Research 112.

Muriithi, F.K., 2015. Centerd log-ratio (clr) transformation and robust principal component analysis of long-term NDVI data reveal vegetation activity linked to climate processes. Climate 3, 135-149.

Mustard, J.F., Pieters, C.M., Isaacson, P.J., Head, J.W., Besse, S., Clark, R.N., Klima, R.L., Petro, N.E., Staid, M.I., Sunshine, J.M., Runyon, C.J., Tompkins, S., 2011. Compositional diversity and geologic insights of the Aristarchus crater from Moon Mineralogy Mapper data. Journal of Geophysical Research 116.

Mustard, J.F., Sunshine, J.M., 1999. Spectral analysis for earth science: investigations using remote sensing data. Remote sensing for the earth sciences: Manual of remote sensing 3, 251-307.

Naik, P., Dalponte, M., Bruzzone, L., 2021. Prediction of Forest Aboveground Biomass Using Multitemporal Multispectral Remote Sensing Data. Remote Sensing 13, 1282.

Naik, P., Kumar, A., 2021. A Stochastic Approach for Automatic Collection of Precise Training Data for a Soft Machine Learning Algorithm Using Remote Sensing Images, Soft Computing for Problem Solving. Springer, pp. 285-297.

Neal, L.C., Wilkinson, J.J., Mason, P.J., Chang, Z., 2018. Spectral characteristics of propylitic alteration minerals as a vectoring tool for porphyry copper deposits. Journal of Geochemical Exploration 184, 179-198.

Nemec, G., Babicka, J., Oborsky, A., 1936. Uber das Vorkommen von Gold in den Schachtelhalmen. International Academy of Science of Bohemia Bulletin Nos 1 7, 1-13.

Nidamanuri, R.R., Zbell, B., 2010. A method for selecting optimal spectral resolution and comparison metric for material mapping by spectral library search. Progress in Physical Geography 34, 47-58.

Northey, S.A., Mudd, G.M., Werner, T.T., Jowitt, S.M., Haque, N., Yellishetty, M., Weng, Z., 2017. The exposure of global base metal resources to water criticality, scarcity and climate change. Global Environmental Change 44, 109-124.

Notesco, G., Kopačková, V., Rojík, P., Schwartz, G., Livne, I., Ben Dor, E., 2014a. Mineral classification of land surface using multispectral LWIR and hyperspectral SWIR remote-sensing data. a case study over the Sokolov lignite open-pit mines, the Czech Republic. Remote Sensing 6, 7005-7025.

Notesco, G., Kopačková, V., Rojík, P., Schwartz, G., Livne, I., Dor, E., 2014b. Mineral Classification of Land Surface Using Multispectral LWIR and Hyperspectral SWIR Remote-Sensing Data. A Case Study over the Sokolov Lignite Open-Pit Mines, the Czech Republic. Remote Sensing 6, 7005-7025.

Notesco, G., Ogen, Y., Ben-Dor, E., 2015. Mineral Classification of Makhtesh Ramon in Israel Using Hyperspectral Longwave Infrared (LWIR) Remote-Sensing Data. Remote Sensing 7, 12282-12296.

Nude, P.M., Asigri, J.M., Yidana, S.M., Arhin, E., Foli, G., Kutu, J.M., 2012. Identifying Pathfinder Elements for Gold in Multi-Element Soil Geochemical Data from the Wa-Lawra Belt, Northwest Ghana: A Multivariate Statistical Approach. International Journal of Geosciences 03, 62-70.

Olesik, J.W., 1991. Elemental analysis using ICP-OES and ICP/MS. Journal of Analytical Chemistry 63, 12A-21A.

Othman, H., Qian, S.-E., 2006. Noise reduction of hyperspectral imagery using hybrid spatial-spectral derivative-domain wavelet shrinkage. IEEE Transactions on Geoscience and Remote Sensing 44, 397-408.

Pandit, C.M., Filippelli, G.M., Li, L., 2010. Estimation of heavy-metal contamination in soil using reflectance spectroscopy and partial least-squares regression. International Journal of Remote Sensing 31, 4111-4123.

Parsa, M., 2021. A data augmentation approach to XGboost-based mineral potential mapping: An example of carbonate-hosted ZnPb mineral systems of Western Iran. Journal of Geochemical Exploration, 106811.

Patinha, C., Ferreira da Silva, E., Cardoso Fonseca, E., 2004. Mobilisation of arsenic at the Talhadas old mining area—Central Portugal. Journal of Geochemical Exploration 84, 167-180.

Paul, D., Bair, E., Hastie, T., Tibshirani, R., 2008. "Preconditioning" for feature selection and regression in high-dimensional problems. The Annals of Statistics 36, 1595-1618.

Payet, V., Flahaut, J., Ito, G., Barthez, M., Breton, S., 2020. Automated denoising for mineral identification on hyperspectral data, The Eleventh Moscow Solar System Symposium 11M-S3, pp. 79-80.

Peters, W.C., 1987. Exploration and mining geology.

Pirajno, F., 2012. Hydrothermal mineral deposits: principles and fundamental concepts for the exploration geologist. Springer Science & Business Media.

Pirajno, F., Bentley, P.N., 2012. Greisen-related scheelite, gold and sulphide mineralisation at Kirwans Hili and Bateman Creek, Reefton district, Westland, New Zealand. New Zealand Journal of Geology and Geophysics 28, 97-109.

Pitcairn, I.K., Teagle, D.A.H., Craw, D., Olivio, G.R., Kerrich, 2006. Sources of Metals and Fluids in Orogenic Gold Deposits: Insights from the Otago and Alpine Schists, New Zealnd. Economic Geology 101, 1525-1546.

Pour, A.B., Hashim, M., 2011. Identification of hydrothermal alteration minerals for exploring of porphyry copper deposit using ASTER data, SE Iran. Journal of Asian Earth Sciences 42, 1309-1323.

Pratas, J., Prasad, M.N.V., Freitas, H., Conde, L., 2005. Plants growing in abandoned mines of Portugal are useful for biogeochemical exploration of arsenic, antimony, tungsten and mine reclamation. Journal of Geochemical Exploration 85, 99-107.

Pullanagari, R., Kereszturi, G., Yule, I., 2018. Integrating Airborne Hyperspectral, Topographic, and Soil Data for Estimating Pasture Quality Using Recursive Feature Elimination with Random Forest Regression. Remote Sensing 10.

Pullanagari, R., Kereszturi, G., Yule, I.J., Ghamisi, P., 2017a. Assessing the performance of multiple spectral–spatial features of a hyperspectral image for classification of urban land cover classes using support vector machines and artificial neural network. Journal of Applied Remote Sensing 11.

Pullanagari, R.R., Kereszturi, G., Yule, I., 2017b. Quantification of dead vegetation fraction in mixed pastures using AisaFENIX imaging spectroscopy data. International journal of applied earth observation and geoinformation 58, 26-35.

Pullanagari, R.R., Kereszturi, G., Yule, I.J., 2016. Mapping of macro and micro nutrients of mixed pastures using airborne AisaFENIX hyperspectral imagery. ISPRS Journal of Photogrammetry and Remote Sensing 117, 1-10.

Pullanagari, R.R.Y., I.J.;Tuohy, M.P.; Hedley, M.J.; Dynes, R.A.; King, W.M.;, 2012. In-field hyperspectral proximal sensing for estimating quality parameters of mixed pasture. Precision Agric 13, 351-369.

Rasti, B., Ghamisi, P., Gloaguen, R., 2021. OptFus: Optical Sensor Fusion For The Classification of Multi-source Data: Application to Mineralogical Mapping. IEEE Geoscience and Remote Sensing Letters.

Rasti, B., Hong, D., Hang, R., Ghamisi, P., Kang, X., Chanussot, J., Benediktsson, J.A., 2020. Feature Extraction for Hyperspectral Imagery: The Evolution From Shallow to Deep: Overview and Toolbox. IEEE Geoscience and Remote Sensing Magazine 8, 60-88.

Rasti, B., Scheunders, P., Ghamisi, P., Licciardi, G., Chanussot, J., 2018. Noise reduction in hyperspectral imagery: Overview and application. Remote Sensing 10, 482.

Rasti, B., Sveinsson, J.R., Ulfarsson, M.O., Benediktsson, J.A., 2013. Hyperspectral image denoising using first order spectral roughness penalty in wavelet domain. IEEE Journal of Selected Topics in Applied Earth Observations and Remote Sensing 7, 2458-2467.

Rasti, B., Ulfarsson, M.O., Sveinsson, J.R., 2016. Hyperspectral feature extraction using total variation component analysis. IEEE Transactions on Geoscience and Remote Sensing 54, 6976-6985.

Rathod, P.H., Brackhage, C., Müller, I., Van der Meer, F.D., Noomen, M.F., 2018. Assessing Metal-Induced Changes in the Visible and Near-Infrared Spectral Reflectance of Leaves: A Pot Study with Sunflower (Helianthus annuus L.). Journal of the Indian Society of Remote Sensing 46, 1925-1937.

Rathod, P.H., Brackhage, C., Van der Meer, F.D., Müller, I., Noomen, M.F., Rossiter, D.G., Dudel, G.E., 2015. Spectral changes in the leaves of barley plant due to phytoremediation of metals—Results from a pot study. European Journal of Remote Sensing 48, 283-302.

Rattenbury, M.S., Stewart, M., 2000. Structural setting of the Globe-Progress and Blackwater gold mines, Reefton goldfield, New Zealand. New Zealand Journal of Geology and Geophysics 43, 435-445.

Rencz, A.N.W., G.P., 1989. Biogeochemistry and LANDSAT TM data: application to gold exploration in northern New Brunswick. Journal of Geochemical Exploration, 271-284.

Richter, R., Schläpfer, D., 2002. Geo-atmospheric processing of airborne imaging spectrometry data. Part 2: atmospheric/topographic correction. International Journal of Remote Sensing 23, 2631-2649.

Richter, R., Schläpfer, D., 2010. Geo-atmospheric processing of airborne imaging spectrometry data. Part 2: Atmospheric/topographic correction. International Journal of Remote Sensing 23, 2631-2649.

Richter, R., Schläpfer, D., 2011. Atmospheric/topographic correction for airborne imagery. ATCOR-4 user guide, 565-502.

Richter, R., Schläpfer, D., 2019. Atmospheric and topographic correction (ATCOR theoretical background document). DLR IB, 564-503.

Rincheval, M., Cohen, D.R., Hemmings, F.A., 2019a. Biogeochemical mapping of metal contamination from mine tailings using field-portable XRF. Science of Total Environment 662, 404-413.

Rincheval, M., Cohen, D.R., Hemmings, F.A., 2019b. Biogeochemical mapping of metal contamination from mine tailings using field-portable XRF. Science of the Total Environment 662, 404-413.

Robinson, B.A., 2018. Structural setting and paragenesis of the mineralised veins in the Waipori goldfield, southeast Otago, New Zealand, Department og Geology. University of Otago, Dunedin.

Robson, T.C., Braungardt, C.B., Keith-Roach, M.J., Rieuwerts, J.S., Worsfold, P.J., 2013. Impact of arsenopyrite contamination on agricultural soils and crops. Journal of Geochemical Exploration 125, 102-109.

Rodriguez-Gomez, C., Kereszturi, G., Reeves, R., Rae, A., Pullanagari, R., Jeyakumar, P., Procter, J., 2021. Lithological mapping of Waiotapu Geothermal Field (New Zealand) using hyperspectral and thermal remote sensing and ground exploration techniques. Geothermics 96, 102195.

Rodríguez, G.A., Bierlein, F.P., 2003. Nature and dimension of orogenic gold-related hydrothermal alteration at Minas Azules, NW Argentina, Society for Geology Applied to Mineral Deposits Biennial Meeting 2003. Millpress Science, pp. 807-810.

Rogge, D.R., Benoit; Segl, Karl; Grant, Brian; Feng, Jilu;, 2014. Mapping of NiCu–PGE ore hosting ultramafic rocks using airborne and simulated EnMAP hyperspectral imagery, Nunavik, Canada. Remote Sensing of Environment, 302-317.

Rojas, R., 2013. Neural networks: a systematic introduction. Springer Science & Business Media.

Roshanravan, B., Kreuzer, O.P., Mohammadi, S., Bruce, M., Davis, J., Briggs, M., 2021. Cuckoo optimization algorithm for support vector regression potential analysis: An example from the Granites-Tanami Orogen, Australia. Journal of Geochemical Exploration 230, 106858.

Rosipal, R., Trejo, L.J., 2001. Kernel partial least squares regression in reproducing kernel hilbert space. Journal of machine learning research 2, 97-123.

Roudier, P., Burge, O.R., Richardson, S.J., McCarthy, J.K., Grealish, G.J., Ausseil, A.-G., 2020. National scale 3D mapping of soil pH using a data augmentation approach. Remote Sensing 12, 2872.

Ruffin, C., King, R.L., Younan, N.H., 2013. A Combined Derivative Spectroscopy and Savitzky-Golay Filtering Method for the Analysis of Hyperspectral Data. GIScience & Remote Sensing 45, 1-15.

Sabins, F.F., 1999. Remote sensing for mineral exploration. Ore Geology Reviews 14, 157-183.

Salama, W., Anand, R.R., Verrall, M., 2016. Mineral exploration and basement mapping in areas of deep transported cover using indicator heavy minerals and paleoredox fronts, Yilgarn Craton, Western Australia. Ore Geology Reviews 72, 485-509.

Santos-Jallath, J., Castro-Rodríguez, A., Huezo-Casillas, J., Torres-Bustillos, L., 2012. Arsenic and heavy metals in native plants at tailings impoundments in Queretaro, Mexico. Physics and Chemistry of the Earth, Parts A/B/C 37-39, 10-17.

Sato, M., Mooney, H.M., 1960. The electrochemical mechanism of sulfide self-potentials. Journal of Geophysics 25, 226-249.

Savitzky, A., Golay, M.J.E., 1964. Smoothing an dDifferentiation of Data by Simplified Least Squares Procedures. Analytical Chemistry 36, 1627-1639.

Schläpfer, D., Richter, R., 2002. Geo-atmospheric processing of airborne imaging spectrometry data. Part 1: parametric orthorectification. International Journal of Remote Sensing 23, 2609-2630.

Senesi, G.S., Manzari, P., Consiglio, A., De Pascale, O., 2018. Identification and classification of meteorites using a handheld LIBS instrument coupled with a fuzzy logic-based method. Journal of Analytical Atomic Spectrometry 33, 1664-1675.

Shahid, M., Dumat, C., Khalid, S., Schreck, E., Xiong, T., Niazi, N.K., 2017. Foliar heavy metal uptake, toxicity and detoxification in plants: A comparison of foliar and root metal uptake. Journal of Hazardous Materials 325, 36-58.

Shanmugam, S., Srinivasa Perumal, P., 2014. Spectral matching approaches in hyperspectral image processing. International Journal of Remote Sensing 35, 8217-8251.

Sheffield, C., 1985. Selecting Band Combinations from Multi Spectral Data. Photogrammetric Engineering and Remote Sensing 58, 681-687.

Shi, T., Wang, J., Chen, Y., Wu, G., 2016. Improving the prediction of arsenic contents in agricultural soils by combining the reflectance spectroscopy of soils and rice plants. International journal of applied earth observation and geoinformation 52, 95-103.

Shin, Yu, Wang, Kim, Koh, 2019. Investigation of Spectral Variation of Pine Needles as an Indicator of Arsenic Content in Soils. Minerals 9.

Shrestha, G., Calvelo-Pereira, R., Roudier, P., Martin, A., Turnbull, R., Kereszturi, G., Jeyakumar, P., Anderson, C., 2022. Quantification of multiple soil trace elements by combining portable X-ray fluorescence and reflectance spectroscopy. Geoderma 409, 115649.

Simpson, M.P., Christie, A.B., 2019. Hydrothermal alteration mineralogical footprints for New Zealand epithermal Au-Ag deposits. New Zealand Journal of Geology and Geophysics 62, 483-512.

Sims, D.A., Gamon, J.A., 2002. Relationships between leaf pigment content and spectral reflectance across a wide range of species, leaf structures and developmental stages. Remote sensing of environment 81, 337-354.

Singh, D., Prasad, G., Rupainwar, D., 1996. Adsorption technique for the treatment of As (V)-rich effluents. Colloids and Surfaces A: Physicochemical and Engineering Aspects 111, 49-56.

Smith, E., 1998. Arsenic in the environment: a review. Advances in agronomy.

Souza, M.V., Horbe, A.M.C., da Silva, B.C., Peixoto, S.F., Castro, R.T., 2021. Regolith LANDSAT-8/OLI and Hyperion/EO-1 images classification in midwest of Brazil. Journal of South American Earth Sciences 111, 103460.

Spuller, C., Weigand, H., Marb, C., 2007. Trace metal stabilisation in a shooting range soil: Mobility and phytotoxicity. Journal of Hazardous Materials 141, 378-387.

Staenz, K., Schwarz, J., Vernaccini, L., Vachon, F., Nadeau, C., 1999. Classification of hyperspectral agricultural data with spectral matching techniques. Government of Canada.

Stednick, J., Klem, R., Riese, W., 1987. Temporal variation of metal concentrations in biogeochemical samples over the Royal Tiger Mine, Colorado, part I: Within year variation. Journal of Geochemical Exploration 29, 75-88.

Steinberg, A., Chabrillat, S., Stevens, A., Segl, K., Foerster, S., 2016. Prediction of Common Surface Soil Properties Based on Vis-NIR Airborne and Simulated EnMAP Imaging Spectroscopy Data: Prediction Accuracy and Influence of Spatial Resolution. Remote Sensing 8.

Strangway, D., Swift Jr, C., Holmer, R., 1973. The application of audio-frequency magnetotellurics (AMT) to mineral exploration. Journal of Geophysics 38, 1159-1175.

Su, J., Yi, D., Liu, C., Guo, L., Chen, W.-H., 2017. Dimension reduction aided hyperspectral image classification with a small-sized training dataset: experimental comparisons. Sensors 17, 2726.

Sugiyama, M., Idé, T., Nakajima, S., Sese, J., 2010. Semi-supervised local Fisher discriminant analysis for dimensionality reduction. Journal of Machine Learning 78, 35.

Swayze, G.A., Clark, R.N., Goetz, A.F., Livo, K.E., Breit, G.N., Kruse, F.A., Sutley, S.J., Snee, L.W., Lowers, H.A., Post, J.L., 2014. Mapping advanced argillic alteration at Cuprite, Nevada, using imaging spectroscopy. Economic Geology 109, 1179-1221.

Tay, S.L., Scott, J.M., Craw, D., 2021. Natural rehabilitation of arsenic-rich historical tailings at the Alexander mine, Reefton, New Zealand. New Zealand Journal of Geology and Geophysics 64, 558-569.

Teagle, D.A.H.N., Richard J.; Craw Dave, 1990. Structural Controls on Gold-Bearing Quartz Mineralization in a Duplex

Thrust System, Hyde-Macraes Shear Zone, Otago Schist, New Zealand. Economic Geology 85, 1711-1719.

Thiele, S.T., Bnoulkacem, Z., Lorenz, S., Bordenave, A., Menegoni, N., Madriz, Y., Dujoncquoy, E., Gloaguen, R., Kenter, J., 2021a. Mineralogical Mapping with Accurately Corrected Shortwave Infrared Hyperspectral Data Acquired Obliquely from UAVs. Remote Sensing 14, 5.

Thiele, S.T., Lorenz, S., Kirsch, M., Acosta, I.C.C., Tusa, L., Herrmann, E., Möckel, R., Gloaguen, R., 2021b. Multi-scale, multi-sensor data integration for automated 3-D geological mapping. Ore Geology Reviews 136, 104252.

Thomas, R., 2013. Practical guide to ICP-MS: a tutorial for beginners. CRC press.

Timperley, M.H., 1971. Biogeochemical studies of nickel and copper in New Zealand: a thesis presented in partial fulfilment of the requirements for the degree of Doctor of Philosophy at Massey University. Massey University.

Timperley, M.H., Brooks, R.R., Peterson, P.J., 1970. Prospecting for copper and nickel in New Zealand by statistical analysis of biogeochemical data. Economic Geology 65, 505-510.

Tomašević, M., Vukmirović, Z., Rajšić, S., Tasić, M., Stevanović, B., 2005. Characterization of trace metal particles deposited on some deciduous tree leaves in an urban area. Chemosphere 61, 753-760.

Townsend, P.A., Foster, J.R., Chastain, R.A., Currie, W.S., 2003. Application of imaging spectroscopy to mapping canopy nitrogen in the forests of the central Appalachian Mountains using Hyperion and AVIRIS. IEEE Transactions on Geoscience and Remote Sensing 41, 1347-1354.

Tripathi, P., Garg, R., 2021. Integration of Raman, emission, and reflectance spectroscopy for earth and lunar mineralogy. Journal of Applied Remote Sensing 15, 036502.

Tsai, F., Philpot, W., 1998. Derivative analysis of Hyprspectral Data. Remote Sensing of Environment 66, 41-51.

Turnbull, I., Mortimer, N., Craw, D., 2001. Textural zones in the Haast Schist—a reappraisal. New Zealand Journal of Geology and Geophysics 44, 171-183.

Ullah, S., Schlerf, M., Skidmore, A.K., Hecker, C., 2012. Identifying plant species using mid-wave infrared (2.5–6 µm) and thermal infrared (8–14 µm) emissivity spectra. Remote Sensing of Environment 118, 95-102.

Uzu, G., Sobanska, S., Sarret, G., Munoz, M., Dumat, C., 2010. Foliar lead uptake by lettuce exposed to atmospheric fallouts. Environmental science & technology 44, 1036-1042.

van der Meer, F., Kopačková, V., Koucká, L., van der Werff, H.M., van Ruitenbeek, F.J., Bakker, W.H., 2018a. Wavelength feature mapping as a proxy to mineral chemistry for investigating geologic systems: An example from the Rodalquilar epithermal system. International journal of applied earth observation and geoinformation 64, 237-248.

van der Meer, F., Kopačková, V., Koucká, L., van der Werff, H.M.A., van Ruitenbeek, F.J.A., Bakker, W.H., 2018b. Wavelength feature mapping as a proxy to mineral chemistry for investigating geologic systems: An example from the Rodalquilar epithermal system. International Journal of Applied Earth Observation and Geoinformation 64, 237-248.

van der Meer, F.D., 2001. Spectral Matching using pixel cross-correlograms for the analysis of LANDSAT TM data. JAG 3.

van der Meer, F.D., 2018. Near-infrared laboratory spectroscopy of mineral chemistry_ A review. International Journal of Applied Earth Observation and Geoinformation 65, 71-78.

van der Meer, F.D., Bakker, W., 1997. Cross Correlogram Spectral Matching: Application to Surface Mineralogical Mapping by Using AVIRIS Data from Cuprite, Nevada. Remote Sensing Environment.

van der Meer, F.D., Bakker, W., 1998. Validated surface mineralogy from high-spectral resolution remote sensing: a review and a novel approach applied to gold exploration using AVIRIS data. Surface mineralogy from high-resolution remote sensing 10, 112-119.

van der Meer, F.D., van der Werff, H.M.A., van Ruitenbeek, F.J.A., Hecker, C.A., Bakker, W.H., Noomen, M.F., van der Meijde, M., Carranza, E.J.M., Smeth, J.B.d., Woldai, T., 2012. Multi- and hyperspectral geologic remote sensing: A review. International Journal of Applied Earth Observation and Geoinformation 14, 112-128.

van Ruitenbeek, F.J.A., Bakker, W.H., van der Werff, H.M.A., Zegers, T.E., Oosthoek, J.H.P., Omer, Z.A., Marsh, S.H., van der Meer, F.D., 2014. Mapping the wavelength position of deepest absorption features to explore mineral diversity in hyperspectral images. Planetary and Space Science 101, 108-117.

van Ruitenbeek, F.J.A., Cudahy, T., Hale, M., van der Meer, F.D., 2005. Tracing fluid pathways in fossil hydrothermal systems with near-infrared spectroscopy. Geology 33.

Vanonckelen, S., Lhermitte, S., Van Rompaey, A., 2013. The effect of atmospheric and topographic correction methods on land cover classification accuracy. International Journal of Applied Earth Observation and Geoinformation 24, 9-21.

Vapnik, V., 1998. The support vector method of function estimation, Nonlinear modeling. Springer, pp. 55-85.

Varmuza, K., Filzmoser, P., 2016. Introduction to multivariate statistical analysis in chemometrics. CRC press.

Villa, A., Chanussot, J., Benediktsson, J.A., Jutten, C., Dambreville, R., 2013. Unsupervised methods for the classification of hyperspectral images with low spatial resolution. Pattern Recognition 46, 1556-1568.

Vishnu, S., Nidamanuri, R.R., Bremananth, R., 2013. Spectral material mapping using hyperspectral imagery: a review of spectral matching and library search methods. Geocarto International 28, 171-190.

Wang, F.G., Jay.; Zha, Yong., 2018. Hyperspectral sensing of heavy metals in soil and vegetation: Feasibility and challenges. ISPRS Journal of Photogrammetry and Remote Sensing 136, 79-84.

Wang, G., Carr, T.R., Ju, Y., Li, C., 2014. Identifying organic-rich Marcellus Shale lithofacies by support vector machine classifier in the Appalachian basin. Computers & Geosciences 64, 52-60.

Wang, L.Z., Chunhui, 2016. Hyperspectral Image Processing-Springer-Verlag Berlin Heidelberg. Springer.

Wang, Z., He, B., 2011. Locality perserving projections algorithm for hyperspectral image dimensionality reduction, 2011 19th International Conference on Geoinformatics. IEEE, pp. 1-4.

Ward, N., Brooks, R., 1978. Gold in some New Zealand plants. New Zealand Journal of Botany 16, 175-177.

Warner, T.A., Foody, G.M., Nellis, M.D., 2009. The SAGE handbook of remote sensing. Sage Publications.

Warner, T.A., Shank, M.C., 1997. Spatial autocorrelation analysis of hyperspectral imagery for feature selection. Remote Sensing of Environment 60, 58-70.

Warren, H.V., R.E., D., Barakso, J., 1968. Arsenic content of Doughlas fir as a giude to some gold, silver and metal deposits. Canadian Mining and Metallurgical Bulletin 61, 860-&.

Wei, L., Pu, H., Wang, Z., Yuan, Z., Yan, X., Cao, L., 2020. Estimation of Soil Arsenic Content with Hyperspectral Remote Sensing. Sensors (Basel) 20.

Wei, Q., Bioucas-Dias, J., Dobigeon, N., Tourneret, J.-Y., 2015. Hyperspectral and multispectral image fusion based on a sparse representation. IEEE Transactions on Geoscience and Remote Sensing 53, 3658-3668.

Weightman, E., Craw, D., Snow, T., Christenson, H., Kerr, G., 2021. Stratigraphy and mineralogy of tailings at Macraes gold mine, southern New Zealand. New Zealand Journal of Geology and Geophysics, 1-17.

Whitehead, N., Brooks, R., Coote, G., 1971. GAMMA RADIATION OF SOME PLANTS AND SOILS FROM A URANIFEROUS AREA IN NEW ZEALAND. Massey Univ., Palmerston North, NZ.

Williams, G.J., 1974. Economic geology of New Zealand.

Wilson, S.C., Lockwood, P.V., Ashley, P.M., Tighe, M., 2010. The chemistry and behaviour of antimony in the soil environment with comparisons to arsenic: a critical review. Environmental pollution 158, 1169-1181.

Winsor, C., 1991. The relationship between the Hyde-Macraes Shear Zone, deformation episodes, and gold mineralisation potential in eastern Otago, New Zealand. Jounrnal of Geology and Geophysics 34, 237-245.

Wold, S., Sjöström, M., Eriksson, L., 2001. PLS-regression: a basic tool of chemometrics. Chemometrics and intelligent laboratory systems 58, 109-130.

Wu, C., Niu, Z., Tang, Q., Huang, W., 2008. Estimating chlorophyll content from hyperspectral vegetation indices: Modeling and validation. Agricultural and forest meteorology 148, 1230-1241.

Wu, J.-z., Yan, W.-d., Ni, W.-p., Bian, H., 2013. Feature extraction for hyperspectral data based on MNF and singular value decomposition, 2013 IEEE International Geoscience and Remote Sensing Symposium-IGARSS. IEEE, pp. 1430-1433.

Xi, J., He, M., Lin, C., 2010. Adsorption of antimony (V) on kaolinite as a function of pH, ionic strength and humic acid. Environmental Earth Sciences 60, 715-722.

Xiong, S.-q., Zhou, F.-h., Yao, Z.-x., XUE, D.-j., 2007. Aero magnetic survey in central and western Qinghai-Tibet Plateau. Journal of Geophysical and Geochemical Exploration 5.

Xu, Y.M.H.P.S., 2014. Study on identification of altered rock in hyperspectral imagery using spectrum of field object. Ore Geology Reviews, 584-595.

Yang, H., Du, Q., Ma, B., 2010. Decision Fusion on Supervised and Unsupervised Classifiers for Hyperspectral Imagery. IEEE Geoscience and Remote Sensing Letters 7, 875-879.

Yokoya, N., Grohnfeldt, C., Chanussot, J., 2017. Hyperspectral and multispectral data fusion: A comparative review of the recent literature. IEEE Geoscience and Remote Sensing Magazine 5, 29-56.

Yousefi, M., Tabatabaei, S.H., Rikhtehgaran, R., Pour, A.B., Pradhan, B., 2021. Application of Dirichlet Process and Support Vector Machine Techniques for Mapping Alteration Zones Associated with Porphyry Copper Deposit Using ASTER Remote Sensing Imagery. Minerals 11, 1235.

Yu, L., Porwal, A., Holden, E.-J., Dentith, M.C., 2012. Towards automatic lithological classification from remote sensing data using support vector machines. Computers & Geosciences 45, 229-239.

Yuen, P.W.T., Killey, A., Hobson, S., Bishop, G., 2004. Atmospheric Correction Preprocessing and Techniques in Hyperspectral Remote Sensing, 1st EMRS DTC Technical Conference.

Yule, I., Pullanagari, R., Irwin, M., McVeagh, P., Kereszturi, G., White, M., Manning, M., 2015. Mapping nutrient concentration in pasture using hyperspectral imaging. Journal of New Zealand Grasslands, 47-50.

Zengin, F.K., Munzuroglu, O., 2005. Effects of some heavy metals on content of chlorophyll, proline and some antioxidant chemicals in bean (Phaseolus vulgaris L.) seedlings. Acta Biologica Cracoviensia Series Botanica 47, 157-164.

Zhai, Y., Zhang, L., Wang, N., Guo, Y., Cen, Y., Wu, T., Tong, Q., 2016. A modified locality-preserving projection approach for hyperspectral image classification. IEEE Geoscience and Remote Sensing Letters 13, 1059-1063.

Zhang, E., Zhang, X., Yang, S., Wang, S., 2013a. Improving hyperspectral image classification using spectral information divergence. IEEE Geoscience and Remote Sensing Letters 11, 249-253.

Zhang, H., He, W., Zhang, L., Shen, H., Yuan, Q., 2013b. Hyperspectral image restoration using low-rank matrix recovery. IEEE transactions on geoscience and remote sensing 52, 4729-4743.

Zhang, S., Fei, T., You, X., Wan, Y., Wang, Y., Bian, M., 2021. Two hyperspectral indices for detecting cadmium and lead contamination from arice canopy spectrum. Land Degradation & Development 32, 66-78.

Zhou, C., Chen, S., Zhang, Y., Zhao, J., Song, D., Liu, D., 2018. Evaluating metal effects on the reflectance spectra of plant leaves during different seasons in post-mining areas, China. Remote Sensing 10, 1211.

Zhou, Q., Zhou, H., Zhou, Q., Yang, F., Luo, L., 2014. Structure damage detection based on random forest recursive feature elimination. Mechanical Systems and Signal Processing 46, 82-90.

Zhuang, L., Ng, M.K., 2020. Hyperspectral Mixed Noise Removal By $\ell _1 $-Norm-Based Subspace Representation. IEEE Journal of Selected Topics in Applied Earth Observations and Remote Sensing 13, 1143-1157.

Zou, H., 2006. The adaptive lasso and its oracle properties. Journal of the American statistical association 101, 1418-1429.

Zuzana, L., Lukáš, B., Lucie, K., Veronika, K., Markéta, P., Jan, M., Aleš, K., Monika, K., Jana, A., 2013. Detection of multiple stresses in Scots pine growing at post-mining sites using visible to near-infrared spectroscopy. Environmental Science: Processes & Impacts 15, 2004-2015.

MASSEY UNIVERSITY
TE KUNENGA KI PŪREHUROA
UNIVERSITY OF NEW ZEALAND

GRADUATE
RESEARCH
SCHOOL

STATEMENT OF CONTRIBUTION
DOCTORATE WITH PUBLICATIONS/MANUSCRIPTS

We, the candidate and the candidate's Primary Supervisor, certify that all co-authors have consented to their work being included in the thesis and they have accepted the candidate's contribution as indicated below in the *Statement of Originality*.

Name of candidate:	Rupsa Chakraborty
Name/title of Primary Supervisor:	Gabor Kereszturi

In which chapter is the manuscript /published work: Chapter 3

Please select one of the following three options:

● The manuscript/published work is published or in press

- Please provide the full reference of the Research Output:

Chakraborty, R., Kereszturi, G., Pullanagari, R., Durance, P., Ashraf, S., Anderson, C., 2022. Mineral prospecting from biogeochemical and geological information using hyperspectral remote sensing-Feasibility and challenges. Journal of Geochemical Exploration, 106900.

○ The manuscript is currently under review for publication – please indicate:

- The name of the journal:
- The percentage of the manuscript/published work that was contributed by the candidate:
- Describe the contribution that the candidate has made to the manuscript/published work:

○ It is intended that the manuscript will be published, but it has not yet been submitted to a journal

Candidate's Signature:	Rupsa Chakraborty Digitally signed by Rupsa Chakraborty Date: 2022.09.15 13:26:06 +12'00'
Date:	15-Sep-2022
Primary Supervisor's Signature:	Gabor Kereszturi Digitally signed by Gabor Kereszturi Date: 2022.09.15 13:30:14 +12'00'
Date:	15-Sep-2022

This form should appear at the end of each thesis chapter/section/appendix submitted as a manuscript/ publication or collected as an appendix at the end of the thesis.

MASSEY UNIVERSITY
TE KUNENGA KI PŪREHUROA
UNIVERSITY OF NEW ZEALAND

GRADUATE
RESEARCH
SCHOOL

STATEMENT OF CONTRIBUTION
DOCTORATE WITH PUBLICATIONS/MANUSCRIPTS

We, the candidate and the candidate's Primary Supervisor, certify that all co-authors have consented to their work being included in the thesis and they have accepted the candidate's contribution as indicated below in the *Statement of Originality*.

Name of candidate:	Rupsa Chakraborty
Name/title of Primary Supervisor:	Gabor Kereszturi

In which chapter is the manuscript /published work: Chapter 4

Please select one of the following three options:

○ The manuscript/published work is published or in press

- Please provide the full reference of the Research Output:

● The manuscript is currently under review for publication – please indicate:

- The name of the journal:

Journal of Geochemical Exploration

- The percentage of the manuscript/published work that was contributed by the candidate: 80.00

- Describe the contribution that the candidate has made to the manuscript/published work:

Methodology, Analysis/Interpretation and Writing

○ It is intended that the manuscript will be published, but it has not yet been submitted to a journal

Candidate's Signature:	Rupsa Chakraborty Digitally signed by Rupsa Chakraborty Date: 2022.09.15 13:27:18 +12'00'
Date:	15-Sep-2022
Primary Supervisor's Signature:	Gabor Kereszturi Digitally signed by Gabor Kereszturi Date: 2022.09.15 13:32:20 +12'00'
Date:	15-Sep-2022

This form should appear at the end of each thesis chapter/section/appendix submitted as a manuscript/ publication or collected as an appendix at the end of the thesis.